Scattering of atoms and diatomic molecules from non-metal surfaces

A thesis submitted for the degree of:
Doctor in Chemistry

Candidate:
Alberto Pablo Sánchez Muzas

Supervisors:
Dr. Fernando Martín
Dr. Cristina Díaz

Departamento de Química
Facultad de Ciencias
Universidad Autónoma de Madrid
(Madrid, Spain)

April 11, 2016

RESUMEN

Para poder alcanzar conclusiones fiables en ciencia de superficies, necesitamos tanto información extraída de estudios teóricos como de estudios experimentales. Desde el punto de vista de un científico teórico, es difícil obtener resultados precisos sin ningún tipo de información de origen experimental previa a la simulación del sistema de interés, sobretodo, si poco se sabe sobre la estructura de la propia superficie que interviene en la interacción. Los cálculos necesarios para simular sistemas gas-superficie requieren típicamente mucho tiempo de computación. Debido a esto, se han de tomar un buen número de aproximaciones ideales. Por lo tanto, la comparación con datos experimentales ayudará a mejorar las herramientas teóricas disponibles para llegar a un buen equilibrio entre la precisión de los cálculos frente al tiempo de computación que consumirán. Desde el punto de vista de un científico experimental, es difícil entender los eventos que ocurren a escala atómica en un determinado experimento sin ninguna guía teórica. De hecho, a veces los modelos experimentales son demasiado simples, pudiendo aquí tratamientos teóricos más complejos incluso mejorar futuras medidas experimentales. Como resultado, la ciencia de superficies en un entorno perfecto para la colaboración teoría-experimento.

Una de los más recientes tópicos abiertos en la ciencia de superficies en donde la colaboración teoría-experimento es prometedora, es el estudio de la difracción de proyectiles rápidos en condiciones de incidencia rasante. El surgimiento de esta nueva técnica de análisis de superficies, ha revitalizado el estudio de la interacción de proyectiles no cargados con superficies no metálicas. En particular, el entendimiento de experimentos GIFAD* ha animado a científicos teóricos a desarrollar modelos cuánticos detallados para estudiar esta clase de eventos. Sin embargo, estas simulaciones teóricas presentan un gran desafío debido a las enormes energías que poseen los proyectiles atómicos y moleculares involucrados, bajo estas condiciones.

Para reducir el coste computacional de estos cálculos, se ha venido utilizando con asiduidad la aproximación de la canalización axial superficial (ASC†) [1–3] y métodos de dinámica semi-cuánticos [4–6]. Dentro de la aproximación ASC, la dimensionalidad del sistema es reducida a dos dimensiones (2D). Esto se consigue considerando que el proyectil *siente* un potencial promediado a lo largo de la dirección de incidencia. En la literatura [7, 8], se ha constatado ya que esta aproximación sólo se sostiene cuando los proyectiles *sienten* un potencial

*Del inglés, Grazing Incidence Fast Atom Diffraction.
†Del inglés, Axial Surface Channeling.

cuasi-periódico y siguen trayectorias casi paralelas al plano de superficie [1]. Por lo tanto, la aproximación ASC puede fallar, por ejemplo, para superficies con parámetro de red grandes, como ya ha sido demostrado en el caso de la difracción de átomos de hidrógeno sobre una superficie Al_2O_3 $(11\bar{2}0)$ reconstruida (12×4) [9].

Pese al incremento en el número de estudios, tanto teóricos como experimentales, del fenómeno GIFAD, se ha prestado poca atención al caso en el cual se usa una molécula como proyectil. De hecho, debido a los grados de libertad internos que posee una molécula, se espera que los espectros de difracción para éstas sean más ricos que los obtenidos para átomos [10]. Si acudimos a lo que se sabe del modelado de experimentos de haces moleculares a energías térmicas, debemos esperar que sea necesario desarrollar superficies de energía potencial (SEPs) que incluyan al menos los grados de libertad del proyectil para simular procesos de difracción rotacional y vibracionalmente inelásticos [11–14]. Afortunadamente, a lo largo de las últimas décadas se han desarrollado métodos de construcción de SEPs con resultados bastante exitosos. Algunos ejemplos son el método CRP [15], MS [16, 17], NN [18], PIP-NN [19] y RFF [20] *

Todos los antecedentes expuestos hasta aquí nos han animado a desarrollar en esta tesis una combinación de métodos teóricos, comúnmente aplicados en la descripción de experimentos de haces moleculares a energías térmicas, para modelizar procesos GIFAD, especialmente GIFMD†. Los objetivos de esta tesis son:

- Explorar la posibilidad de realizar dinámicas completamente cuánticas mientras describimos todos los grados de libertad del proyectil incidente. Concretamente, aprovecharemos la eficiencia del método MCTDH‡ [21, 22] para llevar a cabo dinámicas 3D y 6D.

- Desarrollar SEPs precisas de 3 y 6 dimensiones con el método CRP para realizar cálculos cuánticos que puedan describir tanto procesos en condiciones de incidencia normal con energías térmicas, como procesos bajo condiciones de ángulo rasante. Hemos escogido los sistemas $H_2(D_2)$/Li(001) y H(D)/LiF(001) para probar nuestra metodología. En particular, vamos a desarrollar la primera SEP de 6 dimensiones con el método CRP para describir la interacción de una molécula di-atómica con una superficie aislante.

- Probar la aplicabilidad de estudios de dinámica cuasi-clásica, combinados con el método *classic binning* [23, 24], para analizar

*Estos acrónimos proceden del inglés: Corrugation Reducing Procedure (CRP), Modified Shepard (MS), Neural Networks (NN), Permutation Invariant Polynomia Neural Networks (PIP-NN) y Reactive Force Fields (RFF).

†Difracción de moléculas rápidas bajo condiciones de ángulo rasante.

‡Del inglés, Multiconfigurational Time-Dependent Hartree.

cualitativamente la modulación de intensidad de los picos de difracción obtenidos en condiciones GIFAD/GIFMD, para una variedad amplia de condiciones experimentales.

- Combinar un método de dinámica cuántica (MCTDH) con un método de construcción de SEPs (MS) que sean fácilmente generalizables para tratar proyectiles poliatómicos en sistemas gas-superficie. Hemos escogido como test, el sistema $H_2(D_2)$/Methyl-Si(111), en el cual recientemente se han llevado a cabo medidas de probabilidad de difracción rotacionalmente inelástica.

ÍNDICE GENERAL

ÍNDICE DE FIGURAS

ÍNDICE DE CUADROS

$\hat{\partial}_u$	$\frac{\partial}{\partial u}$
$\underline{\underline{F}}$	a second order array, i.e. a matrix.
$\underline{F}$	a first order array ordered in column form.
$\underset{\mathbb{A}}{\mathcal{L}}\{\mathbf{u}_1, \mathbf{u}_2, ...\}$	Set composed by linear combinations of vectors $\{\mathbf{u}_1, \mathbf{u}_2, ...\}$ whose coefficients belong to the set $\mathbb{A}$.
$l \in [a]_b$	Number l satisfies: $l \mod b = a$.

ACRONYMS

ASC	axial surface channeling
BOA	Born-Oppenheimer approximation
BOSS	Born-Oppenheimer static surface
CAP	complex absorbing potential
CRP	corrugation reducing procedure
DFT	density functional theory
DFT-GGA	density functional theory within the generalized gradient approximation
DOF	degree of freedom
DOS	density of states
DVR	discrete variable representation
FGI	fast grazing incidence
FBR	finite basis representation
FFT	fast Fourier transform
GIFAD	grazing incidence fast atom diffraction
GIFMD	grazing incidence fast molecule diffraction
GGA	generalized gradient approximation
HAS	Helium Atom Scattering
irrep	irreducible representation
LC-SAFT	linear combination of symmetry adapted Fourier terms
LDA	local density approximation
LEED	Low Energy Electron Diffraction
MCTDH	Multi-Configurational Time Dependent Hartree
MS	modified Shepard
NN	neural networks
PAW	projector augmented-wave

PBC	periodic boundary conditions
PBE	Perdew-Burke-Ernzerhof
PES	potential energy surface
RFF	reactive force field
RHEED	Reflection High-Energy Electron Diffraction
PIP-NN	permutation invariant polynomia neural networks
RID	rotationally inelastic diffraction
SAFT	symmetry adapted Fourier term
SNI	slow normal incidence
SPF	single particle function
TDS	time dependent Schrödinger
TDWP	time dependent wave packet
TEMS	Thermal-Energy Molecule Scattering
US-PP	ultrasoft pseudo-potential
VASP	Vienna ab initio simulator package

Part I

INTRODUCTION

Here, we present the historical context of the problems treated in this thesis, as well as its main motivations

1

INTRODUCTION

ATOMS AND MOLECULES INTERACTING WITH SURFACES

The development and refinement of new technologies demands a better knowledge of how atoms and molecules interact on different material surfaces. Some particular phenomena in which surface science plays a major role are, among others, *heterogeneous catalysis*, fundamental for most of the usual industrial synthetic processes [25–27]; *corrosion* processes; or *hydrogen storage* [28, 29]. These examples give us an idea of the wide amount of different opened topics within the atom, molecule/surface dynamics field. Probably, the most clear sign of the increasing importance of surface dynamics studies, in our daily life, is the concession of the Nobel Prize award in Chemistry to Gerhard Ertl in 2007, for his studies of chemical processes on solid surfaces [30, 31], specially of the Haber process.

A surface can be though as a two-dimensional (2D) cut of an existing three-dimensional (3D) crystal of a certain material. In a first naive approach, one could think that this surface would have exactly the structure given by the 3D crystal, but truncated at some point in the perpendicular direction to the surface plane. Thus, knowing the structure of a surface would reduce to know the bulk structure of the 3D crystal and the orientation of the surface plane respect to this bulk. However, the rupture of the crystal symmetry in one direction provokes a reorganization of the latter layers of atoms of the surface to compensate the new balance of inter-atomic forces. When this changes are not dramatic, this process is called *relaxation*, whereas if the changes are dramatic, is called *reconstruction*. Both, reconstruction and relaxation make surfaces to have different properties than their bulky 3D versions, making surface science not reducible to the study of the properties of 3D crystals.

The interaction of a projectile* with this semi-infinite structures, is more complex than the usual molecule-molecule interaction in a pure gas phase framework. It can be influenced by a large number of physical conditions, for instance, the surface temperature (molecule-phonon interaction), electron-hole pair excitations, the presence of impurities adsorbed on the surface (difficult to control experimentally), the presence of local defects, the surface coverage, the energy available to the impinging projectile, etc. Thus, a theoretical dynamical approach is needed to catch the essential physics of the problem.

*Hereinafter, we will use the word *projectile* to refer to the gas-phase atom or molecule that is interacting with the surface.

Despite the great computational power available for theoretical calculations, a "complete" quantum modeling of the dynamics of gas/-surface interactions at experimental conditions cannot be achieved in most cases, and several approximations have to be taken.

PROJECTILE/SURFACE INTERACTION MECHANISMS

In this section, we focus on the interaction of atoms and diatomic molecules with surfaces. A good qualitative knowledge of these, in principle, simple systems is necessary to understand the basic physics that underlies more complex processes on surfaces.

We can divide projectile-surface processes in three big groups:

1. **Adsorption:** a projectile coming from the vacuum transfers its momentum to the lattice, such that it equilibrates with the surface and is stuck on it. Depending on the nature of the interaction of the adsorbed projectile with the surface, we can distinguish two types of adsorption:

   a) *Physisorption*: the electronic structure of the projectile is hardly perturbed upon adsorption. Its equivalent in molecular physics is the van der Waals bonding. There is a weak interaction between projectile-surface induced dipole moments.

   b) *Chemisorption*: the electronic structure of both, the projectile and the surface, is strongly perturbed. It resembles the situation of covalent or ionic bond formation in molecular physics.

   There are three possible mechanisms for a projectile to be stuck on a surface:

   a) *Projectile-surface adsorption mechanism* (Fig. 1.1)*:* the impinging projectile coming from the vacuum is chemisorbed or physisorbed on the surface, but remains intact.

   b) *Dissociative chemisorption mechanism* (only for molecules, Fig. 1.2)*:* the impinging molecule relaxes its internal bond as it approaches to the surface, due to the individual atom-surface interaction. Finally, the intramolecular bond is broken and the individual atoms are adsorbed on the surface, i.e. they form new bonds with the surface. We can differentiate two kind of reactive systems based on how reaction probability behave as a function of the projectile incidence energy:

      i. *Non-activated systems*: there are reaction paths in which projectiles do not have to overcome any energetic barrier to dissociate. Thus, there is a high probability of

dissociation even at low incidence energies. Reaction probability can show a complicated dependence with the incidence energy and internal quantum state due to the presence of steering processes [32].

ii. *Activated systems*: projectiles have to overcome an energetic barrier to dissociate. Therefore, there is a low reaction probability below the energy threshold of the barrier. The reaction probability increases monotonically with the incidence energy.

In this work, we are interested in non-activated systems. However, under the incidence conditions studied here, reactions are either not expected or scarcely seen*.

c) *Abstraction mechanism* (only molecules, Fig. 1.3): similar to dissociative chemisorption mechanism, but only one atom remains on the surface. The other atom is scattered back to the vacuum.

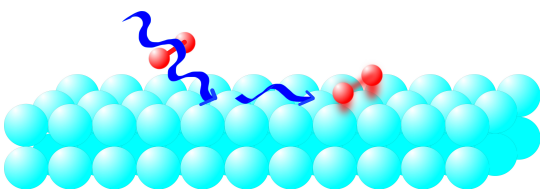

Figure 1.1: Adsorption mechanism.

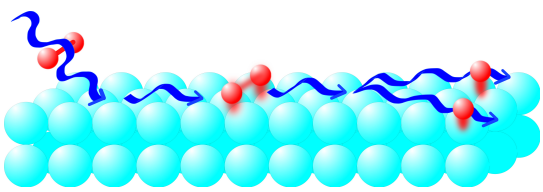

Figure 1.2: Dissociative chemisorption mechanism.

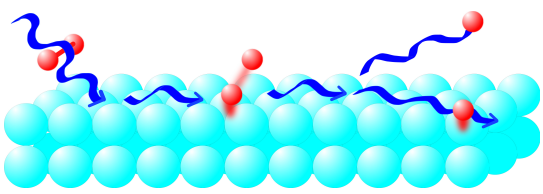

Figure 1.3: Abstraction mechanism.

2. **Desorption:** it is the opposite process to adsorption, i.e. a projectile already adsorbed on the surface is released to the vacuum. There are three possible mechanisms:

*Projectiles cannot overcome reaction barriers. Scattering is difficult to study in too reactive systems.

a) *Langmuir-Hinshelwood mechanism* (Fig. 1.4)*:* projectiles already adsorbed and thermally equilibrated with the surface spend a time traveling on it and later collide in such a way that a new molecule is generated, and scattered back to the vacuum. It is the reverse process of dissociative chemisorption mechanism.

b) *Eley-Rideal mechanism:* an atom coming from the vacuum collide with an atom adsorbed on the surface. An immediate reaction takes place, and a molecule (the product) is scattered back to the vacuum. Reverse process of abstraction mechanism.

c) *Hot-atom or Harris-Kasemo mechanism:* an atom adsorbed on the surface, in equilibrium with it, reacts with another atom that has recently arrived from the gas phase (not equilibrated yet).

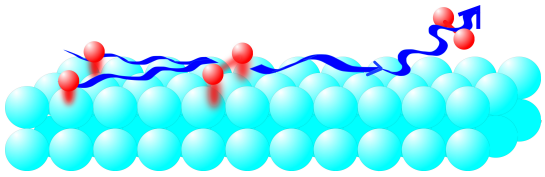

Figure 1.4: If both initial adsorbed atoms are in thermal equilibrium with the surface, this figure depicts a Langmuir-Hinshelwood mechanism. If only one of the adsorbed atoms is in thermal equilibrium with the surface, this figure depicts a Harris-Kasemo mechanism.

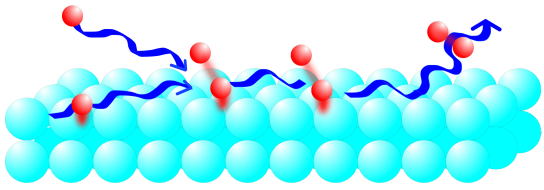

Figure 1.5: Eley-Rideal mechanism.

3. **Scattering:** a projectile coming from the vacuum is reflected by the repulsive force generated by the surface at short distances (Fig. 1.6). During this process, there may be an energy exchange between the projectiles degrees of freedom (DOFs) or with the surface (in case of a non-frozen surface). Thus, the final state of the projectile, can change respect to the initial one. We can classify scattering into two groups, according to the coherence of the final dispersion of the scattered projectiles:

   a) *Coherent or diffractive scattering:* when the parallel momentum to the surface of the scattered projectiles can only

change by discrete amounts. Diffraction is observed whenever the wavelength associated to the particle is in the order of the surface lattice parameter. This is a well-known quantum effect that makes the angular distribution of a molecular beam scattered from a surface to present a discrete peaks distribution.

b) *Incoherent scattering:* when the projectiles parallel change of momentum is not quantized. This can occur either if its associated wavelength is not in the order of the surface lattice parameter or if the surface is too hot*.

We can classify scattering into two other groups, according to the change of some magnitude, e.g. vibrational or rotational state, after the collision with the surface:

a) *Elastic scattering:* the magnitude did not change after the collision.

b) *Inelastic scattering:* the magnitude changed after the collision.

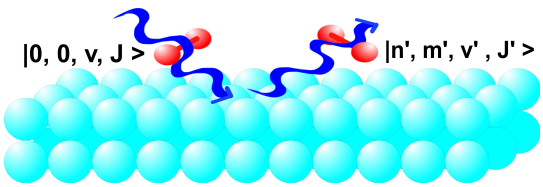

Figure 1.6: A general scattering scheme. (v) is the vibrational quantum number, (J) the rotational quantum number, and (n, m) the diffraction numbers.

From the above exposed list of gas-surface mechanisms, we focus only in the scattering of atoms and di-atomic projectiles from non-metal surfaces.

*Surface atoms are moving from their equilibrium positions and the projectile cannot feel the periodicity of the surface anymore.

2

SCATTERING OF ATOMS AND DI-ATOMIC MOLECULES FROM A SURFACE

HISTORICAL CONTEXT

The most important early studies of gas-surface scattering experiments were those performed by Stern and Estermann [33] in 1930, when they provided the first evidence of atomic diffraction in He/LiF(001) system, and hence, confirmed the wave nature of atomic and molecular beams. These experiments, were performed at thermal energies, condition in which the related de Broglie wavelength of the He projectiles is of the order of 1 Å, comparable to the typical lattice parameter that surfaces exhibit*. These experimental results, in conjunction with the discovery of selective adsorption, encouraged the development of the first successful quantum mechanical theory of gas-surface interaction by J.E. Lennard Jones and A.F. Devonshire [34, 35] in 1936. This theory described the intensity of the diffracted beams and could be used to extract information of the He/Li(001) potential by comparison with experimental data.

50 years later, with the advent of supersonic expansion technology, molecular(atomic) beam diffraction experiments became a common surface analysis technique [36], like the Helium Atom Scattering (HAS), and $H_2(D_2)$ Thermal-Energy Molecule Scattering (TEMS). At thermal energies†, atomic or molecular projectiles are physically unable to penetrate into the solid and interact only with the outermost atoms of the surface, giving to this techniques high sensitivity to the surface structure, in comparison with other techniques that use mass-less projectiles, like X-ray diffraction, or use light projectiles, like Low Energy Electron Diffraction (LEED) or Reflection High-Energy Electron Diffraction (RHEED) [37]. Another advantage of HAS and TEMS techniques is that they do not perturb, in general, the electronic state of adsorbates, allowing their use in determining the structure of ad-atoms‡ on surfaces.

With the pass of the years, the quality of of the experimental set ups improved up to the situation in which out-of-plane diffraction§ [23, 38, 39] could be measured and even the internal state of the molecular

*In optics, a wave cannot experiment diffraction if its wavelength is not comparable to the separation of the periodic arrangement of dispersers.

†Between 10-300 meV

‡We use ad-atom in a generic way. We include here ad-molecules if not stated otherwise.

§Projectiles that are scattered out of the plane formed by the incidence beam and a vector perpendicular to the surface plane.

projectiles could be selected [40, 41]. The latter technical advance, in conjunction with the ability to measure the final internal state of the projectile, gave rise to state-to-state measurements, which are of particular interest to test theoretical models. Some examples of gas-metal systems studied by molecular(atomic) beam experiments are:

- He on Ni/Cu(100) [42], H-Cu(111) [43], Ni(977) [44] and Ru(0001) [45].
- Ne on Ag(111) [46], Rh(110) [47], Ni(111) [48], NiAl [49] and Ru(0001) [45].
- H_2 on Cu(100) [40], Cu(110) [50], Cu(111) [51], Ag(111) [52], Ni(100) [53], Pd(111) [41], Pt(111) [54, 55].
- D_2 on Cu(100) [56], Cu(111) [57], NiAl(110) [58] and Ni(110) [59].
- HD on Cu(001) [60] and Pt(111) [61].

Examples of studies of gas-non metal systems are:

- He on $\left(\sqrt{2} \times 3\sqrt{2}\right)_{R=45^\circ}$ acetylene-NaCl(100), KCN-KBr(001) [62], (2×1) H-InSb(100) [63] and graphite [64].
- Ne on LiF(001) [65, 66], NaF(001) [67] and Si(111) [68].
- H_2 on LiF(001) [69–71], MgO(100) [72] and NaCl(001) [73].
- D_2 on LiF(001) [74–76].

As we can see from the references, a lot of effort was put on the study of gas-metal surface systems in the last 30 years.

GAS-METAL SURFACE INTERACTION

The importance of gas-metal surface interactions comes from the peculiar electronic structure of metals. A metal, is a chemical system that can be considered to be a collection of nuclei, each one screened by a set of strong-bonded core electrons, and a set of weakly-bonded electrons that can move freely along the system [77, 78]. This situation gives rise to what is known as a band structure (see Sec. 5.4) grouping of its electronic levels.

In particular, by definition, metals have the property of being conductors, which allows the possibility of infinitesimal excitations of surface electrons, with the consequent higher probability of electronic interactions with impinging projectiles. Thus, the following phenomena can arise:

- Charge transfer between projectile and surface.

- Electronic (de)excitation of the projectile.
- Energy exchange between the internal DOF of the projectile and the surface electrons (electron-hole pair excitations).

All three enumerated processes are of special interest for surface scientist to understand non-adiabatic processes on surfaces [79–84] and to what extent is the adiabatic theoretical approximation (Born-Oppenheimer) valid to model these kind of systems. In fact, the modeling of electron-hole pair excitations is a splendid example of theory-experiment collaboration. The comparison with experimental results has played a major role in developing friction approaches to non-adiabatic dynamics*, making them as computationally cheap as possible while maintaining a reasonable accuracy [85].

In addition, the mobility of band electrons in metals cause a phenomenon called *screening* or image charge creation. As a charge distribution comes closer to a metal surface, electrons in the surface are polarized in such a way that a perfect image of the incoming projectile is created under the surface plane with the opposite charge. This phenomenon enhances physisorption and chemisorption processes [37], which are important for topics like heterogeneous catalysis or self-assembling mechanisms.

THE IMPORTANCE OF GAS-NON METAL SURFACE SYSTEMS

From the previous section, it is clear why gas-metal surfaces have attracted so much attention in the latter 30 years. However, in this work, we are interested in the scattering of projectiles from non-metal surfaces.

In the last 20 years, works studying the scattering of projectiles from insulator and semi-conductor surfaces have increased considerably. One of the reasons of this increase, comes from the versatility of semi-conductor electronic properties that make them suitable to form part of electronic devices. A good example are the applications of Si(111) in photo-electrodes in electrochemical cells and bio-sensing electronics [86–91].On the other hand, semi-conductors often present reconstruction and highly corrugated 2D-sctuctures which offers a real challenge to theoretical model development. Some important studies in this matter are the ones performed by Cardillo *et al.* [92] in He/GaAs(110) and Lambert *et al.* in He/Ge(100) .

Regarding insulators, most of the experimental effort is focused in the study of electron transfer phenomena using neutral or charged projectiles, and how band gaps affect this process. This topic is of special interest to theoreticians in order to refine the description of charge transfer mechanisms from insulators, which are different to

*The dynamics of these systems are modeled with Langevin-like equations of motion.

those in metals. Some representative phenomena studied in these experiments are: negative ions formation, interaction of multi-charged ions, energy-loss of projectiles during the scattering event, etc. (see Ref. [93] and references therein). Usually, these studies are carried out under fast grazing incidence (FGI) conditions. On the other hand, insulators have a band gap big enough to assure that non-adiabatic effects do not play a major role in scattering events under thermal-energy regime, and, with some restrictions, under FGI conditions [94, 95]. This make them a perfect benchmark system to measure vibrationally and rotationally inelastic scattering neglecting non-adiabatic effects. The comparisons with this kind of experiments can be used to test the accuracy of theoretical adiabatic models, specially if the projectile-surface electronic structure is properly described. Some examples of rotationally inelastic scattering experiments in H_2/LiF(001) system are in Refs. [70] and [96], and for D_2/LiF(001) Refs. [74–76]. Apart from inelastic scattering experiments, we can find in the literature studies about structure determination of physisorbed species like CH_3F, CH_3Br, CH_3Cl, HCl and NH_3 on Xe-graphite [97, 98], or CO orientation on (1x1) NaCl(100) [99], via HAS technique.

Fast grazing incidence diffraction of neutral projectiles

In the year 2007, atom diffraction beyond the regime of thermal energies was reported by two different experimental groups [100, 101]. They detected pronounced diffraction patterns in neutral atom and molecule scattering experiments from insulator surfaces, with energies up to several keV at grazing incidence conditions. These experimental observations have revitalized, in the later years, the study of non-metal surfaces as targets by both, experimentalist and theoreticians. Examples of studies using atomic projectiles/insulator systems are: H/LiF(001) [94, 95, 102], He/LiF(001) [4, 95], H/NaCl(001) [103] or He/KCl(001) [104]. In the case of molecules, we can mention: H_2/LiF(001) [105] or D_2/LiF(001) [106]. For more information, see Ref. [107] end references therein. Years later, the phenomenon of grazing incidence fast atom diffraction (GIFAD) or grazing incidence fast molecule diffraction (GIFMD), was observed as well in semi-conductor surfaces [108], metal surfaces with ordered layers of adsorbates [109, 110], ultra-thin films [111, 112], and recently, even clean metal surfaces [113, 114].

At first sight, diffraction of massive projectiles at FGI is not expected to occur. The reason is threefold:

1. The de Broglie wavelength associated with a projectile* with such an energy is several orders of magnitude smaller than the typical lattice parameter of a surface.

*As massive as an atom or a molecule.

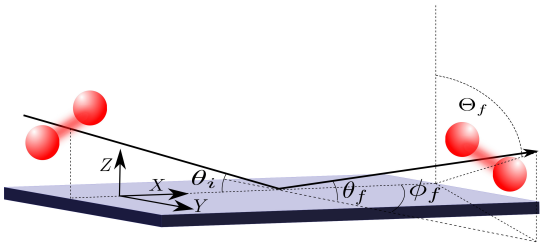

Figure 2.1: Scheme of a di-atomic molecule colliding with a surface. . ϕ_f is the azimuthal exit angle. Θ_f is the polar exit angle. θ_i is the incidence angle. θ_f is the exit angle.

2. There is a high probability to excite electrons of target surfaces by incoming fast atoms or ions [115, 116].

3. The de Broglie wavelength associated with these projectiles is even smaller than the mean thermal displacement of surface atoms, favoring quantum decoherence [117].

However, a careful analysis of how incidence energy is partitioned in translational DOFs can explain where this diffraction comes from.

In Fig. 2.1, we show a schematic view of a molecule scattered under FGI conditions. If this projectile has an initial kinetic energy E_i, then it is partitioned as follows:

$$E_{xy} = E_i \cos^2 \theta_i \tag{2.1}$$

$$E_z = E_i \sin^2 \theta_i \ , \tag{2.2}$$

where xy is the plane parallel to the surface, z is the direction perpendicular to the surface, and θ_i is the incidence angle measured from the surface to the projectile. When $\theta_i \approx 1°$, $\sin^2 \theta_i$ is a factor of about 1×10^{-4}, making E_z being four orders of magnitude smaller than the total initial kinetic energy. The de Broglie wavelength associated with E_z is, therefore, about 60 times bigger* than the total de Broglie wavelength of the projectile. For high incidence energies†, λ_z can be still comparable to the typical lattice parameter of a surface, and bigger to the mean thermal displacement surface atoms, allowing diffraction phenomena. The situation is similar to an approaching wave, with wavelength "λ_z", to a dispersive periodic media, with periodicity "a", disposed along the perpendicular plane to the incidence direction.

Features of GIFAD spectra

In Fig. 2.2, we show several GIFAD spectra taken from Ref. [107]. Without entering into too much details about the measurements, we can use them to stress some particular features that are present:

*$\lambda_z = \left(\frac{1}{\sin\theta_i}\right) \cdot \lambda$. If $\theta_i \approx 1°$, then $\left(\frac{1}{\sin\theta_i}\right) \approx 57.298688$.
†$\lambda \ll 1$ Å

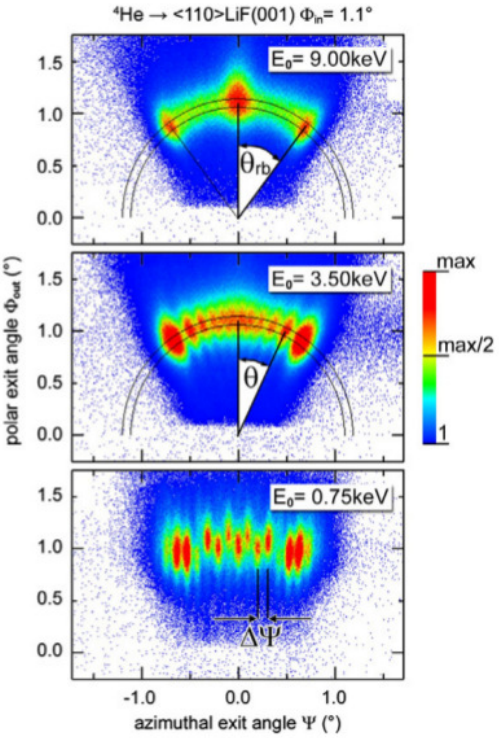

Figure 2.2: Several GIFAD spectra of ^{4}He/LiF(001) along $\langle 110 \rangle$ direction taken from Ref. [107]. The angle nomenclature is different from the one in Fig. 2.1.Ψ is our ϕ_f, and θ is our Θ_f. θ_{rb} (Θ_f^{rb} in out nomenclature), is the so called rainbow scattering angle.

- Diffraction signals lye within a circumference of radius $R = L \sin\theta_i$ [107], L being the distance from the target to the plane of the position sensitive detector in the experiment. This phenomenon arises because the change of momentum during diffraction is perpendicular to the direction of the incident beam. Thus, momentum exchange occurs between Y and Z directions (see Fig. 2.1). Theoretically, this situation can be explained in two ways: (i) attending to the periodicity of the interaction between the projectile and the surface (see Sec. 8.1); or (ii) assuming that the projectile "feels" an average potential along the incidence direction (X), in which we neglect the corrugation. The latter "picture" has been widely studied in works about *channeling* conditions [118, 119].

- There are different scattering regimes depending on the incidence energy. If we keep fixed the incidence angle θ_i, and we vary E_i, projectiles will impinge upon the surface with different E_z. If we maintain λ_z high enough to allow diffraction, then we obtain diffractograms with different peak intensities (situation of panels 2 and 3 from Fig. 2.2). Studying this modulation, gives information about the interaction projectile-surface. If λ_z no longer allows diffraction, then projectiles behave like a classical particle. For example, diffractograms measured under these conditions exhibit the well known *rainbow* effect (panel 1 of Fig. 2.2). The rainbow angle, Θ_f^{rb}, gives information about the corrugation of the potential*.

INELASTIC SCATTERING

As we already introduced en Sec. 1.2, molecules can be scattered from a surface with changes in their internal state. This processes can be enhanced by how the projectile internal DOFs are coupled with themselves or with translational DOFs in the presence of a surface. Here, we focus only in those inelastic channels present for di-atomic molecules interacting with a frozen surface in the absence of non-adiabatic effects.

Rotationally inelastic scattering

The rotation of a diatomic molecule is fully described by its rotational angular momentum $\mathbf{J}$ (see Fig. 2.3). However, from quantum mechanics, it follows that the rotational motion of a molecule is quantized and that we can only measure its module, $|\mathbf{J}|$, and its projection onto

*Within a very simple model, assuming that the interaction projectile-surface is well described by a hard wall cosine potential, the rainbow angle takes the value: $\Theta_f^{rb} = 2\arctan(\frac{\Delta z}{a}\pi)$, Δz being the corrugation of the potential, and a its periodicity.

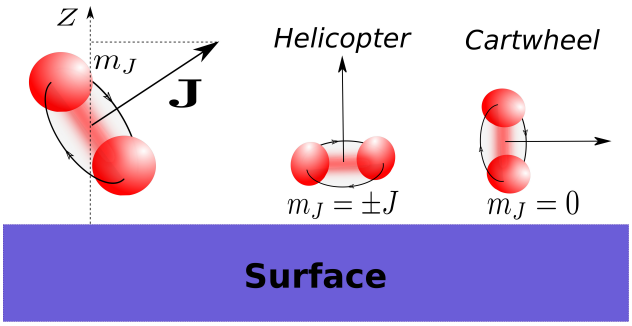

Figure 2.3: Di-atomic molecule rotating in the proximity of a surface. **J** is its rotational angular momentum, and m_J is its projection on the perpendicular direction to the surface.

an arbitrary axis, m_J, at the same time. We have used the commonest choice of this axis to define m_J, which is the perpendicular direction to the surface plane, Z. In Fig. 2.3, we have plotted as well two interesting geometries of the projectile respect to the surface that are of common use in the literature, namely, helicoptering ($m_J = \pm J$) and cartwheeling ($m_J = 0$) conformations.

The rotational energy of a diatomic projectile*, E_{rot}, is:

$$E_{rot} = \frac{|J|^2}{2\mu r^2}\,, \tag{2.3}$$

where μ is its reduced mass, and r its inter-atomic distance. $|J|$ can only take quantized values $\sqrt{J(J+1)}$, J being a natural number†, called rotational quantum number. The rotational magnetic quantum number, m_J, is an integer number that can take values from $-J$ to J. Thus, there are $2J+1$ valid m_J states for a given J state. Note that E_{rot} only depends on J and not on m_J.

In rotationally inelastic scattering, both J and m_J quantum numbers can change respect to their initial values. Hereinafter, we use the subscript "i" to represent initial conditions , (J_i, m_{J_i}), and "f" to represent final conditions, (J_f, m_{J_f}). When $J_f > J_i$ the molecule has been rotationally excited, whereas if $J_f < J_i$, it has been de-excited. Changes in m_J only affect the relative orientation of the rotating molecule respect to the surface.

In order to have rotational excitation, the projectile should have enough energy to make a transition from J_i to J_f. Within a frozen surface model, this energy must come either from the translational DOFs, usually from Z, or from the vibrational motion. When the projectile suffers a rotational de-excitation, the energy loss is transferred to other **dofs!** (**dofs!**). In either inelastic processes, the surface plays a major role coupling all the projectile DOFs.

*Strictly speaking, Eq. 2.3, only stands for the classical representation of E_{rot} and for a rigid rotor in quantum mechanics. If we introduce centrifugal distortion effects, the formula is more complicated.

†Including zero.

For rotational (de)excitation to occur, the molecule-surface potential should be anisotropic. The potential is anisotropic if the interaction of the projectile with the surface changes significantly if we vary rotational DOFs. The higher the anisotropy, the higher the probability to have rotational (de)excitation.

Vibrationally inelastic scattering

Di-atomic molecules exhibit vibrational motion, even at the lowest energy level, around their equilibrium internuclear distance. From quantum mechanics, this movement is quantized , and therefore, the vibrational energy can only have discrete values, $E_{vibr} = \omega_0(v + 1/2)$ [*], where $v \geq 0$ is a natural number called the vibrational level of the molecule.

After scattering, the vibrational level can change by (de)excitation mechanisms, like in the case of rotation. In both cases, the transferred energy is taken from or given to the rest of DOFs, respectively. Vibrational (de)excitation is enhanced when the reaction path presents high curvature in front of the reaction barrier [120, 121]. Note that a vibrational excitation in the limit of $\Delta v \to \infty$ is a dissociation.

All gas-surface systems studied in this thesis, under the conditions explored in this work, do not have enough available energy to present vibrational excitation events. In addition, as we did not study in depth vibrationally excited projectiles, we do not have vibrational de-excitation events.

[*]This equation stands when the inter-atomic interaction is a harmonic potential.

3

MOTIVATION AND OUTLINE

MOTIVATION AND OBJECTIVES OF THIS WORK

In order to achieve reliable conclusions in surface science, we need both theoretical and experimental information. From the point of view of a theorist, it is difficult to obtain accurate results without any previous knowledge of the system that it is being simulated, specially if the surface structure is not known. Calculations in surface science are usually time-consuming and a lot of ideal approximations should be taken. Hence, comparison with experiment always helps surface scientists to sharpen the theoretical tools available in order to get a good compromise between accuracy and time expense. From the point of view of an experimentalist, it is difficult to know what is happening at the atomic scale level without any theoretical guidance. Sometimes experimental models are too simplistic and theoretical treatments can provide a good way to improve future measurements. As a result, surface science is a perfect environment to theory-experiment collaboration.

One of the recently opened branches in surface science in which the complementarity theory-experiment is most promising, is the diffraction of fast projectiles under grazing incidence conditions. The arise of this new technique has re-attracted surface scientist attention to the study of neutral projectiles interaction with non-metal surfaces. In particular, the understanding of GIFAD experiments has encouraged theorists to perform detailed quantum theoretical studies. However, these theoretical simulations present a major challenge due to the huge incidence energy used in the experiment.

In order to reduce the computational effort, and make the calculations feasible using reasonable computational resources, the axial surface channeling (ASC) approximation [1–3] and dynamics semiquantum approaches [4–6] has been widely used. Within the ASC approximation, the dimensionality of the system is reduced to two-dimensions (2D) by considering that the projectile feels an average potential along the incidence direction. As already discussed in the literature [7, 8], this approximation holds whenever the projectile feels a quasi-periodic potential and follows trajectories that are nearly parallel to the surface [1], i.e, whenever the condition $a \ll (E_i/\tan\theta_i)/(dV/dZ)$ is fulfilled* [23]. Thus, this approximation may fail, for example, for

*a being the lattice constant, E_i and θ_i the incidence energy and polar angle, respectively, and dV/dZ the variation of the potential energy surface over Z. See Figs. 2.1 and 6.1 for coordinates definition.

surfaces with large lattice parameters, as recently shown for the case of diffraction of H atoms from the reconstructed (12×4) phase of the $Al_2O_3(11\bar{2}0)$ surface [9], whose experimental diffraction spectra displays several Laue circles revealing the three-dimensionality of the system.

Despite the increasing number of theoretical and experimental GIFAD studies, little attention has been devoted to molecular projectiles, although diffraction spectra are richer, due to the internal molecular DOFs [10]. In fact, from the modeling of molecular beam experiments at thermal-energies, it is well-established that high-dimensional* descriptions of the interaction of the projectile with the surface should be performed to describe properly phenomena like inelastic rotational and vibrational scattering [11–14]. Some successful methods developed to construct such high-dimensional potentials in the last decades are: the corrugation reducing procedure (CRP) [15], the modified Shepard (MS) [16, 17], the neural networks (NN) [18], the permutation invariant polynomia neural networks (PIP-NN) [19], and the reactive force field (RFF) method [20].

With all the previously exposed antecedents in mind, we have felt encouraged to combine theoretical models and methodology commonly applied to describe atomic(molecular) beam experiments under thermal-energy incidence conditions to GIFAD and GIFMD processes. The objectives of this thesis are:

- Explore the possibility of performing full quantum dynamics calculations while describing all the DOFs of the projectile† with techniques commonly used to model atomic(molecular) beam experiments under thermal-energy incidence conditions. Concretely, we have taken advantage of the Multiconfigurational Time-Dependent Hartree method [21, 22] efficiency to perform 3D and 6D dynamics calculations.

- Develop accurate 3D and 6D potential energy surfaces (PESs) with the CRP method to perform dynamics calculation that can describe both, experiments under slow normal incidence (SNI) and FGI conditions. We have chosen as test systems $H_2(D_2)/Li(001)$ and H(D)/LiF(001). In particular, we will implement the first 6D-CRP-PES for a di-atomic molecule interacting with an insulator surface‡.

- Test the applicability of classical dynamics, in combination with the *classical binning method* [23, 24], to perform qualitative analysis of diffraction peaks intensity modulation for a wide variety of initial conditions.

*At least all the DOFs of the projectile.
†Three and six dimensions for atomic and di-atomic projectiles, respectively
‡H_2/LiF(001) system

- Combine a quantum dynamics method (MCTDH) and a PES-building method (MS) that can be easily generalized to treat any polyatomic projectile in order to model gas-surface systems. We have chosen as a test system $H_2(D_2)$/Methyl-Si(111), in which recently experiments measuring rotationally inelastic diffraction (RID) probabilities have been performed.

OUTLINE

This thesis is divided in four parts:

- **In part I**, we expose the main information needed to understand the historical background of the problems treated in this thesis.
  - In chapter I, we briefly present how di-atomic molecules and atoms can interact with a surface.
  - In chapter II, we center out attention in the scattering phenomena.
  - In chapter III, we expose the motivations and objectives of this work.
- **In part II**, we carefully present step by step the approximations needed to make computationally feasible dynamics calculations to model gas-surface systems. We have tried to give details only in those particular theoretical tools developed in this thesis.
  - In chapter 4, we present the most fundamental approximation taken in this thesis, the Born-Oppenheimer approximation, which allows to separate electron and nuclei dynamics.
  - In chapter 5, we expose all the theoretical approximations made to perform electronic calculations, in which our developed potential energy surfaces are based.
  - In chapter 6, we explain in detail two techniques to build potential energy surfaces: the corrugation reducing procedure, and the surface symmetry adapted Modified-Shepard method.
  - In chapter 7, we present the description two dynamics methods: the Multiconfigurational Time-Dependent Hartree method, and the quasi-classic dynamics method in combination with the classical binning method.
- **In part III**, we present the particular results obtained in this thesis.
  - In chapter 8, we compile the results obtained for H(D)/LiF(001) system. We have carried out both, classical and quantum dynamics calculations under FGI conditions.

  - In chapter 9, we compile the results obtained for $H_2(D_2)$/LiF(001) system. We have carried out both, classical and quantum dynamics calculations under FGI and SNI conditions.
  - In chapter 10, we compile the results obtained for $H_2(D_2)$/Methyl-Si(111) system. We have used both, classical and quantum dynamics simulations to understand the high probability of RID events for D_2, and why RID peaks are barely seen in H_2.

- **In part IV**, we expose in Spanish a summary of all the conclusions obtained in part III.

- **In part V**, we compile all the complementary information that is too specific to be explained in detail in the main body of this work.

Part II

THEORY

From a theoretical point of view, studying the interaction of chemical compounds with a solid surface implies dealing with complex many-body systems. In this part, we expose the main approximations and ideas used in our work to make this kind of problems manageable with the available computational resources.

4

THE BORN-OPPENHEIMER APPROXIMATION

In general, any chemical system is composed by a set of nuclei and electrons that interact with each other. If each nucleus has spatial coordinates $\mathbf{R}_i$ and each electron has spatial coordinates $\mathbf{r}_i$, the time-dependent Schrödinger equation that describes the time evolution of the system has the form:

$$i\hat{\partial}_t \left|\Psi\left(\mathbf{R},\mathbf{r},t\right)\right\rangle = \hat{H}\left|\Psi\left(\mathbf{R},\mathbf{r},t\right)\right\rangle \ , \tag{4.1}$$

where $\left|\Psi\left(\mathbf{R},\mathbf{r},t\right)\right\rangle$ is the quantum state of the system at time t, $\hat{H}$ is a non relativistic Hamiltonian operator and $\mathbf{R} = (\mathbf{R}_1, \mathbf{R}_2, ..., \mathbf{R}_N)$ and $\mathbf{r} = (\mathbf{r}_1, \mathbf{r}_2, ..., \mathbf{r}_M)$ the set of all nuclear and electronic coordinates respectively. The Hamiltonian operator $\hat{H}$ contains all the interactions between nuclei and electrons of the system and can be written as:

$$\hat{H} = \hat{T}_n\left(\mathbf{R}\right) + \hat{T}_e\left(\mathbf{r}\right) + V_{nn}\left(\mathbf{R}\right) + V_{ee}\left(\mathbf{r}\right) + V_{ne}\left(\mathbf{R},\mathbf{r}\right) \ , \tag{4.2}$$

where $\hat{T}_n$ is the total kinetic energy operator of the nuclei, $\hat{T}_e$ the total kinetic energy operator of the electrons, V_{nn} the Coulomb interaction between nuclei, V_{ee} the Coulomb interaction between electrons and V_{ne} the Coulomb interaction between nuclei and electrons (see App. A for explicit formulas). As $\hat{H}$ does not have an explicit dependence on time, Eq. 4.2 can be simplified into:

$$\left|\Psi\left(\mathbf{R},\mathbf{r},t\right)\right\rangle = \sum_{k=0}^{\infty} a_k\left(t_0\right) e^{-iE_k(t-t_0)} \left|\psi_k\left(\mathbf{R},\mathbf{r}\right)\right\rangle \tag{4.3}$$

$$\hat{H}\left|\psi_k\left(\mathbf{R},\mathbf{r}\right)\right\rangle = E_k\left|\psi_k\left(\mathbf{R},\mathbf{r}\right)\right\rangle \ , \tag{4.4}$$

which means that we can compute the time evolution of a chemical system if we can find the eigenvectors of $\hat{H}$. In fact, Eq. 4.4 is a central equation in theoretical chemistry, known as the time-independent Schrödinger equation.

Seen the complex form of $\hat{H}$ (Eq. 4.2 and App. A), it is easy to realize that obtaining its eigenvectors is not a trivial task at all. The existence of the term $V_{ne}\left(\mathbf{R},\mathbf{r}\right)$ prevents the Hamiltonian to be separated in a pure nuclear part ($\mathbf{R}$ dependent) and a pure electronic part ($\mathbf{r}$ dependent), which would simplify the problem. The objective of the Born-Oppenheimer approximation (BOA) is to provide such simplification taking advantage of the fact that electrons are much faster than nuclei (due to their mass mismatch), and therefore, that electrons can adapt instantaneously to a differential movement of the nuclei, i.e. electrons follow the motion of the nuclei adiabatically. Mathematically, this means that Eq. 4.4 should be somehow reducible to two

equations acting separately on the state space of the electrons and on the state space of the nuclei. Under this assumption, one can define a set of electronic functions $\{|\chi_m(\mathbf{R},\mathbf{r})\rangle\}_{m=1}^{\infty}$ that depend parametrically in $\mathbf{R}$. Thus, the electronic Hamiltonian can be written as:

$$\hat{H}_e = \hat{T}_e(\mathbf{r}) + V_{ee}(\mathbf{r}) + V_{ne}(\mathbf{R},\mathbf{r}) + V_{nn}(\mathbf{R}) \tag{4.5}$$

$$\hat{H}_e |\chi_m(\mathbf{R},\mathbf{r})\rangle = \epsilon_m(\mathbf{R}) |\chi_m(\mathbf{R},\mathbf{r})\rangle \ . \tag{4.6}$$

If Eq. 4.6 is solved for a dense set of nuclear geometries $\mathbf{R}$, the set of parametrically obtained eigenvalues $\{\epsilon_m(\mathbf{R})\}_{\mathbf{R},m}$ takes the form of a set of functions in $\mathbf{R}$, $\{V_m(\mathbf{R})\}_m$, each one known as the m-th PES of the system. These functions encode the interaction of the electrons with the nuclei of the system without any explicit reference to the electronic DOFs. At this point, one can propose that for each electronic state m, there may exist a basis of nuclear states, $\{|\phi_l^m(\mathbf{R})\rangle\}_{l=1}^{\infty}$, which, in addition to $\{|\chi_m(\mathbf{R},\mathbf{r})\rangle\}_{m=1}^{\infty}$ basis, can be used to expand $|\psi_q(\mathbf{R},\mathbf{r})\rangle$ states as follows:

$$|\psi_q(\mathbf{R},\mathbf{r})\rangle = \sum_{l=1}^{\infty}\sum_{m=1}^{\infty} C_{lm}^q |\phi_l^m(\mathbf{R})\chi_m(\mathbf{R},\mathbf{r})\rangle \tag{4.7}$$

without the loss of any generality. Unfortunately, the action of $\hat{H}$ on the new basis elements $|\phi_l^m(\mathbf{R})\chi_m(\mathbf{R},\mathbf{r})\rangle$ is still not separable due to the operator $\hat{T}_n(\mathbf{R})$:

$$\hat{H}|\phi_l^m(\mathbf{R})\chi_m(\mathbf{R},\mathbf{r})\rangle = \left[\hat{T}_n(\mathbf{R}) + V_m(\mathbf{R})\right]|\phi_l^m(\mathbf{R})\chi_m(\mathbf{R},\mathbf{r})\rangle$$

In order to neglect the action of $\hat{T}_n(\mathbf{R})$ on electronic states, it is enough to assume that the gradient of the electronic states wave function $\chi_m(\mathbf{R},\mathbf{r})$ respect to all coordinates of the nuclei is approximately zero, or formally:

$$\vec{\nabla}_\alpha \chi_m(\mathbf{R},\mathbf{r}) \approx \vec{0}, \forall\alpha, m \ , \tag{4.8}$$

where $\vec{\nabla}_\alpha$ is the gradient respect to the coordinates of the α-th nucleus. Physically, this approximation is equivalent to assume that the momentum matrix of each nuclear DOF in the basis of the electronic states is zero: $\forall\alpha,l,k\ \langle\chi_l(\mathbf{R},\mathbf{r})|\hat{P}_\alpha|\chi_k(\mathbf{R},\mathbf{r})\rangle \approx 0$. Now, the nuclear kinetic operator $\hat{T}_n(\mathbf{R})$ acting on a state $|\phi_l^m(\mathbf{R})\chi_m(\mathbf{R},\mathbf{r})\rangle$, which in general does not have a separable form, can be reduced to $|\hat{T}_n(\mathbf{R})\{\phi_l^m(\mathbf{R})\}\chi_m(\mathbf{R},\mathbf{r})\rangle$. This allow us to write the action of H on $|\phi_l^m(\mathbf{R})\chi_m(\mathbf{R},\mathbf{r})\rangle$ basis as follows:

$$\hat{H}_n^{(m)} = \hat{T}_n(\mathbf{R}) + V_m(\mathbf{R}) \tag{4.9}$$

$$\hat{H}_n^{(m)} |\phi_l^m(\mathbf{R})\rangle = \epsilon_{lm}^{BO} |\phi_l^m(\mathbf{R})\rangle \tag{4.10}$$

$$\hat{H}|\phi_l^m(\mathbf{R})\chi_m(\mathbf{R},\mathbf{r})\rangle = \epsilon_{lm}^{BO}|\phi_l^m(\mathbf{R})\chi_m(\mathbf{R},\mathbf{r})\rangle \tag{4.11}$$

where $\hat{H}_n^{(m)}$ is the nuclear Hamiltonian on the m-th electronic state of the system, and ϵ_{lm}^{BO} is the Born-Oppenheimer approximation to the

energy of the nuclear state $\left|\phi_l^m(\mathbf{R})\right\rangle$. Now, the nuclear state space is separated completely from the electronic state space, in the sense that $|\chi_m(\mathbf{R},\mathbf{r})\rangle$ does not intervene explicitly in the calculation of the set of eigenvalues $\{\epsilon_{lm}^{BO}\}$ and eigenfunctions $\left\{\left|\phi_l^m(\mathbf{R})\right\rangle\right\}$, but they do interact implicitly through the PES $V_m(\mathbf{R})$. Applying Eq. 4.10 to the time dependent Schrödinger equation simplifies the initial dynamics complex problem to something that only depends on nuclear DOFs and a set of potential energy surfaces:

$$i\hat{\partial}_t \sum_{m=1}^{\infty} \left|\Phi^{(m)}(\mathbf{R},t)\right\rangle = \sum_{m=1}^{\infty} \hat{H}_{nucl}^{(m)} \left|\Phi^{(m)}(\mathbf{R},t)\right\rangle \tag{4.12}$$

$$\left|\Phi^{(m)}(\mathbf{R},t)\right\rangle = \sum_{l=1}^{\infty} c_{lm}(t) \left|\phi_l^m(\mathbf{R})\right\rangle \ , \tag{4.13}$$

which can be further simplified if one considers that nuclei only interact with one PES:

$$i\hat{\partial}_t \left|\Phi^{(m)}(\mathbf{R},t)\right\rangle = \hat{H}_{nucl}^{(m)} \left|\Phi^{(m)}(\mathbf{R},t)\right\rangle \ . \tag{4.14}$$

Usually, m is chosen so that $V_m(\mathbf{R})$ is the lowest potential energy surface of the system. This means that Eq. 4.14 would describe the dynamics of nuclei moving within the ground electronic state of the system. This is a reasonable approximation as long as electronic excitations of the system are negligible or play a minor role during dynamics.

In this work we have taken advantage of the BOA to divide the dynamics of molecule-surface systems into two parts: (i) the calculation of the potential energy surface in the ground state of the system $V(\mathbf{R})$, and (ii) performing the dynamics of nuclei (quantum or classical) using as interaction potential $V(\mathbf{R})$. In the following chapters we expose which approximations we have been taken to perform single point electronic calculations to obtain $\{\epsilon_0(\mathbf{R})\}_{\mathbf{R}}$, how to construct the PES $V(\mathbf{R})$ from this set of single point calculations, and how to perform classical and quantum calculations to analyze some gas-surface systems of interest.

5

ELECTRONIC STRUCTURE OF PERIODIC SYSTEMS

PERIODIC STRUCTURE OF CRYSTALS AND SURFACES

Crystals are periodic arrangements of atoms or molecules in space. They can be represented by a 3D Bravais Lattice $\mathcal{B}^{3D}$, which is an infinite set of points generated by all the integer linear combinations of three non-coplanar vectors called primitive vectors $\boldsymbol{u}_1$,$\boldsymbol{u}_2$ and $\boldsymbol{u}_3$:

$$\mathcal{B}^{3D} = \underset{\mathbb{Z}}{\mathcal{L}} \{\mathbf{u_1}, \mathbf{u}_2, \mathbf{u}_3\} \ . \tag{5.1}$$

$\boldsymbol{u}_1$,$\boldsymbol{u}_2$ and $\boldsymbol{u}_3$ are linear independent vectors that define the smallest parallelepiped in the real space that can generate the periodic crystal structure by only applying translation operations, which is known as the primitive cell. The set formed by these three primitive vectors $\{\mathbf{u_1}, \mathbf{u}_2, \mathbf{u}_3\}$ is the minimum basis set for $\mathcal{B}^*$. In 3D space, there are 14 non equivalent Bravais lattices that classify all possible symmetric translations of points in space. In order to name a point of the lattice, a set of integer coefficients (ν_1, ν_2, ν_3) is used [77]. Each symmetric point in a Bravais lattice can represent not only one atom, but a set of them called basis or motive. As this motive is a finite set of elements, its inner symmetry belongs to a point symmetry group, which combined with the pertinent translational symmetry gives rise to a spatial symmetry group. The set of all spatial symmetry groups (230) can be obtained combining all possible point groups with all possible Bravais lattices in space. In order to provide some examples of crystal bulk structures, we have plotted in Fig. 5.1 the converged structures of lithium fluoride (LiF) and silicon (Si) crystals. Both bulk structures are important within this work because we have studied H(D)/LiF(001), $H_2(D_2)$/LiF(001) and $H_2(D_2)$/Methyl-Si(111) systems (see Part. iii).

A surface, in contrast to a 3D crystal, is a periodic arrangement of atoms or molecules in a plane. Thus, their translational symmetry can be represented by a Bravais lattice in 2D, $\mathcal{B}^{2D} = \underset{\mathbb{Z}}{\mathcal{L}} \{\mathbf{s_1}, \mathbf{s}_2\}$, $\mathbf{s}_1$ and $\mathbf{s}_2$ being the surface primitive vectors. As the only difference with their definition respect to a crystal is the dimensionality of the space in which they are periodic, everything that we have explained so far for crystals can be applied to surfaces. The only differences that we have to take into account are the following: (i) there are only

*However, in crystallography, it is usually preferred to represent bigger unit cells to make clear the crystal symmetry at first sight

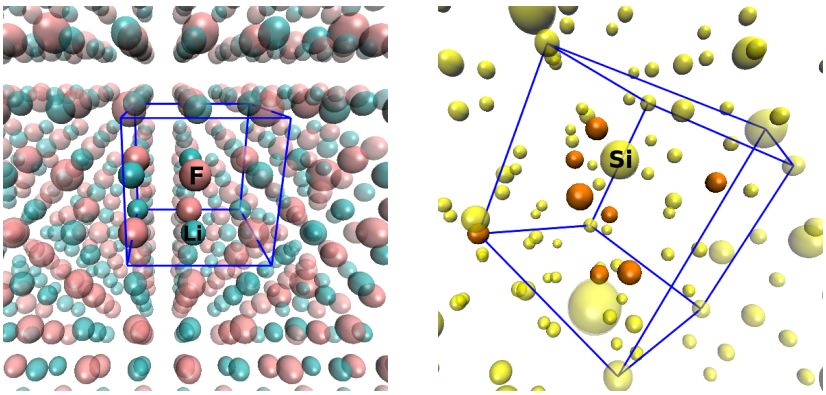

Figure 5.1: Left panel: primitive cell of LiF crystal. Opaque atoms are part of the basis (motive). Right panel: square unit cell of Si crystal. Despite it is not the primitive cell for this system, it is useful to appreciate its diamond structure. In orange we have plotted those Si atoms that are part of the motive in this cell.

5 possible Bravais lattices in 2D, (ii) symmetry groups in 2D are called wallpaper groups, and (iii) there are only 17 of them, instead of 230.

Surfaces are obtained by cutting a crystal following a very specific plane, which is characterized by three integers (hkl), called Miller indexes [77]. These indexes can be calculated taking the inverse of the length of the intersection of the surface plane with the OX, OY and OZ axis, respectively. A much simpler definition of these indexes will be given in the next section once the concept of reciprocal lattice has been introduced. Some examples of surface structures used in this work can be seen in Fig. 5.2: LiF(001) and Methyl-Si(111).

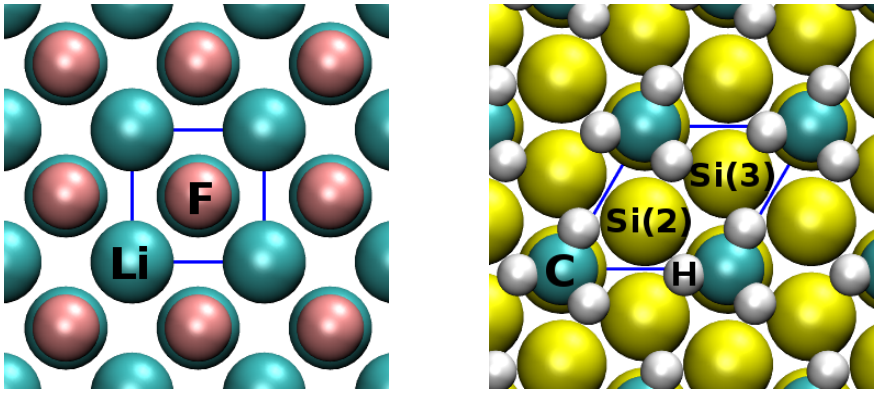

Figure 5.2: Structure of LiF(001) (left panel) and Methyl-Si(111) (right panel) surfaces. Blue lines are the boundaries of the primitive cell of each surface. On right panel, numbers between parentheses refer to the layer to which the silicon atoms belong to. Silicon atoms on the first layer are eclipsed in this view by carbon atoms.

RECIPROCAL LATTICE

The reciprocal lattice $\mathcal{B}^r$ of a given 3D Bravais lattice $\mathcal{B}$ is a new Bravais lattice whose minimal basis $\{\mathbf{G}_1, \mathbf{G}_2, \mathbf{G}_3\}$ is closely related to the minimal basis of $\mathcal{B}$ following the expression:

$$\mathcal{B}^r = \underset{\mathbb{Z}}{\mathcal{L}} \{\mathbf{G}_1, \mathbf{G}_2, \mathbf{G}_3\} \ : \ \mathbf{G}_i \mathbf{u}_j = 2\pi\delta_{ij} \ . \tag{5.2}$$

It can be demonstrated that if $\mathcal{B}^r$ is the reciprocal lattice of $\mathcal{B}$, $\mathcal{B}$ is the reciprocal lattice of $\mathcal{B}^r$ as well. An example of a few $\mathcal{B} \longrightarrow \mathcal{B}^r$ transformations for the 2D case are shown in Fig. 5.3. To understand the physical meaning of $\mathcal{B}^r$, provided that $\mathcal{B}$ defines the translational symmetry of a given physical system in real space, let us consider an observable $O(\mathbf{r})$ that depends on the spatial coordinates $\mathbf{r} \in \mathcal{R}^*$, and that it follows strictly the translational symmetry defined in $\mathcal{B}$. This last property of O can be condensed in the following equation:

$$O(\mathbf{r}) = O(\mathbf{r} + \mathbf{t}) \ , \forall \mathbf{t} \in \mathcal{B} \ , \tag{5.3}$$

where $\mathbf{t}$ is a translation vector formed by multiplying each primitive vector of $\mathcal{B}$ by an integer number, i.e. $\mathbf{t}$ is an element of $\mathcal{B}$. If now we expand O in a general Fourier basis, $O(\mathbf{r}) = \int c(\mathbf{k}) \cdot e^{i\mathbf{kr}} d\mathbf{k}$ and introduce it in Eq. 5.3, we obtain the expression: $\int c(\mathbf{k}) \cdot e^{i\mathbf{kr}} \left(e^{i\mathbf{kt}} - 1\right) d\mathbf{k} = 0$, which can be only true if:

$$e^{i\mathbf{kt}} = 1, \forall \mathbf{t} \in \mathcal{B} \tag{5.4}$$

after discarding the trivial option $c(\mathbf{k}) = 0$. As from complex analysis we know that $1 = e^{i2\pi n}$, n being any integer number, Eq. 5.4 can be reduced to:

$$\mathbf{kt} = 2\pi n, \ n \in \mathbb{Z} \ , \tag{5.5}$$

which means that only $\mathbf{k}$ vectors that satisfy this last equation can enter the Fourier expansion of O. One interesting implication of Eq. 5.5 is that now we have a discrete set of allowed $\mathbf{k}$ vectors. Thus, we no longer need a continuous Fourier expansion of O, but a discrete one, $O(\mathbf{r}) = \sum_{\forall \mathbf{k} \in \mathcal{A}} c(\mathbf{k}) \cdot e^{i\mathbf{kr}}$, where $\mathcal{A}$ is the set of allowed $\mathbf{k}$ elements. If we try to characterize this vector space $\mathcal{A}$ by creating a suitable minimal basis $\{\mathbf{G}_1, \mathbf{G}_2, \mathbf{G}_3\}$ that respects Eq. 5.5, we will end up deducing exactly the definition of $\mathcal{B}^r$ basis vectors, namely, $\mathbf{G}_i \mathbf{u}_j = 2\pi\delta_{ij}$.

In conclusion, the elements of the reciprocal lattice $\mathcal{A} = \mathcal{B}^r$, $\mathcal{B}$ being the Bravais lattice of a crystal (3D) or a surface (2D), are exactly those $\mathbf{k}$ vectors needed for the discrete Fourier expansion of any function that follows strictly the translational symmetry of the system. Another interpretation of $\mathbf{k}$ vectors comes from the fact that a Fourier

*$\mathcal{R}$ is the set of all spatial geometries of the system

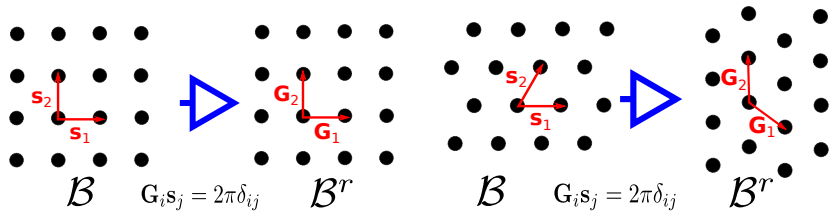

Figure 5.3: Two examples of transformations of Bravais lattices to their reciprocal lattice equivalent. On the left panel: $\mathcal{B}$ is an square Bravais lattice. Right panel: $\mathcal{B}$ is an hexagonal Bravais lattice.

element $e^{i\mathbf{kr}}$ is related to a plane wave with momentum $\mathbf{k}$. This momentum is perpendicular to the wave front plane and its modulus is inversely proportional to its wavelength. This allows us to think that each vector $\mathbf{k}$ in the reciprocal lattice is a class of equidistant parallel planes of the original Bravais lattice, whose surfaces are perpendicular to $\mathbf{k}$ and whose inter-plane distance is $\lambda = \frac{2\pi}{|\mathbf{k}|}$. In fact, when a plane in the real space is labeled with Miller indexes (hkl), we are really using the $\mathbb{Z}^3$ representation of a $\mathbf{k}$ vector in $\mathcal{B}^r$. As a final remark, it is important to explicitly say that the reciprocal space lattice of a given system is not exactly the reciprocal space $(\mathcal{G})$ of that system. $\mathcal{G}$ is an extension of $\mathcal{B}^r$ that can be constructed from linear combinations of vectors $\{\mathbf{G}_1, \mathbf{G}_2, \mathbf{G}_3\}$ with real coefficients, i.e. $\mathcal{G} = \underset{\mathbb{R}}{\mathcal{L}}\{\mathbf{G}_1, \mathbf{G}_2, \mathbf{G}_3\}$, whilst $\mathcal{B}^r$ is constructed using integer coefficients. In fact, $\mathcal{B}^r$ is a subset of $\mathcal{G}$, $\mathcal{B}^r \subset \mathcal{G}$.

DFT THEORY IN BRIEF

Assuming that the BOA provides a good description of our system of interest, all the information of its electronic structure can be obtained from Eq. 4.6. There are two main families of methods to resolve this electronic structure problem, namely, wave function formalisms, in which observables are considered to take the form of a functional of the wave function of the system (see Ref. [122]) and DFT formalisms, in which observables take the form of a functional of the density of the system. In this work, all the electronic structure calculations were performed following the DFT formalism. For completeness reasons, despite this work is not focused on the details of those calculations, we will briefly discuss in this section the basics of DFT.

The DFT is based on the Hohenberg-Kohn theorems, which demonstrate that there is a bijective map between the ground-state density of a system, its external potential and the ground-state wave function of the system. As a consequence, all the ground-state expectation values of an observable $\hat{O}$ have the form of a unique functional of the ground-state density $\rho_0(\mathbf{r})$, $O[\rho_0] = \langle \Psi[\rho_0] | \hat{O} | \Psi[\rho_0] \rangle$, including the energy of the system. Thus, in order to obtain ρ_0, the explicit dependence of the energy on the density $E[\rho]$ should be known. In

fact, ρ_0 must minimize the value of this functional. Despite DFT is an exact theory for a many-body problem, the exact expression of the functional $E[\rho]$ is not known, specially when the interactions between the constitutive elements of the system are taken into account. However, in 1965, Kohn and Sham [123] proposed to substitute the many-body interacting problem by an auxiliary independent-particle system which happens to have the same electron density than the real physical system, so that the original electronic Schrödinger equation (Eq. 4.6) is converted to N independent mono-electronic equations, which have the form:

$$\hat{H}^{KS} = \hat{T}_{e^-}(\mathbf{r}) + V_{eff} \tag{5.6}$$

$$V_{eff}(\mathbf{r}) = V_{nucl-e^-}(\mathbf{r}) + \int \frac{\rho(\boldsymbol{r}')}{|\boldsymbol{r}-\boldsymbol{r}'|} d\boldsymbol{r}' + \frac{\delta E_{xc}[\rho]}{\delta\rho(\mathbf{r})} \tag{5.7}$$

$$\hat{H}^{KS}\psi_n^{KS}(\boldsymbol{r}) = \varepsilon_n^{KS}\psi_n^{KS}(\boldsymbol{r}) \tag{5.8}$$

$$\psi^{KS}(\boldsymbol{r}_1, \boldsymbol{r}_2, ..., \boldsymbol{r}_N) = \frac{1}{\sqrt{N!}} \left| \psi_1^{KS}\psi_2^{KS}...\psi_N^{KS} \right| , \tag{5.9}$$

where N is the total number of electrons, $\hat{H}^{KS}$ is the Kohn-Sham mono-electronic effective Hamiltonian, ψ_n^{KS} is the n-th eigenfunction of $\hat{H}^{KS}$ (a Kohn-Sham orbital), ε_n^{KS} is the eigenvalue associated to ψ_n^{KS}, ψ^{KS} is the total wave function of the system expressed as a Slater determinant, and $E_{xc}[\rho]$ is the exchange-correlation energy functional. This functional contains all the information regarding the many-body correlation-exchange effects and is crucial to carry out accurate calculations. At this point, it should be noticed that all equations stand for a given nuclear geometry $\mathbf{R}^*$, but it has been omitted on purpose to keep the notation simple. The energy of the interacting system $E^{KS}[\rho]$ has the form:

$$E^{KS}[\rho] = \sum_{i=1}^{N} \varepsilon_i^{KS} + E_{xc}[\rho] + \frac{1}{2}\int\int \frac{\rho(\boldsymbol{r})\rho(\boldsymbol{r}')}{|\boldsymbol{r}-\boldsymbol{r}'|} d\boldsymbol{r}' d\boldsymbol{r} - \int \frac{\delta E_{xc}[\rho]}{\delta\rho(\mathbf{r})}\rho(\boldsymbol{r}) d\boldsymbol{r} . \tag{5.10}$$

From Eq. 5.8, $\hat{H}^{KS}$ is completely defined once the exchange-correlation functional E_{xc} and a trial density ρ is provided. Therefore, the ground state energy $E_0^{KS} = E^{KS}[\rho_0]$ can be obtained by minimizing $E^{KS}[\rho]$ value varying the form of the density ρ as it follows from the variational principle:

$$E_0^{KS} < E^{KS}[\rho] , \quad \rho \neq \rho_0 . \tag{5.11}$$

The minimization is done in a self consistent iterative fashion. Initially, we start with a guess of the electron density of the system. From this guess $\hat{H}^{KS}$ is uniquely determined and we can obtain its eigenvalues and eigenfunctions $\left\{\psi_n^{KS}(\boldsymbol{r}), \varepsilon_n^{KS}\right\}$. From the set of Kohn-Sham orbitals, a new better guess of the trial electron density $\rho'(\mathbf{r}) =$

*we are working within the BOA

$\sum_{i=1}^{N} \left|\psi_i^{KS}(\boldsymbol{r})\right|^2$ is constructed and the cycle continues until we obtain a minimum value of $E^{KS}[\rho]$. At this point, the trial density ρ should be very similar to ρ_0 up to some threshold error. Despite the fact that the way of obtaining ρ_o is variational, there is not a systematic way to improve DFT results if the functional $E_{xc}[\rho]$ is proven to be wrong for the modeled physical system. That is why one should always test theoretical results obtained by different functionals with benchmark calculations or experiments, to chose the one that keeps the correct physics of the system. At this point, it is worth remembering that E_0^{KS} takes the form of a PES, $E_0^{KS}(\mathbf{R})$ (see Chap. 4).

The exchange-correlation energy functionals used in this work follow the generalized gradient approximation (GGA) to DFT. Within this approach, $E_{xc}[\rho]$ has the general form:

$$E_{xc}^{GGA}[\rho] = \int \rho(\boldsymbol{r})\epsilon_{xc}[\rho(\boldsymbol{r}), \nabla\rho(\boldsymbol{r})]\, d\boldsymbol{r}\,, \tag{5.12}$$

where ϵ_{xc}, which has units of exchange-correlation energy per volume unit, depends on the density and the gradient of the density, and is constructed from some ideal model that satisfies certain boundary conditions. This makes the density functional theory within the generalized gradient approximation (DFT-GGA) a semi-local approximation in contrast with the older local density approximation (LDA), where the exchange-correlation functional only depends on the density. The improvements that DFT-GGA introduces respect to DFT-LDA allow one to construct more accurate PESs, to be used to study molecule/surface dynamics phenomena, which are rather sensible to the PES shape. In this work, we have used three different DFT-GGA PESs, namely, H(D)/LiF(001), $H_2(D_2)$/LiF(001) and $H_2(D_2)$/Methyl-Si(111). The first two ones, were obtained using the Perdew-Wang (PW91[124]) exchange-correlation functional, while the third one was obtained using the Perdew-Burke-Ernzerhof (PBE [125]) functional*. In both cases, these functionals were chosen because they predict theoretical bulk structures parameters in reasonable agreement with the available experimental data.

THE BLOCH THEOREM AND THE SUPER-CELL MODEL

Within the DFT formalism (see previous section), the PES can be calculated solving a set of mono-electronic equations described in Eq. 5.8, where each equation only depends on 3 DOFs (x, y, z). However, for molecule-surface system there are, in principle, an infinite number of electrons if further approximations are not taken. Taking advantage of the 2D symmetry of the system†, we know that there is a finite re-

*Notice that the PBE functional was developed in such a way that the obtained energies matched the PW91 ones.

†We are dealing with periodic surfaces

gion in space that can generate the entire surface applying translation operations (see Sec. 5.1). Thus, Eq. 5.8 can be solved for the finite system inside the primitive cell of the surface (motive) adding the effects that periodicity introduce to the equations. These effects are encoded in what it is called the Bloch theorem. This theorem states that a Hamiltonian that follows some translation symmetry $\mathcal{B}$ in the real space (space of geometries) commutes with any translation operator $\hat{\tau}_{\mathbf{t}}$, and therefore, eigenstates of $\hat{H}$ should be eigenfunctions of $\hat{\tau}_{\mathbf{t}}$ as well, the so-called Bloch waves $f_{\mathbf{q}}(\mathbf{r})$:

$$f_{\mathbf{q}}(\mathbf{r}) = e^{i\mathbf{q}\mathbf{r}} u_{\mathbf{q}}(\mathbf{r}), \quad \mathbf{q} \in \mathcal{G}_B \tag{5.13}$$

$$\hat{\tau}_{\mathbf{t}} f_{\mathbf{q}}(\mathbf{r}) = f_{\mathbf{q}}(\mathbf{r}+\mathbf{t}) = e^{i\mathbf{q}\mathbf{t}} f_{\mathbf{q}}(\mathbf{r}), \quad \forall \mathbf{t} \in \mathcal{B} \tag{5.14}$$

$$u_{\mathbf{q}}(\mathbf{r}) = u_{\mathbf{q}}(\mathbf{r}+\mathbf{t}), \quad u_{\mathbf{q}+\mathbf{G}}(\mathbf{r}) = u_{\mathbf{q}}(\mathbf{r}), \quad \forall \mathbf{G} \in \mathcal{B}^r, \tag{5.15}$$

where $\mathcal{G}_B$ is a special subspace of the reciprocal space $\mathcal{G}$ called the (first) Brillouin zone ($\mathcal{G}_B \subset \mathcal{G}$) of the system, defined as the set of the nearest vectors $\mathbf{q}$ to a given point $\mathbf{G}$ of the reciprocal lattice. A pictorial example of the Brillouin zone of a hexagonal Bravais lattice is given in Fig. 5.4. Despite the fact that we can define one Brillouin zone for each element $\mathbf{G} \in \mathcal{B}^r$, namely $\mathcal{G}_B(\mathbf{G})$, it is enough to consider only one of them, as the previous equations are invariant when any vector $\mathbf{G}$ is added to $\mathbf{q}$. Applying the Bloch theorem to DFT basic equations, we obtain the following set of equations:

$$\sum_{\mathbf{G}'} H_{\mathbf{G}\mathbf{G}'}(\mathbf{q})\, c_{n,\mathbf{q}+\mathbf{G}'} = \epsilon_{n,\mathbf{q}} c_{n,\mathbf{q}+\mathbf{G}} \tag{5.16}$$

$$H_{\mathbf{G}\mathbf{G}'}(\mathbf{q}) = \frac{1}{2}|\mathbf{q}+\mathbf{G}|^2 \delta_{\mathbf{G}\mathbf{G}'} + V^F_{eff}(\mathbf{G}-\mathbf{G}') \tag{5.17}$$

$$\psi_{n,\mathbf{q}}(\mathbf{r}) == \frac{1}{\sqrt{\Omega_{cell}}} \sum_{\forall \mathbf{G} \in \mathcal{B}^r} c_{n,\mathbf{q}+\mathbf{G}} e^{i(q+\mathbf{G})\mathbf{r}}, \tag{5.18}$$

where Ω_{cell} is the total volume of the unit cell of the system, V^F_{eff} is the Fourier transform of V_{eff} and $\psi_{n,\mathbf{q}}$ is an eigenfunction of $\hat{H}^{KS}$. Notice that hereinafter, we will assume DFT level of theory, so super-index KS has been dropped from equations. Now, the problem we are facing has a finite number of electrons but should be resolved for an infinite number of $\mathbf{q}$ vectors in the Brillouin zone of the system. Fortunately, as electronic wave functions evaluated near a certain value $\mathbf{q}$ are quite similar, we only need to solve the electronic equation 5.17 for a finite number of them. It is interesting to comment here that for each level n, the energy $\epsilon_{n,\mathbf{q}}$ is degenerate with an infinite number of $\mathbf{q}$ states, giving rise to what is known as the electronic band structure of a periodic system [77].

There are various criteria to know which vectors $\mathbf{q}$ should be included in calculations. The most simple one is just divide the Brillouin zone in $N_{\mathbf{G}_1} \cdot N_{\mathbf{G}_2}$ equally distributed regions. If for simplicity we assume that any vector in this discretized zone ($\mathbf{q}_{kl}$) can be expressed as a linear combination $\mathbf{q}_{kl} = \Delta q\,(k\mathbf{G}_1 + l\mathbf{G}_2)$, where k and

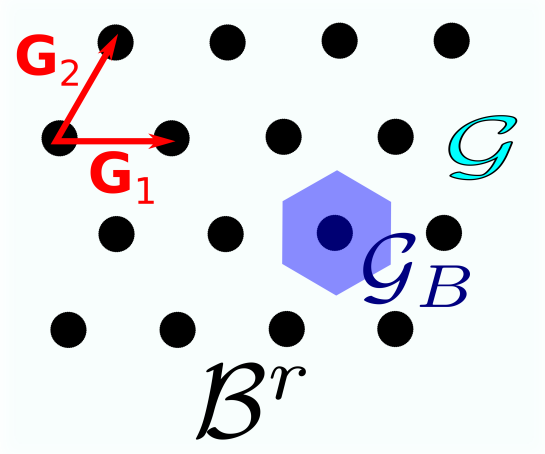

Figure 5.4: Example of a Brillouin zone shape when $\mathcal{B}^r$ is a hexagonal Bravais lattice. $\mathcal{G}$ stands for the reciprocal space (zone in turquoise), $\mathcal{G}_B$ stands for the Brillouin zone (zone in blue) and $\mathcal{B}^r$ for the points of the Bravais lattice (dots in black).

l go from 0 to $N_{\mathbf{G}_1}$ and $N_{\mathbf{G}_2}$, respectively, the discretization has the following meaning: we are imposing that each electronic function $\psi_{n,\mathbf{q}}(\mathbf{r})$ has periodicity $L = \frac{2\pi}{\Delta q}$. This superimposition is called in physics the Born-von Karman boundary condition. It is easy to prove that the volume of the Brillouin zone of a system is inversely proportional to the unit cell volume in real space of the same system. This means that the larger the unit cell the less amount of $\mathbf{q}$ vectors are necessary to have a dense enough representation of its Brillouin zone. We have to remark as well that, in principle, the expansion in the plain waves basis set $\sum_{\forall \mathbf{G} \in \mathcal{B}^r} c_{n,\mathbf{k}+\mathbf{G}} e^{i(q+\mathbf{G})\mathbf{r}}$ is infinite, but in the simulations, it is truncated up to an specific value, the so-called cut-off energy $E_{cut} = \frac{1}{2}\mathbf{G}_{cut}^2$, so that plain waves with an associated kinetic energy higher than the cut off $|\mathbf{q}+\mathbf{G}| > \mathbf{G}_{cut}$ are neglected.

From the simulations point of view, solving Eq. 5.17 using periodic boundary conditions for a molecule-surface system is not a straight forward task, because the system is only periodic in 2 dimensions (surface plane). In contrast, in the perpendicular direction to the surface (z), the system goes from its bulk structure ($z \to -\infty$) to the vacuum ($z \to \infty$). Between these two extremes, we can define two zones: one inside the material, which has a distorted bulk structure due to the lack of z translational symmetry in the regions close to the surface, and one region outside the material but close to it. In the latter region, for example, if we add an atom or a molecule, it would "feel" the presence of the material. Any theoretical model that tries to reliably represent such a system should cut the bulk part at some point and should include all the zones described before (see Fig. 5.5). To solve this problem, the most usual strategy followed is to create a

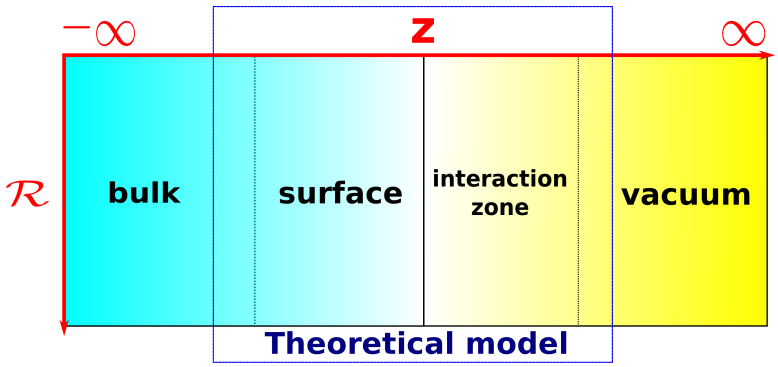

Figure 5.5: Broken symmetry scheme along the perpendicular direction to a surface. Inside the blue square lays the minimum part that should be well described in any theoretical treatment of a surface. $\mathcal{R}$ stands for the real 2D space in which the translational symmetry of the surface is defined.

suitable 3D super-cell that can be repeated periodically in 3D-space, while minimizing artifacts produced by the periodical assumption in the z direction (see Fig. 5.6). When the surface is modeled interacting with some other object, like an atom or a molecule (in our case, H, D, H_2 and D_2) the 2D unit cell should be big enough to make negligible the spurious interaction between the periodic images of the interacting object. Regarding the direction perpendicular to the surface (z), the number of surface layers to be modeled should be large enough to reproduce bulk effects, and the vacuum space between adjacent surfaces should be wide enough to prevent the system to interact with its upper periodic image. The main advantage of this model is that we can use standard periodic calculations codes, without any special modifications, to obtain the electronic data we need to construct the PES, because now Eq. 5.17 holds for the three dimensions of space.

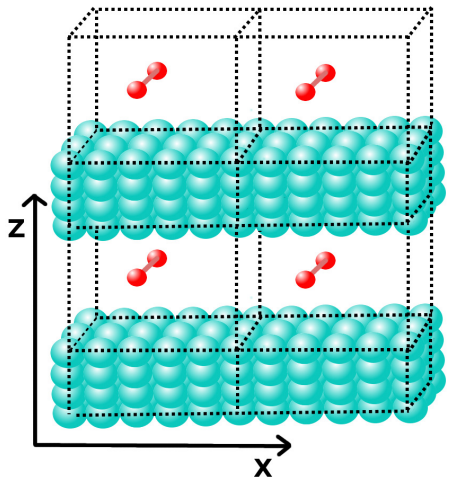

Figure 5.6: Super-cell model expanded only in x and z direction.

CORE PSEUDO-POTENTIALS

At this point, we have reduced the intractable problem of finding the electronic structure of an infinite periodic system to a bounded discrete problem that depends on a series of well-behaved control parameters, such as the super-cell model, the cut-off energy for $\psi_{n,\mathbf{q}}$ expansions, the Brillouin zone discretization, etc. However, there is still a major problem from the computational point of view: all electron calculations are, in general, too expensive to be performed even for a modest amount of atoms in a super-cell model. This inconvenience is worsen by the fact that $\psi_{n,\mathbf{q}}$ wave functions are expanded in a plane-wave basis set, which converges poorly for localized electrons. A common way to solve this problem is to substitute all core electrons (electrons that are close to the nuclei, and therefore more localized) of each nucleus by some smooth function that simulates the average potential and scattering properties that those electrons would have in a full calculation. This function, which is called pseudo-potential, can be obtained from atomic calculations and do not have a trivial form. Only valence electrons are treated rigorously (within all the approximations done up to now) in electronic calculations, although now the periodic potential they "feel" includes the interaction with all core-electrons, encoded in the pseudo-potential.

In a few words, the commoner pseudo-potential methods introduce some kind of radial compartmentalization of the space around an atom in order to distinguish its valence space from its core zone, inside of which the all electron wave function is replaced by a soft nodeless pseudo-wave function. The properties that this pseudo-wave functions should satisfy varies from method to method. Obtaining good pseudo-potentials is itself a wide interesting topic that is outside the purpose of this manuscript (see Refs. [78, 126–128]).

In this work we have used the projector augmented-wave (PAW) [127] method to treat all electron wave functions. Within this method, all electron wave functions $|\Psi\rangle$ can be obtained by a linear transformation $\mathcal{T}$ from their smoother pseudo wave version $|\tilde{\Psi}\rangle$:

$$|\Psi\rangle = \mathcal{T}\,|\tilde{\Psi}\rangle \ . \tag{5.19}$$

This transformation is chosen to be the identity operator plus a sum of transformations $\mathcal{T}_{\mathbf{R}}$ centered at the cores of all atoms of the system:

$$\mathcal{T} = \mathbb{1} + \sum_{\mathbf{R}} \mathcal{T}_{\mathbf{R}} \ . \tag{5.20}$$

Each local transformation $\mathcal{T}_{\mathbf{R}}$ action is confined inside some augmentation sphere $\Omega_{\mathbf{R}}$ centered at $\mathbf{R}$ by defining a set of target functions $|\phi_i\rangle$, called partial waves, that are orthogonal to the core states and complete within $\Omega_{\mathbf{R}}$:

$$|\phi_i\rangle = (\mathbb{1} + \mathcal{T}_{\mathbf{R}})\,|\tilde{\phi}_i\rangle \ , \tag{5.21}$$

where $|\tilde{\phi}_i\rangle$ are the smooth pseudo partial waves of each $|\phi_i\rangle$. After some changes [127], one finds that Eq. 5.19 can be written in a more explicit way:

$$|\Psi\rangle = \left|\tilde{\Psi}\right\rangle + \sum_m c_m \left[|\phi_m\rangle - |\tilde{\phi}_m\rangle\right] \ , \tag{5.22}$$

where index m runs over augmentation spheres and partial wave functions. If now each coefficient c_m is expressed as:

$$c_m = \langle \tilde{p}_m \, | \tilde{\psi} \rangle \ , \tag{5.23}$$

satisfying $\langle \tilde{p}_m \, | \tilde{\phi}_n \rangle = \delta_{mn}$ and $\sum_i |\tilde{\phi}_m\rangle \langle \tilde{p}_m| = 1$ within each convenient $\Omega_{\mathbf{R}}$, the transformation $\mathcal{T}$ can be rewritten as:

$$\mathcal{T} = \mathbb{1} + \sum_m \left[|\phi_m\rangle - |\tilde{\phi}_m\rangle\right] \langle \tilde{p}_m| \ , \tag{5.24}$$

which means that $\mathcal{T}$ is completely determined when functions $|\phi_m\rangle$ and $|\tilde{\phi}_m\rangle$ as well as the projectors $\langle \tilde{p}_m|$ are defined. The way to obtain such elements is out of the scope of this work. The transformation $\mathcal{T}$ can be applied to obtain valence ($|\Psi^v\rangle$) or core ($|\Psi^c\rangle$) all electron wave functions. In fact, core wave functions have the simple expression:

$$|\Psi^c\rangle = \left|\tilde{\Psi}^c\right\rangle + |\phi^c\rangle - |\tilde{\phi}^c\rangle \ , \tag{5.25}$$

$|\phi^c\rangle$ being exactly a core state of an atom of the system extracted from an isolated calculation (frozen core approximation), and $|\tilde{\phi}^c\rangle$ its pseudo wave version within $\Omega_{\mathbf{R}}$.

The power of the PAW method comes from the fact that any semi-local operator $\hat{A}$ that acts on the all electron wave functions can be mapped to a pseudo operator $\tilde{A}$ that acts on pseudo wave functions:

$$\tilde{A} = \mathcal{T}^\dagger \hat{A} \mathcal{T} \ . \tag{5.26}$$

This means that evaluations of observables like $\hat{H}$, forces, etc. can be carried out by only computing the pseudo wave functions $|\tilde{\psi}\rangle$, which are easier to deal computationally than the all electron ones. Nevertheless, the method provides a way to recover the all electron wave functions via Eq. 5.19 when necessary.

SMEARING PROCEDURE

In section 5.4, although a more tractable version of Eq. 5.8 was presented, it was omitted how to calculate the total energy of a discretized periodic system. Introducing symmetry effects yielded to an expression of "orbital" energies $(\epsilon_{n,\mathbf{q}})$ continuum in $\mathbf{q}$, giving rise to the concept of bands. Filling up the infinite number of available energy levels $(\epsilon_{n,\mathbf{q}})$ with the infinite number of electrons of the surface system is not a trivial task at all. The way electronic states $(n,\mathbf{q})$ are populated affects the definition of the fundamental state of the

system, and therefore, the ground energy, among other important observables.

In order to get explicit expressions for the energy, we should define a function called density of states (DOS) $g(\epsilon)$, which counts the number of electronic available states with energy ϵ. In the literature [77] we can find this expression for $g(\epsilon)$:

$$g(\epsilon) = \frac{V}{(2\pi)^3} \sum_{n=1}^{N} \int_{\mathcal{G}_B} d\mathbf{q} 2\delta\left(\epsilon - \epsilon_{n,\mathbf{q}}\right) = \frac{2V}{(2\pi)^3} \sum_{n=1}^{N} \int_{\epsilon_{n,\mathbf{q}}=\epsilon} \frac{dS_{\epsilon_{n,\mathbf{q}}}}{\left|\vec{\nabla}_{\mathbf{q}} \epsilon_{n,\mathbf{q}}\right|} \tag{5.27}$$

$$N = \int_{\mathcal{R}} d\mathbf{r} \rho(\mathbf{r}) = \int_{-\infty}^{\epsilon_F} g(\epsilon) \, d\epsilon \ , \tag{5.28}$$

where V is the volume of the real unit cell of the system*, $dS_{\epsilon_{n,\mathbf{q}}}$ is a differential element normal to a surface in the reciprocal space that has energy $\epsilon_{n,\mathbf{q}}$, and ϵ_F is the Fermi energy of the system. The latter quantity plays a major role in the definition of the fundamental state of a system, because it represents the last occupied electronic state $\psi_{n,\mathbf{q}}$, which now we can call $\psi_{n_F,\mathbf{q}_F}$. From Eq. 5.27 , it can be demonstrated that the shape of the DOS has sharp-pikes when $\vec{\nabla}_{\mathbf{q}} \epsilon_{n,\mathbf{q}} = \vec{0}$, and therefore, that a good sampling of the Brillouin zone should be performed to keep the correct non trivial shape of $g(\epsilon)$, which can make the calculation too expensive from the computational point of view. "Smearing" techniques seek the way to perform such $\mathcal{G}_B$ samplings with the least computational cost introducing some approximations.

Now that the specific case of $g(\epsilon)$ evaluation has been introduced, we can go to a more general case in which we have a known function, f, that depends on $\mathbf{q}$ and measures some observable F. Its energy dependent version $F(\epsilon)$ can always be calculated using a Brillouin zone integral of the type:

$$F(\epsilon) = \int_{\mathcal{G}_B} d\mathbf{q} f(\mathbf{q}) \, \delta\left(\epsilon - \epsilon_{n,\mathbf{q}}\right) \ . \tag{5.29}$$

If we are interested in calculating the observable F, knowing which energy bands are occupied in our material, we should perform an integral of the form:

$$F = \int_{-\infty}^{\infty} d\epsilon \left[1 - \Theta\left(\epsilon - \epsilon_F\right)\right] F(\epsilon) \ , \tag{5.30}$$

where $\Theta(\epsilon - \epsilon_F)$ is the Heaviside step function. Note that Eq. 5.28 can be re-written in the previous way. These both types on integrals converge poorly with the number of $\mathbf{q}$ samples in $\mathcal{G}_B$, because of the appearance of the non derivable abrupt functions $\Theta(\epsilon - \epsilon_F)$ and $\delta\left(\epsilon - \epsilon_{n,\mathbf{q}}\right)$. Thus, "smearing" methods try to change these functions

*g is normalized to this volume

by smoother versions, like in the Methfessel-Paxton [129] procedure. Within this smearing method, Dirac delta functions δ are approximated up to some order M to:

$$\delta\left(\frac{\epsilon-\epsilon_F}{\sigma}\right) \approx D_M\left(\frac{\epsilon-\epsilon_F}{\sigma}\right) = \sum_{l=0}^{M} A_l H_{2l}\left(\frac{\epsilon-\epsilon_F}{\sigma}\right) e^{-\left(\frac{\epsilon-\epsilon_F}{\sigma}\right)} \quad (5.31)$$

and $1-\Theta\left(\frac{\epsilon-\epsilon_F}{\sigma}\right)$ step functions to:

$$1-\Theta\left(\frac{\epsilon-\epsilon_F}{\sigma}\right) \approx S_M\left(\frac{\epsilon-\epsilon_F}{\sigma}\right) = 1 - \int_{-\infty}^{\frac{\epsilon-\epsilon_F}{\sigma}} D_M(\tau)\, d\tau\,, \quad (5.32)$$

where H_{2l} is an even Hermite polynomial, $A_l = \frac{(-1)^l}{l!4^l\sqrt{\pi}}$, and σ a width parameter. It can be proven that substituting $D_M\left(\frac{\epsilon-\epsilon_F}{\sigma}\right)$ for $\delta(\epsilon-\epsilon_F)$ and $S_M\left(\frac{\epsilon-\epsilon_F}{\sigma}\right)$ for $1-\Theta(\epsilon-\epsilon_F)$ in Eqs. 5.29 and 5.30, tend to the exact result in the limit when σ is equal to zero. It is also true that for $M=0$ the result obtained for the energy of the system has a useful physical interpretation: the smearing plays the same role as adding to the system some thermal energy (warming the system), it smooths the distribution of electrons around the Fermi surface $\epsilon_{n_F\mathbf{q}_F}$. In fact the thermal energy added to the system can be regarded as a free-energy at temperature $T \approx \frac{\sigma}{k_B}$. When $M \neq 0$ the physical interpretation is more complicated.

In order to get a correct value of the energy of the system after applying a the Methfessel-Paxton smearing to integrals of type 5.29 and 5.30, an extrapolation $\sigma \to 0$ $(T \to 0)$ must be done. The way the extrapolation is implemented varies from method to method (see Ref. [130]). Finally, the expression for the smeared free energy $F_{M,\sigma}$ and the real total electronic energy E can be written as:

$$F_{M,\sigma}[\rho] = \int_{-\infty}^{\infty} \epsilon S_N\left(\frac{\epsilon-\epsilon_F}{\sigma}\right) g_{M,\sigma}(\epsilon)\, d\epsilon + E_{xc}[\rho] + \\ + \frac{1}{2}\int_{\mathcal{R}}\int_{\mathcal{R}} \frac{\rho(\boldsymbol{r})\rho(\boldsymbol{r}')}{|\boldsymbol{r}-\boldsymbol{r}'|} d\boldsymbol{r}' d\boldsymbol{r} - \int_{\mathcal{R}} \frac{\delta E_{xc}[\rho]}{\delta\rho(\mathbf{r})}\rho(\boldsymbol{r}) d\boldsymbol{r} \quad (5.33)$$

$$g_{M,\sigma}(\epsilon) = \sum_{n=1}^{N}\sum_{\forall\mathbf{q}\in\bar{\mathcal{G}}_B} \frac{1}{\sigma} D_M\left(\frac{\epsilon-\epsilon_{n,\mathbf{q}}}{\sigma}\right) \quad (5.34)$$

$$E[\rho] \approx \lim_{\sigma\to 0} F_{M,\sigma}[\rho]\,, \quad (5.35)$$

where $\bar{\mathcal{G}}_B$ is a discretized version of the Brillouin zone of the system. It is convenient that parameters M and σ are chosen to make $F_{M,\sigma}$ and E as much similar as possible. This way the extrapolation $F_{M,\sigma} \xrightarrow{\sigma=0} E$ is more reliable.

6

POTENTIAL ENERGY SURFACE INTERPOLATION

In this chapter, we will present the methods we used to make the transition from a set of single-point energy calculations $\mathcal{E} = \{\epsilon_{\mathbf{R}}\}_{\mathbf{R}}$ to a well defined continuous function $V(\mathbf{R})$, that contains all the information of nucleus-electron interaction in the fundamental state of the system and respects the correct symmetry.

THE STATIC SURFACE MODEL

Hitherto, we have exposed the assumptions made in this work to calculate the electronic energy of the fundamental state of an atom or a molecule-surface system, for a given fixed nuclei geometry, $\mathbf{R}$. This fixed geometry includes all nuclei coordinates without the distinction between surface or projectile atoms. In such a scheme, dynamics calculations would need to be performed on a PES with $3N$ dimensions, where N stands for the number of nuclei in the super-cell in use. If N is high, not only calculations could be prohibitive, but also the definition of the PES interpolation and its symmetry boundaries would be harder to implement.

In order to avoid such problems, we have kept frozen any DOF that do not belong to the molecular/atomic projectile whose dynamics we are simulating. Nuclei that belong to the surface are fixed at their equilibrium positions. Running dynamics within this scheme can be regarded as modeling the interaction of a chemical compound (in its internal ground state or not) with a frozen surface where no energy exchange is possible. In Fig. 6.1, we have plotted the definition of the DOFs we have followed to model atomic and diatomic projectiles in our systems of interest.

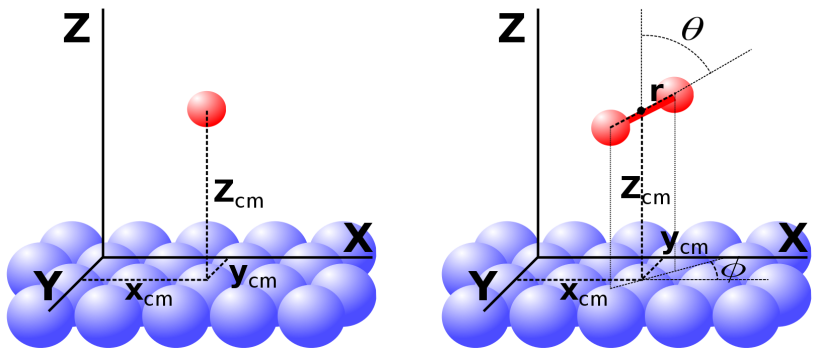

Figure 6.1: DOFs for an atomic (left panel) and a diatomic molecular (right panel) projectiles.

THE CORRUGATION REDUCING PROCEDURE

The corrugation reducing procedure is a PES interpolation method developed by F. Busnengo *et al.* [15], that has been applied successfully to model the interaction between many atom-surface (3D) and di-atomic molecule-surface (6D) systems [15, 131–136]. Within this method, instead of interpolating directly the discrete set of energies $\mathcal{E} = \{\epsilon_{\mathbf{R}}\}_{\mathbf{R}}$ to get the PES ($V(\mathbf{R})$), we interpolate a transformed version of this set ($\tilde{\mathcal{E}}$) in order to get a much smoother function $\mathcal{I}(\mathbf{R})$. The new set $\tilde{\mathcal{E}}$ is defined as:

$$\tilde{\mathcal{E}} = \{\tilde{\epsilon}_{\mathbf{R}} = \epsilon_{\mathbf{R}} - \mathcal{J}(\mathbf{R})\}_{\mathbf{R}} \ , \tag{6.1}$$

where $\mathcal{J}(\mathbf{R})$ is an arbitrary function designed to subtract to each element $\epsilon_{\mathbf{R}}$ the most repulsive part of the interaction projectile-surface. Doing so, the interpolating function $\mathcal{I}(\mathbf{R})$ is enforced to be a smoother version of $V(\mathbf{R})$. Finally, the PES function can be recovered from $\mathcal{I}(\mathbf{R})$ in a very simple way:

$$V(\mathbf{R}) = \mathcal{I}(\mathbf{R}) + \mathcal{J}(\mathbf{R}) \ . \tag{6.2}$$

The reason why the CRP method evaluates the potential V in an indirect way $(\mathcal{E} \to \tilde{\mathcal{E}} \to \mathcal{I} \to V)$, instead of a more efficient direct interpolation $(\mathcal{E} \to V)$, is purely practical. $\mathcal{E}$ can contain points (energies) in regions where the repulsion projectile-surface dominates, i.e. close to a repulsive Coulomb singularity, causing numerical instabilities in the procedure. This means that a direct interpolation, despite it is forced to satisfy $V(\mathbf{R}) = \epsilon_{\mathbf{R}}$, may contain unphysical wells or barriers at intermediate geometries causing wrong dynamics simulations. The only way to prevent this behavior is to add more points to $\mathcal{E}$, specially close to the singularity that is causing the instability. Thus, the direct procedure $(\mathcal{E} \to V)$ ends being less efficient that the CRP method $(\mathcal{E} \to \tilde{\mathcal{E}} \to \mathcal{I} \to V)$ due to the large number of points needed in $\mathcal{E}$.

In order to illustrate how numerical instabilities can affect the interpolated PES values, we have plotted in Fig. 6.2 several Z-cuts of the H/LiF(001) potential performed with the CRP method (full lines) and a raw interpolation (dashed lines). We have included as well single point evaluations of the energy (colored points) performed with the Vienna ab initio simulator package (VASP) code in order to stress the deviation of the interpolated PES from them. Green lines stand for Z-cuts on top of a Li atom ("c" site), which is a site that contains points that were included in the interpolation definition, i.e. there are points in $\mathcal{E}$ that belong to this site. Red and blue lines stand for Z-cuts on sites ("a" and "b", respectively) not included in the interpolation definition, i.e. no point in $\mathcal{E}$ belongs to these sites. We can see on the left panel that the values of the interpolated CRP-PES are close to DFT energies for the entire domain of Z, even in the surroundings

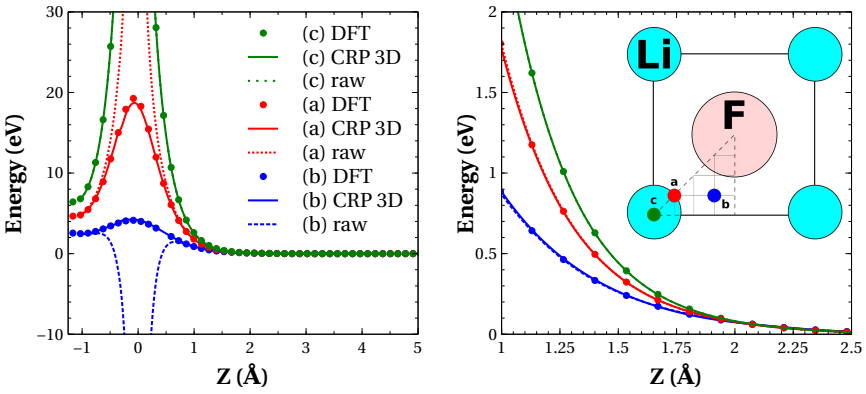

Figure 6.2: Z cuts of the H/LiF(001) potential on three (x, y) sites: "a" (red) and "b" (blue) are Z-cuts on (x, y) positions not included in the development of this CRP3D-PES; "c" (green), is a Z-cut on top of a Li atom and is one of the Wyckoff sites included in the calculation of this potential. Dots represent single point energies obtained from DFT calculations. Full lines are the PES values after a CRP interpolation. Dashed lines are the PES values after a direct interpolation. In the right panel there is an schematic inset of the location of "a", "b" and "c" sites on the LiF surface.

of the Coulomb singularity at $z = 0$. This does not happen with the direct interpolation, which fails to reproduce the correct energies close to the singularity ($|z| \leq 0.5$ Å) at sites that were not included in the interpolation definition. On the right panel, we can see that for $z \geq 1$ Å, both interpolated potentials compare perfectly well with DFT energies.

Eq. 6.2 is the most general formulation of the CRP method. The explicit form of $\mathcal{I}$ and $\mathcal{J}$ varies from system to system, because it has to be adapted to symmetry requirements. In the following sections we will present the implementations of these functions in the case of mono-atomic (3D) and di-atomic (6D) projectiles.

CRP Implementation for mono-atomic projectiles

How to compute $\mathcal{I}_{3D}$

In this case we only have one nucleus interacting with the surface, thus **R** represents three coordinates: x,y and z (see Fig. 6.1, left panel). The 2D surface symmetry in (x, y) is well described within a totally symmetric irreducible representation (irrep) of the point symmetry group associated to the surface*. In the standard notation of point group symmetry, such an irrep is represented by the letter "A" and may have some sub(super)-indexes. When there is more than one "A"

*a wallpaper group symmetry can be regarded as the action of translational symmetry to a point group.

irrep to choose, it must be chosen the one with all characters equal to one, i.e. A, A_1, A_g, A_{1g}, A' or A'_1. Thus, $\mathcal{I}_{3D}$ can be written:

$$\mathcal{I}_{3D}(x,y,z) = \sum_{\forall \mathbf{k} \in \mathcal{B}^r_+} \sum_{\forall \odot} c^{A,\odot}_{\mathbf{k}}(z) \cdot f^{A,\odot}_{\mathbf{k}}(x,y) \ , \tag{6.3}$$

where $f^{A,\odot}_{\mathbf{k}}$ are SAFTs as explained in App. B.2.1, $\mathcal{B}^r_+$ is a subset of the reciprocal lattice related to the translational symmetry of the surface (also explained in App. B.2.1), and coefficients $c^{A,\odot}_{\mathbf{k}}(z)$ are functions of z due to the lack of symmetry along this direction*.

In order to calculate $c^{A,\odot}_{\mathbf{k}}(z)$ coefficients, a set of single point energies, calculated systematically to sample high symmetry regions of the PES, is required. This sampling should be carried out keeping constant x and y for the chosen set of high-symmetry regions, varying z. In order to chose these high symmetry points, it is specially useful the concept of Wyckoff sites in crystallography. These sites are special (x,y) points in the plane whose point group symmetries are conjugate subgroups of the wallpaper group. Wyckoff sites are classified attending to their point subgroup order with letters a, b, c, ... , having the Wyckoff site "a" more symmetry operations than "b" and so on. This classification can help in choosing which Wyckoff sites are worth to be included in the expansion of $\mathcal{I}$. In general, it is preferable to include Wyckoff sites in order of symmetry.

Let us suppose that our PES interpolation is going to be based on N Wyckoff sites, labeled "w", and that there are n_w single point estimations of the potential along the z direction for each Wyckoff site. Then, we can define an arbitrary interpolation function $g_w(z)$ for each w that should satisfy:

$$g_w(z_l) = \tilde{\epsilon}_{w,z_l}, \text{ for } l = 1, ..., n_w \text{ and } w = 1, ..., N \ , \tag{6.4}$$

where $\tilde{\epsilon}_{w,z_l}$ is the value of the energy of the l-th single point calculation at Wyckoff site w and $z = z_l$ after smoothing it out with the subtraction of $\mathcal{J}_{3D}$ function (see Eq. 6.1). We assume the following order: $z_l < z_{l+1}$. With this new convenient nomenclature, $\tilde{\mathcal{E}}$ is partitioned as follows:

$$\tilde{\mathcal{E}} = \bigcup_{w=1}^{N} \{\tilde{\epsilon}_{w,z_l}\}_{l=1}^{n_w} \ . \tag{6.5}$$

In this work, we have used the commonest implementation of g_w in the literature, which is a piecewise cubic spline function:

$$g_w(z) = \begin{cases} s^w_1(z) & \text{if } z \in [z_1, z_2) \\ s^w_2(z) & \text{if } z \in [z_2, z_3) \\ \vdots & \vdots \\ s^w_{n_w-1}(z) & \text{if } z \in [z_{n_w-1}, z_{n_w}] \end{cases} \ , \tag{6.6}$$

*Notice that z forced symmetry exposed in Sec. 5.4 was imposed for the electronic single point calculations. For the PES construction this is not desirable.

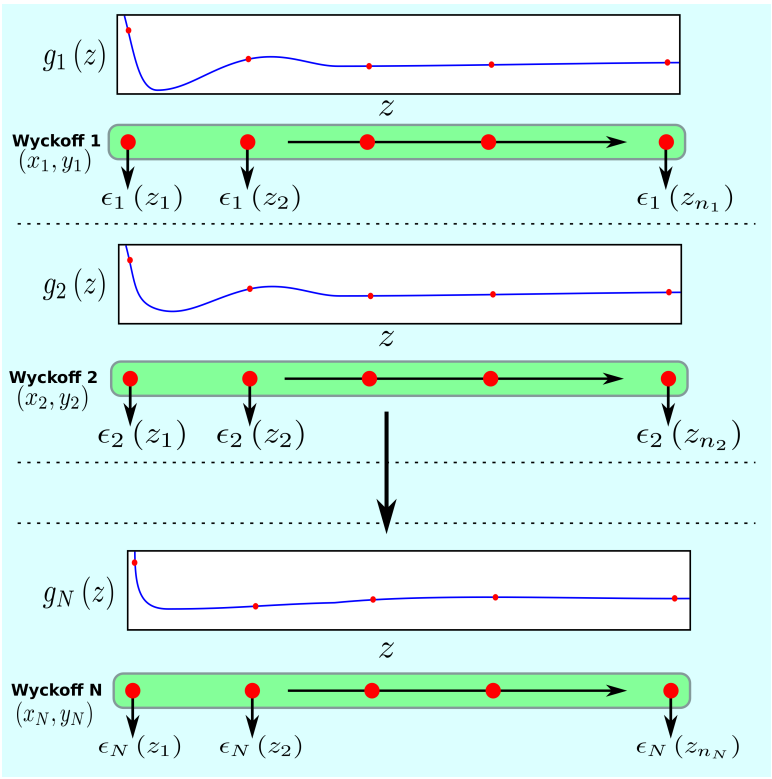

Figure 6.3: Schematic representation of the grouping of energy single point calculations $\{\epsilon_w(z)\}_{w,z}$ in Wyckoff sites. Each Wyckoff site contains a series of energy evaluations with fixed $x = x_w$ and $y = y_w$ values varying z. The set of functions $\{g_w(z)\}_w$ interpolates those energy values.

where each function s_j^w is a third order polynomial with origin at z_j, and real coefficients $\left(\Lambda_{j,0}^w, \Lambda_{j,1}^w, \Lambda_{j,2}^w, \Lambda_{j,3}^w\right)$. In Fig. 6.3, we have plotted a schematic representation of the grouping of data done so far to make it more clear.

At this point, the problem of obtaining $g_w(z)$ functions for each Wyckoff site is equivalent to obtaining the set of all polynomial coefficients described previously for $w = 1, ..., N$ and $j = 1, ..., n_{w-1}$. Obviously, solving such a system of equations requires more boundaries than those obtained from 6.4, so we require the following extra conditions:

$$s_j^w(z_{j+1}) = s_{j+1}^w(z_{j+1}) \tag{6.7}$$

$$\frac{\mathrm{d}}{\mathrm{d}z} s_j^w(z_{j+1}) = \frac{\mathrm{d}}{\mathrm{d}z} s_{j+1}^w(z_{j+1}) \tag{6.8}$$

$$\frac{\mathrm{d}^2}{\mathrm{d}z^2} s_j^w(z_{j+1}) = \frac{\mathrm{d}^2}{\mathrm{d}z^2} s_{j+1}^w(z_{j+1}) \tag{6.9}$$

$$\frac{\mathrm{d}}{\mathrm{d}z} s_1^w(z_1) = \frac{\mathrm{d}}{\mathrm{d}z} s_{n_w-1}^w(z_{n_w}) = 0\,, \tag{6.10}$$

which enforce each $g_w(z)$ to be continuous and derivable up to second order. The last condition enforces z gradients at the extremes of each Wyckoff z-grid to be zero. This is strictly true for $s^w_{n_w-1}(z_{n_w})$ if z_{n_w} is close to the vacuum region of the super-cell (see Fig. 5.5). $s^w_1(z_1)$ gradients can be set arbitrarily if z_1 is chosen to be in a region far away from the physical relevant zone of the PES, e.g. below the surface plane.

Once that the set of functions $\{g_w\}_{w=1}^N$ is completely defined, we can proceed to calculate $c^{A,\odot}_{\mathbf{k}}(z)$ coefficients. First of all, Eq. 6.3 must be truncated so that the total number of coefficients to be evaluated is exactly N. This truncation is, in principle, arbitrary, but in order to include the most important coefficients to the expansion, it is advisable to use the following recommendations:

- If we have two families of terms $c^{A,\odot}_{\mathbf{k}}(z)\cdot f^{A,\odot}_{\mathbf{k}}(x,y)$ and $c^{A,\odot}_{\mathbf{q}}(z)\cdot f^{A,\odot}_{\mathbf{q}}(x,y)$ with $\mathbf{k}\neq\mathbf{q}$, which we will call hereinafter $(\mathbf{k},\odot)$ and $(\mathbf{q},\odot)$ respectively, we will include with preference the ones that have the lowest diffraction order. This means that we will prefer $(\mathbf{k},\odot)$ over $(\mathbf{q},\odot)$ only if $|\mathbf{k}|<|\mathbf{q}|$.

- If we include in the expansion a family of terms $(\mathbf{k},\odot)$, we should include all families of terms $(\mathbf{q},\odot)$ that have the same diffraction order, i.e. $|\mathbf{q}|=|\mathbf{k}|$.

- If we include a family of terms $(\mathbf{k},\odot)$, we should include both $(\mathbf{k},\oplus)$ and $(\mathbf{k},\ominus)$ terms if they do not vanish by symmetry. If for some reason we cannot fulfill this recommendation, i.e. if we cannot include both $(\mathbf{k},\oplus)$ and $(\mathbf{k},\ominus)$ non-vanishing terms, we can average their value creating a unique term named $(\mathbf{k},\bigcirc)$, which has the form:

$$(\mathbf{k},\bigcirc)\equiv c^{A,\bigcirc}_{\mathbf{k}}(z)\cdot\left[f^{A,\ominus}_{\mathbf{k}}(x,y)+f^{A,\oplus}_{\mathbf{k}}(x,y)\right]\ . \tag{6.11}$$

  The symbol "$\bigcirc$" stresses that $(\mathbf{k},\bigcirc)$ is neither even $(\oplus)$ nor odd $(\ominus)$.

N values that allow a selection that satisfies the previous recipe are preferable to those that do not.

From now on, in order to simplify equations notation, we will use "η" for a concrete choice of indexes $(\mathbf{k},\odot)$. Now, the working equation to calculate $c^{A,\odot}_{\mathbf{k}}$ coefficients (c^A_η with the new notation) can be written as follows:

$$\sum_{\eta=1}^{N} c^A_\eta(z)\cdot f^A_\eta(x_w,y_w)=g_w(z),\ \text{for } w=1,2,...,N\ , \tag{6.12}$$

where (x_w, y_w) are the fixed x and y coordinates of Wyckoff site w. In matrix form Eq. 6.12 can be written as:

$$\underline{C}(z) = \underline{\underline{F}}^{-1} \cdot \underline{G}(z) \tag{6.13}$$

$$\underline{C}(z) = \begin{bmatrix} c_1^A(z) & c_2^A(z) & \dots & c_N^A(z) \end{bmatrix}^T \tag{6.14}$$

$$\underline{G}(z) = \begin{bmatrix} g_1(z) & g_2(z) & \dots & g_N(z) \end{bmatrix}^T \tag{6.15}$$

$$\underline{\underline{F}} = \begin{bmatrix} f_1^A(x_1,y_1) & f_2^A(x_1,y_1) & \dots & f_N^A(x_1,y_1) \\ f_1^A(x_2,y_2) & f_2^A(x_2,y_2) & \cdots & f_N^A(x_2,y_2) \\ \vdots & \vdots & \ddots & \vdots \\ f_1^A(x_N,y_N) & f_2^A(x_N,y_N) & \dots & f_N^A(x_N,y_N) \end{bmatrix} . \tag{6.16}$$

When the gradient of $\mathcal{I}_{3D}$ is required for a given geometry (x, y, z), it is easy to compute $\frac{\partial}{\partial x}\mathcal{I}_{3D}$ and $\frac{\partial}{\partial y}\mathcal{I}_{3D}$ contributions. We only need $c_\eta^A(z)$ coefficients (already calculated in the estimation of $\mathcal{I}_{3D}$) and the evaluation of functions $\frac{\partial}{\partial x}f_\eta^A(x,y)$ and $\frac{\partial}{\partial y}f_\eta^A(x,y)$ respectively. In the case of $\frac{\partial}{\partial z}\mathcal{I}_{3D}$, we have to solve the following system of equations:

$$\sum_{\eta=1}^{N}\left[\frac{\mathrm{d}}{\mathrm{d}z}c_\eta^A(z)\right]\cdot f_\eta^A(x_w,y_w) = \frac{\mathrm{d}}{\mathrm{d}z}g_w(z), \text{ with } w = 1,2,...,N\ , \tag{6.17}$$

which can be done in a similar way to Eq. 6.12. Notice that the $\underline{\underline{F}}$ matrix was already inverted so $\underline{\underline{F}}^{-1}$ does not need to be computed another time.

In Fig. 6.4, we present some examples to illustrate how smooth is $\mathcal{I}_{3D}$ function (dashed lines) compared with V_{3D} (full lines) for several z-cuts at four different Wyckoff sites.

How to compute $\mathcal{J}_{3D}$

In principle, there is not a pre-established way to build $\mathcal{J}_{3D}$ as long as it ensures a stable smooth interpolation of $\mathcal{I}_{3D}$. However, in the literature [15, 132] is recommended to define $\mathcal{J}_{3D}$ as a sum of repulsive 1D potentials:

$$\mathcal{J}_{3D}(x,y,z) = \sum_{\alpha=1}^{N_s}\sum_{s=1}^{\infty} v^\alpha\left(r_s^\alpha\right)\ , \tag{6.18}$$

where v^α is the interaction potential of the atomic projectile with α surface-atom, N_s is the total number of types of atoms present in the surface, and r_s^α is the distance from the point (x, y, z) to the nearest s-th neighbor α surface-atom. $v^\alpha(r)$ functions can be obtained from direct interpolation of Wyckoff site samplings in z, i.e., from the sets of energies $\{\epsilon_{w,z}\}_z$, on the (x_w, y_w) positions that coincides with the top position of α-type surface atom. The sum over s neighboring surface atoms can be truncated up to some critical order s_{max} that satisfies: $v^\alpha\left(r_s^\alpha\right) \approx 0$ when $s > s_{max}$.

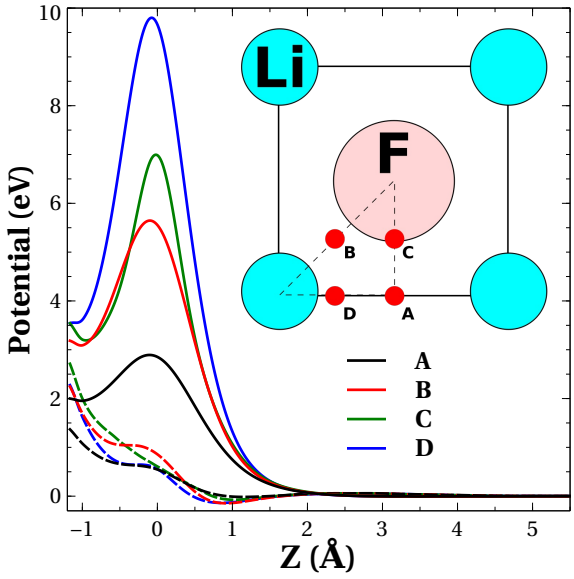

Figure 6.4: Some z-cuts over Wyckoff sites in the specific case of H/LiF(001) PES. Full lines stand for evaluations of the PES, V_{3D}, keeping constant x and y according to the surface scheme, and varying z. Dashed lines stand for $\mathcal{I}_{3D}$ evaluations for the same sites and z-range.

In this work we propose a variation of the conventional corrugation subtracting function definition ($\mathcal{J}_{3D}$), which can be written as follows:

$$\mathcal{J}_{3D}(x,y,z) = L_{z_0,\delta z}(z) \cdot \sum_{\alpha=1}^{N_s} \sum_{s=1}^{\infty} v^{\alpha}(r_s^{\alpha}) \tag{6.19}$$

$$L_{z_0,\delta z}(z) = \left[1 + \exp\left(\frac{z - z_0}{\delta z}\right)\right]^{-1} . \tag{6.20}$$

This definition slightly modifies Eq. 6.18. We have only added a multiplying factor $L_{z_0,\delta z}(z)$, which is a logistic switch function that controls the amount of CRP correction to $\mathcal{I}_{3D}$ as a function of z. The idea of introducing the $L_{z_0,\delta z}$ factor comes from the fact that at long distances from the surface ($z \longrightarrow \infty$), V_{3D} is already smooth enough to be interpolated directly without the subtraction of the $\sum_{\alpha=1}^{N_s} \sum_{s=1}^{\infty} v^{\alpha}(r_s^{\alpha})$ repulsive term. In fact, at long distances subtracting the repulsive term introduces numerical noise to $\mathcal{I}^{3D}$. An example for the specific case of the H/LiF(001) PES is shown in Fig. 6.5. This numerical noise amplitude will depend on the accuracy of the single energy point calculations $\mathcal{E}$. In order to further clarify the need of the logistic factor introduction, we can consider two limiting cases, when the projectile is far from the surface and when it is close to it:

1. Far from the surface:
   $\lim_{z\to\infty} \mathcal{I}_{3D}(x,y,z) = V_{3D}(x,y,z)$
   $\mathcal{I}_{3D}$ is a pure interpolation of V_{3D}, because $\lim_{z\to\infty} L_{z_0,\delta z} = 0$.

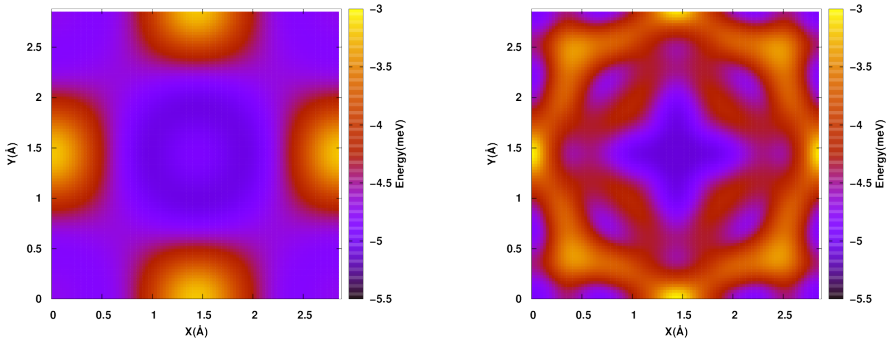

Figure 6.5: xy-cuts of H/LiF(001) V_{3D} potential including the action of a logistic function $L_{z_0,\delta z}$ with parameters $z_0 = 5$ a.u. and $\delta z = 0.2$ a.u. (left panel) and without it (right panel). Both cuts were done at $Z = 4.23$ Å. Complex shapes in right panel come from the Fourier interpolation of a more noisy smooth potential $\mathcal{I}_{3D}$.

2. Close to the surface:
   $\lim_{z\to-\infty} \mathcal{I}_{3D}(x,y,z) = V_{3D}(x,y,z) - \sum_{\forall\alpha s=1}^{\infty} v^{\alpha}(r_s^{\alpha})$
   $\mathcal{I}_{3D}$ is a pure CRP interpolation of V_{3D} as presented in Ref. [15], because $\lim_{z\to-\infty} L_{z_0,\delta z} = 1$

For any other case, the choice of parameters δz and z_0 will control the "amount of CRP" applied to the interpolation. A good general picture of the behavior of $L_{z_0,\delta z}$ is depicted in Fig. 6.6.

Resume of the CRP implementation for mono-atomic systems

Here, we summarize the steps needed to evaluate the potential V_{3D} within the CRP method. At the beginning of each entry, we have added between brackets the frequency of the step, assuming that the energy evaluation algorithm is integrated inside some program that performs dynamics simulations. This makes easier to follow the computational cost of one dynamics simulation using a CRP-PES. We assume that the set of single point calculations $\mathcal{E}$ has been already performed in a previous step:

1. [OpD*]. Perform direct interpolations $\{g_w(z)\}_w$ on the set of energy points $\{\epsilon_{w,z}\}_w$ that belong to Wyckoff sites that correspond to top sites for the surface, i.e., to positions of the basis set surface atoms. Use these special interpolations to define the repulsive functions: $v^{\alpha} = g_{w_\alpha}$. Define $\mathcal{J}_{3D}(x,y,z)$.

2. [OpD]. Create the set of smooth energies $\tilde{\mathcal{E}} = \{\tilde{\epsilon}_{w,z}\}_{w,z}$, where $\tilde{\epsilon}_{w,z} = \epsilon_{w,z} - \mathcal{J}_{3D}(x_w, y_w, z)$.

*Once per Dynamics

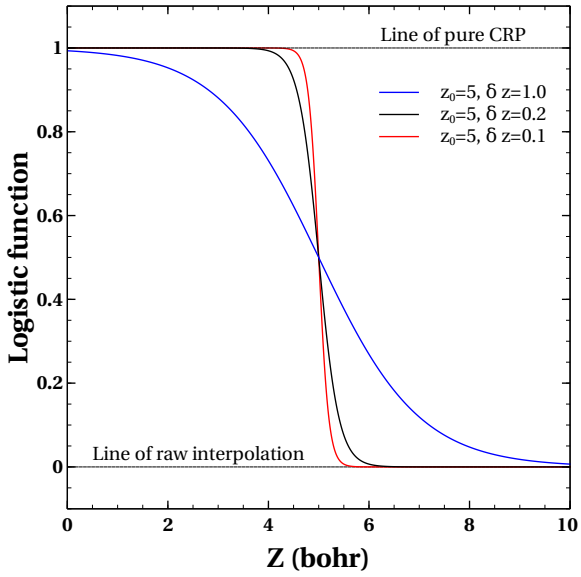

Figure 6.6: Examples of logistic function values for different z_0 and δz. The z_0 parameter controls where the $L_{z_0,\delta z}$ function is centered and δz how fast it stabilizes on its right side to 0 (no CRP contribution) and on its left side to 1 (full CRP contribution).

3. [OpD]. Perform interpolations $\{g_w(z)\}_w$ on the set of energy points $\{\tilde{\epsilon}_{w,z}\}_w$ for all Wyckoff sites.

4. [OpEE*]. Obtain the Fourier coefficients $\underline{C}(z)$.

5. [OpEE]. Evaluate $\mathcal{I}_{3D}(x,y,z)$ (see Fig. 6.7) and $V_{3D}(x,y,z)$.

CRP Implementation for di-atomic projectiles

How to compute $\mathcal{I}_{6D}$

In this case **R** represents the translational (x, y, z) and the internal (r, θ, ϕ) DOFs of the molecule (see Fig. 6.1). The 2D surface symmetry not only affects x and y, but it affects as well the angle ϕ. Thus, $\mathcal{I}_{6D}$ can be expanded in the product basis of 2D-SAFTs $\left(\left\{f_{\mathbf{k}}^{\Gamma,\odot}(x,y)\right\}_{\mathbf{k}}\right)$ for (x,y) and 1D-SAFTs $\left(\left\{f_l^{\Gamma',\odot'}(\phi)\right\}_l\right)$ for ϕ (see App. B.2 for detailed definitions). The existence of internal DOFs makes the totally symmetric representation used in the $\mathcal{I}_{3D}$ case insufficient. Therefore we have to expand $\mathcal{I}_{6D}$ over different irreps (Γ). The final expression of $\mathcal{I}_{6D}$ can be written as:

*Once per Energy Evaluation

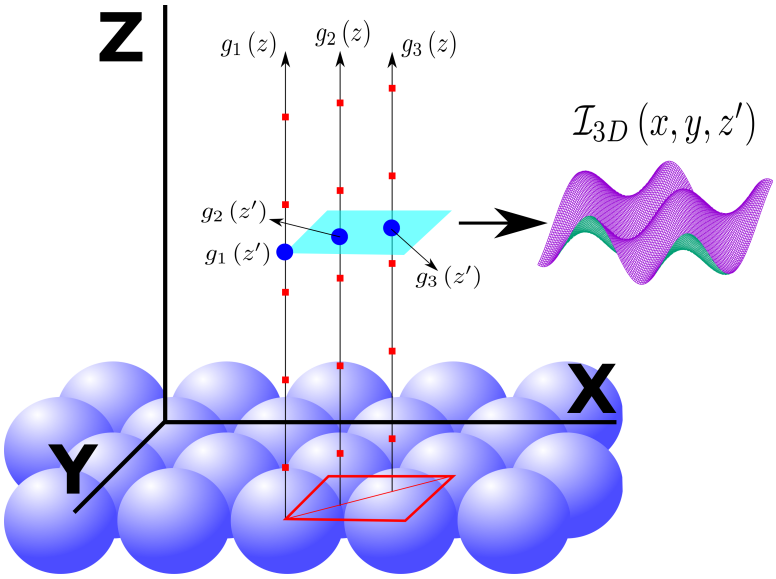

Figure 6.7: Schematic view of the domain of $g_w(z)$ interpolation functions for three Wyckoff sites. The smooth function $\mathcal{I}_{3D}$ is constructed as a symmetry adapted Fourier interpolation along (x,y) plane for fixed value z'.

$$\mathcal{I}_{6D}(x,y,z,r,\theta,\phi) = \sum_{\mathbf{k},l} \sum_{\odot,\odot'} \sum_{\Gamma,\Gamma'} c_{\mathbf{k},l}^{\Gamma,\odot;\Gamma',\odot'}(z,r,\theta)\, \zeta_{\mathbf{k},l}^{\Gamma,\odot;\Gamma',\odot'}(x,y,\phi) \tag{6.21}$$

$$\zeta_{\mathbf{k},l}^{\Gamma,\odot;\Gamma',\odot'}(x,y,\phi) = f_{\mathbf{k}}^{\Gamma,\odot}(x,y)\cdot f_{l}^{\Gamma',\odot'}(\phi)\ , \tag{6.22}$$

where Fourier coefficients $c_{\mathbf{k},l}^{\Gamma,\odot;\Gamma',\odot'}$ are functions of z, r and θ, and $\zeta_{\mathbf{k},l}^{\Gamma,\odot;\Gamma',\odot'}$ are basis functions of the tensor product space spanned by $f_{\mathbf{k}}^{\Gamma,\odot}(x,y)$ and $f_{l}^{\Gamma',\odot'}(\phi)$ SAFTs.

In order to calculate coefficients $c_{\mathbf{k},l}^{\Gamma,\odot;\Gamma',\odot'}$, we have to group single point calculations in a similar way to the atomic CRP. Because the presence of r, θ and ϕ complicates the procedure, it is better to explain it following a series of steps:

1. Choose N Wyckoff sites, and for each one of them, define the set of angles $\Theta_w = \{\theta_w\}_\theta$ and $\Phi_w = \{\phi_w\}_\phi$ to include in the calculations. The total number of fixed θ and ϕ values to include in one Wyckoff site "w" will be equal to the number of all combinations of angles $\{(\theta_w,\phi_w)\}$, where $\theta_w \in \Theta_w$ and $\phi_w \in \Theta_w$, i.e. all elements of the product $\Theta_w \times \Phi_w$. Notice that for $\theta_w = 0$, the angle ϕ is not defined because the molecule is in a "cartwheel" conformation. Therefore, with only one calculation $(0,\phi_w)$ we obtain all possible results $(0,\phi)$ for any value of $\phi \in [0,2\pi)$. We can regard the elements of $\Theta_w \times \Phi_w$ as the points of a 2D-grid mesh in θ and ϕ.

2. For each Wyckoff site, define a 2D-grid mesh for z and r, i.e. the set $R_w \times Z_w$

3. For each Wyckoff site, perform single point calculations $\epsilon_{w,z,r,\theta,\phi}$, where $(\theta,\phi) \in \Theta_w \times \Phi_w$. This means, keeping frozen $x = x_w$, $y = y_w$, $\theta = \theta_w$ and $\phi = \phi_w$, varying z and r according to the previously defined 2D-grid $R_w \times Z_w$. Later, we subtract to each value $\epsilon_{w,z,r,\theta,\phi}$ the function $\mathcal{J}_{6D}\left(x_w, y_w, z, r, \theta, \phi\right)$ to create the set $\tilde{\mathcal{E}}$.

With this nomenclature, the set $\tilde{\mathcal{E}}$ can be partitioned as follows:

$$\tilde{\mathcal{E}} = \bigcup_{w=1}^{N} \bigcup_{(\theta,\phi)\in\Theta_w\times\Phi_w}^{N} \left\{\tilde{\epsilon}_{w,r,z,\theta,\phi}\right\}_{(z,r)\in R_w\times Z_w} . \tag{6.23}$$

At this point, we can introduce the set of 2D interpolation functions $\left\{g_{w,\theta,\phi}\left(z,r\right)\right\}_{w,\theta,\phi}$ that interpolates each set of data $\left\{\tilde{\epsilon}_{w,z,r,\theta,\phi}\right\}_{z,r}$. We have used the most common implementation of such functions, i.e., each one of them is a piecewise function made of bi-cubic splines. Functions $g_{w,\theta,\phi}\left(z,r\right)$ can be written as:

$$g_{w,\theta,\phi}\left(z,r\right) = \sum_{k=1}^{3}\sum_{l=1}^{3} \Lambda_{ijkl}\left(r - r_i\right)^k \left(z - z_j\right)^l , \tag{6.24}$$

where z_j and r_i are configurations in the $Z_w \times R_w$ grid, $z_j < z < z_{j+1}$, and $r_i < r < r_{i+1}$. The set of all coefficients Λ_{ijkl}, for $i = 1, 2, ..., \#R_w - 1$ and $j = 1, 2, ..., \#Z_w - 1$, can be obtained by enforcing the condition $g_{w,\theta,\phi}\left(z,r\right) = \tilde{\epsilon}_{w,z,r,\theta,\phi}$ for all (r,z) in the grid $R_w \times Z_w$, and by requiring that each interpolation function is continuous and can be derived respect to r, z, and both at the same time. The last requirements compel us to compute the values of all those derivatives at grid points using finite differences.

Once we have the set of $\left\{g_{w,\theta,\phi}\left(z,r\right)\right\}_{w,\theta,\phi}$ functions, we have to construct a new set $\left\{g_{w,\phi}\left(z,r,\theta\right)\right\}_{w,\phi}$ of interpolation functions over the Θ_w 1D-grids. As θ is an angle, each $g_{w,\phi}$ function can be expanded as a linear combination of symmetry adapted Fourier terms (LC-SAFT). Depending on whether the diatomic molecule is homo-nuclear or hetero-nuclear, this expansion will be a totally symmetric representation (A) of C_{2v} or C_1 symmetry respectively. Thus, we can write each function $g_{w,\phi}\left(z,r,\theta\right)$ as:

$$g_{w,\phi}\left(z,r,\theta\right) = \sum_{l}\sum_{\forall\odot} c_l^{A,\odot}\left(z,r\right) \cdot f_l^{A,\odot}\left(\theta\right) , \tag{6.25}$$

where the number of elements in the summation must be $\#\Theta_w$. The choice of these elements , i.e. choosing pairs $(l,\odot)$ of indexes to include in the expansion, should follow the same rules we proposed in previous section to choose Fourier terms of $\mathcal{I}_{3D}$. All coefficients

$c_l^{A,\odot}(z,r)$ can be calculated if we impose $g_{w,\phi}(z,r,\theta) = g_{w,\theta,\phi}(z,r)$ for all $\theta \in \Theta_w$.

Following the same procedure, we have to create a new set of interpolation functions $\{g_w(z,r,\theta,\phi)\}_w$. As ϕ is an angular variable, each function $g_w(z,r,\theta,\phi)$ can be written as a LC-SAFT of the point group symmetry associated with the Wyckoff site, w, within the totally symmetric irrep. Thus, $g_w(z,r,\theta,\phi)$ functions take the form:

$$g_w(z,r,\theta,\phi) = \sum_l \sum_{\forall\odot} c_l^{A,\odot}(z,r,\theta) \cdot f_l^{A,\odot}(\phi) \ , \tag{6.26}$$

where the number of elements in the summation must be $\#\Phi_w$. All coefficients, $c_l^{A,\odot}(z,r,\theta)$ can be obtained if we enforce $g_w(z,r,\theta,\phi) = g_{w,\phi}(z,r,\theta)$ for all $\phi \in \Phi_w$.

Finally, as we have one function $g_w(z,r,\theta,\phi)$ per Wyckoff site, we can now perform a 2D-Fourier interpolation over x and y to obtain $\mathcal{I}_{6D}(x,y)$. The working equation to get Fourier coefficients is:

$$\sum_{\mathbf{k},l} \sum_{\odot,\odot'} \sum_{\Gamma,\Gamma'} c_{\mathbf{k},l}^{\Gamma,\odot;\Gamma',\odot'}(z,r,\theta)\, \zeta_{\mathbf{k},l}^{\Gamma,\odot;\Gamma',\odot'}(x_w,y_w,\phi) = g_w(z,r,\theta,\phi)\,, \tag{6.27}$$

for all ϕ in Φ_w, where Γ and Γ' are irreps of the point group symmetry associated with the wallpaper group of the surface. The total number of SAFTs that have to be included in the summation is $\sum_{w=1}^{N}(\#\Phi_w)$.

Defining a general and unique criterion to choose the indexes $(\Gamma, \mathbf{k}, \odot, \Gamma', l, \odot')$, given a number of terms $\sum_{w=1}^{N}(\#\Phi_w)$, is a much more difficult task than in the case of $\mathcal{I}_{3D}$. This means that some arbitrariness will be allowed. Nevertheless, we propose the following guidelines to generate an interpolation coherent with the set of single point calculations $\mathcal{E}$ performed:

1. Locate those functions $f_{\mathbf{k}}^{\Gamma,\odot}(x,y)$ that present maxima and/or minima at geometries that correspond to Wyckoff sites included in the calculations. Classify their indexes $(\Gamma, \mathbf{k}, \odot)$ depending on the kind of extrema they have on each Wyckoff site. Try to choose a combination that includes opposite behaviors (maximum vs minimum) at Wyckoff sites and their equivalent positions* by symmetry. This way, the linear combination will be more flexible. Always include the term which is constant over (x,y) plane†.

2. Each xy-term $(\Gamma, \mathbf{k}, \odot)$ should be multiplied by ϕ-terms $(\Gamma', l, \odot')$ whose associated SAFT have the symmetry of the Wyckoff site which $(\Gamma, \mathbf{k}, \odot)$ is describing with a maximum or a minimum.

*Wyckoff sites have an inherent multiplicity, which means they can have equivalent positions by symmetry inside the unit cell.

†Usually it has indexes: $(A, \mathbf{0}, \oplus)$

3. There should be a compromise between the number of $(\Gamma, \mathbf{k}, \odot; \Gamma', l, \odot')$ terms included in the expansion, which must be equal to $\sum_{w=1}^{N} (\#\Phi_w)$, and the accuracy of (x, y) plane and (ϕ) symmetry description.

We can obtain coefficients $c_{\mathbf{k},l}^{\Gamma,\odot;\Gamma',\odot'}$ solving a set of linear equation like the one in Eq. 6.13.

How to compute $\mathcal{J}_{6D}$

The commonest way to implement the corrugation subtracting function $\mathcal{J}_{6D}$ is given by:

$$\mathcal{J}_{6D}(x, y, z, r, \theta, \phi) = V_{1,3D}(x_1, y_1, z_1) + V_{2,3D}(x_2, y_2, z_2) \ , \tag{6.28}$$

where $V_{i,3D}$ is the atomic potential of the i-th atom of the molecule interacting alone with the surface, and (x_i, y_i, z_i) are the coordinates of these atoms subject to molecular geometry $(x, y, z, r, \theta, \phi)$. If the molecule is homo-nuclear, then $V_{1,3D}$ and $V_{2,3D}$ are the same function (see Sec. 9.2.1). $V_{i,3D}$ can be built within the CRP method as well. In this work, we have used an slightly modified version of $\mathcal{J}_{6D}$, in which each function $V_{i,3D}$ is multiplied by a logistic switch function, which allows to control the amount of repulsive interaction that is taken into account to calculate the smooth potential $\mathcal{I}_{6D}$. Its explicit form can be written as:

$$\mathcal{J}_{6D}(x, y, z, r, \theta, \phi) = V_{1,3D}(\mathbf{R}_1) L_{z_0,\delta z}(z_1) + V_{2,3D}(\mathbf{R}_2) L_{z_o,\delta z}(z_2) \tag{6.29}$$

$$L_{z_0,\delta z}(z_i) = \left[1 + \exp\left(\frac{z_i - z_0}{\delta z}\right)\right]^{-1} \ , \tag{6.30}$$

where $\mathbf{R}_i$ stands for (x_i, y_i, z_i) coordinates. The addition of this logistic terms to the repulsive parts V_{3D}, ensures a more stable interpolation when the distance to the surface becomes long enough $(z \longrightarrow \infty)$ so that a pure interpolation of DFT points introduces less numerical noise than a complete CRP interpolation (see Sec. 6.2.1). This numerical noise can produce spurious fluctuations of the potential, making the interpolated PES more wrinkled than the correct one. Some illustrative examples for the H_2/LiF(001) PES can be seen in Fig. 6.8, where several ϕ cuts on different (x, y) sites are plotted. Each colored line represents a ϕ cut of an interpolated PES obtained with different procedures: avoiding the use of CRP (dashed blue); using CRP with no logistic function (full green); and using CRP with the logistic function activated (full black). For all the chosen cases (A,B,C and D panels), activating $L_{z_0,\delta z}$ at $z_0 = 1.06$ Å with a width of $\delta z = 0.21$Å, yields to a fairly good agreement with DFT single point calculations (red dots). On the contrary, a standard CRP interpolation for most

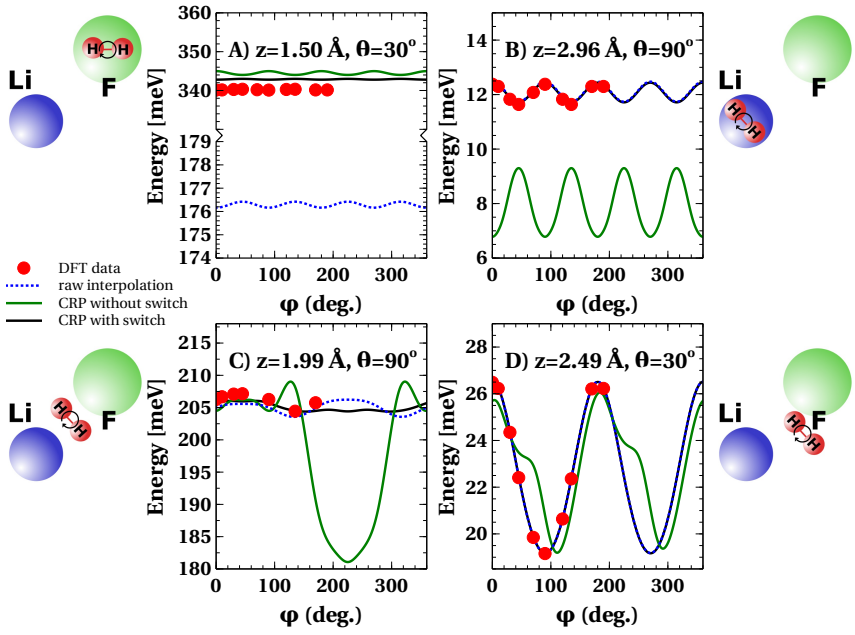

Figure 6.8: V_{6D} cuts along the ϕ DOF. In all panels, $r = 0.80$ Å. z and θ values are specified in each panel. Red dots stand for DFT single point calculations, blue dotted lines represent potential cuts from a raw DFT data interpolation, full green lines come from pure CRP interpolation (logistic function is switched off) and full black lines are CRP interpolations using a logistic function with parameters: $z_0 = 1.06$ Å and $\delta z = 0.21$ Å. (**A**): top F site. (**B**): top Li site. (**C**): F-Li bridge site. (**D**): random (x, y) position outside a high symmetry site, $x = 0.96$ Å and $y = 0.48$ Å .

of the cases (B,C, and D panels) yields to worse results than the raw interpolation with no smoothing procedure. The point at which the noise inherent to the CRP scheme starts to introduce meaningful deviations from the real potential depends on each particular system, and on the accuracy of the single point calculations. The typical form of a logistic function can be found in Sec. 6.2.1 (Fig. 6.6).

Resume of the CRP implementation for di-atomic molecule systems

Finally, we summarize the procedure to evaluate the potential for any molecular configuration. Between brackets we have added the frequency of the step, assuming that the energy evaluation algorithm is integrated inside some program that performs dynamics simulations. We assume as well that we already have a set of single point energy calculations $\mathcal{E}$ and the required 3D potentials $V_{i,3D}$:

1. [OpD*]. Build function $\mathcal{J}_{6D}(x, y, z)$.

*Once per Dynamics

2. [OpD]. Create the set of smooth energies $\tilde{\mathcal{E}} = \left\{\tilde{\epsilon}_{w,z,r,\theta,\phi}\right\}$, where $\tilde{\epsilon}_{w,z,r,\theta,\phi} = \epsilon_{w,z,r,\theta,\phi} - \mathcal{J}_{6D}\left(x_w, y_w, z, r, \theta, \phi\right)$ for all (r, z) in the grid $Z_w \times R_w$ and (θ, ϕ) in the grid $\Theta_w \times \Phi_w$.

3. [OpD]. Perform interpolations $\left\{g_{w,\theta,\phi}\left(z, r\right)\right\}_{w,\theta,\phi}$ over the set of energy points $\left\{\tilde{\epsilon}_{w,z,r,\theta,\phi}\right\}_{w,\theta,\phi}$ for all Wyckoff sites and (θ, ϕ) values in the grid $\Theta_w \times \Phi_w$.

4. [OpD]. Perform interpolations $\left\{g_{w,\phi}\left(z, r, \theta\right)\right\}_{w,\phi}$ over the set of points $\left\{g_{w,\theta,\phi}\left(z, r\right)\right\}_{w,\theta,\phi}$ for all Wyckoff sites and ϕ values in the set Φ_w.

5. [OpD]. Perform interpolations $\left\{g_w\left(z, r, \theta, \phi\right)\right\}_w$ over the set of points $\left\{g_{w,\phi}\left(z, r, \theta\right)\right\}_{w,\phi}$ for all Wyckoff sites.

6. [OpEE*]. Obtain the Fourier coefficients $\underline{C}\left(z, r, \theta\right)$.

7. [OpEE]. Evaluate $\mathcal{I}_{6D}\left(x, y, z, r, \theta, \phi\right)$ and $V_{6D}\left(x, y, z, r, \theta, \phi\right)$.

MODIFIED SHEPARD INTERPOLATION WITH WALLPAPER GROUP SYMMETRY

The modified Shepard interpolation was developed originally to build PESs for reactive molecular systems in gas phase [137–139]. Later, due to its successfulness and general formulation, it was applied to model the reactivity of molecule-surface systems including to some extent the effects of the surface periodicity [140–142]. In this work, we have used the algorithm implemented by Frankcombe *et al. [17]* that includes strictly the plane group symmetry and the translational periodicity of the surface.

Representation of the PES

The modified Shepard interpolation method describes the PES as a weighted sum of Taylor expansions that are centered at each point inside the grid of single point energy calculations $\mathcal{E} = \{\epsilon_{\mathbf{X}}\}_{\mathbf{X}}$, where $\mathbf{X}$ represent the Cartesian coordinates of the nuclei $\mathbf{X} = (X_1, X_2, ..., X_{3N})$ and N is the total number of nuclei in the projectile. We call N_{data} to the total number of data points in this set. Since it is well know that Cartesian coordinates are not an optimum choice to perform such an interpolation [143], a new set of coordinates $\mathbf{Z}$ is defined. They are known as the "set of redundant coordinates" $\mathbf{Z} = (Z_1, Z_2, ..., Z_{N_{red}})$ with $N_{red} > 3N$. The coordinates are chosen so that they: (i) are a faithful representation of the periodic plane group of the surface; (ii) are a faithful representation of the permutation group of the molecule;

*Once per Energy Evaluation

(iii) are invariant to lattice translations; (iv) span the $3N$ space described by Cartesian coordinates $\mathbf{X}$; (v) describe properly the projectile in the vacuum. The chosen set of coordinates $\mathbf{Z}$ used in this work are:

- the set of $N(N-1)/2$ inverse nuclear distances between atoms in the projectile.
- the inverse of the height of each nucleus of the projectile over the surface plane.
- a set of redundant sines and cosines functions.

Although, for interpolation purposes, the new set of coordinates Z is a better choice than a set of Cartesian coordinates, they are not an optimal choice for Taylor expansions centered at specific positions inside the PES. In fact, we need one optimal choice of coordinates per point in the set $\mathcal{E}$, because the surroundings of the PES around a geometry $\mathbf{X}$ (or $\mathbf{Z}$) can vary significantly from point to point. Thus, Taylor expansions may not be reliable if the same coordinates $\mathbf{Z}$ are used for all data points. In order to define local coordinates, we use the Wilson $\underline{\underline{B}}(i)$ matrix formalism for each data point "i" in $\mathcal{E}$:

$$B_{\alpha\beta}(i) = \frac{\partial Z_\alpha}{\partial X_\beta} , \tag{6.31}$$

where $\alpha = 1, 2, ..., N_{red}$ and $\beta = 1, 2, ..., 3N$. This matrix relates local infinitesimal variations of $\mathbf{Z}$ coordinates with local infinitesimal variations in $\mathbf{X}$ coordinates around data point i, which can be written as:

$$\underline{\delta Z}(i) = \underline{\underline{B}}(i) \cdot \underline{\delta X}(i) , \tag{6.32}$$

with

$$\underline{\delta Z}(i) = \begin{pmatrix} dZ_1 & dZ_2 & ... & dZ_{N_{red}} \end{pmatrix}^T \tag{6.33}$$

and

$$\underline{\delta X}(i) = \begin{pmatrix} dX_1 & dX_2 & ... & dX_{3N} \end{pmatrix}^T . \tag{6.34}$$

After a single value decomposition, $\underline{\underline{B}}$ can be written as follows:

$$\underline{\underline{B}}(i) = \underline{\underline{U}}(i) \cdot \underline{\underline{\Lambda}}(i) \cdot \underline{\underline{V}}^T(i) , \tag{6.35}$$

where $\underline{\underline{V}}(i)$ is a $3N \times 3N$ unitary matrix, $\underline{\underline{U}}(i)$ is a $N_{red} \times N_{red}$ unitary matrix, and $\underline{\underline{\Lambda}}(i)$ a $N_{red} \times 3N$ diagonal matrix. As there are only $3N$ independent coordinates, $\underline{\underline{\Lambda}}(i)$ contains the $3N$ positive singular values of $\underline{\underline{B}}$ inside its diagonal. Using $\underline{\underline{\Lambda}}(i)$ and $\underline{\underline{U}}(i)$ matrices, we can define $3N$ local orthogonal coordinates $\begin{pmatrix} \zeta_1 & \zeta_2 & ... & \zeta_{3N} \end{pmatrix}^T = \underline{\zeta}(i)$ in the vicinity of the i-th data point with the form:

$$\underline{\zeta}(i) = \left(\underline{\underline{\Lambda}}^{-1}(i) \cdot \underline{\underline{U}}^T(i) \right) \cdot \underline{Z} . \tag{6.36}$$

With this last formula, we can transform any conformation of the projectile represented in redundant coordinates $\mathbf{Z}$, to the optimal choice of coordinates for the i-th data point in $\mathcal{E}$. Now, performing a Taylor expansion centered at the i-th data point evaluated at $\underline{\zeta}(i)$ is safer than performing the interpolation directly in redundant coordinates.

The exact form of Taylor expansions in the vicinity of a data point "i" truncated at second order can be written as:

$$T_{(i)}(\mathbf{Z}) = \epsilon_i + \underline{\nabla\epsilon}^T(i) \cdot \underline{\Delta\zeta}(i) + \frac{1}{2}\underline{\Delta\zeta}^T(i) \cdot \underline{\underline{\nabla^2\epsilon}}(i) \cdot \underline{\Delta\zeta}(i) \tag{6.37}$$

$$\underline{\Delta\zeta}(i) = \underline{\underline{\Lambda}}^{-1}(i) \cdot \underline{\underline{U}}^T(i) \cdot [\underline{Z} - \underline{Z}(i)] \ , \tag{6.38}$$

where ϵ_i is the energy at data point i, $\underline{\nabla\epsilon}$ is the vector of first derivatives at data point i with respect to $\underline{\zeta}(i)$ coordinates, and $\underline{\underline{\nabla^2\epsilon}}$ is the Hessian matrix respect to $\underline{\zeta}(i)$ coordinates. The appearance of the gradient and Hessian matrices, in the expression of local Taylor expansions $T_{(i)}$, means that we need to evaluate the first and second derivatives of the potential for each data point in $\mathcal{E}$. Those values can be extracted either from the program that is performing the single point calculations or using finite differences (see Sec. 6.3.3 for more details).

The global definition of the PES has the form:

$$V(\mathbf{Z}) = \sum_{i=1}^{N_{data}} \sum_{g \in G_{CNP} \times G_{PG}} w_{(g \circ i)}(\mathbf{Z}) \cdot T_{(g \circ i)}(\mathbf{Z}) \ , \tag{6.39}$$

where w are weight functions, G_{CNP} is the complete nuclear permutation group for the atoms of the projectile, and G_{PG} is the wallpaper group symmetry of the surface. The index $g \circ i$ denotes that the quantity for data point i has been changed applying a symmetry operation $g \in G_{CNP} \times G_{PG}$. Since there is a sum over all transformations g in $G_{CNP} \times G_{PG}$, V is enforced to have the correct symmetry of the system.

The weight functions $w_{(g \circ i)}$control the contribution of each local Taylor expansion $T_{(g \circ i)}$ to the potential. Therefore, when $\mathbf{Z}$ is in the surroundings of a data point "i", the weight $w_{(i)}$ must take a predominant value in the expansion whereas weights $w_{(j \neq i)}$ far from $\mathbf{Z}$ should vanish. To keep this behavior, the weight functions must satisfy the following constrains:

$$w_{(g \circ i)}(\mathbf{Z}(g \circ i)) = 1 \tag{6.40}$$

$$\sum_{i=1}^{N_{data}} \sum_{g \in G_{CNP} \times G_{PG}} w_{(g \circ i)}(\mathbf{Z}) = 1 \ , \tag{6.41}$$

for all $\mathbf{Z}$, which can be achieved defining them in terms of primitive weights ν according to:

$$w_{(i)}(\mathbf{Z}) = \frac{\nu_{(i)}(\mathbf{Z})}{\sum_{j=1}^{N_{data}} \sum_{g \in G_{CNP} \times G_{PG}} \nu_{(g \circ j)}(\mathbf{Z})} \ . \tag{6.42}$$

Requiring that each primitive weight $\nu_{(i)}(\mathbf{Z})$ should satisfy:

$$\lim_{\mathbf{Z}-\mathbf{Z}(i)\to 0} \nu_{(i)}(\mathbf{Z}) = \infty \tag{6.43}$$

and

$$\lim_{\mathbf{Z}-\mathbf{Z}(i)\to \infty} \nu_{(i)}(\mathbf{Z}) = 0\,, \tag{6.44}$$

ensures that $w_{(i)}$ weights respect constrains 6.40 and 6.41.

When the set of data points $\mathcal{E}$ is small, we use "one part" weights ν:

$$\nu_{(i)}(\mathbf{Z}) = \|\mathbf{Z} - \mathbf{Z}(i)\|^{-2p}\,. \tag{6.45}$$

For gas phase problems it is proven [137] that the PES converges for p greater than the number of internal DOFs of the molecule. For gas-surface systems, such an affirmation is not proven, but it is expected that the PES converges for $p > 3N$ [17]. When the set of data points $\mathcal{E}$ is dense enough to define an elliptical confidence volume for the local Tailor expansions in the vicinity of each data point i, we use the so-called "two part" weight functions:

$$\nu_{(i)}(\mathbf{Z}) = \left[\eta_{(i)}(\mathbf{Z})^{2p} + \eta_{(i)}(\mathbf{Z})^{2q}\right]^{-1}\,, \tag{6.46}$$

where q is a small integer and $\eta_{(i)}(\mathbf{Z})$ is a local weighted distance in the redundant coordinate space,

$$\eta_{(i)}(\mathbf{Z})^2 = \sum_{j=1}^{N_{red}} \left(\frac{Z_j - Z_j(i)}{d_j(i)}\right)^2\,, \tag{6.47}$$

in which Z_j and $Z_j(i)$ are the j-th coordinate of $\underline{Z}$ and $\underline{Z}(i)$ arrays. Elements $d_j(i)$ form a vector $\mathbf{d}(i)$ that defines the confidence volume around each data point i. This vector is obtained by using Bayesian arguments (see Ref. [144] for more details). Within this approach, the decay of the primitive weight functions when $\mathbf{Z}$ is close to the confidence volume of a data point is reduced, because the term $\eta_{(i)}(\mathbf{Z})^{2q}$ prevails to $\eta_{(i)}(\mathbf{Z})^{2p}$ $(q \ll p)$. When $\mathbf{Z}$ is far from the confidence volume, the primitive weight is dominated by $\eta_{(i)}(\mathbf{Z})^{2p}$, and behaves like a "one part" weight. This makes the PES converge faster with the number of data points in $\mathcal{E}$, because the surroundings of each single point energy are better described.

The Grow *algorithm*

The modified Shepard interpolation method does not assume any predefined way of constructing the set of single point energy calculations, $\mathcal{E}$. Thus, simply adding extra data points to $\mathcal{E}$ would yield to a better representation of the interpolated PES. However, doing this addition without any strategy is not possible, because the configuration

space of the system, i.e. all possible values of nuclear coordinates $\mathbf{Z}$, is infinite. In oder to overcome this problem, the modified Shepard interpolation method is mostly used in conjunction to the so-called *Grow* algorithm. This algorithm is designed to, under some criteria (see below), choose which new points are worth including in the set of single point energies, $\mathcal{E}$, based on the information of a batch of classical trajectories performed on the interpolated PES. Repeating this procedure iteratively increases step by step the amount of data points in $\mathcal{E}$, and increases gradually the accuracy of the interpolated PES. This way of building a PES is often called "growing", which gives name to the algorithm. To make more clear the procedure, let us explain it step by step:

1. There is a initial set of data points $\mathcal{E}_1$ over which an interpolated PES $V_{\mathcal{E}_1}$ can be defined.

2. A small (~ 10) batch of classical trajectories is performed using $V_{\mathcal{E}_1}$ as the interaction potential.

3. Under some criteria (see below), the algorithm choses some points $\mathbf{X}_1$,$\mathbf{X}_2$,...,$\mathbf{X}_N$ sampled by the classical trajectories whose associated energies should be included as data points in $\mathcal{E}_1$.

4. Perform single point energy calculations for $\mathbf{X}_1$,$\mathbf{X}_2$,...,$\mathbf{X}_N$ conformations in order to obtain the set of energies: $\epsilon(\mathbf{X}_1)$,$\epsilon(\mathbf{X}_2)$,...,$\epsilon(\mathbf{X}_N)$.

5. Create a new set of data points $\mathcal{E}_2 = \mathcal{E}_1 \bigcup \{\epsilon(\mathbf{X}_1), \epsilon(\mathbf{X}_2), ..., \epsilon(\mathbf{X}_N)\}$.

6. Iterate the procedure using $\mathcal{E}_2$ as the initial set of data points. After several iterations, go to step 7.

7. Run a big batch of trajectories $\left(\sim 10^3\right)$ and evaluate some observables of particular interest for the study, e.g. reaction probabilities, diffraction probabilities, etc. If the value is converged, i.e. have not changed too much compared to the previous evaluation of the observable, the PES is considered to be converged and the "growing" procedure finishes. Otherwise, cycle from step 1.

The initial position and momentum of the classical trajectories are generated randomly under the typical constraints of a micro-canonical ensemble. These constrains are imposed by the user and should be chosen so that the trajectories sample the relevant dynamics regions of the PES, important for the calculation of observables of particular interest. In fact, the PES will be called "converged" when the successive estimations of the observables do not vary up to some threshold value when increasing the number of points in $\mathcal{E}$. This means that within the *Grow* procedure, a converged PES may not be good to measure observables that were not taken into account in the "growing" procedure. However, this PES can always be extended with the

inclusion of the new observable in the convergence criteria. If the convergence study is not performed for a given observable for some reason*, the PES can still be used, but under the assumption that the physical representative part of the configuration space related to the new observable is already well described. We should stress here that the convergence criteria not only depends on the chosen observables, but also on the conditions in which they are evaluated. For example, if we are interested in some reaction rate and we use classical trajectories within a certain energy range to grow the surface, we can only converge the PES for reaction rates measured within this energy range.

During the grow process, the set of all configurations $\mathbf{Z}(i)$ "visited" within a given batch of trajectories is stored. From this set of points, two main criteria are established to select which ones should be included in the next set of single point calculations. The first one states that we should include configurations that are frequently "visited" by the trajectories, provided that they are far enough to any other one to avoid redundancies. This criterion allows to include one point per trajectory defining a score function called h-weight:

$$h(i) = \frac{\sum_{m=1, m\neq k}^{N_{traj}} \nu_{(m)}[\mathbf{Z}(i)]}{\sum_{j=1}^{N_{traj}} \nu_{(j)}[\mathbf{Z}(i)]}, \tag{6.48}$$

where N_{traj} is the number of configurations sampled in one batch of trajectories and $\nu_{(j)}$ are calculated like primitive weights (one part or two part). The point chosen for each trajectory is the one that maximizes the value of $h(i)$. This function tend to zero when either $\mathbf{Z}(i)$ is too close or too far from a point already sampled. The second criterion states that we should add points to the PES at those configurations in which the interpolation is more inaccurate. In order to evaluate the inaccuracy of the interpolation at a given configuration $\mathbf{Z}(i)$, we use the following statistic:

$$\sigma^2(i) = \sum_{j=1}^{N_{traj}} w_{(j)}[\mathbf{Z}(i)] \cdot \left\{ T_{(j)}[\mathbf{Z}(i)] - V[\mathbf{Z}(i)] \right\}^2, \tag{6.49}$$

where $V[\mathbf{Z}(i)]$ is the interpolated value of the energy at $\mathbf{Z}(i)$, $T_{(j)}$ is a local second order Taylor expansion at configuration "j", and $w_{(j)}[\mathbf{Z}(i)]$ is a weight function similar to the ones used in Eq. 6.39. If a number of data points with significant weights disagree about the value of the PES at $\mathbf{Z}(i)$, then $\sigma^2(i)$ will be large. Therefore, the chosen geometries to "grow" the PES will be the ones that maximize this quantity.

*For example, the study is too complex, lack of resources, etc.

As a final remark, we must empathize that despite the fact that the *Grow* algorithm generates PESs that are based on classical trajectories sampling, they can be used to perform quantum dynamics studies. In this case, we should assume that the configuration space that was sampled by classical dynamics (which is well described by a converged PES) is also the one of physical importance to describe the quantum phenomenon of interest.

Interface with VASP program

In this work, we have developed an interface between the home-made *Grow* program, applied to gas-surface problems*, and the commercial code VASP. The *Grow* procedure only needs three inputs in each iteration from the "calculator"† program: (i) a set of energies evaluated at the geometry points of the configurational space of the system ($\mathcal{E}$); (ii) the sets of their first order derivatives ($\mathcal{E}'$); and (iii) the set of their second order derivatives ($\mathcal{E}''$). It is trivial to get the first set of information from single point calculations for any interfaced calculator. The second set can be easily obtained if the linked calculator evaluates the forces at each geometry. The problem comes with the third set. It requires to perform more than one calculation in the vicinity of the geometry $\mathbf{X}$ in order to evaluate the second derivatives by finite differences.

Taken into account that we are enforced to carry out more than one single point calculation, per point included in the PES, and that the VASP code evaluates energies using a smearing procedure in its integrals (see Sec. 5.6), we propose two schemes to get the information needed ($\mathcal{E}$, $\mathcal{E}'$ and $\mathcal{E}''$):

- **Full consistent sets $\mathcal{E}$, $\mathcal{E}'$ and $\mathcal{E}''$.** In this scheme, we get energy values, $\epsilon(\mathbf{X})$, from VASP energies, and first and second derivatives, $\frac{\partial\epsilon(\mathbf{X})}{\partial X_i}$ and $\frac{\partial^2\epsilon(\mathbf{X})}{\partial X_i \partial X_j}$, from the evaluation of VASP energies in a grid of single point calculations in the vicinity of $\mathbf{X}$, applying the finite differences method. By doing so, we approximate first and second derivatives of the energy to:

$$\frac{\partial\epsilon(\mathbf{X})}{\partial X_i} \approx \delta_{2h}[\epsilon](X_i) = \frac{\epsilon(X_i + h) - \epsilon(X_i - h)}{2h} \tag{6.50}$$

*Developed by T. Frankcombe *et al.*

†We will call "calculator" to the program that it is actually performing single point energy calculations for *Grow*

$$\frac{\partial^2 \epsilon\left(\mathbf{X}\right)}{\partial X_j \partial X_i} \approx \delta_{2h}\left[\delta_{2h}\left[\epsilon\right]\left(X_i\right)\right]\left(X_j\right) = \frac{\epsilon\left(X_i+h, X_j+h\right) - \epsilon\left(X_i+h, X_j-h\right)}{4h^2} - \frac{\epsilon\left(X_i-h, X_j+h\right) - \epsilon\left(X_i-h, X_j-h\right)}{4h^2}, \quad (6.51)$$

where $\delta_{2h}\left[\epsilon\right]\left(X_i\right)$ is the central finite difference operator acting on the i-th X coordinate of function ϵ, and h is the step size value. Expressions like $\epsilon\left(X_i + h\right)$ means that the geometry $\mathbf{X}$ is kept frozen except coordinate X_i, which is changed to $X_i + h$. We need $3N\left(3N+1\right)$ extra calculations apart from the central single point calculation at $\mathbf{X}$ to compute all first and second derivatives within this scheme. Notice that we do not use any information of the calculated VASP forces. We only use the values of energy evaluated in the grid. Therefore, if we assume that the calculator gives good enough energies to build the PES, the accuracy of first and second order derivatives depends only on parameter h.

- **Mixed inconsistent sets $\mathcal{E}$, $\mathcal{E}'$ and $\mathcal{E}''$.** In this scheme, we get energy values $\epsilon\left(\mathbf{X}\right)$ from VASP energies, first derivatives, $\frac{\partial \epsilon(\mathbf{X})}{\partial X_i}$, from VASP forces, and second derivatives, $\frac{\partial^2 \epsilon(\mathbf{X})}{\partial X_i \partial X_j}$, from the evaluation of VASP forces in a grid of points in the vicinity of $\mathbf{X}$ applying finite differences. Obtaining sets $\mathcal{E}$ and $\mathcal{E}'$ from VASP energies and forces, respectively carries an inherent inconsistency, because of the way in which the VASP code performs integrals over the Brillouin zone of the system. Energies evaluated with this program are obtained using a smearing method. This means that they are extrapolated from some calculated free-energy to zero thermal energy (see Sec. 5.6). However, forces are calculated using the Hellman-Feynman theorem,

$$\left\langle F_{X_i} \right\rangle = -\frac{\left\langle \Psi \left| \partial_{X_i} \hat{H}_{e^-} \right| \Psi \right\rangle}{\left\langle \Psi \left| \Psi \right. \right\rangle},$$

F_{X_i} being the force on coordinate X_i, $\hat{H}_{e^-}$ being the electronic Hamiltonian of the system, and Ψ its total wave function. Extracting gradients from these forces gives information of the gradients of the free-energy surface in which VASP is performing the calculations, but not of the real PES with zero thermal energy. This is why we call this scheme "inconsistent". Fortunately, if VASP parameters are optimized so that the free-energy surface is close to zero thermal energy surface, F_{X_i} forces should converge to the results that we would obtain within the consistent scheme. Second order derivatives are approximated to:

$$\frac{\partial^2 \epsilon\left(\mathbf{X}\right)}{\partial X_j \partial X_i} \approx \delta_{2h}\left[-\left\langle F_{X_i} \right\rangle\right]\left(X_j\right) = \frac{\left\langle F_{X_i} \right\rangle|_{X_j - h} - \left\langle F_{X_i} \right\rangle|_{X_j + h}}{2h}, \quad (6.52)$$

where $\langle F_{X_i} \rangle|_{X_j \pm h}$ stands for the value of the force in coordinate X_i at geometry $\left(X_1, ..., X_j \pm h, ..., X_{3N}\right)$. In this scheme we only need $6N$ extra calculations to form the set $\mathcal{E}''$, apart for the central single point calculation at $\mathbf{X}$. In this case the accuracy of first and second order derivatives not only depend on the step size h, but also on how reliable are the forces $\langle F_{X_i} \rangle$.

In both methods, the Hessian matrix is obtained via finite differences, $\underline{\underline{\nabla^2 \epsilon}}_{FD}$. That means that derivatives $\frac{\partial^2 \epsilon(\mathbf{X})}{\partial X_i \partial X_j}$ and $\frac{\partial^2 \epsilon(\mathbf{X})}{\partial X_j \partial X_i}$ may not lead to the same result, breaking the symmetry of this matrix. In order to solve this problem, we have enforced the Hessian matrix given to the *Grow* program, $\underline{\underline{\nabla^2 \epsilon}}_{Grow}$, to be symmetric: $\underline{\underline{\nabla^2 \epsilon}}_{Grow} = \frac{1}{2}\left(\underline{\underline{\nabla^2 \epsilon}}_{FD} + \underline{\underline{\nabla^2 \epsilon}}_{FD}^{T}\right)$.

7

DYNAMICS

In this chapter we present the type of dynamics simulation that we have performed for the study of H(D)/LiF(001), $H_2(D_2)$/LiF(001) and $H_2(D_2)$/Methyl-Si(111) gas-surface systems.

CLASSICAL DYNAMICS

Equations of motion

Classically, the dynamics of a molecule/surface system can be obtained by integration of either the Newton equations of motion:

$$m_i \ddot{\mathbf{R}}_i = -\nabla_{\mathbf{R}_i} V(\mathbf{R}) \,, \tag{7.1}$$

where $\mathbf{R}_i$ represents the Cartesian spatial coordinates of the i-th atom of the system, or the Hamilton equations of motion:

$$\dot{q}_k = \frac{\partial H}{\partial p_k}, \quad \dot{p} = -\frac{\partial H}{\partial q_k} \,, \tag{7.2}$$

where q_k and p_k are the generalized spatial coordinates and conjugate momenta of the system. Within the Born-Oppenheimer static surface (BOSS) approximation, the DOFs of the system are reduced to three (x, y, z), in the case of atomic projectiles; and six $(x, y, z, r, \theta, \phi)$, in the case molecular projectiles (see Fig. 6.1). Therefore, the classical Hamiltonian of these 3D and 6D systems can be written:

$$H_{3D} = \frac{p_x^2 + p_y^2 + p_z^2}{2M} + V_{3D}\,(x, y, z) \,, \tag{7.3}$$

and

$$H_{6D} = \frac{p_x^2 + p_y^2 + p_z^2}{2M} + \frac{p_r^2}{2\mu} + \frac{1}{2\mu r^2}\left(p_\theta^2 + \frac{p_\phi^2}{\sin^2\theta}\right) + V_{6D}(x, y, z, r, \theta, \phi) \,, \tag{7.4}$$

where V_{6D} and V_{3D} are the 3D and 6D potential energy surfaces, M is the total mass of each system, and μ is the reduced mass of the di-atomic molecule. In this work, we have integrated the Hamilton equations of motion using the Bulirsch–Stoer algorithm [145]. During the integration process, we have imposed that the energy of each trajectory cannot fluctuate more than 10^{-3} meV at each integration step, in order to conserve the total energy of the system.

One way to extract information from the sampling of a PES with classical trajectories, is to classify the final status of each trajectory according to the different typical final channels for a molecule/surface systems. To get good statistics, the size of the batch of trajectories integrated should be in the range of $\sim 10^4 - 10^5$ trajectories. The program used in this work to integrate Hamilton equations of motion can distinguish from the following final channels:

- **Scattering/reflection:** trajectory reaches the initial Z_0 value with its velocity vector pointing to the vacuum.
- **Dissociation (only molecules):** the inter-atomic distance is greater or equal to some critical value (2.22 Å for H_2) and its radial velocity is positive ($\dot{r} > 0$). Depending on the energy of each part of the molecule, it can have atoms adsorbed (dissociative adsorption).
- **Atom adsorption:** trajectories that, after the total integration time, are close to the surface ($z \leq 3$ Å) and have a negative potential energy.
- **Molecular adsorption:** trajectories that, after the total integration time, have their atoms close to the surface ($z <$3 Å) and a negative interaction energy with the surface.
- **Absorption/penetration:** trajectories that reach a z value lower than the minimum z value where the PES is known*. They may penetrate the surface plane.
- **Dynamical trapping:** trajectories that do not fulfill previous conditions before the total integration time has finished, and have changed the sign of p_z twice† at least.
- **Stopped/timed out:** trajectories that do not fulfill previous conditions before the total integration time has finished. Probably, they did not have enough time to reach their final status.
- **Pathological:** something unexpected happened during the integration of the trajectory. It is symptom of a bad choice of accuracy for the integrator or a poor PES description.

Only the first six channels have physical meaning. The last two ones exist for debugging/convergence purposes.

In this work we have studied scattering and diffraction phenomena, therefore, we are only interested in the fraction of trajectories that reach status "scattered".

*varies from -0.5 Å in the atomic case to 0.05 Å in the diatomic case

†Each time p_z changes its sign, we call it a "z-bounce"

Initial conditions

Initial conditions for our classical trajectories are compatible with a micro-canonical ensemble. In the case of an atomic projectile, we have to generate conditions that respect simply some translational energy, T, and an incidence direction in space. The case of diatomic molecules, its more complicated. They do not only have to satisfy some translation requirements, but they must have as well a specific internal energy, E_{int}. This internal energy arises from the internal quantum state of the molecule, but this is not described at all by classical dynamics. Therefore, we enforce our trajectories to have the most similar state that under classical dynamics can represent a given quantum state and its given internal energy.

A. **Atomic projectile.** An atomic projectile only has translational motion. Thus, let us consider that Ω_T is its phase space with elements of the form $\omega_T = (x, y, z, p_x, p_y, p_z)$. We can only include in calculations states ω_T with an associated energy T, and a given incidence condition described by two angles α and β, α being the incidence angle measured respect to the surface plane and β respect to the OX axis. Thus, the momentum of such states are written as:

$$p_x = \sqrt{2MT}\cos\alpha\cos\beta \tag{7.5}$$

$$p_y = \sqrt{2MT}\cos\alpha\sin\beta \tag{7.6}$$

$$p_z = -\sqrt{2MT}\sin\alpha\ . \tag{7.7}$$

p_z momentum is negative because the trajectories are moving upon the surface. The coordinate z represents the distance of the projectile to the surface, and its starting value is long enough to assure that projectiles are starting from the vacuum, where there is not interaction between the projectile and the surface. At this distance, (x, y) coordinates can be sampled randomly over the unit cell of the system.

B. **Diatomic molecule projectile.** The phase space of a diatomic molecule can be regarded as the multiplication of a translational phase space Ω_T, with similar properties to the atomic projectile case, and an internal phase space Ω_{int}. Elements of the later space have the form: $\omega_{int} = (r, \theta, \phi, p_r, p_\theta, p_\phi)$ and should form a micro-canonical ensemble of energy E_{int}. The time evolution of radial variables $\omega_r = (r, p_r)$ is separated from the angular part $\omega_\alpha = (\theta, \phi, p_\theta, p_\phi)$ if the angular momentum $L = p_\theta^2 + \frac{p_\phi^2}{\sin^2\theta}$ is fixed. In addition, the time evolution of angular variables only depend on the radial variables via r. Therefore, these two spaces can be sampled separately. First ω_r, for a fixed angular momentum L_0 and fixed internal energy E_{int}. Then ω_α, once

that r is fixed and L_0 is constant. For a detailed description of this procedure, see App. D. In order to select L_0, we choose exactly the same angular momentum associated with the quantum state that we want to represent, i.e. if we want an internal energy $E_{int}(v, J)$, then $L_0 = \sqrt{J(J+1)}$. This way of selecting internal states to simulate the zero point energy of quantum systems within a classical dynamics approach is often called quasi classical (QC) dynamics.

Quantification of final rotational and vibrational states

Variables used in classical dynamics are not quantified. Thus, in order to compare classical results with quantum calculations or state-resolved experiments we have to discretize these continuous variables.

In the case of the final angular momentum (J_f), we have used the expression:

$$L^2 = J(J+1) \implies J_f = \text{Int}\left\{\frac{-1+\sqrt{1+4L^2}}{2}\right\}, \tag{7.8}$$

where the operator Int$\{\}$ means that we just take the closest integer value to the real value inside the brackets. In the case of diatomic homo-nuclear molecules, the discretization procedure has to take into account that only J_f values satisfying: $J_f = J_i \pm 2n$ with $n \in \mathbb{Z}$ and $J_f \geq 0$ are physically possible.

In the case of vibrational motion, we have followed the action variable formalism [146]:

$$S_r = \int_C p_r dr \implies v = \text{Int}\left\{\frac{S_r}{\pi} - \frac{1}{2}\right\}, \tag{7.9}$$

where the action variable (S_r) is integrated through the contour (c) between the classic turning points of (r) in the asymptotic potential $V(r)$ for the isolated molecule.

Quantification of diffraction spectra: the classical binning method

Classical dynamics cannot describe quantum effects like the diffraction of molecular/atomic projectiles from surfaces. This phenomenon arises from the wave nature of the mater. Incoming projectiles with an associated de Broglie wave length*, λ, are reflected by the surface with different phases. The outcoming flux of projectiles will be measurable only at those final directions in with these corpuscular waves interact constructively. The final diffraction pattern will depend on the symmetry of the surface. However, a systematic binning

*Whose length should be of the order of the lattice parameter of the surface

of classical scattering data has proven to be a good tool to rapidly* estimate relative intensities of diffraction peaks and qualitative trends in diffraction experiments [23, 147]. Here, we proceed to explain how the systematic quantification of classical scattering data is performed.

If we reduce the complex diffraction problem to scattering from a periodic distribution of points in one dimension like the one shown in Fig. 7.1, we can write a simple expression for the Bragg law:

$$d \sin\theta' - d \sin\theta = n\lambda \, , \lambda \in \mathbb{Z} \, . \tag{7.10}$$

If we write now the previous equation as a function of the wave number associated to the projectile, $k = \frac{2\pi}{\lambda}$; and we call $k \sin\theta = k_{\parallel}$, we obtain:

$$k'_{\parallel} - k_{\parallel} = \frac{2\pi}{d} n \, . \tag{7.11}$$

The latter equation states that in this mono dimensional case, we obtain diffraction whenever the variation of the wave number parallel to the surface plane (in this case, a line) is exactly an integer number of times $\frac{2\pi}{d}$, which is exactly the space between points in the reciprocal lattice generated by the mono-dimensional chain of periodicity "d" (see Sec. 5.2). Moreover, the wave number and the momentum of a plane wave in the vacuum follows the relationship: $p = \hbar k$, which in atomic units leads to $p = k$. This means that the diffraction law can be understood in terms of quantified changes of momentum. Generalizing the idea to the case of a real surface we get the simple rule:

$$\Delta \mathbf{p}_{\parallel} \in \mathcal{B}^r \, , \tag{7.12}$$

which means that we have only diffraction when the change of momentum of the projectile parallel to the surface is exactly a reciprocal space vector, generated by the translational symmetry of the surface $\mathcal{B}$.

We can take advantage of equation 7.12 to discretize the final classical outcome of trajectories. Let us suppose that we have performed a batch of classical trajectories, and that we are analyzing the ones classified with the status "scattered". If those trajectories had an initial parallel momentum $\mathbf{p}_i^{\parallel}$ and a final parallel momentum $\mathbf{p}_f^{\parallel}$, we can assign to them a total change of momentum $\Delta \mathbf{p}_{\parallel} = \mathbf{p}_f^{\parallel} - \mathbf{p}_i^{\parallel}$. We can regard $\Delta \mathbf{p}_{\parallel}$ vectors as elements of the reciprocal space $\mathcal{G}$. If we now partition $\mathcal{G}$ in the Brillouin zones associated with all reciprocal lattice points $\mathcal{G}_B(\mathbf{k})$ so that $\mathcal{G} = \bigcup_{\forall \mathbf{k} \in \mathcal{B}^r} \mathcal{G}_B(\mathbf{k})$, we can map each classical trajectory with a reciprocal lattice point $\mathbf{k}$ as follows:

$$\Delta \mathbf{p}_{\parallel} \in \mathcal{G}_B(\mathbf{k}) \implies \Delta \mathbf{p}_{\parallel} \sim \mathbf{k} \, . \tag{7.13}$$

The previous equation allow us to define the classical diffraction probabilities for a given peak $\mathbf{k}$, $P(\mathbf{k})$, as the probability that a classical trajectory experiments a momentum change lying within the

*Compared to full-quantum calculations.

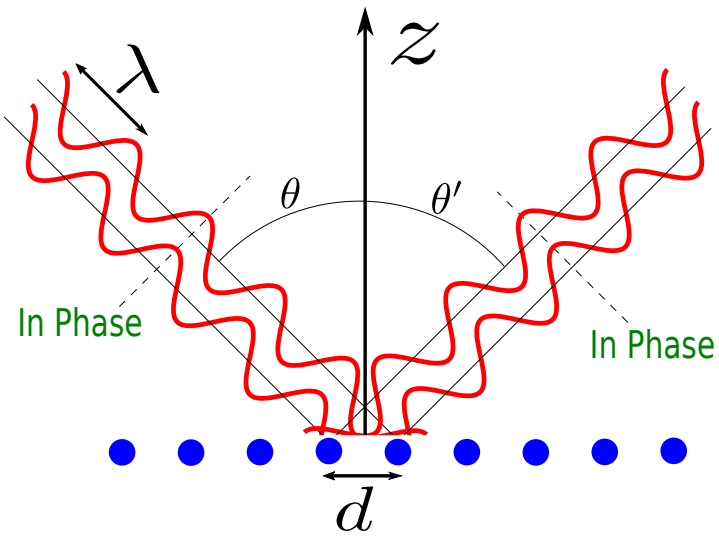

Figure 7.1: Schematic view of a test-book case of diffraction in one dimension. θ and θ' are the incidence angle of two incoming waves that are in phase. "d" the periodic symmetry of the surface in this simple case.

Brillouin zone associated with it. This probability can be estimated summing up all trajectories associated with peak $\mathbf{k}$, $N_{\mathbf{k}}$, and dividing it by the total number of trajectories, N_{tot}, i.e.:

$$P(\mathbf{k}) = \frac{N_{\mathbf{k}}}{N_{tot}} \,. \tag{7.14}$$

A pictorial representation of this algorithm is presented in Fig. 7.2 for the case of a square reciprocal Bravais lattice. The statistical error of a given probability $P(\mathbf{k})$ can be estimated as follows:

$$\sigma^2(\mathbf{k}) = \frac{P(\mathbf{k}) \cdot [1 - P(\mathbf{k})]}{N_{tot} - 1} \,. \tag{7.15}$$

With the last expression, we have calculated in table 7.1 the total number of scattered trajectories needed to evaluate a set of typical classical trajectory probabilities with a given relative error (10% and 1%). This table illustrates well the approximate order of magnitude of classical trajectories needed to have good statistics in probability analysis within the classical binning method.

QUANTUM DYNAMICS: MULTI-CONFIGURATIONAL TIME DEPENDENT HARTREE METHOD

Equations of motion

Within the BOSS approximation, the time evolution of our gas-surface systems follows the time-dependent Schrödinger equation shown in Eq. 4.14. The standard approach to solve this equation is the numerical exact propagation of the nuclear wave function of the system in a

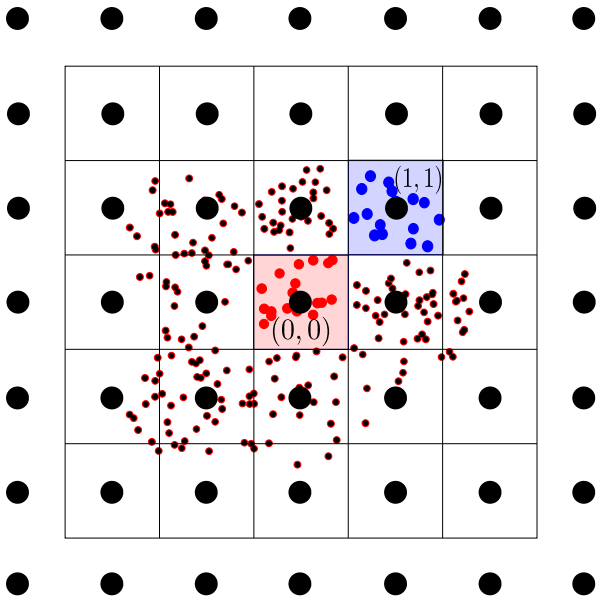

$$P\left(\mathbf{k}_{00}\right) = \frac{N_{00}}{N_{tot}} \qquad P\left(\mathbf{k}_{11}\right) = \frac{N_{11}}{N_{tot}}$$

Figure 7.2: Partition of the reciprocal space into Brillouin zones (squares in this example) centered on reciprocal lattice points (big black dots). Small black dots stand for the projection of $\Delta p_{\parallel}$ for each scattered trajectory after a classical dynamics calculation. In red and blue we have highlighted those trajectories that lay inside the Brillouin zones related to peaks $(0,0)$ and $(1,1)$, respectively. $P\left(\mathbf{k_{00}}\right)$ and $P\left(\mathbf{k_{11}}\right)$ are the classical diffraction probabilities for peaks $(0,0)$ and $(1,1)$. N_{00} and N_{11} are the number of trajectories inside the Brillouin zones centered at $(0,0)$ (red region) and $(1,1)$ (blue region). N_{tot} is the total number of trajectories.

Probability	$N_{tot}\,(\mathcal{E}_r = 10\%)$	$N_{tot}\,(\mathcal{E}_r = 1\%)$
0.1	$\sim 9 \times 10^2$	$\sim 9 \times 10^4$
0.01	$\sim 9.9 \times 10^3$	$\sim 9.9 \times 10^5$
0.001	$\sim 9.99 \times 10^4$	$\sim 9.99 \times 10^6$

Table 7.1: Number of trajectories needed to evaluate classical probabilities (first column) with a relative error of 10% (second column) and 1% (third column). The relative error is defined as $\mathcal{E}_r = \frac{\sigma(\mathbf{k})}{P(\mathbf{k})}$.

product basis set of time-independent functions. This ansatz can be written as:

$$\Phi(\mathbf{Q},t) = \sum_{j_1=1}^{N_1} \cdots \sum_{j_f=1}^{N_f} c_{j_1 \ldots j_f}(t) \prod_{\kappa=1}^{f} \chi_{j_\kappa}^{(\kappa)}(Q_\kappa) \ , \tag{7.16}$$

where f is the total number of DOFs, Q_κ is the κ-th DOF, $\mathbf{Q}$ is the array containing all DOFs Q_κ, $\chi_{j_\kappa}^{(\kappa)}$ are the time-independent basis functions for DOF κ, and $c_{j_1 \ldots j_f}$ denote the time-dependent coefficients of the expansion. If we introduce ansatz 7.16 to the nuclear time-dependent Schrödinger equation and apply the Dirac-Frenkel variational principle, we obtain the following expression:

$$i\dot{c}_J(t) = \sum_{JL} H_{JL} c_L(t) \ , \tag{7.17}$$

J and L being multi-indexes $J = j_1 \ldots j_f$ and $L = j'_1 \ldots j'_f$, and H the matrix representation of the Hamiltonian in the product basis $\chi_{j_\kappa}^{(\kappa)}$. From this equation, coefficients c_J can be obtained solving a coupled linear first-order ordinary differential equations. The effort of solving such a system grows exponentially with the number of degrees of freedom, and therefore, it is quite a challenge to apply it to more than five or six DOFs with the computational resources available at the moment.

In the MCTDH approach , the wave function is expanded in time-dependent Hartree product configurations:

$$\Phi(\mathbf{Q},t) = \sum_J A_J(t) \cdot \Xi_J(\mathbf{Q},t) \tag{7.18}$$

$$\Xi_J(\mathbf{Q},t) = \prod_{\kappa=1}^{f} \xi_{j_k}^{(k)}(Q_\kappa,t) \ , \tag{7.19}$$

where $\Xi_J(\mathbf{Q},t)$ are time-dependent Hartree product configurations, $\xi_{j_k}^{(k)}(Q_\kappa,t)$ is the time-dependent single particle function (SPF) for DOF κ, and A_J are time-dependent expansion coefficients. Introducing this ansatz to the nuclear time-dependent Schrödinger equation and applying the variational principle, yields to two separate equations [148]:

$$\left\langle \delta\Phi \left| i\hat{\partial}_t - \hat{H} \right| \Phi \right\rangle_A = 0 \tag{7.20}$$

$$\left\langle \delta\Phi \left| i\hat{\partial}_t - \hat{H} \right| \Phi \right\rangle_{SP} = 0 \ . \tag{7.21}$$

In the first equation, only coefficients A_J are varied whereas in the second one, variations are made in the single particle functions. To perform variations in single particle functions, they are represented in an explicit form. They are expanded in a time-independent basis set $\left\{\chi_l^{(\kappa)}(Q_\kappa)\right\}$:

$$\xi_{j_k}^{(k)}(Q_\kappa,t) = \sum_l B_{j_\kappa,l}^{(\kappa)}(t) \cdot \chi_l^{(\kappa)}(Q_\kappa) \ , \tag{7.22}$$

which is known as the "primitive" basis set of Q_κ coordinate. The variational equations only have a uniquely determined solution after applying the following constrains to the single particle functions:

$$\left\langle \xi_n^{(k)}(t) \middle| \xi_m^{(k)}(t) \right\rangle = \delta_{nm} \tag{7.23}$$

and

$$\left\langle \xi_n^{(\kappa)}(t) \middle| \dot{\xi}_m^{(\kappa)}(t) \right\rangle = -i\xi_n^{(\kappa)}(t) \left| g^{(\kappa)} \right| \dot{\xi}_m^{(\kappa)}(t) \,. \tag{7.24}$$

Eq. 7.23 is simply an orthonormality condition. Eq. 7.24 is a generic constraint that depends on $g^{(\kappa)}$, which is an arbitrary Hermitian operator. In the most simple implementation, $g^{(\kappa)} = 0$. Under these constrains, MCTDH working equations can be shown to read [21]:

$$iA_J = \sum_L \langle \Xi_J | \hat{H} | \Xi_L \rangle A_L \tag{7.25}$$

$$i\dot{\xi}_j^{(\kappa)} = \sum_{lm} \left(1 - P^{(\kappa)}\right) \left(\rho^{(\kappa)-1}\right)_{jl} \langle H \rangle_{lm}^{(\kappa)} \xi_m^{(\kappa)} \,, \tag{7.26}$$

where $P^{(\kappa)} = \sum_{j=1}^{n_\kappa} \left|\xi_j^{(\kappa)}\right\rangle \left\langle \xi_j^{(\kappa)}\right|$ is the projector to the space spanned by single particle functions of κ-th degree of freedom, $\langle H \rangle_{jl}^{(\kappa)} = \left\langle \Phi_j^{(\kappa)} \middle| \hat{H} \middle| \Phi_l^{(\kappa)} \right\rangle$ is a mean field built from "single-hole functions", $\Phi_j^{(\kappa)*}$, and $\rho_{jl}^{(\kappa)} = \left\langle \Phi_j^{(\kappa)} \middle| \Phi_l^{(\kappa)} \right\rangle$ is the density matrix of κ-th DOF. These equations resemble somehow to the structure of Eq. 7.16. However, they offer two major advantages: (i) the number of physical important SPFs is always smaller than the number of time-independent basis functions used in the standard approach; and (ii) each SPF can group more than one DOF of the system. In fact, within the MCTDH algorithm, Q_κ coordinates are called SPF modes due to this flexibility to describe more than one degree of freedom.

The full potential of the MCTDH method comes when the Hamiltonian of the system can be separated in sums of products of single particle operators:

$$\hat{H} = \sum_{r=1}^{s} c_r \prod_{\kappa=1}^{f} \hat{h}_r^{(\kappa)} \,, \tag{7.27}$$

with expansion coefficients c_r. Under such conditions, and when equations of motion are propagated with the efficient constant mean field integrator [149], the RAM memory usage and CPU effort scales as follows:

$$RAM \sim fmN + N^f \tag{7.28}$$

$$CPU \sim sfNm^2 + sf^2N^{f+1} \,, \tag{7.29}$$

*A single-hole function is defined as: $\Phi_j^{(\kappa)} = \left\langle \xi_j^{(\kappa)} | \Phi \right\rangle$

where m is the number of primitive functions per SPF, N is the number of SPFs functions per mode*, s is the number of Hamiltonian terms, and f is the number of modes. We can see that the great advantage comes from the fact that the exponential terms do not depend on the number of primitive functions or degrees of freedom, but on the number of SPFs (N) and modes (f), which are much less in number.

All quantum dynamics calculations performed in this work were made with the Heidelberg MCTDH Package [150].

Separable potential: the POTFIT algorithm

The Hamiltonian nuclear operators for an atomic (3D) and a di-atomic (6D) projectile interacting with a surface have the form:

$$\hat{H}_{3D} = \frac{-1}{2M}\hat{\nabla}^2_{x,y,z} + V_{3D}\left(x,y,z\right) \tag{7.30}$$

and

$$\hat{H}_{6D} = \frac{-1}{2M}\cdot\hat{\nabla}^2_{x,y,z} - \frac{1}{2\mu r}\cdot\hat{\partial}^2_r r + \frac{1}{2\mu r^2}\cdot\hat{J}^2 + V_{6D}\left(x,y,z,r,\theta,\phi\right)\ , \tag{7.31}$$

$\hat{\nabla}^2_{x,y,z}$ being the operator: $\partial^2_x + \partial^2_y + \partial^2_z$ and $\hat{J}^2$ the rotational momentum operator of a di-atomic molecule, $\frac{1}{\sin\theta}\hat{\partial}_\theta \sin\theta\hat{\partial}_\theta + \frac{1}{\sin^2\theta}\hat{\partial}^2_\theta$. All the terms in these Hamiltonians can be written in a suitable format (Eq. 7.27), for MCTDH equations of motion, except two: the potential functions V_{3D} and V_{6D}. In order to benefit from the computational advantages of MCTDH these potentials should be rewritten as a linear combination of products of one-dimensional functions. To do so, we have used the POTFIT algorithm [151, 152] provided with the Heidelberg MCTDH Package.

Within the POTFIT algorithm, any multi-dimensional potential can be written as:

$$V\left(Q^{(1)}_{i_1},...,Q^{(f)}_{i_f}\right) \approx V_{app} = \sum_{j_1=1}^{m_1}\cdots\sum_{j_f=1}^{m_f} c_{j_1\ldots j_f}\cdot\chi^{(1)}_{j_1}\left(Q^{(1)}_{i_1}\right)\cdots\chi^{(1)}_{j_1}\left(Q^{(f)}_{i_f}\right)\ , \tag{7.32}$$

where $\chi^{(\kappa)}_{j_\kappa}\left(Q^{(\kappa)}_{i_\kappa}\right)$ is the j_κ-th mono-dimensional function used to describe of coordinate "κ" . These functions are exactly the ones used to expand single SPFs in Eq. 7.22. The coefficients $c_{j_1\ldots j_f}$ can be obtained as a linear combination of the eigenvector components of the "potential density matrices" defined from a product grid representation† of

*These efficiency equations assume for simplicity reasons that we have a constant number of SPFs to describe each mode of the system, N, and that all SPFs are described by the same number of primitive functions, m.

†i.e., in the form of a discrete set of evaluations for a grid of geometries.

V. If we call $V_{i_1 \ldots i_f}$ the value of the potential at the $i_1 \ldots i_f$ point of the grid and we define the potential density matrices as follows:

$$\rho_{jl}^{(\kappa)} = \sum_{i_1=1}^{N_1} \cdots \sum_{i_{\kappa-1}=1}^{N_{\kappa-1}} \sum_{i_{\kappa+1}=1}^{N_{\kappa+1}} \cdots \sum_{i_f=1}^{N_f} V_{i_1 \ldots i_{\kappa-1} j i_{\kappa+1} \ldots i_f} V_{i_1 \ldots i_{\kappa-1} l i_{\kappa+1} \ldots i_f} \,, \quad (7.33)$$

then the explicit expression for coefficients $c_{j_1 \ldots j_f}$ is:

$$c_{j_1 \ldots j_f} = \sum_{i_1=1}^{N_1} \cdots \sum_{i_f=1}^{N_f} V_{i_1 \ldots i_f} \cdot v_{i_1 j_1}^{(1)} \ldots v_{i_f j_f}^{(f)} \,, \quad (7.34)$$

$v_{i_\kappa j_\kappa}^{(\kappa)}$ being the i_κ-th component of the j_κ-th eigenvector of the potential density matrix $\rho_{jl}^{(\kappa)}$. Note that the number of mono-dimensional functions $v_{j_\kappa}^{(\kappa)}\left(Q_{i_\kappa}^{(\kappa)}\right)$ for a given κ-DOF (m_κ) is not enforced to be the number of point used in the grid along that coordinate (N_κ). This means that for a grid representation $V_{i_1 \ldots i_f}$, we can construct multiple expansion like the one in Eq. 7.32. In order to choose the most suitable expansion with the least computational cost, the POTFIT code provides different parameters to evaluate the quality of the potential at grid points [153]. The error of V_{app} at grid points is only strictly zero when $m_\kappa = N_\kappa$ for all κ.

Representation of wave functions for gas-surface systems

The possibility of combining more than one DOF per SP-mode $Q^{(\kappa)}$, and the convenience of minimizing the total number of modes used in the MCTDH equations, opens the question of which is the most suitable way to represent the wave function of our system of interest within the MCTDH ansatz.

In the case of an atomic projectile, we can write the wave function as:

$$\Phi(\mathbf{Q}, t) = \sum_{h=1}^{N_x} \sum_{k=1}^{N_y} \sum_{l=1}^{N_z} c_{hkl}(t) \cdot \xi_h^{(x)}(x,t)\, \xi_k^{(y)}(y,t)\, \xi_l^{(z)}(z,t) \,. \quad (7.35)$$

The Hamiltonian H_{3D} can be perfectly separated in sums of mono-dimensional operators acting on x, y and z coordinates, so the memory and CPU power needed within this scheme scales according to Eqs. 7.28 and 7.29 as:

$$RAM \sim 3mN + N^3 \quad (7.36)$$

$$CPU \sim 12Nm^2 + 36N^4 \,, \quad (7.37)$$

which keeps the system manageable up to $m \approx 10^3$ and $N \approx 10$.

In the case of a di-atomic projectile, we have combined all the DOFs of the molecule inside 3 SP-modes as follows:

$$\Phi(\mathbf{Q},t) = \sum_{h=1}^{N_{xy}}\sum_{k=1}^{N_{zr}}\sum_{l=1}^{N_{\theta\phi}} c_{hkl}(t)\cdot \xi_h^{(xy)}(x,y;t)\,\xi_k^{(zr)}(z,r;t)\,\xi_l^{(\theta\phi)}(\theta,\phi;t)\ . \tag{7.38}$$

This scheme has been used previously to study the reactive and non reactive scattering of molecules from surfaces [154] with success. All those pairs of DOFs, which are the most correlated, are kept in the same SP-mode. Thus, the potential energy surface V_{6D} requires less primitive basis functions to converge, and therefore, the dynamics simulations are faster. The memory and CPU power consumption within this scheme is:

$$RAM \sim 3mN + N^3 \tag{7.39}$$

$$CPU \sim 18Nm^2 + 54N^4\ . \tag{7.40}$$

From this equations we can see that the memory usage scales like in the 3D case, due to the combination of all six DOFs in three single particle modes. However, the CPU time required in the 6D is of the order of 50% more than in the mono-atomic case for the same selection of N and m.

Another possible selection of the wave function for di-atomic-surface systems is to combine its 6 DOFs in 4 SP-modes as follows:

$$\Phi(\mathbf{Q},t) = \sum_{h=1}^{N_{xy}}\sum_{q=1}^{N_z}\sum_{k=1}^{N_r}\sum_{l=1}^{N_{\theta\phi}} c_{hqkl}(t)\cdot \xi_h^{(xy)}(x,y;t)\,\xi_q^{(z)}(z;t)\,\xi_k^{(r)}(r;t)\,\xi_l^{(\theta\phi)}(\theta,\phi;t)\ , \tag{7.41}$$

whose RAM memory and CPU power requirements scales as:

$$RAM \sim 4mN + N^4$$

$$CPU \sim 24Nm^2 + 96N^5\ .$$

In principle, this choice is worst than the one in Eq. 7.38, either from the computational time point of view, or from the memory storage. In fact, there are studies [154] that demonstrates that combining z and r in one single mode yields to faster convergence of the POTFIT algorithm to represent V_{6D} in a suitable form. Nevertheless, this scheme allow us to measure state-to-state scattering probabilities as a function of the final diffraction and rovibrational channel of the projectile. This cannot be done within the 3-mode representation of Φ, due to the implementation of the flux operators inside Heidelberg MCTDH Package.

The initial wave packet

In order to study the scattering properties of a gas-surface system, it is of crucial importance to define correctly the initial conditions of the wave packet to match specific incidence regimes.

In the case of a mono-atomic projectile, the initial wave function can be written as a product of plane waves and a Gaussian function as follows:

$$\Phi_{3D}\left(\mathbf{Q}; t=0\right) = N \cdot e^{ip_x x} e^{ip_y y} e^{-\left(\frac{z-z_0}{2\cdot\Delta z}\right)^2} e^{ip_z(z-z_0)} \ , \tag{7.42}$$

where p_x, p_y and p_z* are the initial momentum of the atom, z_0 denotes the place in the z axis in which the wave packet is centered, N is a normalization constant, and Δz is the width of the wave packet. p_x, p_y and p_z should satisfy Eqs. 7.5, 7.6 and 7.7.

In the case of a di-atomic projectile, the initial wave packet can be written as:

$$\Phi_{6D}\left(\mathbf{Q}; t=0\right) = \Phi_{3D}\left(x, y, z; t=0\right) \cdot \Phi_{v,J}\left(r\right) \cdot \Phi_J^{m_J}\left(\theta\right) \ , \tag{7.43}$$

where $\Phi_{v,J}$ and Φ_{J-m_J+1} functions satisfy:

$$\left\{-\frac{1}{2\mu r}\cdot\hat{\partial}_r^2 r + \frac{J\left(J+1\right)}{2\mu r^2} + V_{asymp}\left(r\right)\right\}\Phi_{v,J}\left(r\right) = E_{v,J}\Phi_{v,J}\left(r\right) \tag{7.44}$$

$$\Phi_J^{m_J}\left(\theta\right) = \sqrt{\frac{2J+1}{2}\cdot\frac{\left(J-m_J\right)!}{\left(J+m_J\right)!}}\cdot P_J^{m_J}\left(\cos\theta\right) \ , \tag{7.45}$$

Φ_{3D} being the same function as the one used to describe initial conditions for a mono-atomic projectile, $\Phi_{v,J}\left(r\right)$ are the eigenstates associated to the internal asymptotic Hamiltonian with quantum numbers (v, J), $P_J^{m_J}$ is a Legendre function associated with quantum rotational numbers (J, m_J), $V_{asymp}\left(r\right) = \lim_{z\to\infty} V_{6D}$, and $E_{v,J}$ represents the internal rovibrational energy of the di-atomic projectile.

Flux analysis of the wave function: state-to-state probabilities

The last step in solving a quantum mechanical molecular(atomic) dynamics problem is the determination of observable quantities from the time-dependent wave function. In our case, we are interested in computing state-to-state transition probabilities, i.e. the probability of a molecule to go from an initial state $\left|p_x, p_y, p_z, v_i, J_i, m_{Ji}\right\rangle = \left|A\right\rangle$ to a final state $\left|h_f, k_f, v_f, J_f, m_{Jf}\right\rangle = \left|\Omega\right\rangle$ after reaching the scattering exit channel†. Initial states $\left|A\right\rangle$ are constructed as previously detailed in Sec. 7.2.4. Final scattering states $\left|\Omega\right\rangle$can be written as:

$$\left|h_f, k_f, v_f, J_f, m_{Jf}\right\rangle = N \cdot \left|e^{ih_f\Delta b_x x} e^{ik_f\Delta b_y y}\Phi_{v_f,J_f}\left(r\right)\Phi_{J_f}^{m_{Jf}}\left(\theta\right)\right\rangle \ ,$$

where $\left(h_f, k_f\right)$ indexes stand for diffraction numbers, $\left(v_f, J_f, m_{Jf}\right)$ indexes specify the internal final rovibrational state of the projectile (if

*p_z is always negative, because the atom is moving upon the surface

†After colliding with the surface, the projectile is scattered back to the vacuum. In this region the projectile does not interact anymore with the surface and keeps its final state unalterable.

applicable), and Δb_x and Δb_y are the spacing between reciprocal lattice points along x and y directions.

In principle, the probability $|A\rangle \rightarrow |\Omega\rangle$ transitions at energy "E" can be calculated evaluating the elements of the so-called S-matrix:

$$|S_{\Omega,A}(E)|^2 = |\langle \Omega(E) | A(E) \rangle|^2 \ . \tag{7.46}$$

Within the MCTDH algorithm, this evaluations can be efficiently performed by augmenting the system Hamiltonian with a complex absorbing potential [155]. The augmented Hamiltonian $\left(\hat{H}_{aug}\right)$ is then written as:

$$\hat{H}_{aug} = \hat{H} - i\left(W_{scatt}(z) + W_{react}(r)\right) \ , \tag{7.47}$$

where iW_{scatt} and iW_{react} are two complex absorbing potentials (CAPs) that absorb the part of the wave function that enters the scattering and reactive channels, respectively*. They have the explicit form:

$$W_{scatt}(z) = \eta_{scatt} \cdot (z - z_{scatt})^{n_{scatt}} \cdot \Theta(z - z_{scatt}) \tag{7.48}$$

$$W_{react}(r) = \eta_{react} \cdot (r - r_{react})^{n_{react}} \cdot \Theta(r - r_{react}) \ , \tag{7.49}$$

η_i being the absorption strength of asymptotic channel "i", n_i the order of the CAP, and Θ a Heaviside step function. z_{scatt} and r_{react} are parameters that control the region at which W_{scatt} and W_{react} do not vanish. Parameters η_i and n_i should be chosen carefully so that the CAP absorbs efficiently the MCTDH wave function in the range of energies involved in the analysis. Depending on the gas-surface problem, the Hamiltonian can be augmented with more CAPs, for example, if there was a moderate probability for the projectile to penetrate the surface, it would be a good idea to define a CAP close to the surface in order to absorb the wave function that gets too close. The flux operator associated with a generic CAP "γ" $\left(\hat{F}_\gamma\right)$ is written as the commutator of the augmented Hamiltonian and the Heaviside step function associated with channel γ†:

$$\hat{F}_\gamma = i\left[\hat{H}_{aug}, \Theta(x - x_\gamma)\right] \tag{7.50}$$

and it is related to the S-matrix elements as follows:

$$\left\langle \alpha(E) \left| \hat{P}_\gamma^\Omega F_\gamma \hat{P}_\gamma^\Omega \right| \alpha(E) \right\rangle = \frac{1}{2\pi} |S_{\Omega,A}(E)|^2 \ , \tag{7.51}$$

where $\hat{P}_\gamma^\Omega$ is a projector onto state $|\Omega_\gamma\rangle$ within the asymptotic channel γ: $\hat{P}_\gamma^\Omega = |\Omega_\gamma\rangle\langle\Omega_\gamma|$. If γ represents the scattering channel, the projector has the simple form: $\hat{P}_{scatt}^\Omega = |\Omega\rangle\langle\Omega|$

*The scattering region comprehends all configuration space with $z > z_{scatt}$. The reactive region comprehends all the configuration space with $r > r_{react}$.

†We have already given two examples of asymptotic channels: the scattering and the reactive regions of the configuration space. There may be more for more complex studies.

The final expression to compute state-to-state probabilities within channel γ can be demonstrated to be [21]:

$$\left|S^{\gamma}_{|\Omega\rangle,|A\rangle}(E)\right|^2 = \frac{2}{\pi\left|\Delta(E)\right|^2} \cdot \mathrm{Re}\left[\int_0^{\infty} g^{\gamma}_{\Omega}(\tau)\, e^{iE\tau} d\tau\right] , \tag{7.52}$$

where $\Delta(E)$ is the energy distribution of the initial wave packet. $g^{\gamma}_{\Omega}(\tau)$ is defined as:

$$g^{\gamma}_{\Omega}(\tau) = \int_0^{\infty} \left\langle \Phi(t) \left| \hat{P}^{\Omega}_{\gamma} W_{\gamma} \hat{P}^{\Omega}_{\gamma} \right| \Phi(t+\tau) \right\rangle d\tau . \tag{7.53}$$

Part III

RESULTS

Here, we present the outcome of this thesis, in which we have developed three potential energy surfaces, namely, for H(D)/LiF(001), $H_2(D_2)$/LiF(001) and $H_2(D_2)$/Methyl-Si(111) gas-surface systems.

8

FIRST PRINCIPLES THEORETICAL STUDY OF H(D) DIFFRACTION FROM LIF(001): FROM SLOW NORMAL INCIDENCE TO FAST GRAZING INCIDENCE CONDITIONS

In this chapter, we present the H/LiF(001) CRP-PES and two dynamics studies based on it. The first one is a classical systematic study of the diffraction spectra for different initial conditions of H and D atoms under grazing incidence conditions. The second one is a quantum dynamics study of how hydrogen diffraction spectra varies from slow normal incidence to fast grazing incidence conditions. Contents are based on the following publications:

- A.S. Muzas, F. Martín, C. Díaz*; Nucl. Instr. Meth. B* **354** (2015) 9-15. *[156]*
- A.S. Muzas, F. Gatti, F. Martín, C. Díaz*; Nucl. Instr. Meth. B.* (to be published)

MOTIVATION

Since its theoretical prediction [23, 157], and especially, since the first independent experimental measurements few years later [101, 158], the diffraction of atoms and molecules from surfaces under FGI conditions has attracted much attention (see Ref. [107] and references therein), mainly due to its potential use as a surface analysis tool.

As already discussed in the literature [12, 23, 101, 147], the physical mechanism behind this phenomenon is the strong decoupling between the fast motion parallel to the surface, and the slow motion normal to it. Due to the grazing incidence conditions, the potential felt by the projectile is periodic (or quasi-periodic). If we apply the perturbation theory to the case of a classical particle moving on a periodic potential [159], it can be seen that the parallel momentum change along the incidence direction x is given by $\Delta K_x = -\frac{1}{v_x}\int_0^a dx \frac{\partial V(x,y)}{\partial x} = 0$, a being the parameter periodicity of the potential along the incidence direction, V the potential felt by the projectile, and v_x its velocity. In contrast, the parallel momentum change along the perpendicular direction, y, is given by $\Delta K_y = -\frac{1}{v_x}\int_0^a dx \frac{\partial V(x,y)}{\partial y} \neq 0$. Therefore, the change of the wave vector along the incidence direction is zero (or almost zero). Thus, any significant change of the parallel wave vector (**K**), induced in the projectile when approaching the surface, is due to a transfer of momentum from the slow motion, normal to the surface, to the motion parallel to the surface, and perpendicular to the incidence direction. At this point, it should be remembered that

diffraction occurs whenever the change of the parallel wave vector ($\mathbf{K}_f - \mathbf{K}_i$) coincides with a reciprocal lattice vector ($\mathbf{G}_{n,m}$), $\mathbf{K}_i$ and $\mathbf{K}_f$ being the initial and final parallel wave vector, respectively. And that the de Broglie wave length associated with the slow normal motion ($\lambda = 2\pi/k_\perp$) is of the order of magnitude of $\mathbf{G}_{n,m}$, which allows the observation of diffraction.

Diffraction under FGI conditions has been already observed for many different systems, including atomic (Ar, Ne, He and H) and molecular (H_2) projectiles, and a wide variety of surfaces [107]. First measurements were performed in 2007 on insulators, LiF(100) [101, 158] and NaCl(001) [101, 103]. At that time, it was unclear whether diffraction from metal surfaces could be measured, due to electronic excitations. But one year later, first diffraction measurements from a metal surface were published [113]. Since then, grazing incidence experiments have been performed in a wide diversity of systems: He, Ne, Ar, N/KCl(001) [104]; He/Ni(110) [114]; He, Ar/Al(111) [160]; He, H_2/Mo(112) [111]; He/Ag(110) [161]; He/monolayer of silica in Mo(112) [119]; He/c(2 × 2) reconstructed ZnSe(001) [108]; He, H_2/c(2 × 2)S- Fe(110) and He, H_2/c(1 × 3)O-Fe(110) [110]; He/c(2 × 4)O-Mo(112) [162]; H/ Al_2O_3 ($11\bar{2}0$) [163]; H, He/MgO(001) [164]. However, diffraction of H and, in particular, He atoms from LiF(100) is still the most studied system [2, 94, 102, 111, 163, 165]. Among theses experimental studies, it is worth mentioning the study of decoherence induced by electronic excitations carried out by Winter et al. [94, 163] for H and He/LiF(100). They have shown, on the one hand, that electronic excitations are far more important for H than for He atoms, in contrast to previous studies for slow projectiles scattered from metal surfaces [166]. And, on the other hand, they have shown that, even in the case of H atoms, the decoherece induced by the electronic excitations in the scattering process is not strong enough to prevent diffraction.

This fruitful experimental effort has encouraged theorists to perform detailed quantum theoretical studies aiming to analyze and understand GIFAD experiments. However, these theoretical simulations present a major challenge due to the huge incidence energy used in the experiment. For example, Ruiz et al. [167, 168] have studied the momentum and the energy transfer between the intramolecular DOFs in the quasiresonance region, using classical trajectory calculations and a diatom-rigid surface collision model. Classical trajectory calculations have also been used to study classical rainbow angles [104]. In this latter study, Hartree-Fock based pair potentials were employed. But, subsequent semiclassical studies, using DFT based potentials, have shown that superposition of interatomic pair potentials may not be adequate to describe atom/surface interactions under FGI conditions [111, 160]. Schüller et al. [164], using a semiclassical approach, have shown that potentials based on superposition of

individual Hartree-Fock pair potentials describe fairly well classical scattering phenomena, whereas DFT based potentials are needed to describe diffraction for normal incidence energies below 0.1 eV. Angular distributions and interference structures have been investigated by means of the surface eikonal approximation [4, 165], and very recently [161, 169] by using a three-dimensional (3D) PES, obtained by applying the CRP method to a set of DFT data points. Mason et al. [170] have developed a theory based on quantum-mechanical transition rates, aiming to study thermal effects. These thermal effects have also been studied using a quantum trajectory Monte Carlo method [2, 3].

In Sec. 8.3, we have analyzed to what extent classical dynamics can be used to analyze experimental measurements of scattering (and diffraction) of atoms from surface under FGI conditions. The reliability of our study is supported by previous studies, performed for molecular diffraction at thermal and quasi-thermal energies [23, 24, 171–174], showing that a classical binning method, proposed for the first time by Bowman et al. [171, 172], is able to reproduce qualitatively quantum theoretical and experimental diffraction peaks. The binning method should work better under FGI conditions, because the parallel momentum change (respect to the total momentum) leading to diffraction is smaller than in the case of thermal energies.

In Sec. 8.4, using as benchmark system H/LiF(001), we have investigated how to reduce the computational effort required to study GIFAD phenomena, keeping the full dimensionality of the system. When performing quantum dynamics calculations of atom(molecule)/surface systems using grid methods [22, 154, 175] the computational effort is fundamentally linked to the number of basis functions required to describe accurately each DOF: the higher the energy associated to a specific DOF the higher the number of basis functions needed to properly describe the motion along this DOF. In fact, we have estimated that GIFAD calculations at typical experimental conditions demand twice more RAM memory and ten times more CPU time than typical low energy diffraction calculations -within the MCTDH method framework (see Sec. 8.2). These requirements could imply prohibitive calculations, for example, when molecular projectiles are involved. In order to reduce this computational effort, we have to take into account that GIFAD diffraction is mainly governed by the projectile low normal incidence energy (E_n), and that one can usually disregard the projectile total (E_i) and parallel (E_p) energies. Thus, the same diffraction spectra should be observed for a range of E_p's and polar incidence angles, θ_i (see Fig. 8.1), while keeping E_n constant. Of course, higher θ_i's imply lower E_p's, and therefore, lower computational effort. Our working hypothesis is that we can perform GIFAD calculations to much lower incidence energy that in experiment, and still be directly comparable with experimental re-

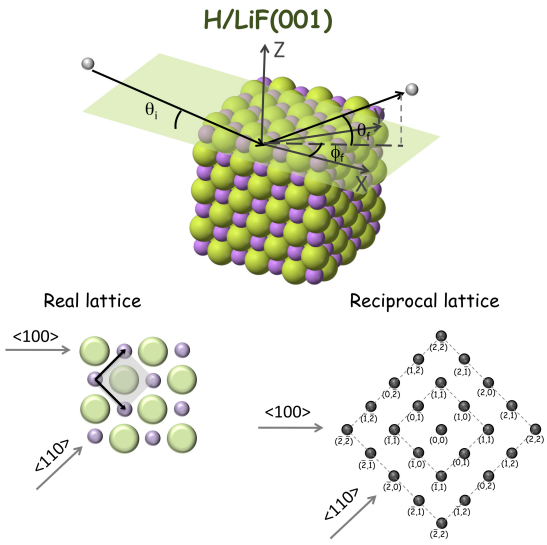

Figure 8.1: Top: schematic representation of the H/LiF(100) system and the Cartesian coordinates system. Bottom: real and reciprocal lattices. Dashed gray lines show diffraction orders as defined in this work. Number within bracket indicate the incidence direction considered in this work.

sults obtained at fast grazing incidence. In addition, with the aim of proposing a method to reduce the computation effort, while keeping the accuracy of the theoretical analysis, we have tested to what extend quantum calculations at slow normal incidence could be used to simulate GIFAD experiments and by extension GIFMD experiments.

THEORETICAL MODEL

The H/LiF(001) potential energy surface

Taking advantage of the different time scales of the nuclear and electronic motions, we describe the interaction between the atoms and the surface within the BOA. The validity of the BOA is supported by recent experiments [94] showing that, although there are electronic excitations inducing decoherence in the system, they neither suppress completely nor modify the diffraction patterns. In fact, in Ref. [94] it was shown that diffraction can be observed experimentally for total energies (E_T) up to 1 keV and incidence angles (θ_i) up to 1.7°. In Ref. [94], it was also shown that diffraction patterns could be recorded for higher E_T values (up to 1.5 keV) using smaller θ_i values.

The 3D PES, describing the electronic structure of the system, has been computed by applying a slightly modified version of the CRP method of Busnengo et al. [15] to a set of DFT-GGA data. As the general CRP scheme has been already discussed in section 6.2, here we

will only expose the details of the implementation for the H/LiF(001) system. The explicit form of the 3D PES (V_{3D}) is written as:

$$V_{3D}(\boldsymbol{r}) = \mathcal{I}_{3D}(\boldsymbol{r}) + \left[\sum_{\forall i} V_{1D}^{Li}\left(d_i^{Li}\right) + \sum_{\forall i} V_{1D}^{F}\left(d_i^{F}\right)\right] L_{z_0,\delta z}(z) \quad (8.1)$$

$$L_{z_0,\delta z}(z) = \left[1 + \exp\left(\frac{z - z_0}{\delta z}\right)\right]^{-1} \quad (8.2)$$

where $\boldsymbol{r}$ represents the Cartesian coordinates of the H atom over the surface, ${d_i}^{Li}$ and d_i^F are the distance of the i-th nearest Lithium or Fluorine atom to the H projectile, V_{1D}^{Li} and V_{1D}^{F} are the repulsive one-dimensional interactions between the H atom and the Li or F atoms respectively, $\mathcal{I}_{3D}$ is the interpolated smooth 3D potential and $L_{z_0,\delta z}$ is a logistic switch function.

The smooth $\mathcal{I}_{3D}$ function has been interpolated over Z using third-order cubic splines, and over (x, y) using a symmetry adapted Fourier expansion. The DFT-GGA data set contains 510 single points energy values, computed over the six sites shown in Fig. 8.2 (red dots). For each site, 85 DFT single point energies for z values between -1.16 Å and 5.45 Å have been evaluated. The overall errors in the fitting procedure are found to be smaller than 1%. DFT calculations have been performed with the package VASP [130, 176]. In applying the GGA, the PW91 functional [124] has been used. The PAW method [127] is used to describe the ion cores. And to model the system adsorbate/substrate a five-layer slab and a (2×2) surface unit cell have been used. To avoid artifacts caused by the use of periodic boundary conditions in the direction perpendicular to the slab, a vacuum layer of 20 Å has been placed between the slabs in the z direction. The plane-wave expansion has been limited by a cutoff energy of 800 eV, and a $5 \times 5 \times 1$ k-point grid has been used to sample the Brillouin zone. Using these parameters, the lattice constant (see Fig 8.2) has been found to be 2.88 Å, in good agreement with previous theoretical results [3, 177], and with the experimental value of 2.84 Å [178]. The interlayer distance after relaxation has been found to be 1.98 Å, the top-most layer presents a rumpling of 0.065 Å, with the F^- ions displaced outwards and the Li^+ ions inwards, in good agreement with previous theoretical calculations [3, 179, 180].

In Fig. 8.3 we display several 2D(x,y) cuts showing the characteristics of the interpolated 3D-PES. From this plot it can be seen that far from the surface (Z $\geq$ 1.66 Å) the potential over the F (V_{1D}^F) ion is higher than over the Li (V_{1D}^{Li}) ion. For distances around Z=1.5 Å, both potentials are very similar. Closer to the surface (1.33 Å $\leq$ Z), $V_{1D}^{Li} > V_{1D}^{F}$. When the H atom reaches shorter distances Z $\leq$ 0.6 Å, V_{1D}^{F} becomes higher than V_{1D}^{Li} once again. The corrugation complexity of this PES is reflected in the diffraction patterns, as we discussed in Sec. 8.3

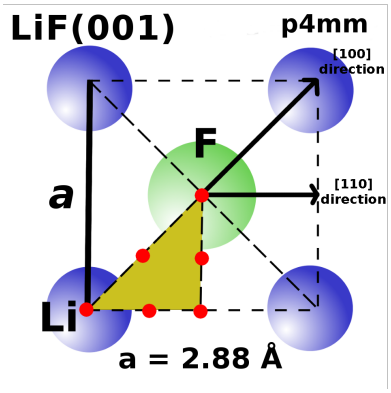

Figure 8.2: Schematic representation of the LiF(100) unit cell. Red dots represent the configurations used to compute the DFT data set. Golden colored area marks the irreducible Wigner-Seitz cell of the system.

Dynamics

To study the scattering of H(D) atoms from LiF(100), we have performed both, classical [23, 147] and quantum calculations.

Within the classical dynamics framework, a classical trajectory is computed by solving the Hamilton equations of motion. The classical scattering probability as a function of the polar angle, θ_i, (see Fig. 8.1), and the incidence energy (E_T) is calculated as an average over 15000 trajectories, which ensures low statistical errors. But, in order to compare our theoretical simulations with experimental measurements, diffraction probabilities have to be evaluated. Since diffraction is a quantum phenomenon related to discrete changes of the parallel wave vector, in principle, quantum calculations would be needed. However, as already shown in the case of diffraction of molecules at low incidence energy [171, 172, 181], molecular and atomic diffraction can be qualitatively evaluated by means of a classical binning method, which was widely explained in Sec. 7.1.4.

We have carried out quantum dynamics calculations by solving the time dependent Schrödinger (TDS) equation for the nuclear Hamiltonian of the system. To solve the TDS equation, we have made use of the Heidelberg MCTDH package [21, 22, 150, 153, 154], which has been already successfully used to study molecular reactive scattering from surface [55, 182–184], and also diffraction of atoms from surfaces at low incidence energy [185]. Details about the MCTDH were already presented in Sec. 7.2. To obtain diffraction probabilities, we have performed a flux analysis of the reflected wave function, which is absorbed by a complex absorbing potential placed in the non-interaction Z region (see Sec. 7.2.5). The main parameters used in the quantum calculations are listed in Tab. 8.1. Dynamics simulations have been performed on the three-dimensional (3D) PES described on

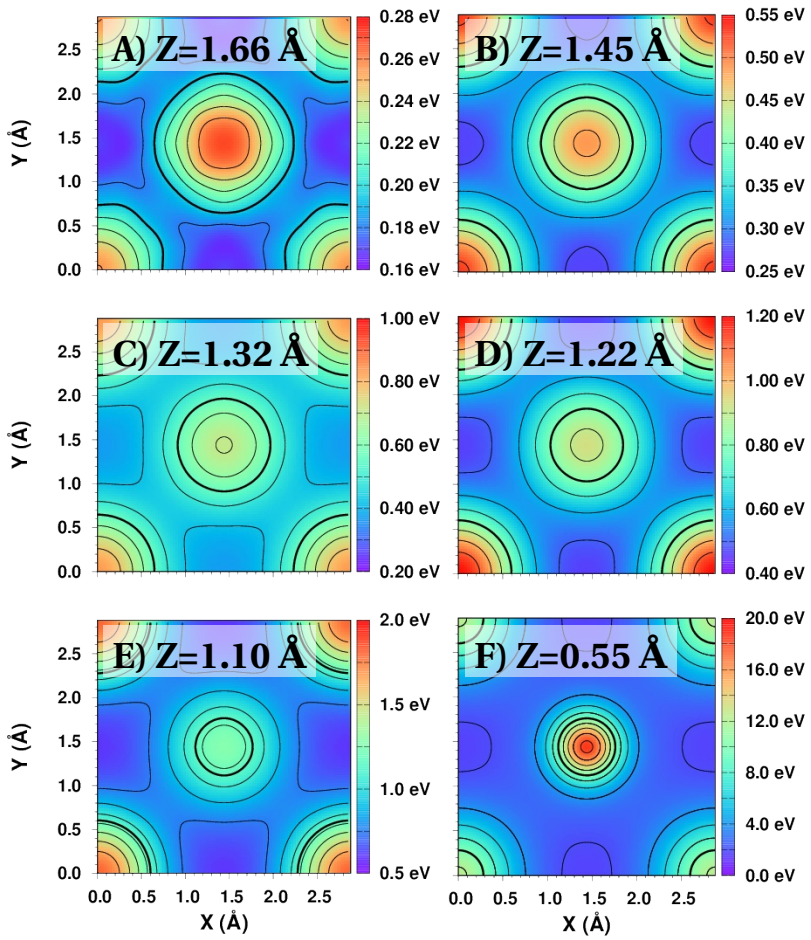

Figure 8.3: 2D (X,Y) cuts of the H/LiF(001) PES. Thick black lines represent a different energy value per panel, E_{black}. The spacing between isoenergetic lines, ΔE, is different in each panel as well. (**A**) E_{black} =0.195 eV, ΔE =0.015 eV; (**B**) E_{black} =0.4 eV, ΔE =0.004 eV; (**C**) E_{black} =0.56 eV, ΔE =0.07 eV; (**D**) E_{black} =0.8 eV, ΔE =0.1 eV; (**E**) E_{black} =1.15 eV, ΔE =0.15 eV; (**F**) E_{black} =10.0 eV, ΔE =2.0 eV. Each panel specifies the Z value kept constant during the 2D-cut.

	$\theta_i \geq 5^\circ$ ($\leq 2^\circ$)
Initial wave packet	
Width, ΔZ_0 (Å)	0.5
Position, Z_0 (Å)	6.5
Grid parameter	
Type X, Y, Z	FFT
X, Y-range (Å)	[0.0, 11.52]
$N_{X,Y}$	600(1500)
Z-range (Å)	$[-0.75, 15.0]$
N_Z	
Complex absorbing potential	
Z-range (Å)	[6.5, 15.0]
Strength (a.u.)	5.70×10^{-5}
SPF per DOF X, Y, Z	9, 9, 9
Propagation time (fs)	450

Table 8.1: MCTDH calculation parameters as a function of the initial polar angle (θ_i). $N_{X,Y}$ and N_Z are the FFT primitive functions for coordinates X, Y and Z, respectively. See Fig. 8.1 for coordinates definition. Specific parameters used for incidence conditions $\theta_i \leq 2^\circ$ are given within brackets.

previous section. However, as the MCTDH method is more efficient when combined with PESs that have the form of sum of products of one-dimensional functions (see Sec. 7.2), we have used the POTFIT [151, 152] algorithm to transform our 3D non-separable potential into this suitable form, as explained in Sec. 7.2.2. Parameters related to the POTFIT procedure and the accuracy of the approximated potential (V^{approx}) are given in Tab. 8.2.

ANALYSIS OF DIFFRACTION PATTERNS FOR H AND D USING A CLASSIC BINNING METHOD

In order to test the classical binning method, a detailed comparison between experimental and theoretical simulated diffraction spectra have been performed. In Fig. 8.4 (b) we show the diffraction pattern of H/LiF(100) for $E_T = 0.8$ keV and $\theta_i = 1.48$ deg. obtained by Winter et al. [107]. This spectrum shows, additionally to the specular peak, first and second order peaks. Furthermore, the first order peaks are more intense than the specular one. Our classical theoretical simulations, displayed in Fig. 8.4 (a), show the same trend, i.e., five peaks are present in the spectrum, and the first order peaks are more intense

Natural potential basis	
N_x,N_y	25, 25
N_z	Contr.
Relevant region of the fit	
Z (Å)	> 0.5
V (eV)	< 3
POTFIT *accuracy*	
N_{iter}	4
Δ^{rw}_{rms},Δ^{w}_{rms} (meV)	0.15, 5.03
$\max(\epsilon^r)$, $\max(\epsilon)$ (meV)	4.54, 306

Table 8.2: Parameters used to represent the H/LiF(001) PES in a suitable form for the MCTDH equations of motion using the POTFIT algorithm. Δ^{w}_{rms} and Δ^{rw}_{rms} represent the root mean square error on all grid points and on relevant grid points, respectively. $\max(\epsilon)$ and $\max(\epsilon^r)$ represent the maximum error on all grid points and on relevant grid points, respectively.

that the specular one, which supports the suitability of our method. At this point, it should be noticed that in order to compare with this experimental spectrum, our delta-shape theoretical diffraction probabilities have been convoluted using a 2D Gaussian function.

The above comparison is merely qualitative, a more quantitative comparison is shown in Fig. 8.5. In this figure we compare our classical results with a corrected version (P. Roncin *et al.*, private communication*) of the diffractogram obtained by Rousseau et al. [105] for diffraction of H atoms along the $\langle 100 \rangle$ direction. This set of experimental data shows that there is a remarkable change of the relative intensities of diffraction peaks when increasing the incidence normal energy, E_z, from 290 meV (red crosses) to 450 meV (blue x-symbols). For E_z =290 meV, the first order peaks are less intense than the specular one, whereas at higher normal energy, E_z =450 meV, the specular peak is slightly higher than the first order peaks. Our classical results follow the same experimental trend when increasing E_z from 300 meV (red dashed line) to 400 meV (blue dashed line).

Although, to our knowledge, experimental data as a function of the normal energy have not been systematically recorded for H/LiF(100), we show this theoretical study in Fig. 8.6. In this figure we have displayed a series of theoretical diffractograms as a function of the normal energy, for a total energy (incidence angle) between 1.0 keV (0.81 deg.) and 2.0 keV (1.21 deg.), for diffraction along the crystal-

*A few months after publishing our results (see Ref. [156]), P. Roncin *et al.* explained us in a private communication that there were some incorrect experimental data in Ref. [105]. In the same private communication, they provided us with the correct ones.

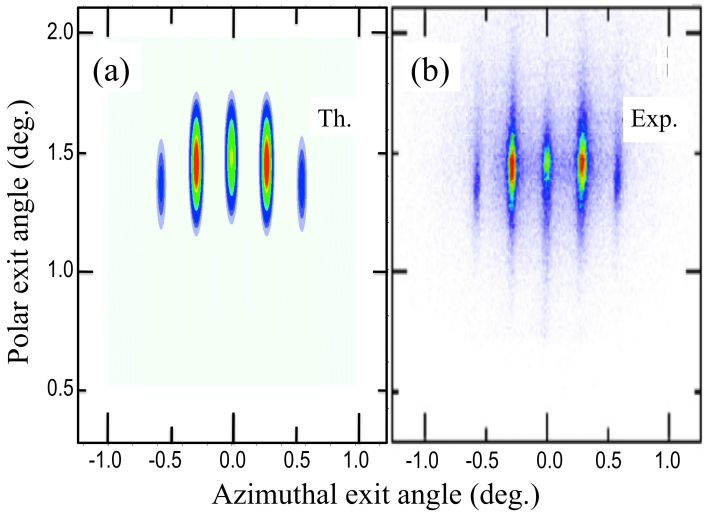

Figure 8.4: (**a**) 2D (θ_f,ϕ_f) calculated intensities for the diffraction spectrum along the incidence direction <100> for $E_T = 0.8$ keV and $\theta_i = 1.48$ deg. 2D results have been convoluted with a 2D Gaussian function of width $\sigma_{\phi_f} = 0.025$ deg. and $\sigma_{\theta_f} = 0.12$ deg. to simulate a typical experimental resolution. (**b**) Diffraction spectrum measured by Winter et al. taken from Ref. [107].

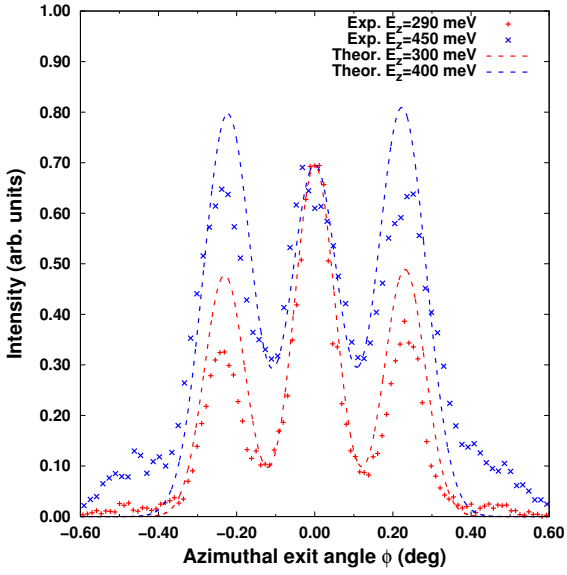

Figure 8.5: Diffraction spectrum of H/LiF(001) along the ⟨100⟩ direction. Red crosses: Experimental data from Ref. [105]. Dashed lines: classical theoretical results, which have been convoluted with a 1D Gaussian function of width $\sigma_{\phi_f} = 0.052$ deg. (red line) and $\sigma_{\phi_f} = 0.062$ deg. (blue line) to simulate the experimental resolution. E_z is the normal energy.

lographic directions <110> and <100>. At this point, it should be pointed out that, to avoid spurious results on the simulated diffraction probabilities due to the classical rainbow effect, [186], classical trajectories with a final azimuthal angle $\phi \geq \phi_{CR}^{+} - 0.005$ deg. or $\phi \leq \phi_{CR}^{-} + 0.005$ deg. are not taken into account during the binning procedure. In these two equations ϕ_{CR}^{+} and ϕ_{CR}^{-} represent the positive and negative rainbow angle, respectively (see 8.6 and 8.7).

From Figs. 8.6 and 8.7 several interesting properties of this system are observed: (i) The normal energy for which the first order peaks become higher than the specular peak is smaller for incidence along the <100> direction, in good agreement with experimental results by Rousseau and et al. [105]. These authors have shown that along the <110> direction, the specular peak is still more intense than the first order ones for $E_z = 560$ meV; (ii) The number of diffraction peaks, along the <100> direction is higher than along the <110> direction, despite the fact that the parallel momentum change required to excite a diffraction peak along the <110> direction is smaller than the one required to excite a peak along the <100> one. This latter result also agrees with the experimental findings [105]. Thus, both experiment and theory agree in the fact that the corrugation felt by the atoms is higher along the <100>. It is also worthy to mention that the experimental diffraction spectra recorded for H_2 and He show, as expected, more diffraction along the <110>. The unexpected results obtained for H/LiF(100) reveal the complexity of the system, which is essentially captured by the classical binning method.

The complexity of H/LiF(100) may be understood by turning our attention to the geometrical structure factor, because the amplitude of the diffraction peaks, for polyatomic surfaces, depends on it. The geometrical structure factor can be written as a function of the atomic form factors as:

$$S_{\mathbf{G}} = f_{Li}(\boldsymbol{G}) \cdot e^{i\boldsymbol{G}\boldsymbol{r}_{Li}} + f_F(\boldsymbol{G}) \cdot e^{i\boldsymbol{G}\boldsymbol{r}_F} \tag{8.3}$$

where f_{Li} and f_F are the atomic form factors for Li and F ions, respectively. $\mathbf{G} = n\mathbf{b}_1 + m\mathbf{b}_2$ represents the reciprocal lattice for LiF(100) (see Fig. 8.8), and $\mathbf{r}_{Li}$ and $\mathbf{r}_F$ are the atomic basis set vectors. From Eq. 8.3 we see that $S_{\mathbf{G}}$ is equal to $f_{Li} + f_F$ if $n + m$ is an even number, and equal to $f_{Li} - f_F$ if $n + m$ is an odd number. This equation reveals the first remarkable difference between the two incidence directions. All the diffraction peaks observed along the <100> direction correspond to $n + m =$ even, i.e., for all of them $S_{\mathbf{G}} = f_{Li} + f_F$. On the other hand, diffraction along the <110> direction shows peaks with $n + m$ even and odd alternately, which may explain the stronger modulation on this direction. It should be also remembered that the atomic form factors depend on the electronic density, i.e., there is a close relationship between the form factors and the corrugation of the PES, which varies, for H/LiF(001), quite a lot as a function of the distance to the

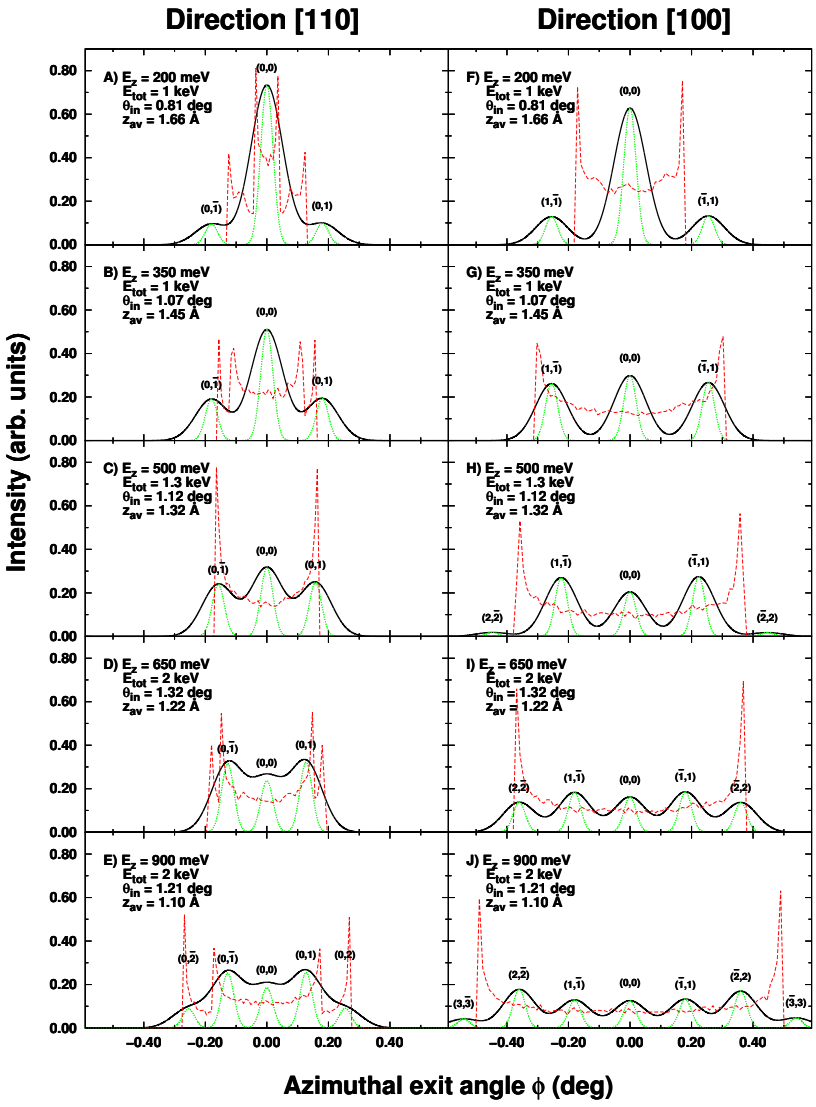

Figure 8.6: Simulated diffraction spectra for H/LiF(100) as a function of the azimuthal angle. Left panels: Incidence direction <110>. Right panels: Incidence direction <100>. Back (green) solid (dotted) line: The results have been convoluted with a Gaussian function of width $\sigma = 0.052$ deg. (0.02 deg.) to simulate the experimental resolution of Ref. [105]. E_z (E_T) represents the normal (total) energy, θ_i the polar incidence angle, and z_{av} the classical turning point. Red dashed line: classical reflection probabilities $\times 10$ without binning.

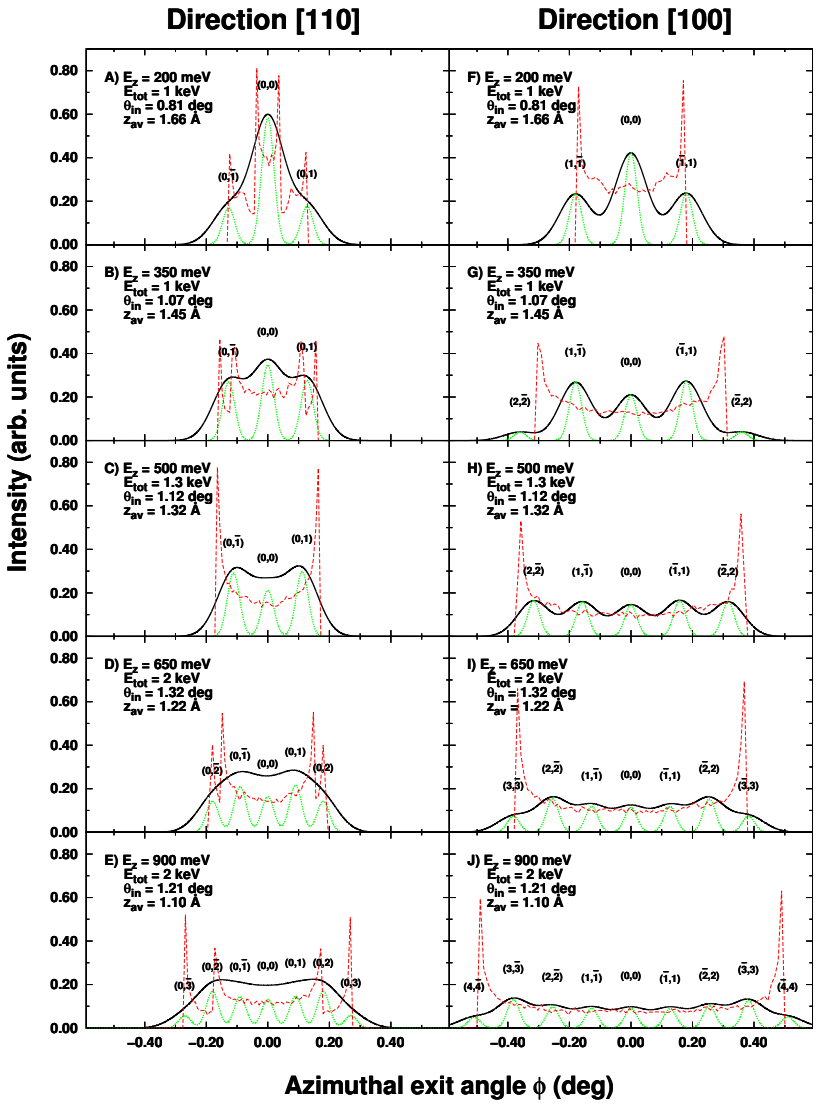

Figure 8.7: Simulated diffraction spectra for D/LiF(100) as a function of the azimuthal angle. Left panels: Incidence direction <110>. Right panels: Incidence direction <100>. Black (green) solid (dotted) line: The results have been convoluted with a Gaussian function of width $\sigma = 0.052$ deg. (0.02 deg.) to simulate a typical experimental resolution of Ref. [105]. E_z (E_T) represents the normal (total) energy, θ_i the polar incidence angle, and z_{av} the classical turning point. Red dashed line: classical reflection probabilities $\times 10$ without binning.

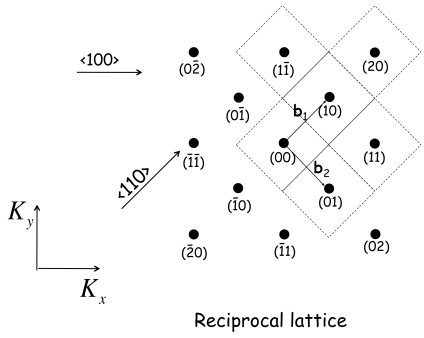

Figure 8.8: Schematic view of the reciprocal space for LiF(001) surface. $\mathbf{b}_1$ and $\mathbf{b}_2$ represent the basis vectors, where $|\mathbf{b}_1| = |\mathbf{b}_2| = 1.15$ au. High symmetry directions, <100> and <110 >, are plotted as well.

surface (see Fig. 8.3). Thus, depending on the classical turning point (z_{av}), $f_{Li} + f_F$ could be similar to $f_{Li} - f_F$, if $f_{Li} >> f_F$ or $f_{Li} << f_F$, or very different, if $f_{Li} \approx f_F$. This phenomenon could explain the results displayed in Fig. 8.6. At this point, it should be noticed that this explanation holds independently of the projectile. And, that the different behavior observed for different projectiles depends on the specific values of the form factors, and therefore, on the corrugation of the PES for each projectile/surface system.

For the sake of completeness, in Figs. 8.6 and 8.7 we have also included the raw classical reflection probabilities, which show the classical rainbow peaks. Interestingly, the angular distributions obtained for the <110> direction show four rainbow peaks, whereas, for the <100> direction, they only show two of them. This is a consequence of the average periodic potential: while in the former case, the potential exhibits two different maxima, over the F-F and Li-Li rows (see Fig. 5.2-3, Ref [107]), in the latter case, it only exhibits one maximum, over the F-Li rows, and one minimum. Furthermore, in the case of the <110> direction, only two rainbow peaks are observed for the incidence conditions, $E_T = 1.3$ keV, $\theta_i = 1.07$ deg. (see Figs. 8.6 and 8.7), for which the classical turning point (z_{av}) is located in a region where the potential over the F atoms is similar to the potential over the Li atoms (see Fig. 8.3).

Finally, we have also corroborated that changing H by D atoms in our classical simulations leads to entirely different diffraction patterns (see Fig. 8.7). At the same energy, a D atom is slower than a H atom, and therefore, its de Broglie wavelength is smaller, which implies that, for the same energy, the diffraction spectra measured for deuterium present a different peaks distribution than the ones measured for hydrogen. This behavior is observed in our classical simulations (see Figs. 8.6 and 8.7). It is important to remark here that pure classical calculations simulating the dynamics of atoms impinging on

a surface under grazing angle conditions predict no isotropic effect on the final scattering angle distribution up to first order approximation (see App. E). Thus, the isotopic differences clearly found in Figs. 8.6 and 8.7 are introduced by the binning procedure. Unfortunately, to our knowledge, D/LiF(100) experimental diffractograms are not available in the literature. Those experimental measurements would help us to further assay our classical binning method.

FROM SLOW NORMAL INCIDENCE TO FAST GRAZING INCIDENCE CONDITIONS. A QUANTUM DYNAMICS STUDY

We have first analyzed the diffraction probabilities as a function of the incidence polar angle θ_i, while keeping the normal incidence energy constant. In Fig. 8.9, we show the evolution of the most intense diffraction peaks (see Fig. 8.1 for peak definition) with θ_i -in the case of symmetric peaks, only one of them is represented. From this figure, we can clearly see that specular peaks probabilities increases and diffraction peaks probabilities decrease with decreasing θ_i, and vanish at $\theta_i \approx 10^\circ$, except for peaks perpendicular to the incidence direction in the reciprocal space (see Fig. 8.1), the only ones observed at grazing incidence. The behavior of the latter peaks as a function of θ_i is also quite interesting, for the $< 110 >$ incidence direction (the one shown in Fig. 8.9), we can see that the first order peaks probability [$(0,1)$ and $(0,\bar{1})$] increases slightly with decreasing θ_i, while the probability of the second order peaks [$(0,2)$ and $(0,\bar{2})$] remains almost constant. Similar results (not shown here) are obtained for the $\langle 100 \rangle$ direction: the first order peaks probability [$(1,\bar{1})$ and $(\bar{1},1)$] increases with decreasing θ_i and the second order peaks one [$(2,\bar{2})$ and $(\bar{2},2)$] remains constant. Once grazing incidence is reached (around $\theta_i = 5^\circ$), these survivor peaks, both the specular and the diffracted ones, remain constant. Interestingly, it should be noticed that, independently of the incidence direction, for incidence angles smaller than 20° only the specular and the perpendicular diffraction peaks have a probability larger than zero, and that the diffraction spectra do not change significantly for θ_i below 5°, i.e., grazing incidence conditions seem to be reached for an initial polar angle around 5°. These results indicate that it is possible to compare experimental results obtained, for example, for $\theta_i = 1^\circ$ with theoretical ones obtained for $\theta_i = 5^\circ$ provided that E_n is the same. Thus, for example, an experiment performed at $E_i = 800$ eV and $\theta_i = 1.11^\circ$ could be described using theoretical simulations for $E_i = 40$ eV and $\theta_i = 5^\circ$. At this point, we should remark that to the best of our knowledge no GIFAD experimental results for $\theta_i \geq 2.5^\circ$ are available in the literature. Lienemann et al [94] have shown that, for H/LiF(001) at $E_i = 1.0$ keV, incoherent scattering due to electronic excitations clearly dominate for $\theta_i \geq 1.5^\circ$. But, in this experiment, E_i was kept fixed, while E_n increased with θ_i. However,

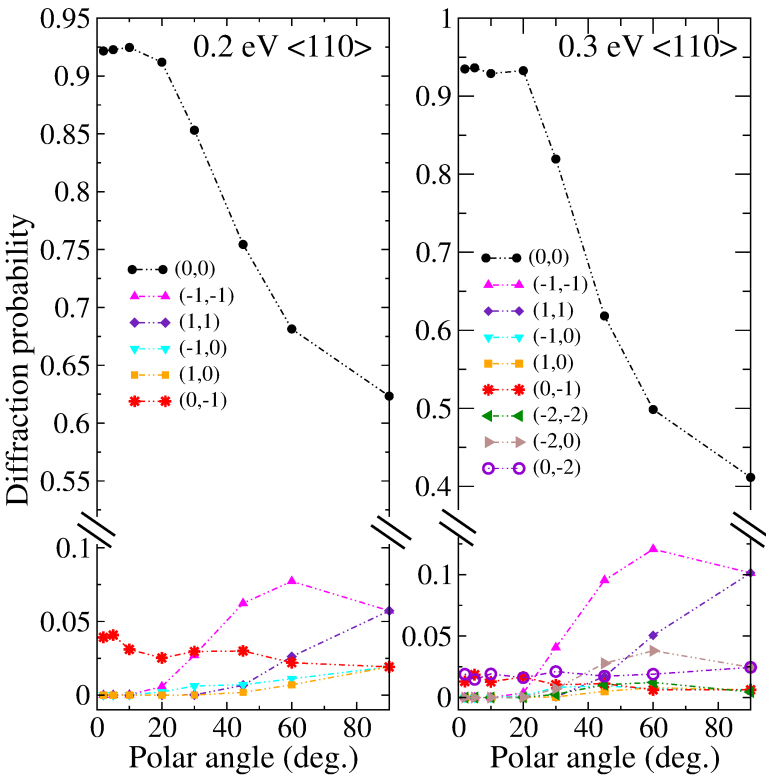

Figure 8.9: Diffraction probabilities as a function of the polar incidence angles (θ_i) along the crystallographic direction <110>, for the most intense diffraction peaks obtained in the simulations. Notice that for the lower incidence angles only peaks perpendicular to the crystallographic direction <110>, i.e., peaks of the form (o,n), are populated (see Fig. 8.1).

no systematic experimental study keeping E_n constant and varying θ_i, aiming to find the maximum θ_i angle that defines grazing incidence, has ever been performed. We hope that our analysis will encourage such experimental study.

For the sake of completeness, we have compared our theoretical results, obtained for $\theta_i = 5°$, with experimental data available in the literature. In Fig. 8.10, we compare experimental results from Ref. [105] with our theoretical results, obtained for $\theta_i = 5°$. From this Fig., we can see that our results reproduce qualitatively experimental observations. In particular, theoretical spectra display, in agreement with experiment, high first order diffraction peaks along the $< 100 >$ direction, and a clear predominance of the specular peak along the $< 110 >$ one. A closer look to Fig. 8.10(a) reveals some disagreement between theory and experiments. The experimental spectrum show first order diffraction peaks more intense than the specular one, whereas the simulated one display a more intense specular peak. However, as shown in Fig. 8.10(a), if we increase the normal energy in our simulations the first order peaks increase and the specular one

decreases. In fact, as shown in the inset of this Fig., for high enough normal energy, we recover the experimental results. Thus, from this analysis, we can conclude that our quantum theoretical results reproduce the experimental ones with a energy shift. Similar agreement with experiments has been previously obtained using a classical binning method and the same PES [156]. Interestingly, we should also point out that the diffractogram shown in the inset of Fig. 8.10 agrees with the 2D diffraction pattern recorded by Winter et al [107] for the same incidence normal energy. Here, we should also remark that the disagreements found between theory and experiment, are most likely due, beyond experimental uncertainties, to the accuracy of the DFT functional used in computing the energy points needed to built the PES. We have not performed a systematic search for the functional reproducing best the experimental measurements because, on the one hand, there are not enough experimental measurements to carry out properly this search (see Ref. [187, 188]), and on the other hand, it was no the aim of this study to reproduce a particular experiment, but to carry out an analysis that could be extrapolated to any system, even to a fictitious one.

Finally, we have also performed a comparison between the spectra obtained at FGI and the spectra that it would be obtained at normal incidence if only the peaks populated at FGI were considered, i.e., if only the peaks perpendicular to the crystallographic incidence direction were considered. In Fig. 8.11, we show such comparison along two crystallographic incidence directions, $< 100 >$ and $< 110 >$, for several normal incidence energies. As we are only interested in relative intensities, in Fig. 8.11, we have renormalized the probability of the normal incidence peaks to the probability of the specular peak obtained at fast grazing incidence. From this figure, we can extract several interesting conclusions: (i) For the lower normal energies, for which only the first order peaks have a significantly intensity, spectra at normal and grazing incidence almost overlap. For higher normal energies, when second order peaks start to show up, the quantitative agreement between both spectra gets a little worse. (ii) The variation of the spectrum at fast grazing incidence as a function of E_n is qualitatively well reproduced by normal incidence simulations. For example, the decrease of the first order peaks and the increase of the second order ones along the $< 110 >$ direction, obtained at fast grazing incidence, is well reproduced by a normal incidence simulation, although at normal incidence second-order peaks are populated faster than at fast grazing incidence. This worsen of the agreement between normal and grazing incidence results (for a fixed θ_i), when the normal energy increases, is related to the deterioration of the grazing incidence conditions. A more quantitative analysis of our results can be performed from the relative intensities of the different diffraction peaks, as they come out from the simulation, listed in Tab. 8.3.

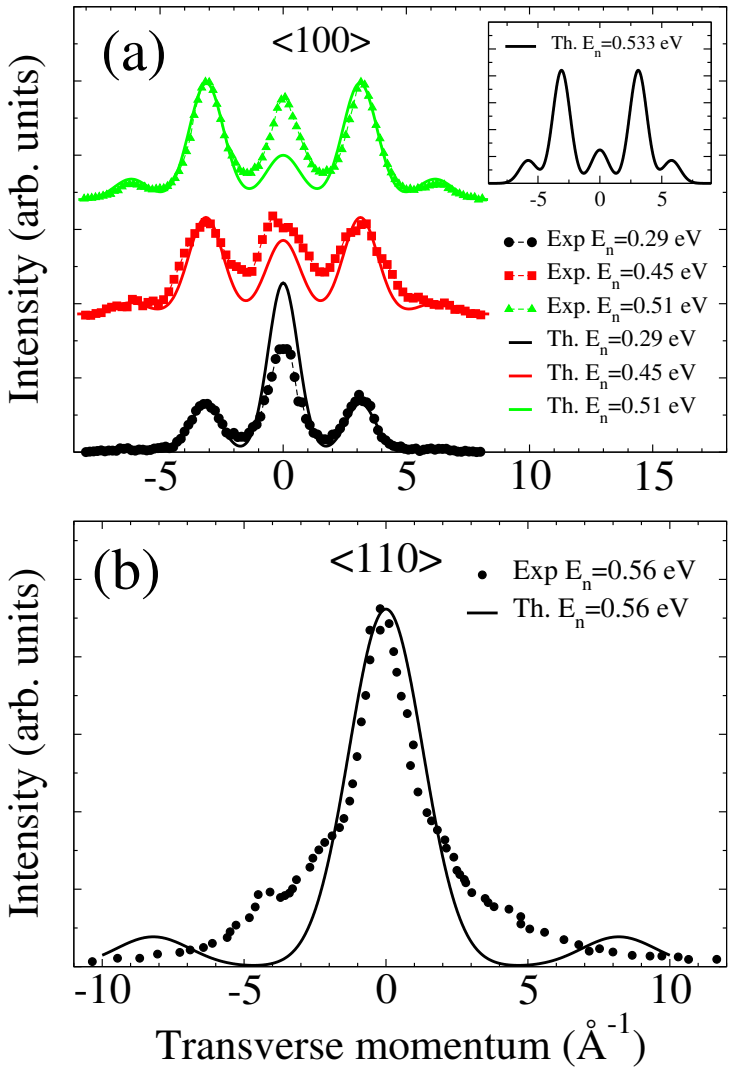

Figure 8.10: Diffraction spectra of H/LiF(001) along the $< 100 >$ **(a)** and $< 110 >$ **(b)** crystallographic directions. Black stars: experimental data from Ref. [105]. Solid lines: Quantum theoretical results ($\theta_i = 5°$), which have been convoluted with a 1D Gaussian function to simulate the experimental resolution. The inset shows the theoretical diffraction spectrum for E_n=0.533 eV.

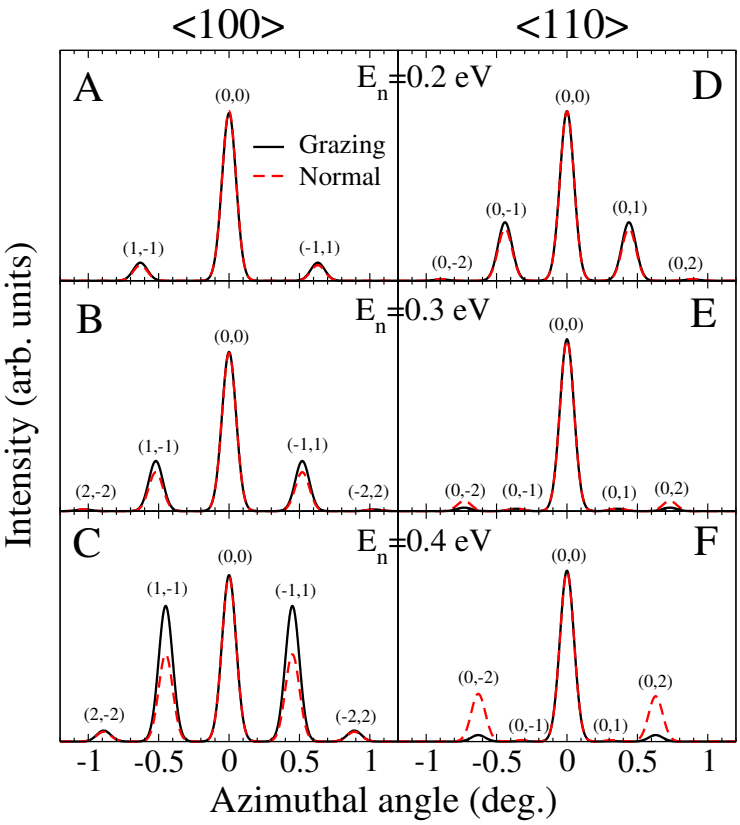

Figure 8.11: Comparison between simulated diffraction spectra at grazing incidence, θ_i=2° and E_i=164 eV (**A** and **D**) 246 eV (**B** and **E**), 328 eV (**C** and **F**), and at normal incidence, θ_i=90° E_i=E_n; for several normal incidence energies and two crystallographic incidence directions. Note that in the case of normal incidence, we have only included in the spectra the diffraction peaks perpendicular to the crystallographic incidence directions corresponding to the FGI calculation we are comparing with. I. e., we have included peaks of the form $(\pm m, \mp m)$ for the incidence direction $\langle 100 \rangle$, and of the form $(0, n)$ for $\langle 110 \rangle$ (see Fig. 8.1). Normal-incidence diffraction peaks have been renormalized to the specular peak obtained at FGI (see text). Delta-functions theoretical diffraction distributions have been convoluted with 1D Gaussian functions of width $\sigma = 0.05°$ to simulate the experimental resolution.

$< 100 >$						
E_z(eV)	0.2		0.3		0.4	
	Norm.	Graz.	Norm.	Graz.	Norm.	Graz.
$I_{(2,\bar{2})} / I_{(0,0)}$	0.001	0.001	0.011	0.011	0.059	0.066
$I_{(1,\bar{1})} / I_{(0,0)}$	0.092	0.108	0.246	0.315	0.527	0.815
$< 110 >$						
E_z(eV)	0.2		0.3		0.4	
	Norm.	Graz.	Norm.	Graz.	Norm.	Graz.
$I_{(0,2)} / I_{(0,0)}$	0.010	0.007	0.060	0.020	0.281	0.027
$I_{(0,1)} / I_{(0,0)}$	0.031	0.035	0.015	0.014	0.008	0.009

Table 8.3: Theoretical relative intensities used to draw spectra shown in Fig. 8.11.

The latter results have important implications from the simulation point of view. They show that with a single normal incidence energy simulation, which requires much less computational resources than a FGI calculation, we can simulate reasonably well the diffraction spectra obtained at grazing incidence, at a given normal incidence energy, along any incidence direction. In other words, by just performing a single *cheap* calculation, one can simulate reasonable well several experimental conditions.

CONCLUSIONS AND SUMMARY

In Sec. 8.3, we have analyzed to what extent classical dynamics can be used to analyze experimental results on scattering of atoms under FGI conditions. To perform this study, we have used an accurate PES built by interpolation of a DFT data set. We have shown that diffraction probabilities obtained using a classical binning method reproduce fairly well the experimental trends. Thus, classical dynamics can be used to perform coarse analysis, which could be used to lead the quantum dynamics simulations to the systems and incidence conditions of most interest. These coarse analysis will be even more useful for molecules/surface systems, for which quantum dynamics simulations are very time-consuming from a computational point of view.

In Sec. 8.4, we have performed MCTDH quantum dynamics calculations, based on a first-principles 3D PES, aimed at evaluating several options to reduce the computational effort required to analyze experimental spectra obtained at FGI conditions. Taking H/LiF(001) as a benchmark system, we have shown that grazing incidence conditions are fulfilled at incidence polar angles $\theta_i \approx 5^o$ higher than the ones typically used in experiments, i.e., we have shown that, for a given

normal incidence energy, the same results can be obtained by using lower total energies than those used in experiment. We have also shown that diffraction at normal incidence can be used, at a first approximation, to simulate FGI, simply by analyzing diffraction peaks perpendicular to the crystallographic incidence direction considered in each specific experiment. Thus, one single *cheap* calculation at normal energy could be used to simulate diffraction spectra measured in GIFAD and GIFMD experiments along several incidence directions and angles. Although here, we have to take into account that the ability of normal incidence simulations to reproduce grazing incidence results worsen when the normal incidence energy increases.

Finally, we should point out that the two approximations analyzed in Sec. 8.4, are valid within the same incidence conditions as the ASC approximation. However, to keep the full dimensionality of the system present some advantages: (i) one can used the same potential and dynamics method to analyze both GIFAD(GIFMD) and quasi-GIFAD (quasi-GIFMD) experiments; (ii) one can use only one slow normal incidence calculation to simulate several experiments carried out, at the same normal incidence, for several crystallographic directions.

9

6D THEORETICAL STUDY OF H_2 SCATTERING FROM LIF(001): FROM THERMAL TO HIGH INCIDENCE ENERGIES

In this chapter a 6D PES for H2/LiF(001) system is presented and tested with various types of dynamics (quantum and semi-classical) using a wide range of initial conditions. Contents are based on the following publications:

- A.S. Muzas, F. Martín and C. Díaz. *Journal of Physics: Conference Series*, **635**, 012029 (2015)
- A.S. Muzas, et al. (to be published)

MOTIVATION

Full-dimensional quantum dynamics has became a standard tool to study diatomic molecule/surface interactions, from reactive scattering [175, 187, 189–191] to molecular diffraction [23, 54, 191]. But, its accuracy to reproduce experimental data, disregarding phonons and electron-hole pair excitations effects, rely on the accuracy of the underlying PES in which the dynamics is carried out [187, 188]. Thus, the large progress made in the microscopic dynamics description of molecule-surface interaction processes has motivated, subsequently, the development of flexible and accurate methods to determine full-dimensional PESs. These methods are commonly based on interpolation of DFT energies, computed for a variable number of configuration. Nowadays a handful of such methods is already available in the literature, such as the CRP [15], the MS [16, 17], the NN [18], the PIP-NN [19], and the RFF method [20]. These methods have been widely used to determine the electronic structure of diatomic molecules interacting with metal surfaces -see Refs. [11, 132, 134, 136, 142, 192–198] for examples of PESs built with CRP; Refs. [13, 140, 141, 199, 200] for MS; Refs. [201–204] for NN; Refs. [205] for PIP-NN. And very recently these interpolation methods have been also used to study polyatomic molecule/metal surface interactions [**shen2014**, 202, 206, 207].

On the other hand, the interaction of light diatomic molecule with insulating surfaces, although widely studied during the last decades of the 20^{th} century, have received much less attention, in the present century, when important developments, related to the theoretical tools, have taken place. For example, diffraction of H_2/LiF(001) was popularly used as benchmark system, to test theoretical models and exper-

imental setups, since the 30's when stern and Co. used to prove the wave nature of atomic and molecular particles [33, 208]; these experimental results were also used to describe for the first time selective adsorption [34]. Later on, experiments on rotationally and diffractionally inelastic scattering showed the H_2 could change its rotational state upon collision with LiF(001) [70].

Rotational polarization [209] and Time-of-fly measurements were also performed in this system [71]. Aiming to understand these experimental measurement, a number a theoretical model were proposed, although most of them suffer from important shortcomings. Some scattering calculations [210–214] were performed making used of analytical potentials which do not contained dependence on the H_2 azimuthal angle ϕ (see Fig. 2.1), i.e., potentials that do not allow Δm_J transitions, m_J being the magnetic rotational quantum number. Other models [215–219] allow this transitions, but do not taken into account the interaction between the electrostatic field of the surface ions and the quadrupole moment of the H_2 molecule. However, as shown by Hill and Co. [220] this interaction play a key role in H_2/LiF(001), because is the main responsible for rotational transitions. In fact, more recently theoretical simulations [221, 222], based on a five-dimensional model (using the rigid rotor approximation), revealed the importance of including the molecule azimuthal angle dependence and the electronic interaction, to reproduce experimental results showing large differences in the diffraction intensities for para-H_2 ($J = 0$) and ortho-H_2 ($J = 0$ and $J = 1$ in the ratio 1:3) [96]. For this system also isotopic effects has been studied [76, 106].

Already in the present century, experiments showing diffraction of atoms and light molecules under fast grazing incidence conditions, upon scattering from insulating surfaces [107], have renewed the interest on this kind of surfaces. Since 2007, when first experimental results for LiF(001) [158] and NaCl(001) [101] were published, the number of measurements and systems studied have increased considerably (see [107] and Refs. therein). From a theoretical point of view, diffraction of atoms from insulating surfaces has been widely studied [1, 4, 111, 156, 160, 161, 164, 165, 167, 169]. However, little attention has been devoted to molecular projectiles, although diffraction spectra are richer, due to the internal molecular DOFs [10]. In this case, theory is called to pay a key role in understanding experimental results. And therefore, accurate 6D PES, describing the electronic structure of diatomic molecules/insulating surfaces systems, are required, together with a computationally efficient dynamics method.

One interesting feature of GIFMD spectra is that the rotational excitation shows up in the diffraction spectra, θ_f vs. ϕ_f (see Fig. 2.1 for angle definition), as a series of concentric circumferences, which results from the approximate energy conservation rule $\Delta k_Z^2/2M + \Delta E_{rot} \approx \Delta k_Y^2/2M$, E_{rot} being the rotational excitation energy, M the mass of

the projectile, Δk_Z the momentum change associated to the perpendicular direction to the surface, and Δk_Y the momentum change associated to the motion parallel to the surface and perpendicular to the incidence direction. However, none of the few molecular spectra available in the literature display this arrangement of concentric circumferences of the diffraction peaks (only one broad circumference is observed), which does not mean that experimental results can be used to conclude that molecular projectiles are not rotational excited upon scattering, it just means that rotational excitation cannot be resolved due to the limited experimental angular resolution. At the typical experimental conditions, for H_2/LiF(001), the polar angle spacing of these concentric circumferences associated, for example, with rotational excitations $H_2(J_i = 0 \rightarrow J_f = 2)$, $H_2(J_i = 1 \rightarrow J_f = 3)$ and $H_2(J_i = 0 \rightarrow J_f = 4)$ are about 0.07°, 0.19° and 0.25°, respectively, whereas the experimental angular resolution is about 0.5° (see Ref. [107]). On the other hand, the initial ro-vibrational state of the incident molecule may have a influence on the final diffraction spectra.

In this chapter, we present, to our knowledge, the first six-dimensional (6D) PES describing the electronic interaction between a diatomic molecule and an insulating surface (H_2/LiF(001)) based on DFT calculations. This PES has been built applying the CRP method to a DFT data set. In order to test the accuracy of this PES we have carried out dynamics simulations, using both the time-dependent wave packet propagation method [175] and the MCTDH method [21].

In Sec. 9.3, we have compared our elastic and inelastic scattering, at low incidence energies (E_i <1 eV), with available experimental data [96], and also with previous theoretical studies. These latter results were obtained using a 5D model potential including electrostatic interactions [76, 96, 222]. Eventually, in Sec. 9.4, to further assess the accuracy of our 6D-PES for a wide range of incidence energies, we have also compared our results for diffraction under fast (E_i>100 eV) grazing ($\theta_i < 4°$) incidence conditions with those obtained experimentally [105, 107]. In Sec. 9.5, we have investigated the influence of the initial ro-vibrational state of the molecules in the diffraction spectra using as benchmark system H_2/LiF(001), for which diffractograms data are available in the literature [105]. We show that direct and accurate comparisons between theory and experiment, similar to the ones perform usually at thermal or quasi-thermal energies [24], require the knowledge of the initial ro-vibrational distribution of the molecules.

THEORETICAL MODEL

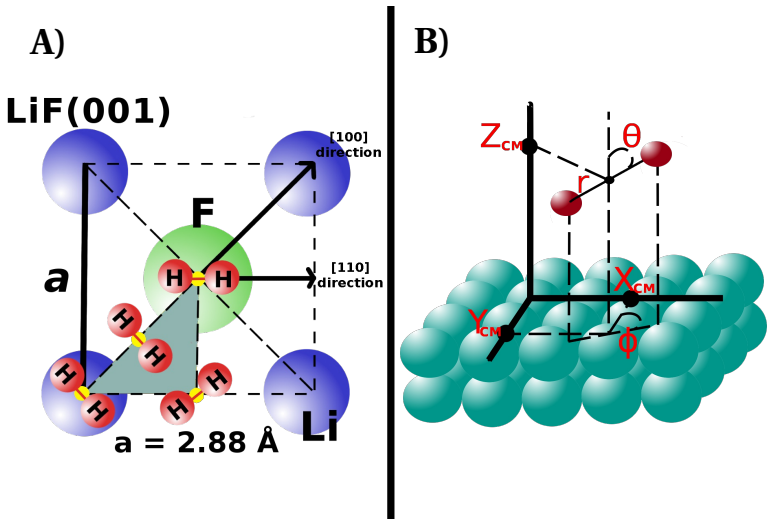

Figure 9.1: Panel (**A**): schematic view of LiF(001) surface. Hydrogen molecules mark the set of high symmetry positions in which our PES interpolation is based on, namely, top Li, top F, bridge (point between Li and F atoms) and hollow (point between Li atoms or F atoms) sites. Panel (**B**): complete set of DOFs that characterize the configuration of a H_2 molecule on the LiF(001) surface.

All our dynamics simulations, either at classical or quantum theory level, have been carried out within the BOSS approximation, which means, that surface atoms were kept frozen at their equilibrium positions, and that H_2 nuclei interaction with electronic DOFs is encoded inside a PES. Thus, prior to any dynamics calculation, a well behaved continuous PES needs to be defined, at least, for the dynamical important regions, i.e., the regions of the configuration space that the projectiles are going to explore within the range of initial conditions to be simulated.

Potential energy surface model

We decided to construct the PES of our system interpolating a dense set of DFT-GGA single point calculations using an slightly modified version of the CRP [15]. This interpolation method, has been applied to model a wide range of molecule/metallic surface systems with great success, and thus, detailed information about its different implementations can be found in the literature [132, 223]. Here we present, to our knowledge, the first 6D PES implementation describing the interaction between a diatomic molecule and an insulating surface. For a more detailed discussion of the CRP method, the reader is encouraged to check Sec. 6.2.

In a few words, the main idea under the CRP interpolation scheme is the subtraction of the most important repulsive parts of the PES prior to any data interpolation. Afterwards, the modified data is interpolated so that a smoother version of the PES is obtained. Finally, when the actual PES requires to be evaluated for a certain projectile geometry, it is enough to add to the smooth potential the value of the repulsive part for the given geometry. In this way, unexpected behaviors of the fitted functions between data points are reduced. The explicit CRP expression for our 6D potential (V_{6D}) can be written as:

$$V_{6D}(\mathbf{R}) = \mathcal{I}_{6D}(\mathbf{R}) + V_{3D}(\mathbf{r}_1) \cdot L_{z_0,\delta z}(z_1) + V_{3D}(\mathbf{r}_2) \cdot L_{z_0,\delta z}(z_2) \tag{9.1}$$

$$V_{3D}(\mathbf{r}) = \mathcal{I}_{3D}(\boldsymbol{r}) + \sum_{\forall i} V_{1D}^{Li}\left(d_i^{Li}\right) + \sum_{\forall i} V_{1D}^{F}\left(d_i^{F}\right) \tag{9.2}$$

$$L_{z_0,\delta z}(z_i) = \left[1 + \exp\left(\frac{z_i - z_0}{\delta z}\right)\right]^{-1} \tag{9.3}$$

where $\mathbf{R}$ characterizes the molecular degrees of freedom $(x, y, z, r, \theta, \phi)$ seen in Fig. 9.1-B, $\mathbf{r}_i$ stands for the coordinates (x_i, y_i, z_i) of the i-th H atom of the molecule, $\mathcal{I}_{6D}$ is the smooth interpolated six dimensional potential, V_{3D} is the atomic potential of H interacting with the same surface as described in Chap. 8 (see also Ref. [156]) but without the use of any switch function, and $L_{z_0,\delta z}$ is a logistic (switch) function which controls the amount of repulsion that is taken into account to calculate the smooth potential $\mathcal{I}_{6D}$.

All DFT-GGA calculations were performed with the VASP code [130, 176], using PW91 exchange-correlation functional [124]. Details about the converged parameters used in these calculations are presented in table 9.1 . In total, we have computed 4116 DFT-GGA single point energies, which are grouped in 21 (x, y, θ, ϕ) configurations (see table 9.2). Each configuration is formed by a set of 196 DFT-GGA energies obtained varying z from 0.25 to 4.0 Å and r from 0.4 to 2.3 Å. The evaluation of $\mathcal{I}_{6D}$ is performed by a bi-cubic spline interpolation of each 2D-cut (z, r) of the grid, and later, by a symmetry adapted Fourier interpolation along θ and ϕ directions for each high symmetry site. This procedure allows not only to define $\mathcal{I}_{6D}$ at each high symmetry site, but also to define its first derivatives. Finally, in order to get $\mathcal{I}_{6D}$ and its derivatives for any geometry, a Fourier interpolation was performed in (x, y) and ϕ based on the previous ones. Following equations and nomenclature exposed in Sec. 6.2, table 9.2 resumes the information of the DFT-GGA data organization and symmetry used during interpolation.

In Fig. 9.2, we show several 2D(r,Z) cuts through the 6D interpolated potential. From these cuts, we can see that, at the typical normal incidence energies we are investigating here, classical turning

Parameters	Values
Basis set	plane waves
Energy cut off for basis	800eV
Functional	PW91
K-space mesh	5x5x1, Γ-centered
Smearing	Gaussian
Sigma parameter	0.1
Core pseudo potentials	PAW [127]
Convergence criterion	10^{-4} eV

Table 9.1: Information about single point calculations performed in VASP in which the PES interpolation is based on.

Wyckoff site	Symmetry	$\{\theta\text{-grid}\}\times\{\phi\text{-grid}\}$	Num. of (z,r)-grids
a (top Li)	4mm	$\{0, \frac{\pi}{4}, \frac{\pi}{2}\} \times \{0, \frac{\pi}{4}\}$	5
b (top F)	4mm	$\{0, \frac{\pi}{4}, \frac{\pi}{2}\} \times \{0, \frac{\pi}{4}\}$	5
c (bridge Li-Li)	mm2	$\{0, \frac{\pi}{2}\} \times \{0, \frac{\pi}{4}, \frac{\pi}{2}\}$	4
f (bridge Li-F)	m	$\{0, \frac{\pi}{2}, \frac{3\pi}{4}\} \times \{0, \frac{3\pi}{10}, \frac{4\pi}{5}\}$	7

Terms used in $\mathcal{I}_{6D}$ interpolation	$\zeta^{A_1^\oplus A_1^\oplus}_{(0,0),0}, \zeta^{A_1^\oplus \times A_1^\oplus}_{(0,0),4}, \zeta^{A_1^\oplus \times A_1^\oplus}_{(1,0),0}, \zeta^{A_1^\oplus \times A_1^\oplus}_{(1,0),4}, \zeta^{A_1^\oplus \times A_1^\oplus}_{(1,1),0}$, $\zeta^{B_1^\oplus \times B_1^\oplus}_{(1,0),2}, \zeta^{B_1^\oplus \times A_1^\oplus}_{(0,0),4}, \zeta^{A_1^\oplus \times A_1^\oplus}_{(2,0),0}, \zeta^{B_2^\oplus \times E^o}_{(1,1),1}, \zeta^{B_2^\oplus \times B_2^\ominus}_{(1,1),2}$

Table 9.2: Top table: compendium of DFT-GGA data points organization. Bottom table: symmetry adapted functions used during the interpolation of $\mathcal{I}_{6D}$. The compact notation used here is explained in Sec. 6.2.

points are between 2.0 Å and 2.7 Å. The Li top site present the higher anisotropy, whereas the lower anisotropy is found for the Li-F bridge site. We can also observe that, as it could be anticipated, helicopter ($\theta = 90°$) configurations are energetically more stable than cartwheel ones over the Li^+ site. However, the contrary holds over the F^- site.

Quantum dynamics

Within the BOSS approximation, the Hamiltonian describing our system can be written as:

$$\hat{H} = -\frac{1}{2M}\left(\hat{\partial}_X^2 + \hat{\partial}_Y^2 + \hat{\partial}_Z^2\right) - \frac{1}{2\mu}\hat{\partial}_r^2 + \frac{\hat{J}}{2\mu r^2} + V_{6D} \,. \tag{9.4}$$

In this equation, M and μ are the total and the reduced mass of H_2, respectively. $\hat{J}$ is the rotation operator, whose eigenfunctions are the spherical harmonics $Y_{Jm_j}(\theta, \phi)$. To study diffractive scattering of H_2 from LiF(001) using this Hamiltonian, we have to solve the TDS equation:

$$\hat{H}\Phi(\mathbf{R}, \mathbf{r}; t) = i\hat{\partial}_t \Phi(\mathbf{R}, \mathbf{r}; t) \,. \tag{9.5}$$

To do so, we have used two different quantum dynamics methods, the TDWP propagation method [175, 190] and the MCTDH method [21, 22]. In this section, we summarize the main characteristics of both methods. For a more detailed description of the TDWP method, see Refs. [175, 190]. For a more detailed description of the MCTDH method see Sec. 7.2 and references therein.

The TDWP method

Within the TDWP [175], we represent the dependence of the wave function on X, Y, Z, and r using a direct product discrete variable representation (DVR) [224] with constant grid spacing, and on θ and ϕ using a non-direct product finite basis representation (FBR) of spherical harmonics. To transform the wave function from DVR to a direct product FBR in momentum space, and *vice versa*, FFTs are used [225]. To transform the wave function from the non-direct FBR to a direct product DVR, and *vice versa*, Gauss-Legendre and Fourier transformations are used [226].

This method is divided in three main steps:

1. The initial wave function (placed in the non-interaction region) is written as the product of a Gaussian wave packet describing the perpendicular motion to the surface, a plane wave function describing the parallel motion, an a ro-vibrational wave function describing the internal initial state of the molecule.

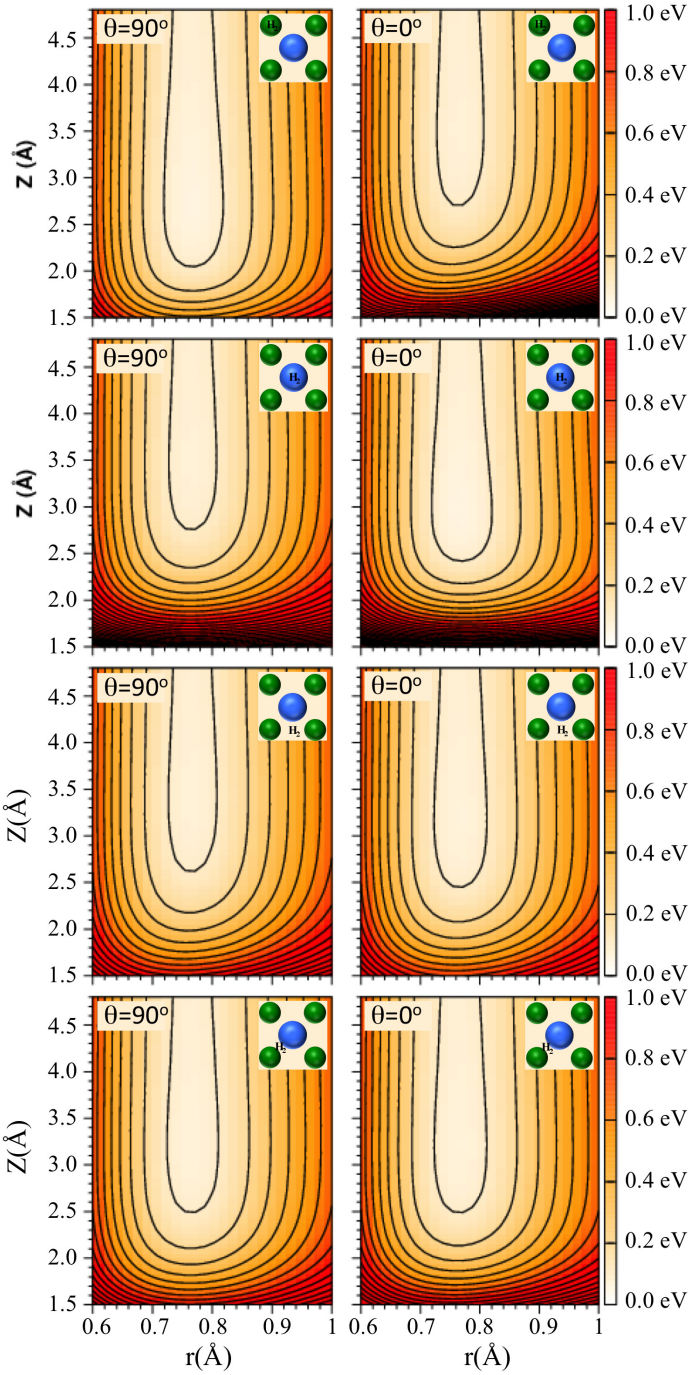

Figure 9.2: 2D cuts through the H_2/LiF(001). Left side panels: helicopter configurations; right side panels: cartwheel configurations. From top to bottom: top Li, top F, Li-Li bridge and Li-F bridge sites. The spacing between the contour levels is 0.1 eV.

Parameter	SNI	FGI
PES parameters		
N_Z	128	224
Z_{start}, $\delta Z(a_0)$	2, 0.15	1.5, 0.1
N_X and N_Y	10	24
$X(Y)_{min}$- $X(Y)_{max}$ Å	0-2.88	0-2.88
N_r	40	60
r_{start}, $\delta r(a_0)$	0.8, 0.15	0.6, 0.1
J_{max}, m_J^{max}	12	14
Initial wave packet		
E_{min}-E_{max} (eV)	0.05-0.15	0.15-0.45
E_{XY} (eV)	0.0	199.7
Z_0 (a_0)	17.75	18.0
Propagation/Analysis		
δt(aut)	5	2
CAP_Z, CAP_r (a_0)	13.25, 3.65	13.50, 3.65

Table 9.3: Input parameters used in the TDWP calculations. A detailed description of the parameters can be found in Ref. [230]. SNI= slow normal incidence, FGI=fast grazing incidence.

2. This initial wave function is propagated using the split operator method [227], in which the kinetic ($\hat{K}$) and potential ($\hat{V}$) propagation part of the Hamiltonian are symmetrically split as:

$$e^{(-i\hat{H}\Delta t)} = e^{-i\hat{K}\frac{\Delta t}{2}} e^{-i\hat{H}_{rot}\frac{\Delta t}{2}} e^{-i\hat{V}\Delta t} e^{-i\hat{H}_{rot}\frac{\Delta t}{2}} e^{-i\hat{K}\frac{\Delta t}{2}} \tag{9.6}$$

   Note that by symmetrizing the splitting, the error of this method is of the order of Δt^3.

3. Eventually, the back scattering wave function is analyzed at the non-interactive region, Z_∞, where the molecule and the surface no longer interact. The analysis is carried out using the Balint-Kurti formalism [228, 229].

In Tab. 9.3, we summarize the relevant parameters used in our TDWP calculations.

The MCTDH method

Within the MCTDH method, the time dependent wave function of our system is represented as a sum of Hartree products of SPFs. Each of these functions depend on both, spatial coordinates and time. In

	6D (SNI)
Primitive Grid parameters	
Type X, Y, Z	FFT
$N_X \times N_Y \times N_z$	$20 \times 20 \times 100$
X, Y-range (Å)	[0.0, 2.88]
Z-range (Å)	[0.25, 12.0]
Type r SPFs	rHO*-DVR
N_r, r-range (Å)	40, [0.1, 3.96]
Type θ, ϕ	2D Legendre DVR
$N_\theta \times N_\phi$	20×17
Wave representation	
$(X, Y) \times (Z, r) \times (\theta, \phi)$ SPFs	$25 \times 14 \times 18$
Propagation/Analysis	
Propagation time (fs)	2540
CAP_Z, CAP_r (Å)	7.5, 2.23
CAP strength: η_Z, η_r (au)	1×10^{-4}, 1.5×10^{-3}

Table 9.4: MCTDH calculation parameters). See Fig. 8.1 for coordinates definition. Specific parameters used for incidence conditions.

the case of 6D dynamics calculations, we represent the di-atomic molecule wave function, Φ^{6D}, as follows:

$$\Phi^{6D}(\mathbf{Q}, t) = \sum_{h=1}^{N_{xy}} \sum_{k=1}^{N_{zr}} \sum_{l=1}^{N_{\theta\phi}} c_{hkl}(t) \cdot \xi_h^{(xy)}(x, y; t)\, \xi_k^{(zr)}(z, r; t)\, \xi_l^{(\theta\phi)}(\theta, \phi; t) \tag{9.7}$$

being $\xi_i^{(j)}$ the ith-SPF for j DOF, and $c_{hkl}(t)$ the time dependent expansion coefficients. In the case of 5D dynamics calculations (rigid rotor model), we drop the r-dependence of $\xi_k^{(zr)}(z, r; t)$ functions. We have used the MCTDH implementation presented in the Heidelberg package [21, 22, 150, 153, 154].

In order to take full advantage of the efficiency of MCTDH equations of motion, the interaction potential used in the Hamiltonian has to be written as a sum of products of one(two)-dimensional functions (see Sec. 7.2). As our 6D-PES, V_{6D}, does not have this form, we have used the POTFIT [151, 152] algorithm to create a new approximate potential $V_{6D}^{approx} \approx V_{6D}$ that fulfills MCTDH requirements. See Sec. 7.2.2 for more details.

In Tabs. 9.4 and 9.5, we summarize the relevant parameters used in our MCTDH calculations.

POTFIT parameters	V_{6D}^{approx}	V_{5D}^{approx}
Natural potential basis		
$N_X \times N_Y$	Contr.	Contr.
$N_Z \times N_r$ or $N_Z{}^*$	50	17
$N_\theta \times N_\phi$	253	253
Relevant region of the fit		
Z-range(Å)	> 0.5	> 0.5
r-range (a_0)	[0.76, 4.0]	–
V (eV)	< 5	< 5
Accuracy		
N_{iter}	5	5
Δ_{rms}^{rw},Δ_{rms}^{w} (meV)	2.65, 27.72	0.04, 2.1
max (ϵ^r),max (ϵ) (meV)	346, 1870	1.3, 162

Table 9.5: Parameters used to represent the H_2/LiF(001) PES in a suitable form for the MCTDH equations of motion using the POTFIT algorithm. Δ_{rms}^{w} and Δ_{rms}^{rw} represent the root mean square error on all grid points and on relevant grid points, respectively. max(ϵ) and max(ϵ^r) represent the maximum error on all grid points and on relevant grid points, respectively.

Quasi-classical dynamics

To perform our qualitative dynamics analysis of diffraction of H_2 from LiF(0001) under FGI as a function of the initial ro-vibrational molecular state, we have taken a similar approach to that used in Ref. [23, 24] to study diffraction of thermal, or quasi-thermal, H_2 (and D_2) molecules from metal surfaces, and in Ref. [156] to study diffraction of fast H from LiF(001) under FGI. Thus, we have taken use of a classical binning method to mimic diffraction probabilities. Briefly, using a classical binning method, the intensity of a given peak, (n,m), can be evaluated as the fraction of classical trajectories in which the molecules scatter with a parallel momentum change contained in the Wigner-Seitz cell of the (n,m) reciprocal lattice point (see Fig. 7.2, and Sec. 7.1.4 for further details).

The choice of this method to perform our analysis is based on previous results [23, 24, 156] showing that the *classical diffraction probabilities* mimic fairly well relative intensities of experimental spectra at thermal (or quasi-thermal) and high impact energies. At this point, it is worth pointing out that the method is expected to work better for fast projectiles, for which the change of parallel momentum (ΔK), respect to the total momentum, leading to diffraction is much lower[†]. On the other hand, in the case of alloys (with two or more

[†]diffraction condition is given by $\Delta K = G$, G being a reciprocal lattice vector.

atoms presented on the surface) the relative intensities of the diffraction peaks are modulated by the geometrical structure factor (see eq. 8.3), which might not be properly described by the classical binning method. However, for the experimental conditions we are considering here, the explicit comparison between classical and quantum results for diffraction of H_2 molecules on their ro-vibrational ground state (J_i=0, v_i=0) suggests that the classical binning method yields reasonable results. Thus, for the sake of computational cost, we have used this classical method in Sec 9.5 to perform the required dynamics simulations as a function of the initial ro-vibrational state.

LOW NORMAL INCIDENCE: QUANTUM RESULTS

In order to test the accuracy of our DFT-based 6D-PES, we have performed quantum dynamics calculations within the MCTDH and the TDWP methods under SNI conditions (with normal energy, E_z =100 meV). Specifically, we have compared scattering probabilities as a function of the final diffraction state (Fig. 9.3, panels **A** and **B**) and the final rotational state (J_f, m_{J_f}) (Fig. 9.3, panels **C** and **D**) with the theoretical results published by Pijper and Kroes [222]. These theoretical results were obtained using quantum dynamics simulations within the TDWP method using a 5D model potential (rigid rotor assumption) in which a special care was put to include the quadrupole interaction of H_2 with the surface.

In panels **A** and **C**, H_2 molecules started with initial rotational state $J_i = 2$ and a statistical distribution of m_{J_i}. In panels **B** and **D**, H_2 molecules started with $J_i = 2$ and $m_{J_i} = 0$. We can see from Fig. 9.3, that our quantum dynamics results are in very good agreement with the theoretical results obtained by Pijper et al.. We reproduce the dramatic change in scattering probabilities when going from a initial statistical distribution of m_{J_i} to the case of all initial H_2 molecules having $m_{J_i} = 0$. It is of special interest the agreement in panel **D**, in which there is a high probability of inelastic m_J transition, from $m_{J_i} = 0$ to $m_{J_f} \neq 0$. This inelasticity could only be observed in Ref. [222] when the quadrupole interaction of H_2 with the surface was activated in the model potential, meaning that our 6D PES includes properly this coupling.

For the sake of completeness, we have included in Fig. 9.3 insets comparing 6D and 5D MCTDH dynamics results. In order to reduce the dimensionality of our PES, we have kept frozen the H_2 interatomic distance to its equilibrium value (r =0.749 Å). These insets show that there is not any special change in features going from a full-dimensional to a rigid rotor model at this normal energy regime. In fact, we take advantage of this 6D-5D agreement to safely reduce the computational cost of FGI calculations in Sec. 9.4 by reducing their dimensionality.

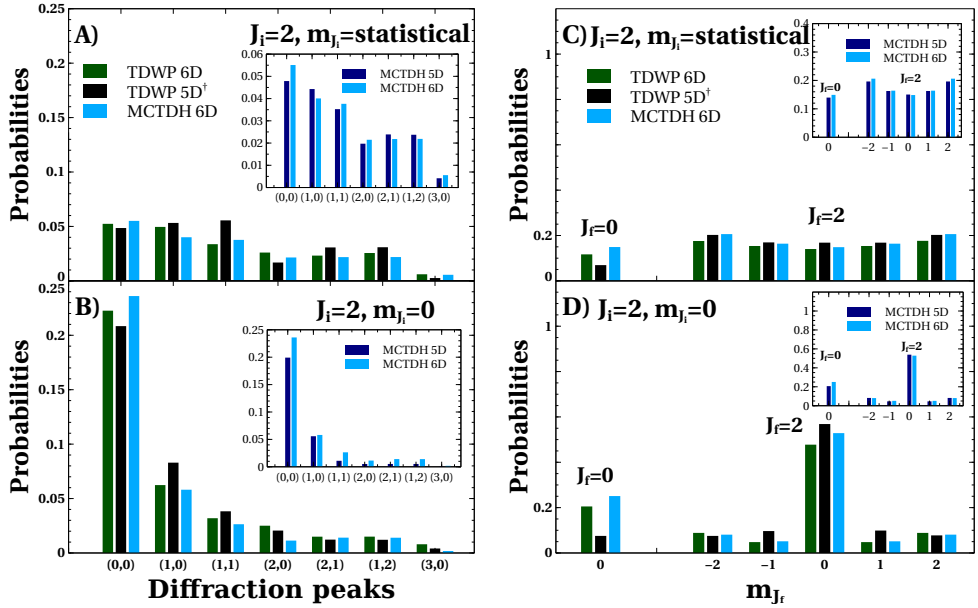

Figure 9.3: Scattering probabilities at low normal incidence conditions, with E_z =100 meV, as a function of the diffraction peaks (panels **A** and **B**) and as a function of the final rotational state (panels **C** and **D**). In panels **A** and **C**, H_2 projectiles started with an initial rotational state $J_i = 2$ and a statistical distribution of m_{J_i}. In panels **B** and **D**, H_2 projectiles started with an initial rotational state $J_i = 2$ and $m_{J_i} = 0$. Cyan, blue and green bars stand for 6D-MCTDH, 5D-MCTDH and 6D-TDWP calculations on our developed DFT-acpes. Black bars (†) are the theoretical results obtained by Pijper and Kroes [222] within the TDWP method on a 5D model potential.

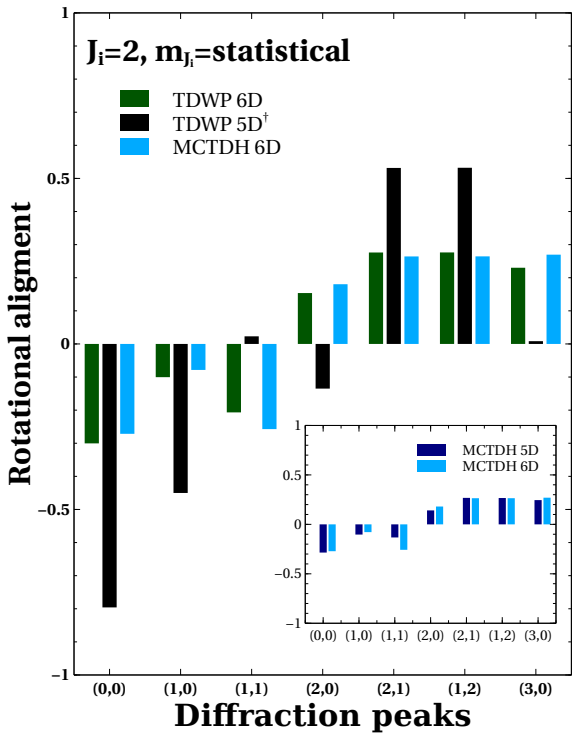

Figure 9.4: Rotational quadrupole alignment $A^2_{J_f=2}$ of the molecules scattered in a particular diffraction channel as a function of the diffraction channel for diffractionally and diffractionally (in)elastic scattering of initially statistical $J = 2$ H_2. Cyan, blue and green bars stand for 6D-MCTDH, 5D-MCTDH and 6D-TDWP calculations on our developed DFT-acpes. Black bars (†) are the theoretical results obtained by Pijper and Kroes [222] within the TDWP method on a 5D model potential.

In addition, we can conclude that differences between our 6D dynamics results and those obtained in Ref. [222] do not come from the dimensionality of the problem but from how the PESs were constructed.

FAST GRAZING INCIDENCE: QUANTUM RESULTS

A CLASSIC STUDY ON THE ROLE OF THE INITIAL RO-VIBRATIONAL STATE IN MOLECULE/SURFACE SCATTERING UNDER FAST GRAZING INCIDENCE

First of all, in order to test the validity of our classical dynamics method, we have performed some simulations at normal incidence and low incidence energy (E_i=100 meV), and we have compared our results with those obtained in Sec. 9.3 with the MCTDH method. At this point, it is worthy to point out that in order to ensure low statistical errors, we have run of the order of 10×10^{-5} trajectories for each classical simulation we discuss below. In Fig. 9.5 (a) we show the probabilities for classical and quantum rotationally (in)elastic scattering for the initial ro-vibrational state of the molecules (J_i=2,m_{J_i}=0). From this first comparison we can see that although classical calculations overestimate rotationally deexcitation and underestimate elastic scattering, they reproduce qualitatively the final distribution of the magnetic rotational quantum number, m_{J_f}. Furthermore, classical simulations yield a m_J change probability equal to 44 %, close to the 35 % found quantically. In Fig. 9.5 (b) we have compared quantum and classical results for diffraction peaks probabilities up to the 3^{rd} diffraction order, for H_2(J_i=2,m_{J_i}=0). Also in this case, the classical results reproduce qualitatively the quantum ones. Specifically, the relative intensities of the quantum diffraction peaks are qualitatively reproduced by our classical simulations. Therefore, from the qualitative agreement shown in Fig. 9.5, and taken into account that classical simulations are expected to work better at higher incidence energies as discussed in the introduction, we can conclude that our methodology is appropriate to perform the qualitative analysis we propose.

Although, we are proposing only a qualitative analysis, we take as references experimental results obtained by Rousseau et al. [105]. In Fig. 9.6 we show the simulated diffraction spectra for incidence along two crystallographic directions ⟨100⟩ and ⟨110⟩ (see Fig. \ref{System}). In both cases, the normal energy is equal to 300 meV. At this point we should remind that diffraction spectra (number of peaks and peaks intensity) under FGI only depend on the normal energy -they are independent of the total energy and incidence angle. A first remarkable feature that can be extracted from this figure is that classical simulations capture pretty well the complexity of the H_2/LiF(100) PES. Simulations performed along the crystallographic incidence direction

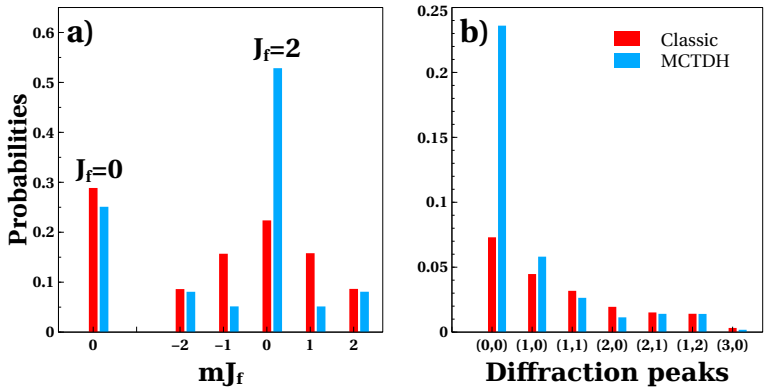

Figure 9.5: (**a**) Rotationally (in)elastic scattering probabilities for $H_2(J_i{=}2,m_{J_i}{=}0) \rightarrow H_2(J_f,m_{J_f})$. (*b*) Diffractionally (in)elastic scattering probabilities for $H_2(J_i{=}2,m_{J_f}{=}0) \rightarrow H_2(J_f{=}2,\sum m_{J_f},(n,m))$. Blue bars: quantum MCTDH results. Red bars: classical results.

$\langle 110 \rangle$ (Fig. 9.6 (b)) yield a higher number of diffraction peaks than along the $\langle 100 \rangle$ one, because the corrugation is much higher along the $\langle 110 \rangle$ direction than along the $\langle 100 \rangle$ one, this result is in agreement with experimental results (see insets Fig. 9.6). Also in agreement with experimental results, we have found a stronger modulation of the diffraction intensity along the crystallographic direction $\langle 110 \rangle$. In this direction, for example, the elastic peak is found to be less intense than the first and the second order ones; furthermore the second order peaks are the most intense ones. To understand this behavior we should remember that the amplitude of the diffraction peaks for polyatomic surfaces is modulated by the geometrical structure factor ($S_{\mathbf{G}}$), which is given by:

$$S_{\mathbf{G}} = f_{Li}(\mathbf{G})e^{i\mathbf{G}\mathbf{d}_{Li}} + f_F(\mathbf{G})e^{i\mathbf{G}\mathbf{d}_F} \,, \tag{9.8}$$

f_{Li} and f_F being the atomic form factors for Li and F ions, respectively. $\mathbf{d}_{Li}$ and $\mathbf{d}_F$ represent the atomic basis set vectors. The geometrical structure factor is equal to $f_{Li} + f_F$ if $n+m$ is an even number, and to $f_{Li} - f_F$ if $n+m$ is an odd number. Along $\langle 100 \rangle$ $n+m$ is always even, whereas along $\langle 110 \rangle$ $n+m$ is even and odd alternatively, which explains the stronger intensity modulation of diffraction peaks observed along this latter direction -for a more detailed discussion about the role of the $S_{\mathbf{G}}$ on diffraction from LiF(100) see Ref. [156] or Sec. 8.3.

A second remarkable feature that can be extracted from Fig. 9.6 is that the diffractive scattering patterns depend on the initial rovibrational state of the molecule. Overall, the agreement between theory and experiment seems to improve when higher rotational states are considered. Let us focus first on the crystallographic direction $\langle 100 \rangle$, from Fig. 9.6 (a) we can see that increasing the rotational quantum number, J, decreases the intensity of the second and third order peaks, which are not observed experimentally (see inset Fig. 9.6 (a)).

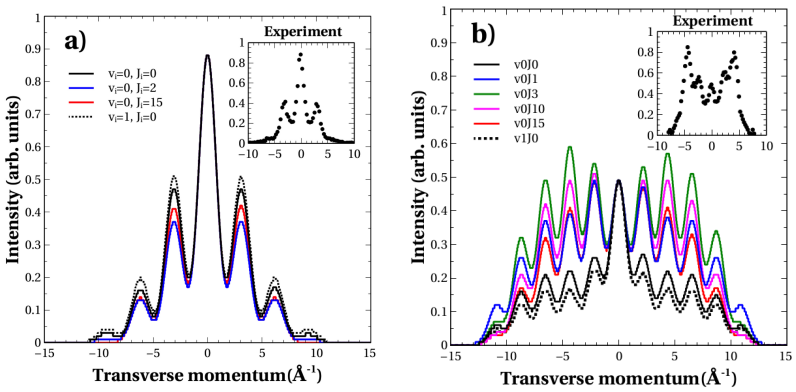

Figure 9.6: Diffraction spectra for H_2/LiF(001) simulated using classical dynamics, for several vibrational and rotational initial states. (**a**) Crystallographic direction $\langle 100 \rangle$, and (*b*) Crystallographic direction $\langle 110 \rangle$. Normal energy 300 meV. The insets show diffraction spectra recorded experimentally, data from Ref. [105].

In fact, for $J = 15$ the third order peaks disappear. Thus, from Fig. 9.6 (a), we can see that the relative intensity of the diffraction peaks depends on the initial J value, and that theoretical results get closer to the experimental ones when the initial J increases. If the initial vibrational state, v, increases the intensity of all the diffraction peaks increases. In this case no modulation respect to relative intensities obtained for $(v = 0, J = 0)$ is observed. In the case of the crystallographic direction $\langle 110 \rangle$ the situation is more complex. For the initial ro-vibrational states $(v = 0/1, J = 0)$ theoretical simulations do not show the intensity modulation measured experimentally (see Fig. 9.6 (b)). Contrary to experimental results, we have found that the specular peak is the more intense. However, when the initial J value increases, the intensity of the diffraction peaks increase with respect to the specular one. For $J = 3$, we recover the behavior observed experimentally, i.e., the second order peaks are the most intense ones. In Fig. 9.6 (b) we also show that the higher diffraction peaks obtained theoretically (but no measured experimentally) disappear for the highest initial J values. These results seem to indicate that an accurate comparison between experimental measurements and theoretical simulations will require some knowledge about the ro-vibrational distribution of the molecular experimental beam. Theoretical results should be weighted according to this initial ro-vibrational distribution. Thus, the probability of a given diffraction peak $I_{n,m}$ should be computed as:

$$I_{n,m} = \sum_{J,v} n(J,v) \cdot I_{n,m}(J,v) \; . \tag{9.9}$$

$n(J,v)$ being the population of the ro-vibrational state (J,v) in the initial molecular beam.

CONCLUSIONS AND SUMMARY

In Sec. 9.5, we have performed classical dynamics simulations, using an accurate DFT-based six-dimensional potential energy surface, to evaluate diffractive scattering of H_2 from LiF(100). We have used quantum dynamics results at normal incidence and low incidence energy (E_i), and experimental results at fast grazing incidence, to validate our methodology. Eventually, we have studied the role of the internal DOFs of the molecule in the diffraction process. We have shown that diffraction spectra may depend on the initial ro-vibrational state of the molecules, and therefore, an accurate comparison between theory and experiment will require some knowledge about the initial ro-vibrational distribution of the molecules beam. We hope that this study will stimulate experimental groups working on this topic to design and develop new experimental setups aiming to measure, or even to control, the initial ro-vibrational state distribution of the molecular projectiles.

10

THEORETICAL STUDY OF ROTATIONALLY INELASTIC DIFFRACTION OF H_2/D_2 FROM METHYL-TERMINATED SI(111)

Here, we present a theoretical study of the inelastic diffraction of H_2/D_2 from Methyl-Si(111) surface in comparison with the measurements carried out by Kevin J. Nihill *et al.* [231]. Contents of this chapter are based on:

- K.J. Nihill, Z.M. Hund, A.S. Muzas, C. Díaz, M. del Cueto, T. Frankcombe, D. Campi, F. Martín, N.S. Lewis and S.J. Sibener. (To be published)

MOTIVATION

We have investigated elastic and rotationally inelastic diffraction of H_2 and D_2 from methyl-terminated Si(111), a high-quality hybrid organic-semiconductor interface with great technological relevance. Improved interfacial electronic properties and surface passivation resulting from a complete (1x1) methyl termination of the underlying lattice make this interface an interesting candidate for applications such as photoelectrodes in electrochemical cells and biosensing electronics [86–91]. This interface has been thoroughly characterized by many experimental and theoretical techniques. The surface structure and extent of methyl termination have been surveyed by elastic helium atom scattering [232–234] and scanning tunneling microscopy [235, 236], and the vibrational dynamics were studied via high-resolution synchrotron photoelectron spectroscopy [237], high-resolution electron energy loss spectroscopy [238], transmission infrared spectroscopy [239, 240], and inelastic helium atom scattering with density functional perturbation theory [233, 234]. Despite the impressive array of studies conducted on this interface, no prior work has probed the anisotropic features of CH3-Si(111), which must be better understood to effectively model the dissociative chemisorption mechanism that controls surface chemical reactions; this is particularly interesting for this system, as functionalized Si surfaces may be used for photocatalysis [87] or attaching molecular catalysts [241].

The nature of gas interactions at solid surfaces has been thoroughly examined through characterizations of chemisorption for a variety of interfaces, providing a strong basis for understanding the processes involved in surface chemical reactions [58]. While a traditional route for understanding molecular chemisorption is monitoring the fraction of molecules that stick to a given surface [242], it has been the-

oretically demonstrated and experimentally proven that diffraction of molecules from a surface can provide complementary and precise information regarding the gas-surface interaction potential [38, 39]. Diffraction patterns of diatomic molecules in particular have highlighted the role of rotational DOFs in the chemisorption process, indicating a direct effect on dissociative probabilities [58, 243].

RID, whereby diatomic molecules impinging upon a surface convert translational energy into rotational energy (or vice versa) and are scattered into unique angular channels, was first reported in experiments involving diffraction of H_2 from MgO and LiF in the 1930s [76, 244, 245]. Since then, this technique has seen improvements through gains in angular resolution that have allowed a more precise investigation of the RID peaks [56, 59]. High angular resolution and a wide range of incident energies have enabled the widespread use of RID, with the goal of investigating the gas-surface potential for a variety of systems [56, 106, 245–247]. These studies have provided a wealth of information not only on the nature of interfacial dynamics, but also on the theory that has been developed to study them [76, 245].

The dependence of molecular orientation on diatomic diffraction processes makes theoretical modeling of the interaction a distinctly more complicated task than for mono-atomic systems such as He [248], because the rotational transitions that occur at the surface are highly sensitive not only to this anisotropic factor, but also to the corrugation of the surface and the coupling of these two factors [76]. However, a number of combined theoretical and experimental studies have already attempted to better understand the effect of parallel momentum transfer on elastic [24, 54, 249] and rotationally inelastic diffraction [106, 245]. State-of-the-art theoretical models have shown some limitations, for example, in accurately reproducing the intensities of rotationally inelastic diffraction peaks relative to their elastic counterparts. However, they have proven very useful in reproducing general trends [38, 190, 250] which are the result of the main features characterizing the underlying PESs, such as the corrugation and the anisotropy.

In this work, we present a theoretical study of the $H_2(D_2)$/Methyl-Si(111) system, to provide a better understanding of the first RID measures on this organic-functionalized semiconductor [231]. In contrast to the various metal and alloy surfaces that have been characterized via RID, CH_3-Si(111) represents a unique class of organic-functionalized semiconductors and soft-film surfaces that have never before been experimented on in this way. High-resolution RID of H_2 and D_2 has been employed to study the anisotropy of the CH_3-Si(111) surface via comparison with quantum dynamics simulations. The low-energy molecular diffraction measurements performed by Nihill *et al.* are completely surface-sensitive, revealing information on the structure and interfacial properties of the surface and its interactions

with impinging molecules. This low incidence energy permits a valid use of the rigid rotor assumption when considered useful, but energetically forbids vibrational excitations [248]. Rotationally inelastic diffraction spectra for H_2 and D_2 are compared, showing much greater rotational excitation probabilities for D_2. Measurements of experimental RID excitations relative to elastic scattering events are examined as a function of incident angle and beam energy. The precisions of these rotational probabilities are improved by employing the Debye-Waller model to account for the attenuation of diffraction peak intensities as a function of increasing surface temperature. Experimentally measured RID probabilities indicate a greater likelihood of rotational excitation for higher beam energies, but show no apparent dependence on incidence angle. The PES of the $H_2(D_2)/CH_3$-Si(111) system has been modeled by interpolation of a DFT energies data set, and used to study rotationally inelastic scattering and to simulate RID probabilities by means of quasi-classical and quantum dynamics. Quantum dynamics simulations have been used to assess the accuracy of the PES through a direct comparison with experimental results, whereas quasi-classical trajectories have been used to track down the regions of the PES responsible for the rotational excitation. These classical turning points show both large corrugation and high anisotropy, as revealed by a close scrutiny of the polar angular dependence of the PES on these regions.

THEORY

Theoretical model

To perform the theoretical analysis of $H_2(D_2)/CH_3$-Si(111), we have worked within the BOSS approximation. The BOA is justified by the different time scales associated with the motion of nuclei and electrons. The static surface approximation is justified by the mass mismatch between the surface-terminating CH_3 layer and the H_2 and D_2 projectiles; although low recoil effects could be expected. Furthermore, experimental results have been extrapolated to a surface temperature of 0 K via the Debye-Waller correction, which allows a direct comparison between experimental measurements and static surface theoretical results. Working within this framework, a six-dimensional (6D) PES is first computed, and then is included in the nuclear Hamiltonian to perform dynamics simulations.

Electronic structure calculations

The 6D PES, whose DOFs are illustrated in Fig. 10.1, has been computed by interpolation of a DFT energy data set. To perform the DFT periodic calculations, the plane-wave-based code VASP [130, 176]

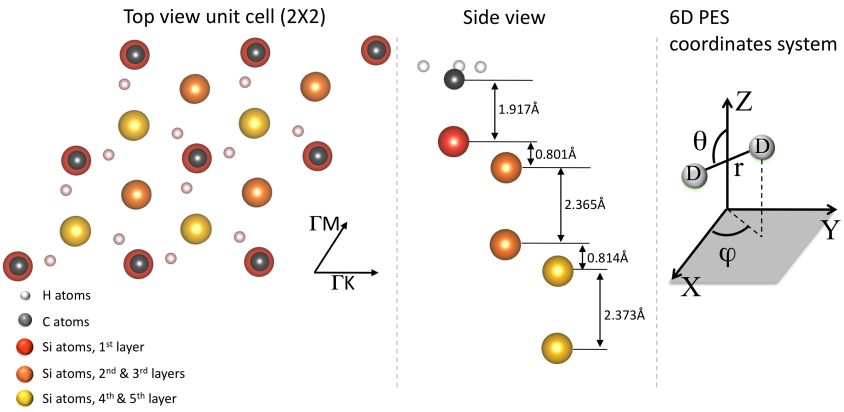

Figure 10.1: Structure of the Methyl-Si(111) surface (left and middle panels) and coordinate system used in the 6D-PES (right panel).

has been used. In these calculations, the exchange-correlation energy of the electrons has been described using the GGA. In applying the GGA the Perdew-Burke-Ernzerhof (PBE) functional [125] has been used. Additionally, the ion cores have been described using the PAW method [127]. The $H_2(D_2)/CH_3$-Si(111) system has been modeled using a five-layer slab and a 2×2 hexagonal surface unit cell, as shown in Fig. 10.1. The size of the unit cell has been chosen to avoid interaction between images molecules in adjacent cells, which are present in the calculations due to the use of periodic boundary conditions (PBC). To avoid artifacts caused by the use of PBC, a vacuum layer of 21 Å has been set in the z direction. A $7 \times 7 \times 1$ Monkhorst-Pack grid of k-points was used to sample the Brillouin zone [251]. The cutoff energy for the plane-wave basis has been set to 650 eV. The lattice bulk parameter has been optimized, finding a value of a =5.48 Å, which is rather close the known experimental value (5.431 Å) [252]. The surface interlayer distances have also been relaxed until the forces were below a 1 meV $Å^{-1}$ threshold.

Modified Shepard interpolation method

To build the continuous 6D PES, $V_{6D}(x, y, z, r, \theta, \phi)$, representing the ground electronic state structure of the $H_2(D_2)$-CH_3/Si(111) system, we have made use of the MS interpolation method, originally developed by Collins *et al.* [137, 144], to study gas-phase reactions, and later on adapted to study reactive scattering of molecules from surfaces [140–142, 253]. Here we have used a recent implementation of the MS method [17], which includes strict plane group symmetry and translational periodicity. In the MS method the interpolated PES is described by a weighted series of Taylor expansions centered on a number of DFT energy data points. These data points are sampled

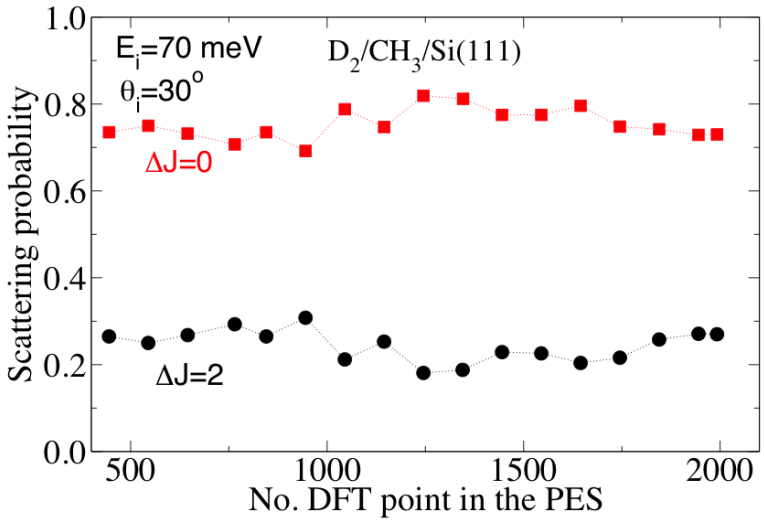

Figure 10.2: Elastic and inelastic scattering probabilities as a function of the number of DFT points added to the PES data set.

throughout the configuration space of the system. Details about this interpolation method was already presented in Sec. 6.3.

It is important to note that the MS method uses a non-homogeneous sampling of the configuration space, so that more DFT energy points are used in the relevant dynamical regions. These regions are selected by using classical dynamics through a feedback process, hereafter called the GROW process (see 6.3.2). The first step begins with an initial basic version of the PES, defined in this case by only 50 DFT energy points. Then a small batch of classical trajectories is run on this basic PES, and from these trajectories new geometries are selected and added to the PES, thereby augmenting it. The new geometries are chosen according to two different criteria [254], either new energy data points are added in the region most frequently visited by the trajectories or they are added in regions suspect to be the most inaccurate ones. Periodically, a larger batch of trajectories is run and used to compute some observables, which in this case are the rotational excitation probabilities. If the probabilities change significantly with the number of DFT data points added to the PES, the procedure goes back to the second step of running a small batch of trajectories. If the probabilities do not change significantly, the PES is considered converged, as illustrated in Fig. 10.2. At this point, it should be pointed out that in order to properly sample the dynamical regions relevant to this analysis, the incidence conditions of the classical trajectories are selected according to the experimental conditions.

Quasi-classical dynamics

Quasi-classical dynamics – i.e., classical dynamics including the zero point energy of the molecule – have been used to both grow and scrutinize the PES. To compute quasi-classical trajectories, the classical equations of motion are solved using the velocity-Verlet algorithm [255]. For each initial energy (E_i) and incidence angle (θ_i), the classical scattering probability is calculated as an average over the molecular initial conditions, i.e., over the internal coordinates and conjugated momenta. The molecular initial conditions are sampled using a Monte Carlo method. To ensure low statistical errors, approximately 2.5×10^4 trajectories are computed for each set of initial conditions (E_i,θ_i). In these calculations a molecule is considered reflected (and the integration ends) whenever the final distance between the molecule and the surface, z_f, becomes equal to initial distance, z_i, with the molecule velocity vector pointing towards the vacuum. To analyze rotational excitation upon scattering using classical dynamics, it must be taken into account that the classical angular momentum (L) follows a continuous distribution. Therefore, to analyze rotational excitations, the continuous representation is transformed into a discrete one [256, 257] (see Sec. 7.1). This transformation is performed, in general, by evaluating the closest integer that satisfies Eq. 7.8. However, quantum selection rules for homonuclear diatomic molecules only allow transitions $\Delta j = \pm 2$. Therefore, to obtain D_2 rotational excitation probabilities, we evaluate the closest even or odd integers that satisfy Eq. 7.8, depending on the initial rotational state of the molecule.

Quantum dynamics

To compute diffraction probabilities, we have solved the TDS equation of the nuclear Hamiltonian using the MCTDH method [21, 150, 258, 259], which has been already successfully used to study diffraction of atomic projectiles [185], as well as reactive scattering of molecular projectiles [55, 182, 184].

In the MCTDH method, the nuclear wave function is written as a sum of product of SPFs. In our particular case, each SPF (χ) combines up to two DOFs, thus we can write the nuclear function of our system as:

$$\Psi(x,y,z,\theta,\phi,t) = \sum_{h=1}^{N_{xy}} \sum_{k=1}^{N_z} \sum_{l=1}^{N_{\theta\phi}} c_{hkl}(t) \cdot \chi_h^{(x,y)}(x,y,t)\, \chi_k^{(z)}(z,t)\, \chi_l^{(\theta,\phi)}(\theta,\phi,t) \ , \tag{10.1}$$

where $(N_{xy}, N_z, N_{\theta\phi})$ are the number of SPFs used to describe each nuclear mode*. All the details regarding the MCTDH method were

*Within the MCTDH method, a mode means an aggregation of DOFs. In our case, there are 3 modes: Q_1 is (x,y), Q_2 is (z) and Q_3 is (θ,ϕ)

Initial wave packet	
Width Δz_0 (Å)	0.9
Position z_0 (Å)	14.74
Momentum k_{z_0} (au)	[4.96, 6.61]
Grid parameter	
Type x,y	FFT DVR
x, y-range (Å)	[0.0, 7.75]
N_{xy}	65
Type z	FFT DVR
z-range (Å)	[−2.66, 15.33]
N_z	200
Type θ, ϕ	Legendre DVR
$N_{\theta\phi}$	20×17
SPF *basis*	
x, y	65
z	17
θ, ϕ	17
Complex absorbing potential	
z-range (Å)	[5.62, 15.33]
Stength (au)	6×10^{-4}

Table 10.1: Parameters used in the 5D($x, y, z, \theta\phi$) MCTDH calculations.

already exposed in Sec. 7.2. At this point, it should be noticed that in order to reduce the computational effort, and taken advantage of the lack of reactivity of $D_2/CH_3/Si(111)$ at the energy range considered here, we have performed five-dimensional calculations, in which the distance atom-atom has been kept frozen at the equilibrium D_2 gas-phase distance (parameters used in the calculations are listed in Tab. 10.1). To obtain elastic and inelastic diffraction probabilities, at the end of the propagation time, we have performed a flux analysis with the aid of a complex absorbing potential located in the non-interaction Z region [260].

Finally, it should be noticed that to take full advantage from the MCTDH formalism, our multidimensional non-separable PES has to be rewritten as a linear combination of products of one-dimensional (1D) or two-dimensional (2D) functions . This transformation can be performed using the POTFIT algorithm (see Sec. 7.2.2), which is based on the approximation theorem of Schmidt [151], provided with the Heidelberg MCTDH package. These 1-2D functions are the ones used to expand the SPFs during dynamics calculations. In table

Natural potential basis	
N_z	20
N_{xy}	*Contr.*
$N_{\theta\phi}$	20
Relevant region of the fit	
z (Å)	> -0.66
V (eV)	< 3
r (Å)	0.767
V_{max} (eV)	20
POTFIT accuracy	
N_{iter}	3
Δ^{rw}_{rms}, Δ^{w}_{rms} (meV)	3.1, 4.1
$\max(\epsilon^r)$, $\max(\epsilon)$ (meV)	150, 226

Table 10.2: Parameter used to represent the PES in a suitable form for the MCTDH equations of motion using POTFIT. Δ^{rw}_{rms},Δ^{w}_{rms} represent the root mean square error on relevant grid points and on all grid points, respectively. $\max(\epsilon^r)$, $\max(\epsilon)$ represent the maximum error on relevant grid points and on all grid points, respectively.

10.2 we present a compendium of parameters used in the POTFIT representation of our 5D-PES.

RESULTS AND DISCUSSION

H_2 and D_2 Diffraction from CH_3-Si(111)

Unlike with atomic diffraction, when a H_2 or D_2 molecule scatters from a surface, it is capable of exchanging energy between its internal rotational and translational DOFs. Thus, we can classify all possible final states of these molecules after scattering by the diffraction quantum numbers (h,k) and the internal energy loss/gain they can experiment, ΔE_{rot}. Only those final states that satisfy the following equation:

$$\boldsymbol{G}_{hk}^2 + 2\boldsymbol{k}_i^{\parallel} \cdot \boldsymbol{G}_{hk} < 2M\left(E_i^{\perp} - \Delta E_{rot}\right) , \tag{10.2}$$

are allowed, where M is the mass of H_2 or D_2, ΔE_{rot} is the energy exchanged between rotational and translational modes*, $\mathbf{G}_{hk}$ is the reciprocal lattice vector (h,k), $\boldsymbol{k}_i^{\parallel}$ is the initial parallel momentum of the projectile, and $E_i^{\perp}$ is the initial perpendicular energy of the surface. Note that symmetry constraints within the hydrogen molecule

*which equals the difference between the molecule's rotational energy levels as determined by the rigid rotor model

impose a rotational selection rule of $\Delta J = \pm 2$. This phenomenon of internal energy exchange (when $\Delta E_{rot} \neq 0$) results in RID peaks scattered at distinct angles from their parent elastic diffraction peaks ($\Delta E_{rot} = 0$), such that:

$$\theta_f^{RID} = \arcsin\left[\frac{\left|\mathbf{k}_i^{\parallel}\right| - |\mathbf{G}_{hk}|}{\left(\mathbf{k}_i^2 - 2m\Delta E_{rot}\right)^{1/2}}\right], \tag{10.3}$$

$\mathbf{k}_i$ being the initial momentum of the projectile.

Experimental results for H_2 scattering from CH_3-Si(111) along <$\bar{1}2\bar{1}$> (Γ-M) and <$01\bar{1}$> (Γ-K) directions performed by Nihill *et al.* [231] show that RID peaks have a poor signal resolution in diffraction spectra and can only be resolved when using time of flight measurements, whereas D_2 RID peaks can be easily studied directly from diffraction spectra as a function of the initial energy and incidence angle. The poor signal and resolution of the H_2 $j = 0 \rightarrow 2$ RID peak is due in part to a poor population of the initial $j = 0$ rotational state. The spin states of the identical H_2 nuclei combine to form either ortho- (symmetric) or para- (antisymmetric) spin isomers. To maintain the antisymmetry of the total molecular wave function, the isomeric designation of a given molecule is paired with a given set of rotational states: odd ($j = 1, 2, 3, \ldots$) for ortho-H2, and even ($j = 0, 2, \ldots$) for para-H_2. The nuclear spin-state degeneracies of H_2 results in a para:ortho population of 1:3 for n-H_2 (normal Hydrogen). Therefore only ~25% of the n-H_2 beam contains H_2 molecules in the $j = 0$ rotational state. For D_2, the total molecular wave function is symmetric, leading to opposite spin isomer-rotational state pairing. The resulting degeneracies create a ~66% population of the $j = 0$ rotational state. Additionally, switching from a H_2 to D_2 beam halves the energy required to transition between rotational states (D_2: $j = 0 \rightarrow 2$, 22.7 meV), thereby increasing the probability of this rotational transition.

Since the principal interest of this work concerns the probability of rotational excitations, well-resolved elastic and inelastic diffraction peaks are required. Thus, we compare our theoretical results only with those obtained experimentally for D_2 RID peaks. As the setup of the experimental instrument does not allow for direct measurements of the pure beam flux, experimental data of RID peaks are provided as probability ratios of inelastic over elastic diffraction intensities [106]. Specifically, to relate a RID peak to its parent elastic peak, the following expression is used:

$$r\left(j_i, j_f, h, k\right) = \frac{I\left(j_i, j_f, h, k\right)}{I\left(h, k\right) \cdot n\left(j_i\right)} \cdot \sqrt{\frac{E_i + \Delta E_{rot}}{E_i}} e^{2W_{j_i, j_f, h, k} - W_{hk}}. \tag{10.4}$$

where $I\left(j_i, j_f, h, k\right)$ and $I\left(h, k\right)$ are the peak-area integrated intensities of D_2 molecules scattered from a crystal of finite surface temperature T_s, $W_{j_i, j_f, h, k}$ and W_{hk} are the Debye-Waller factors for $\left(j_i, j_f, h, k\right)$ and

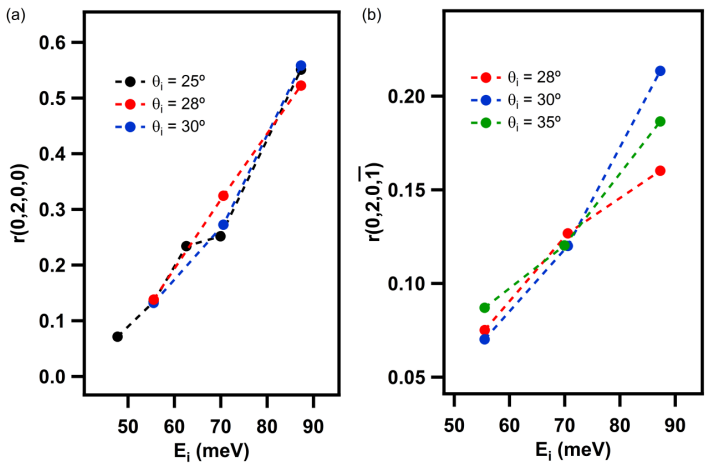

Figure 10.3: Rotational probabilities for the $j = 0 \rightarrow 2$ transition as a function of beam energy and incidence angle for (a) specular and (b) first-order diffraction peaks, as calculated according to equation 10.4.

$(0, 0, h, k)$ peaks, respectively. The square root term corrects for the inverse proportionality of the electron impact ionization efficiency on the velocity of scattered molecules [106]. Additionally, the rotational distributions of the impinging molecules are accounted for with $n(j_i)$. By using these ratios rather than pure probabilities, the effects of surface defects and beam geometry are eliminated and experimental error associated with evaluation of the Debye-Waller factor, $W(T_s)$, is diminished.

In Fig. 10.3, we have plotted the experimental results for $r(0, 2, 0, 0)$ and $r(0, 2, 0, \bar{1})$ ratios as a function of the beam energy. There is an overall increase in rotational excitation probability with increasing beam energy, regardless of whether the rotational excitation arises from the specular or first-order peak. This trend agrees with expectations: the increased energy of an incident molecular beam allows for further penetration into the surface charge density, thereby causing the molecule to experience a more effective corrugation; the increased energy that results from embedding a particle deeper into the PES will impart more torque onto the non-spherical molecule, thus allowing it to achieve a higher rotational state. The relationship between θ_i and the rotational probabilities is not as straightforward. For $r(0, 2, 0, \bar{1})$, a more normal incidence angle entails a slightly higher degree of rotational excitation, whereas no trend can be inferred from the $r(0, 2, 0, 0)$ data.

Theoretical analysis

Quantum and classical dynamics simulations have been carried out with the goal of more accurately interpreting experimental measure-

T_0 (K)	E_B (meV)	T_r (K)	$j=0$	$j=1$	$j=2$
158	47.7	45.0	0.807	0.179	0.013
184	55.5	46.7	0.795	0.189	0.016
208	62.6	57.5	0.718	0.241	0.041
234	70.6	64.9	0.669	0.267	0.063
289	87.3	68.2	0.649	0.276	0.074

Table 10.3: D_2 beam parameters, rotational temperatures, and corresponding rotational populations.

ments. First of all, to assess the accuracy of our theoretical tools and, in particular, of our interpolated PES, we have compared quantum dynamics simulations and experimental measurements obtained at several representative sets of initial conditions (see Fig. 10.4). To perform this comparison, in our quantum simulations, we have taken into account the initial rotational distribution of the molecular beam (see Tab. 10.3). Overall, we obtain a rather good agreement between both sets of data, in particular, our theoretical spectra show, in agreement with the experimental ones, an enhance of the rotational excitation when the incidence energy increases. These results, allow us to conclude that our PES is accurate enough to perform the required analysis. In Fig. 10.5, we compare quantum ratios $r(0,2,0,0)$ and $r(0,2,0,1)$ with the experimental ones. From this Figure we can see that theoretical results reproduce qualitatively experimental results, i.e., the rotational excitation of the specular $(0,0)$ and first order $(0,1)$ peaks increases with the energy beam. It is also worthy to point out that the agreement between theory and experiment is better for the diffraction peak $[r(0,2,0,-1)]$ than for the specular one $[r(0,2,0,0)]$. A similar phenomenon, the increased sensibility of the specular peak on the accuracy of the PES, has been already observed before, for example, in D_2/NiAl(110) [245].

Once established the accuracy of the PES, we can make a deeply analysis of the most relevant regions, the ones that determine the characteristic of the diffraction spectra. To do so, we have taken used of quasi-classical dynamics. First, in order to establish the validity of the classical analysis, we have compared quantum and classical total rotational excitation probabilities. In Fig. 10.6, we show the rotational excitation probabilities for H_2 (only classical results) and D_2 (quantum and classical results) as a function of the beam energy, along the Γ-M direction (see Fig. 10.1), for three different incidence angles. Several remarkable features are evident in this figure: (a) in the case of H_2, rotational excitation stays below 5% over the entire energy range investigated; (b) for D_2, quantum and classical simulations

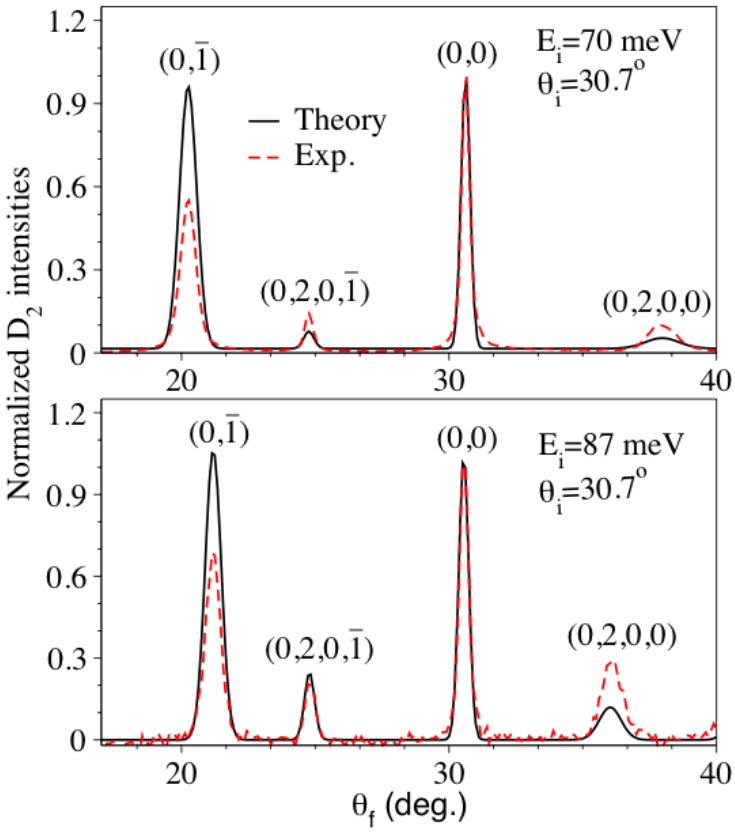

Figure 10.4: Comparison of theoretical (dashed red lines) and experimental (full black lines) D_2 diffraction spectra from Methyl-Si(111) surface along Γ-M direction. Upper panel: initial incidence energy E_i =70 meV, and initial incidence angle θ_i =30.7° . Bottom panel: initial incidence energy E_i =87 meV, and initial incidence angle θ_i =30.7°.

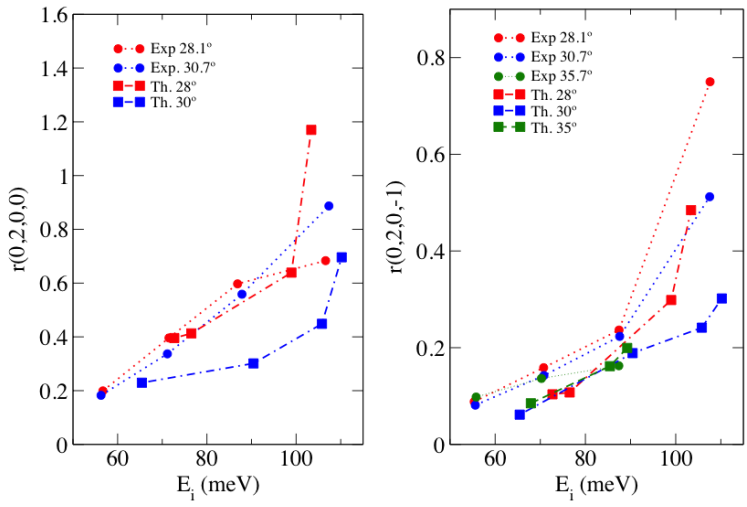

Figure 10.5: Comparison of theoretical (dashed lines) and experimental (dotted lines) values of diffraction ratios $r(0,2,0,0)$ (left panel) and $r(0,2,0,\bar{1})$ as a function of the incidence energy E_i. Red lines: incidence angle $\theta_i \approx 28°$. Blue lines: $\theta_i \approx 30°$. Green lines: incidence angle $\theta_i \approx 35°$.

yield rather similar results, the classical rotational excitation fluctuates around 20-25%, and the quantum ones around 30-35%. These results agree with the experimental results reported above, which show the presence of large RID in the diffraction spectra of D_2, whereas no RID has been observed for H_2 in diffraction spectra. This qualitative agreement between classical and quantum rotational excitation probabilities justifies further analysis of the systems using classical trajectories calculations.

Classical trajectories have revealed that most of the molecules are scattered at a classical turning point around 2.0 Å, with a molecular bond length around 0.78 Å. Given that these values are almost independent of the θ_i and E_i within the range of experimental incidence conditions, the characteristics of the potential have been analyzed at these (z, r) values. Fig. 10.7 illustrates the one-dimensional (1D) potential energy profile along both the (Γ-M) and (Γ-K) azimuthal directions. One important feature of the PES that can be observed in Fig. 10.7 is that the presence of H atoms (from the CH_3 group) is nearly overshadowed by the C atoms, as the only indication of H atoms is the small shoulder seen between the hill and the valley. Another interesting feature that can be extracted is that the projectiles are efficiently driven towards the hollow and bridge sites. It is clear that molecules with incidence energies below 90 meV cannot approach the top site or surrounding sites, and therefore most of the molecules are scattered from the hollow and bridge sites. This behavior is also corroborated by the analysis of the classical trajectories, as shown in Fig. 10.8, where we display the classical turning point distribution (x, y) of

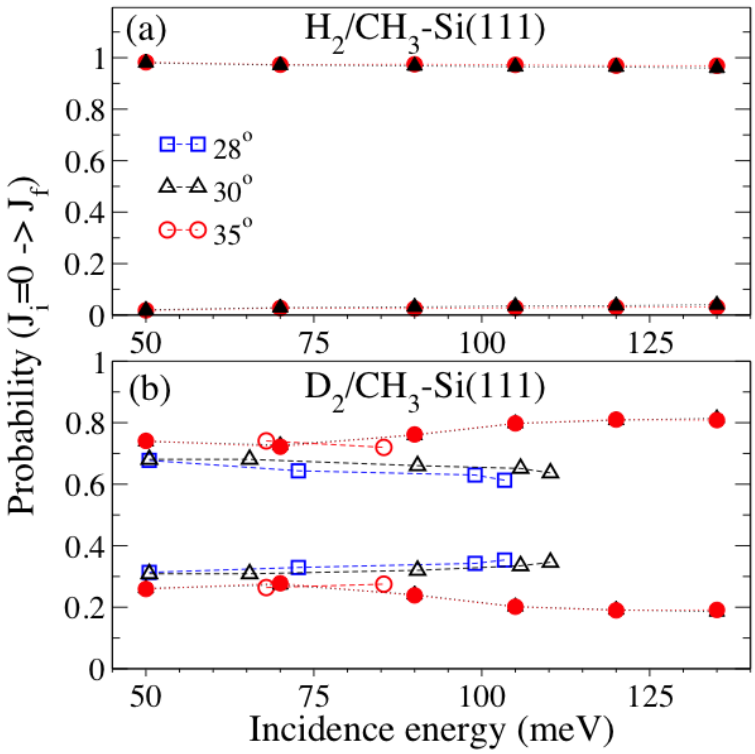

Figure 10.6: Theoretical rotational excitation probabilities $J_i = 0 \rightarrow J_f = 2$ of H_2 (upper panel) and D_2 (bottom panel) scattered on Methyl-Si(111) as a function of the incidence energy. Lines with full symbols: quasi-classical dynamics results. Lines with empty symbols: quantum dynamics results.

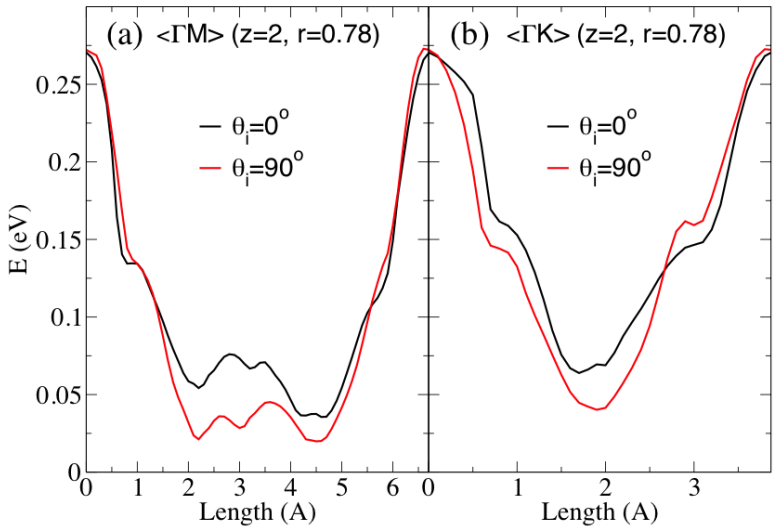

Figure 10.7: 1D PESs along the high-symmetry directions Γ-K and Γ-M with z =2 Å and r = 0.78 Å. (cf. Fig. 10.1)

the scattered molecules, most of the molecules are scattered far from the top site. Results displayed in Fig. 10.8 indicate that the molecules are efficiently steered towards the hollow and bridge sites.

Finally, Fig. 10.7 has also revealed the anisotropy of the potential in classical turning point regions. To more closely observe the potential anisotropy in the most dynamically important regions, Fig. 10.9 displays the relative potential energy as a function of the molecular polar angle, θ_i, at several z-distances from the surface. The anisotropy of the potential is observed to increase rapidly when the molecule approaches the surface, except in the case of the top site, from which molecules do not scatter, as discussed above. This swift increase in the corrugation around the classical turning points is responsible for the substantial rotational excitation found in this system. It is noted that insubstantial differences are obtained for the trajectories followed by H_2 and D_2 molecules, when similar incidence molecular velocities are considered. It can thus be concluded that the anisotropy felt by both isotopes is similar, and therefore that the different rotational excitation observed is due to the differences in rotational level spacing (~45 meV for H_2, ~22 meV for D_2).

Further insight into the nature of the PES can be extracted from Fig. 10.10, which displays a series of 2D xy-cuts for several (θ, ϕ) orientations. In these plots, z and r values have been chosen according to the average values at the classical turning points revealed by a classical trajectory analysis, as discussed above. This Figure evidences the large corrugation of the PES, and shows that the molecular projectile is able to vaguely feel the presence of the H atoms from the CH_3 groups.

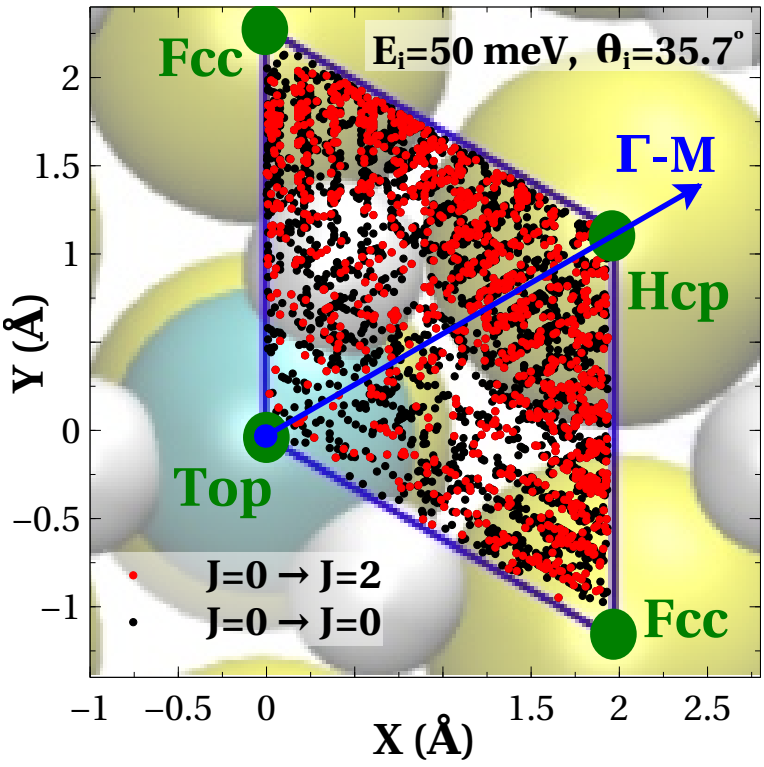

Figure 10.8: Projection of classical turning points on the irreducible Wigner-Seitz of the CH_3-Si(111) surface. Black dots: turning points of trajectories that were elastically scattered ($j = 0 \rightarrow 0$) from the surface. Red dots: turning points of trajectories that were inelastically scattered ($j = 0 \rightarrow 2$) from the surface.

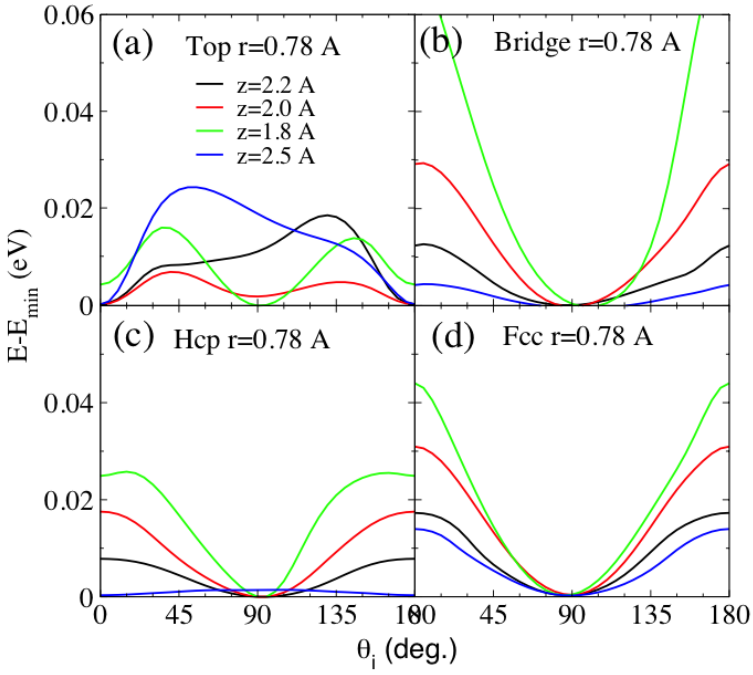

Figure 10.9: Relative 1D PESs as a function of θ_i for four high-symmetry sites at several z values (r =0.78 Å).

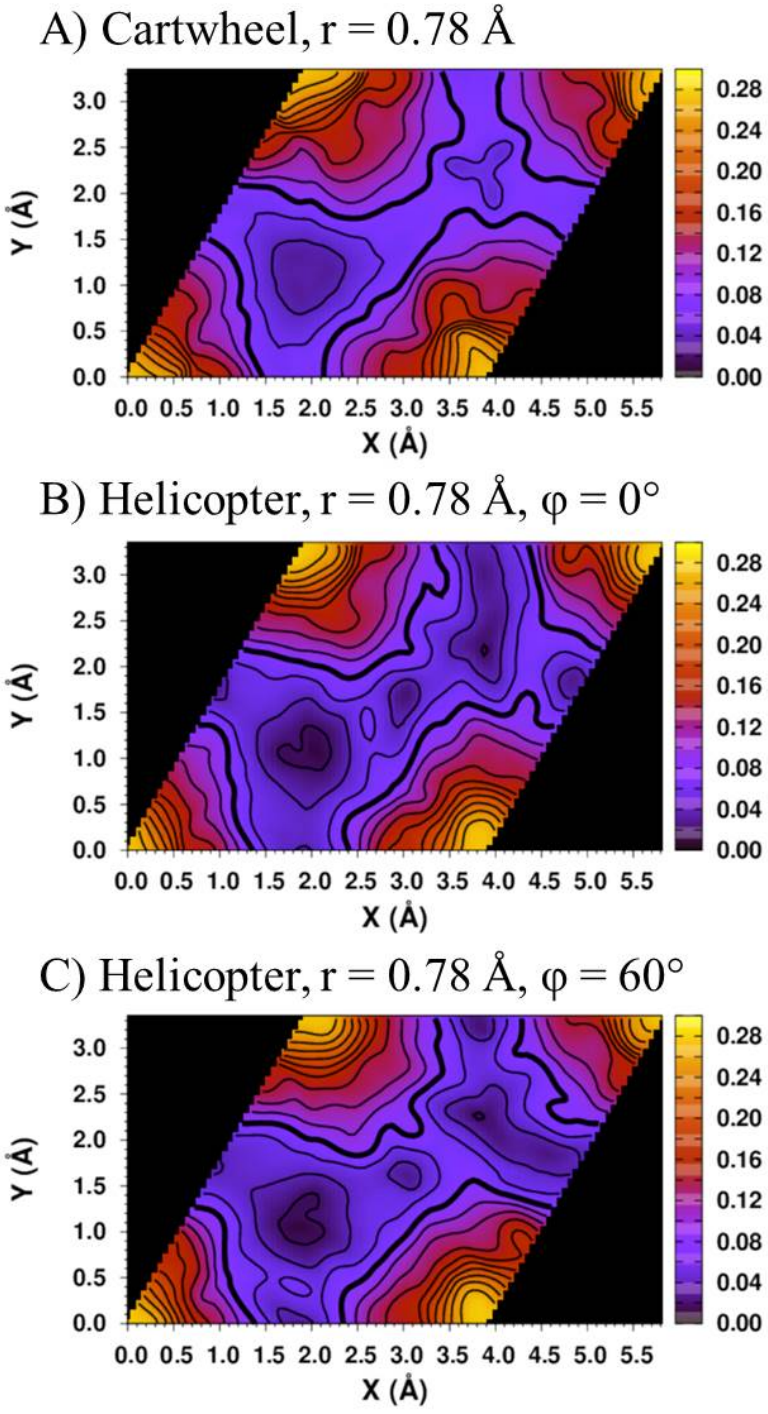

Figure 10.10: 2D x, y-cuts of the PES with z =2 Å. Bold line corresponds to 0.08 eV, and the spacing between the contour levels is 0.02 eV.

CONCLUSIONS AND SUMMARY

The diffraction of H_2 and D_2 molecular beams from CH_3-Si(111) was used to further the understanding of how organic termination of a semiconductor affects the surface dynamics. While the diffraction of H_2 resulted in rotational transitions, as confirmed with time-of-flight measurements, the resolution of these RID peaks was low. The large population of the rotational $J = 0$ ground state and small energy gap between rotational states for D_2 resulted in high-intensity rotationally inelastic diffraction peaks. The probabilities of these rotational transitions were examined over a range of beam energies and scattering angles. The Debye-Waller model was applied to the diffraction peak intensities to correct for thermal attenuation caused by the incoherent motion of CH_3-Si(111) surface atoms at non-zero temperatures. In order to understand these experimental results, the electronic structure of the system has been modeled by means of DFT. A continuous PES for $H_2(D_2)/CH_3$-Si(111) has been constructed by interpolation of DFT energies, and then used to carry out quantum and classical dynamics simulations. The theoretical data from classical simulations show some general agreement with experimental data. Both experimental and theoretical data show high rotational excitation probabilities, which are almost independent of the incidence angle, for the angle range investigated here. Additionally, classical dynamics have identified the classical turning point regions (2 Å over hollow and bridge sites), and a close scrutiny of these regions reveals a large anisotropy, which increases swiftly when the molecule approaches these regions. This characteristic of the PES seems to be responsible for the large rotational excitation found experimentally. Overall, this work has provided new data on a model hybrid organic-semiconductor system, from which the principles governing the gas-surface interaction potential have been elucidated.

Part IV

CONCLUSIONS

Here, we collate all the conclusions obtained in part iii in an orderly way. This part is written in Spanish.

CONCLUSIONES FINALES

En esta tesis, hemos estudiado tres sistemas gas-superficie diferentes, a saber, H(D)/LiF(001), $H_2(D_2)$/LiF(001) y $H_2(D_2)$/Methyl-Si(111). En el primero, hemos simulado sólo procesos GIFAD; en el segundo, hemos simulado tanto condiciones GIFMD como condiciones de incidencia normal para energías térmicas; en el tercero, hemos simulado las condiciones típicas para un experimento de haces moleculares a baja energía a incidencia fuera de la normal. En todos nuestros estudios hemos utilizado cálculos de dinámica clásicos y cuánticos con diferentes objetivos. A continuación exponemos las conclusiones obtenidas.

En la sección 8.3, propusimos estudiar cualitativamente la modulación de los picos de difracción en el sistema H(D)/LiF(001) bajo condiciones de incidencia rasante. En esa sección, mostramos que el método de evaluación de probabilidades de difracción clásicas (classical binning method, CBM) obtiene las tendencias experimentales correctas. De hecho, la comparación de las alturas relativas de dichos picos de difracción con los experimentos de las referencias [107] y [105] son bastante buenos. A la vista de los resultados, hemos aventurado un estudio sistemático para H y D variando la energía de incidencia normal a la superficie. En los espectros de difracción obtenidos, se pueden hallar diferencias entre las direcciones $\langle 100 \rangle$ y $\langle 110 \rangle$ en consonancia con las observaciones experimentales. Esto es una muestra de que el CBM puede, hasta cierto límite, reproducir los efectos en los difractogramas derivados del llamado del factor de forma. Es también destacable que, pese a que en estas condiciones de incidencia un estudio puramente clásico predeciría el mismo patrón de dispersión para H que para D (ver apéndice E), el CBM produce espectros de difracción que presentan un claro efecto isotópico. Esto es debido a que la discretización del espacio recíproco asociado depende de la masa del proyectil simulado.

En la sección 8.4, hemos realizado cálculos cuánticos con el método MCTDH con el objetivo de estudiar diferentes posibilidades de analizar experimentos GIFAD con el menor coste computacional posible. Hemos mostrado que para el sistema test H/LiF(001), podemos alcanzar los resultados obtenidos en incidencia rasante para ángulos de incidencia $\theta_i \approx 5°$, ángulos más grandes que los típicamente utilizados en los experimentos. Esto es, hemos mostrado que para una misma energía de incidencia normal, se pueden obtener los mismos resultados que en el experimento tomando una energía total menor. Hemos también mostrado que la difracción en incidencia normal puede ser usada, en una primera aproximación, para simular condicio-

nes de ángulo rasante de incidencia. Esto se puede hacer simplemente analizando los picos de difracción perpendiculares a la dirección de incidencia considerada en cada experimento. De esta manera, un simple cálculo «barato» a incidencia normal puede ser usado para simular experimentos GIFAD y GIFMD para varias direcciones de incidencia. En este punto debemos resaltar que la habilidad que tienen los cálculos a incidencia normal de reproducir resultados propios de incidencia rasante es peor según aumentamos la energía normal de incidencia. Ambas aproximaciones, tanto utilizar cálculos a mayor ángulo de incidencia, como utilizar directamente cálculos de incidencia normal para simular resultados GIFAD, son validos sólo para las condiciones en las que la aproximación ASC funciona. Sin embargo, conservar la dimensionalidad total del sistema presenta varias ventajas: (i) se puede usar el mismo potencial para simular condiciones de incidencia más amplias; (ii) se puede utilizar un único cálculo a incidencia normal para simular varios experimentos, con la misma energía normal, para direcciones cristalográficas diferentes.

En la sección 9.3, hemos realizado dinámicas cuánticas 6D con los métodos MCTDH y TDWP a incidencia normal con una energía de 100 meV para comparar con los resultados teóricos obtenidos en la referencia [222]. Estos últimos, son resultados de dinámica cuántica 5D utilizando el método TDWP, usando un potencial modelo 5D (rotor rígido) en el cual se puso un especial cuidado en incluir el acoplamiento cuadrupolar de la molécula de H_2 con la superficie iónica. De la buena comparación con estos resultados, validamos la precisión de nuestra CRP-SEP de 6 dimensiones basada en cálculos DFT. En especial, hemos mostrado que nuestro modelo teórico es capaz de reproducir la existencia de un probabilidad alta de difracción rotacionalmente inelástica, donde $\Delta m_J \neq 0$. Este fenómeno solo solo podía ser reproducido por el potencial modelo si se activaba la parte encargada de reproducir el acoplamiento cuadrupolar. Esto nos indica que nuestra SEP basada en DFT está describiendo adecuadamente esta interacción. Por otro lado, hemos comparado el alineamiento rotacional de n-H_2 en función de varios picos de difracción. En esta comparación, es donde encontramos las diferencias más grandes con el modelo de la referencia [222]. Esto nos indica que esta magnitud es mucho más sensible a los detalles de la SEP que las medidas de probabilidades de difracción. La tendencia encontrada es que los las moléculas difractadas con un menor orden de difracción (menor intercambio de momento) tienden a tener un alineamiento rotacional negativo, mientras que si nos fijamos en aquellas difractadas con un mayor orden, la tendencia es a ser positivo. En todas estas comparaciones, hemos usado también un modelo reducido 5D para detectar las discrepancias debidas a la dimensionalidad del problema.

En la sección 10.4, hemos realizado tanto cálculos de dinámica cuántica (MCTDH) 5D, como cálculos de dinámica clásica 6D para

el sistema $H_2(D_2)$/Methyl-Si(111). Con ello, queremos comprender cómo las terminaciones orgánicas acopladas a un semiconductor pueden afectar a la dinámica sobre la superficie se silicio. Para modelizar la interacción proyectil-superficie, i.e., para construir la SEP, hemos usado el método de interpolación MS. Los resultado clásicos muestran un acuerdo general con los resultados obtenidos experimentalmente por Nihill et al.. En ellos, se muestra una alta probabilidad de excitación rotacional del D_2 que apenas es dependiente del ángulo de incidencia, para el rango de ángulos investigados. También se muestra cómo el H_2 presenta una baja probabilidad de excitación rotacional, lo cual concuerda con el hecho de que experimentalmente sólo se pudo detectar la difracción inelástica utilizando técnicas de tiempo de vuelo. Adicionalmente, la dinámica clásica ha identificado que los puntos de retorno clásicos se concentran sobre los sitios *hollow* y *bridge* de la superficie, a una distancia de 2 Å. Un análisis más detallado de esta zona revela una gran anisotropía, la cual incrementa rápidamente cuando los proyectiles se acercan a esta región. Esta característica de la SEP parece ser responsable de las altas excitaciones rotacionales encontradas experimentalmente a bajas energías de incidencia. Cabe destacar que, pese a que el análisis clásico nos da una gran información sobre el mecanismo de excitación rotacional presente, si usamos un análisis CBM (como el usado en la sección 8.3), no podemos reproducir la siguiente tendencia experimental: la razón entre la intensidad de un pico RID* y su pico homólogo elástico (nos centramos específicamente en los picos $(0,0)$ y $(0,\bar{1})$) aumenta con la energía de incidencia en el rango energético estudiado. Esto es debido a que hay demasiados canales abiertos de difracción, y por lo tanto, que la probabilidad asociada a un pico específico es baja. Hemos mostrado que para poder simular las tendencias observadas experimentalmente, tenemos que realizar cálculos cuánticos, lo cuales producen unos resultados en buena concordancia con las observaciones experimentales.

*Del inglés, Rotationally Inelastic Diffraction.

Part V

APPENDIX

Here, we have compiled all supporting information that was too specific to be discussed in the main body of this work.

A

EXPLICIT FORM OF A HAMILTONIAN FOR A CHEMICAL SYSTEM

This appendix is a complement of Chap. 4, where a more compact form of the Hamiltonian for a generic chemical system was introduced. As the details of this Hamiltonian were not fundamental to the discussion of the BOA, the explicit form of the terms of Eq. 4.2 were omitted. Here, we present those omitted terms for completeness reasons:

$$T_{nucl} = -\tfrac{1}{2}\sum_{\alpha=1}^{N}\frac{\hat{\nabla}_\alpha^2}{M_\alpha}$$

$$T_{e^-} = -\tfrac{1}{2}\sum_{i=1}^{M}\hat{\nabla}_i^2$$

$$V_{nucl-nucl}\left(\mathbf{R}\right) = \sum_{\alpha=1}^{N}\sum_{\beta>\alpha}^{N}\frac{Z_\alpha Z_\beta}{\left|\mathbf{R}_\alpha-\mathbf{R}_\beta\right|}$$

$$V_{e^-e^-}\left(\mathbf{r}\right) = \sum_{i=1}^{M}\sum_{j>i}^{M}\frac{1}{\left|\mathbf{r}_i-\mathbf{r}_j\right|}$$

$$V_{nucl-e^-} = -\sum_{\alpha=1}^{N}\sum_{i=1}^{M}\frac{Z_\alpha}{\left|\mathbf{R}_\alpha-\mathbf{r}_i\right|}$$

$$\hat{H} = -\frac{1}{2}\sum_{\alpha=1}^{N}\frac{\hat{\nabla}_\alpha^2}{M_\alpha} - \frac{1}{2}\sum_{i=1}^{M}\hat{\nabla}_i^2 + \sum_{\alpha=1}^{N}\sum_{\beta>\alpha}^{N}\frac{Z_\alpha Z_\beta}{\left|\mathbf{R}_\alpha-\mathbf{R}_\beta\right|} + \sum_{i=1}^{M}\sum_{j>i}^{M}\frac{1}{\left|\mathbf{r}_i-\mathbf{r}_j\right|} - \sum_{\alpha=1}^{N}\sum_{i=1}^{M}\frac{Z_\alpha}{\left|\mathbf{R}_\alpha-\mathbf{r}_i\right|}\,.$$

Greek sub-indexes run over nuclei. Latin sub-indexes run over electrons. M_α and Z_α are the mass and the charge of nucleus α, respectively. ∇_α^2 and ∇_i^2 are the Laplace operators acting on the spatial coordinates of nucleus α or electron i. N is the total number of nuclei in the system. M is the total number of electrons in the system. The rest of quantities are defined in Chap. 4.

B

SYMMETRY ADAPTED FOURIER SERIES

Symmetry adapted Fourier series are of special interest when dealing with PESs for molecule/surface systems. We use them to define well behaved interpolation functions that must have a definite symmetry (see Sec. 6.2). In this appendix we present the origin of the nomenclature used to classify any Fourier term used in this work and some reference SAFT tables.

CASE OF COMPLEX FUNCTIONS

Let's suppose we have a function $F : \mathbb{R}^N \to \mathbb{C}$, where $N \in \mathbb{N}$ and that satisfies some translational symmetry operations: $F(\mathbf{x}) = F(\mathbf{x}+\mathbf{t})$, $\forall \mathbf{t} \in \mathcal{B}$ as explained in sections 5.1 and 5.2. This function can be expanded in the Fourier basis $\left\{e^{i\mathbf{k}\mathbf{x}}\right\}_{\forall \mathbf{k}\in\mathcal{B}^r}$ as follows:

$$F(\mathbf{x}) = \sum_{\forall \mathbf{k}\in\mathcal{B}^r} c_{\mathbf{k}} e^{i\mathbf{k}\mathbf{x}} \quad . \tag{B.1}$$

Now, let's suppose that there is some symmetry equivalence relationship $(\sim)$ in $\mathbb{R}^N$ that gives rise to the definition of a point symmetry group O in $\mathbb{R}^N$:

$$O = \left\{\widetilde{\mathcal{O}}_1, \widetilde{\mathcal{O}}_2, ..., \widetilde{\mathcal{O}}_g\right\} \tag{B.2}$$

$$(\mathbf{x} \sim \mathbf{y}) \implies \exists \widetilde{\mathcal{O}} \in O \ : \ \left(\mathbf{y} = \widetilde{\mathcal{O}}\mathbf{x}\right), \tag{B.3}$$

where $\widetilde{\mathcal{O}} \in O \ : \mathbb{R}^N \to \mathbb{R}^N$, and g is the number of operations in O, also known as group order. If F satisfies:

$$(\mathbf{x} \sim \mathbf{y}) \implies \left[F(\mathbf{x}) = F(\mathbf{y}) = F\left(\widetilde{\mathcal{O}}\mathbf{x}\right)\right] \quad , \tag{B.4}$$

then F can be expanded without any loss of information to a symmetry adapted basis of the different irreps (Γ) of O. To do so, we have to define a projector $\hat{P}^\Gamma$ that acts on any function $\mathbb{R}^N \to \mathbb{C}$ and projects it in terms of adapted symmetry functions of the irrep Γ:

$$\hat{P}^\Gamma = \frac{d_\Gamma}{g}\sum_{i=1}^{g} \mathcal{X}^\Gamma(\widetilde{\mathcal{O}}_i)\cdot\hat{\mathcal{O}}_i \quad , \tag{B.5}$$

$$\sum_{\forall\Gamma} \hat{P}^\Gamma = \hat{\mathbb{1}} \tag{B.6}$$

where d_Γ is the dimension of Γ, $\mathcal{X}(\widetilde{\mathcal{O}}_i)$ is the character of symmetry operation $\hat{\mathcal{O}}_i$ in the irrep Γ,$\hat{\mathcal{O}}_i$ is an operator which transforms any

input function h into $h \circ \widetilde{\mathcal{O}}_i^{-1}$, and $\hat{\mathbb{1}}$ is the identity operator. The action of $\hat{P}^\Gamma$ on F can be written:

$$\hat{P}^\Gamma F(\mathbf{x}) = \sum_{\forall \mathbf{k} \in \mathcal{B}^r} \sum_{l=1}^{g} \frac{d_\Gamma}{g} \cdot c_{\mathbf{k}} \mathcal{X}^\Gamma(\widetilde{\mathcal{O}}_l) \hat{\mathcal{O}}_l \left(e^{i\mathbf{k}\mathbf{x}} \right) \quad , \tag{B.7}$$

which can be simplified to:

$$\hat{P}^\Gamma F(\mathbf{x}) = \sum_{\forall \mathbf{k} \in \mathcal{B}^r} c_{\mathbf{k}} f_{\mathbf{k}}^\Gamma(\mathbf{x}) \tag{B.8}$$

$$f_{\mathbf{k}}^\Gamma(\mathbf{x}) = \sum_{l=1}^{g} \frac{d_\Gamma}{g} \cdot \mathcal{X}^\Gamma(\widetilde{\mathcal{O}}_l) e^{i\mathbf{k} \cdot \left[\widetilde{\mathcal{O}}_l^{-1}(\mathbf{x}) \right]} . \tag{B.9}$$

We will call $F^\Gamma(\mathbf{x}) = \hat{P}^\Gamma F(\mathbf{x})$ a LC-SAFT and $f_{\mathbf{k}}^\Gamma(\mathbf{x})$ a SAFT.

CASE OF REAL FUNCTIONS

It can be demonstrated that requiring F to be a real function, $F : \mathbb{R}^N \to \mathbb{R}$, is equivalent to add the condition:

$$(\forall \boldsymbol{k} \in \mathcal{B}^r)\,(c_{\boldsymbol{k}}^* = c_{-\boldsymbol{k}}) \tag{B.10}$$

to Eq. B.1. If now we partition the set $\mathcal{B}^r$ into three subsets: $\{\mathbf{0}\}$, $\mathcal{B}_+^r$ and $\mathcal{B}_-^r$ so that $(\forall \boldsymbol{k} \in \mathcal{B}_+^r)\,(\exists \boldsymbol{q} \in \mathcal{B}_-^r) : \boldsymbol{k} + \boldsymbol{q} = \mathbf{0}$ we can write the real function F as follows:

$$F(\mathbf{x}) = c_{\mathbf{0}} + \sum_{\forall \boldsymbol{k} \in \mathcal{B}_+^r} \left[c_{\boldsymbol{k}}^{\oplus} \cos(\boldsymbol{k}\boldsymbol{x}) + c_{\boldsymbol{k}}^{\ominus} \sin(\boldsymbol{k}\boldsymbol{x}) \right] \quad , \tag{B.11}$$

where $c_{\boldsymbol{k}}^{\oplus} = 2\mathrm{Re}(C_{\boldsymbol{k}})$ and $c_{\boldsymbol{k}}^{\ominus} = -2\mathrm{Im}(C_{\boldsymbol{k}})$. Super indexes $\oplus$ and $\ominus$ on the coefficients refer to the parity of the term "cos" (even) or "sin" (odd) to which they are related. Applying operator $\hat{P}^\Gamma$ on F gives as a result:

$$\hat{P}^\Gamma F(\mathbf{x}) = c'_{\mathbf{0}} + \sum_{\forall \boldsymbol{k} \in \mathcal{B}_+^r} \sum_{\forall \odot} c_{\boldsymbol{k}}^{\odot} f_{\boldsymbol{k}}^{\Gamma,\odot}(\boldsymbol{x}) \tag{B.12}$$

$$f_{\boldsymbol{k}}^{\Gamma,\odot}(\boldsymbol{x}) = \begin{cases} \sum_{l=1}^{g} \frac{d_\Gamma}{g} \cdot \mathcal{X}^\Gamma(\widetilde{\mathcal{O}}_l) \cos\left(\mathbf{k} \cdot \widetilde{\mathcal{O}}_l^{-1} \boldsymbol{x} \right), & \text{if } \odot = \oplus \\ \sum_{l=1}^{g} \frac{d_\Gamma}{g} \cdot \mathcal{X}^\Gamma(\widetilde{\mathcal{O}}_l) \sin\left(\mathbf{k} \cdot \widetilde{\mathcal{O}}_l^{-1} \boldsymbol{x} \right), & \text{if } \odot = \ominus \end{cases} , \tag{B.13}$$

where the symbol $\odot$ is an index that can take values $\oplus$ or $\ominus$. Terms $f_{\boldsymbol{k}}^{\Gamma,\odot}$ are SAFTs like $f_{\mathbf{k}}^\Gamma$ in Eq. B.9, but now, they have a definite parity $\odot$. In order to evaluate $f_{\boldsymbol{k}}^{\Gamma,\odot}$ terms, we need to perform operations of the form $\widetilde{\mathcal{O}}_l^{-1}\boldsymbol{x}$, which implies that we have to study how $\widetilde{\mathcal{O}}_l$ operations change $\boldsymbol{x}$ coordinates and use a correct representation, e.g. transform the abstract symmetry operation $\widetilde{\mathcal{O}}_l$ into a matrix with the same operational properties over $\mathbf{x}$.

SAFTs for Fourier series acting on an angular variable

When the variable $\mathbf{x}$ stands for an angle $\theta \in [0, 2\pi)$ and $F(\theta)$ is real, the translational symmetry that F must follow is: $F(\theta) = F(\theta + 2\pi)$. That simplifies B.11 to:

$$F(\theta) = c_0 + \sum_{l>0} \left[C_l^{\oplus} \cos(l\theta) + C_l^{\ominus} \sin(l\theta) \right], l \in \mathbb{N} \ , \tag{B.14}$$

which under the action of $\hat{P}^{\Gamma}$ yields to equation:

$$\hat{P}^{\Gamma} F(\theta) = c_0' + \sum_{l>0} C_l^{\odot} f_l^{\Gamma,\odot}(\theta) \tag{B.15}$$

$$f_l^{\Gamma,\odot}(\theta) = \begin{cases} \sum_{i=1}^{g} \frac{d_{\Gamma}}{g} \cdot \mathcal{X}^{\Gamma}(\widetilde{\mathcal{O}}_i) \cos\left[l \cdot \widetilde{\mathcal{O}}_i^{-1}(\theta) \right], & \text{if } \odot = \oplus \\ \sum_{i=1}^{g} \frac{d_{\Gamma}}{g} \cdot \mathcal{X}^{\Gamma}(\widetilde{\mathcal{O}}_i) \sin\left[l \cdot \widetilde{\mathcal{O}}_i^{-1}(\theta) \right], & \text{if } \odot = \ominus \end{cases} . \tag{B.16}$$

SAFT TABLES FOR P4MM WALLPAPER SYMMETRY

A function $F : \mathbb{R}^2 \to \mathbb{R}$ with p4mm wallpaper symmetry respects a translational symmetry represented by a square Bravais lattice $\mathcal{B}$ and a point group symmetry C_{4v}. Within these boundaries, products $\mathbf{kx}$ have the form:

$$\mathbf{kx} = G(hx + ky) \ , \ G = \frac{2\pi}{a} \ , \tag{B.17}$$

where a is the lattice parameter of the square Bravais lattice, and $\mathbf{k} = \begin{bmatrix} h & k \end{bmatrix}^T \in \mathbb{Z}^2$. On the other hand, C_{4v} point group symmetry contains operations:

$$C_{4v} = \left\{ \widetilde{E}, \widetilde{C}_{2z}, \widetilde{C}_{4z}, \widetilde{C}_{4z}^3, \widetilde{\sigma}_{xz}, \widetilde{\sigma}_d^+, \widetilde{\sigma}_d^- \right\} \ , \tag{B.18}$$

whose representation in 2D are:

$E = \begin{pmatrix} 1 & 0 \\ 0 & 1 \end{pmatrix}$	$E^{-1} = E$	$\mathrm{tr}\,(E) = 2$
$C_{2z} = -\begin{pmatrix} 1 & 0 \\ 0 & 1 \end{pmatrix} = -E$	$C_{2v}^{-1} = C_{2v}$	$\mathrm{tr}\,(C_{2z}) = -2$
$C_{4z} = \begin{pmatrix} 0 & -1 \\ 1 & 0 \end{pmatrix}$	$C_{4z}^{-1} = C_{4v}^{3}$	$\mathrm{tr}\,(C_{4z}) = 0$
$C_{4z}^{3} = \begin{pmatrix} 0 & 1 \\ -1 & 0 \end{pmatrix} = -C_{4z}$	$\left(C_{4z}^{3}\right)^{-1} = C_{4v}$	$\mathrm{tr}\,\left(C_{4z}^{3}\right) = 0$
$\sigma_{xz} = \begin{pmatrix} 1 & 0 \\ 0 & -1 \end{pmatrix}$	$\sigma_{xz}^{-1} = \sigma_{xz}$	$\mathrm{tr}\,(\sigma_{xz}) = 0$
$\sigma_{yz} = \begin{pmatrix} -1 & 0 \\ 0 & 1 \end{pmatrix} = -\sigma_{xz}$	$\sigma_{yz}^{-1} = \sigma_{yz}$	$\mathrm{tr}\,(\sigma_{yz}) = 0$
$\sigma_{d}^{+} = \begin{pmatrix} 0 & 1 \\ 1 & 0 \end{pmatrix}$	$\left(\sigma_{d}^{+}\right)^{-1} = \sigma_{d}^{+}$	$\mathrm{tr}\,\left(\sigma_{d}^{+}\right) = 0$
$\sigma_{d}^{-} = -\begin{pmatrix} 0 & 1 \\ 1 & 0 \end{pmatrix} = -\sigma_{d}^{+}$	$\left(\sigma_{d}^{-}\right)^{-1} = \sigma_{d}^{-}$	$\mathrm{tr}\,\left(\sigma_{d}^{-}\right) = 0$

Table B.1: Definition of $\widetilde{\mathcal{O}}_i$ and $\widetilde{\mathcal{O}}^{-1}{}_i$ matrices and some complementary information.

All previous information allows us to deduce the explicit form of all SAFTs of p4mm symmetry:

Γ	$f_{\boldsymbol{k}}^{\Gamma,\oplus}(x,y)$
A_1	$\frac{1}{2}\left[\cos\left(Ghx\right)\cos\left(Gky\right) + \cos\left(Gkx\right)\cos\left(Ghy\right)\right]$
A_2	$\frac{1}{2}\left[\sin\left(Gkx\right)\sin\left(Ghy\right) - \sin\left(Ghx\right)\sin\left(Gky\right)\right]$
B_1	$\frac{1}{2}\left[\cos\left(Ghx\right)\cos\left(Gky\right) - \cos\left(Gkx\right)\cos\left(Ghy\right)\right]$
B_2	$-\frac{1}{2}\left[\sin\left(Gkx\right)\sin\left(Ghy\right) + \sin\left(Ghx\right)\sin\left(Gky\right)\right]$
E	0

Table B.2: Even SAFTs table for 4pmm symmetry

Γ	$f_k^{\Gamma,\ominus}(x,y)$
A_1	0
A_2	0
B_1	0
B_2	0
E	$\sin(Ghx)\cos(Gky)+\cos(Ghx)\sin(Gky)$

Table B.3: Odd SAFTs table for 4pmm symmetry

SAFT tables for angular variables

Tables for [4mm] (C_{4v}) group

C_{4v}	E	C_{2z}	$2C_{4z}$	$2\sigma_{xz,yz}$	$2\sigma_d$
A_1	1	1	1	1	1
A_2	1	1	1	-1	-1
B_1	1	1	-1	1	-1
B_2	1	1	-1	-1	1
E	2	-2	0	0	0

Table B.4: Character table for [4mm] group

E	$E(\theta)=\theta$	$E^{-1}(\theta)=\theta=E(\theta)$
C_{2z}	$C_{2z}(\theta)=\theta+\pi$	$C_{2z}^{-1}(\theta)=\theta-\pi=\theta+\pi=C_{2z}(\theta)$
C_{4z}	$C_{4z}(\theta)=\theta+\frac{\pi}{2}$	$C_{4z}^{-1}(\theta)=\theta-\frac{\pi}{2}=\theta+\frac{3\pi}{2}=C_{4z}^{3}(\theta)$
C_{4z}^3	$C_{4z}^{3}(\theta)=\theta+\frac{3\pi}{2}$	$\left(C_{4z}^{3}\right)^{-1}(\theta)=\theta-\frac{3\pi}{2}=\theta+\frac{\pi}{2}=C_{4z}(\theta)$
σ_{xz}	$\sigma_{xz}(\theta)=-\theta$	$\sigma_{xz}^{-1}(\theta)=-\theta=\sigma_{xz}(\theta)$
σ_{yz}	$\sigma_{yz}(\theta)=\pi-\theta$	$\sigma_{yz}^{-1}(\theta)=\pi-\theta=\sigma_{yz}(\theta)$
σ_d^+	$\sigma_d^{+}(\theta)=\frac{\pi}{2}-\theta$	$\left(\sigma_d^{+}\right)^{-1}(\theta)=\frac{\pi}{2}-\theta=\sigma_d^{+}(\theta)$
σ_d^-	$\sigma_d^{-}(\theta)=\frac{3\pi}{2}-\theta$	$\left(\sigma_d^{-}\right)^{-1}(\theta)=\frac{3\pi}{2}-\theta=\sigma_d^{-}(\theta)$

Table B.5: Definition of $\widetilde{\mathcal{O}}_i$ operations

Γ	$f_l^{\Gamma,\oplus}(\theta)$	$f_l^{\Gamma,\ominus}(\theta)$
A_1	$\cos(l\theta) \iff l \in [0]_4$	0
A_2	0	$\sin(l\theta) \iff l \in [0]_4$
B_1	$\cos(l\theta) \iff l \in [2]_4$	0
B_2	0	$\sin(l\theta) \iff l \in [2]_4$
E	$\cos(l\theta) \iff l \in [1]_2$	$\sin(l\theta) \iff l \in [1]_2$

Table B.6: SAFTs table for [4mm] group.

Table for [mm2] (C_{2v}) group

C_{4v}	E	C_{2z}	σ_{xz}	σ_{yz}
A_1	1	1	1	1
A_2	1	1	-1	-1
B_1	1	-1	1	-1
B_2	1	-1	-1	1

Table B.7: Character table for [mm2] group

σ_{xz} and σ_{yz} can be defined in multiple ways, they only have to be perpendicular to each other:

E	$E(\theta) = \theta$	$E^{-1}(\theta) = \theta = E(\theta)$
C_{2z}	$C_{2z}(\theta) = \theta + \pi$	$C_{2z}^{-1}(\theta) = \theta - \pi = \theta + \pi = C_{2z}(\theta)$
σ_{xz}	$\sigma_{xz}(\theta) = -\theta$	$\sigma_{xz}^{-1}(\theta) = -\theta = \sigma_{xz}(\theta)$
σ_{yz}	$\sigma_{yz}(\theta) = \pi - \theta$	$\sigma_{yz}^{-1}(\theta) = \pi - \theta = \sigma_{yz}(\theta)$

Table B.8: Definition of $\widetilde{\mathcal{O}}_i$ operations. Choice 1 [mm2]: σ_{xz} plane is aligned with x direction. σ_{xz} plane is aligned with y direction.

E	$E(\theta) = \theta$	$E^{-1}(\theta) = \theta = E(\theta)$
C_{2z}	$C_{2z}(\theta) = \theta + \pi$	$C_{2z}^{-1}(\theta) = \theta - \pi = \theta + \pi = C_{2z}(\theta)$
$\sigma_d^{\oplus}$	$\sigma_d^{\oplus}(\theta) = \frac{\pi}{2} - \theta$	$\left(\sigma_d^{\oplus}\right)^{-1}(\theta) = \frac{\pi}{2} - \theta = \left(\sigma_d^{\oplus}\right)^{-1}(\theta)$
$\sigma_d^{\ominus}$	$\sigma_d(\theta) = \frac{3\pi}{2} - \theta$	$\left(\sigma_d^{\ominus}\right)^{-1}(\theta) = \frac{3\pi}{2} - \theta = \left(\sigma_d^{\ominus}\right)^{-1}(\theta)$

Table B.9: Definition of $\widetilde{\mathcal{O}}_i$ operations assuming that θ is an angle. Choice 2 [m45.m135.2]: $\sigma_d^{\oplus}$ plane forms a 45^o angle with x axis. $\sigma_d^{\ominus}$ plane forms a 135^o angle with x axis.

Therefore, we can build two SAFTs tables:

Γ	$f_l^{\Gamma,\oplus}$	$f_l^{\Gamma,\ominus}$
A_1	$\cos(l\theta) \iff l \in [0]_2$	0
A_2	0	$\sin(l\theta) \iff l \in [0]_2$
B_1	$\cos(l\theta) \iff l \in [1]_2$	0
B_2	0	$\sin(l\theta) \iff l \in [1]_2$

Table B.10: SAFTs for [mm2] group. Choice of angles: 1

Γ	$f_l^{\Gamma,\oplus}$	
A	$\cos(l\theta) \iff l \in [0]_4$	
A_2	$\cos(l\theta) \iff l \in [2]_4$	
B_1	0	$\iff l \in [0]_4$
	$\frac{1}{2}[\cos(l\theta) + \sin(l\theta)]$	$\iff l \in [1]_4$
	0	$\iff l \in [2]_4$
	$\cos(l\theta)$	$\iff l \in [3]_4$
B_2	0	$\iff l \in [0]_4$
	$\cos(l\theta)$	$\iff l \in [1]_4$
	0	$\iff l \in [2]_4$
	$\frac{1}{2}[\cos(l\theta) + \sin(l\theta)]$	$\iff l \in [3]_4$

Table B.11: Even SAFTs tables for [mm2] group. Choice of angles: 2.

Γ	$f_l^{\Gamma,\ominus}$	
A	$\sin(l\theta)$	$\iff l \in [2]_4$
A_2	$\sin(l\theta)$	$\iff l \in [0]_4$
B_1	0	$\iff l \in [0]_4$
	$\frac{1}{2}\left[\cos(l\theta) + \sin(l\theta)\right]$	$\iff l \in [1]_4$
	0	$\iff l \in [2]_4$
	$\sin(l\theta)$	$\iff l \in [3]_4$
B_2	0	$\iff l \in [0]_4$
	$\sin(l\theta)$	$\iff l \in [1]_4$
	0	$\iff l \in [2]_4$
	$\frac{1}{2}\left[\cos(l\theta) + \sin(l\theta)\right]$	$\iff l \in [3]_4$

Table B.12: Odd SAFTs tables for [mm2] group. Choice of angles: 2.

Tables for [2] (C_2) group

C_{4v}	E	C_2
A	1	1
B	1	-1

Table B.13: Character table for [2] group

E	$E(\theta) = \theta$	$E^{-1}(\theta) = \theta = E(\theta)$
C_2	$C_2(\theta) = \theta + \pi$	$C_2^{-1}(\theta) = \theta - \pi = \theta + \pi = C_2(\theta)$

Table B.14: Definition of $\widetilde{\mathcal{O}}_i$ operations for [2] group.

Γ	$f_l^{\Gamma,\oplus}$		$f_l^{\Gamma,\ominus}$	
A	$\cos(l\theta)$	$\iff l \in [0]_2$	$\sin(l\theta)$	$\iff l \in [0]_2$
B	$\cos(l\theta)$	$\iff l \in [1]_2$	$\sin(l\theta)$	$\iff l \in [1]_2$

Table B.15: SAFTs table for [2] group.

Tables for [m] (C_s) group

C_{4v}	E	σ
$A^{'}$	1	1
$A^{''}$	1	-1

Table B.16: Character table for [m] group.

σ can be defined in multiple ways:

E	$E(\theta) = \theta$	$E^{-1}(\theta) = \theta = E(\theta)$
σ_{xz}	$\sigma_{xz}(\theta) = -\theta$	$\sigma_{xz}^{-1}(\theta) = -\theta = \sigma_{xz}(\theta)$
σ_d	$\sigma_d(\theta) = \frac{\pi}{2} - \theta$	$(\sigma_d)^{-1}(\theta) = \frac{\pi}{2} - \theta = \sigma_d(\theta)$

Table B.17: Definition of $\widetilde{\mathcal{O}}_i$ operations for [m] group.

Γ	$f_l^{\Gamma,\oplus}$	$f_l^{\Gamma,\ominus}$
A'	$\cos(l\theta)$	0
A''	0	$\sin(l\theta)$

Table B.18: SAFTs table for [m] group when $\sigma = \sigma_{xz}$.

Γ	$f_l^{\Gamma,\oplus}$	
A'	$\cos(l\theta)$	$\iff l \in [0]_4$
	$\frac{1}{2}[\cos(l\theta) + \sin(l\theta)]$	$\iff l \in [1]_4$
	0	$\iff l \in [2]_4$
	$\frac{1}{2}[\cos(l\theta) - \sin(l\theta)]$	$\iff l \in [3]_4$
A''	0	$\iff l \in [0]_4$
	$\frac{1}{2}[\cos(l\theta) - \sin(l\theta)]$	$\iff l \in [1]_4$
	$\cos(l\theta)$	$\iff l \in [2]_4$
	$\frac{1}{2}[\cos(l\theta) + \sin(l\theta)]$	$\iff l \in [3]_4$

Table B.19: Even SAFTs tables for [m] group when $\sigma = \sigma_d$.

Γ	$f_l^{\Gamma,\ominus}$		
A'	0	$\iff$	$l \in [0]_4$
	$\frac{1}{2}\left[\cos\left(l\theta\right) + \sin(l\theta)\right]$	$\iff$	$l \in [1]_4$
	$\sin(l\theta)$	$\iff$	$l \in [2]_4$
	$\frac{1}{2}\left[\cos\left(l\theta\right) - \sin(l\theta)\right]$	$\iff$	$l \in [3]_4$
A''	$\sin\left(l\theta\right)$	$\iff$	$l \in [0]_4$
	$\frac{1}{2}\left[\cos\left(l\theta\right) - \sin(l\theta)\right]$	$\iff$	$l \in [1]_4$
	0	$\iff$	$l \in [2]_4$
	$\frac{1}{2}\left[\cos\left(l\theta\right) + \sin(l\theta)\right]$	$\iff$	$l \in [3]_4$

Table B.20: Odd SAFTs tables for [m] group when $\sigma = \sigma_d$.

C

CONVERGENCE OF BULK STRUCTURES

Here, we present a systematic study of DFT calculated energies for different LiF and Si primitive cells as a function of the cell volume ($E - V$ plots). This study allow us to predict the equilibrium volume*, V_0, of these crystals. To find V_0, we apply some interpolation function to these $E - V$ data plots and we calculate analytically their minimum points $E_0 - V_0$. There are multiple choices for these interpolation functions, but we have chosen them to have the Murnaghan [77] equation of state form:

$$E(V) = E_0 + \frac{B_0 V}{B_0'} \cdot \left[\frac{(V/V_0)^{B_0'}}{B_0' - 1} + 1 \right] - \frac{B_0 V_0}{B_0' - 1} , \qquad \text{(C.1)}$$

where E_0 and V_0 are the equilibrium energy and volume of the primitive cell, B_0 is the bulk modulus at $P = 0$, and B_0' is the first derivative of the bulk modulus respect to the pressure, which is considered constant in this equation.

In Fig. C.1, we have plotted Murnaghan fits to $E - V$ DFT single point energy curves for LiF (left panel) and Si (right panel). The results of these fits are condensed in Tabs. C.1 and C.2. In the case of LiF, we tested four different functionals using PAW pseudo-potentials [127]: PBE[125], PW91 [124], RPBE [261], and RPBEsol [262]; and PW91 with ultrasoft pseudo-potential (US-PP) [126]. In the case of Si, we tested only the PBE functional with PAW pseudo-potentials.

*The volume of the structure with the minimum energy value.

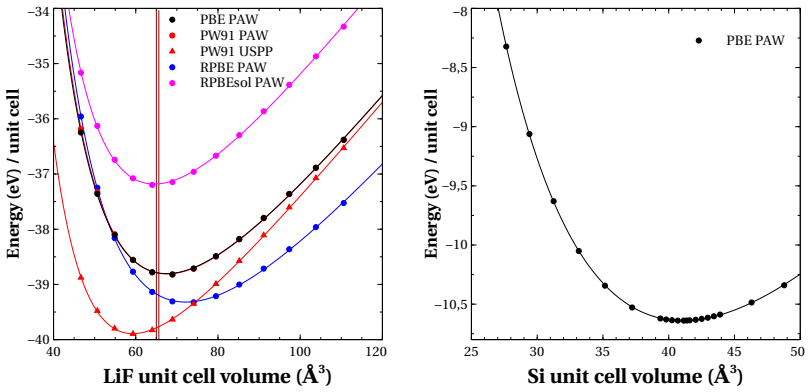

Figure C.1: Murnaghan fits to DFT single point energies as a function of the bulk unit cell volume. Each line color stands for a different functional (see text for references). Lines with circles stand for calculations done with PAW pseudo potentials. Lines with triangles stand for calculations performed with US-PP. Dark red vertical lines mark the range of V_0 benchmark values in Refs. [177, 178, 263]. Left Panel: Murnaghan curves for LiF crystal. Right panel: Murnaghan curves for Si crystal.

	V_0 (Å^3)	B_0 (GPa)	B_0'
PBE PAW	67.5 ± 0.1	63 ± 2	4.31 ± 0.09
PW91 PAW	67.6 ± 0.1	64.0 ± 0.4	4.34 ± 0.08
PW91 US-PP	59.26 ± 0.08	73.0 ± 0.9	5.1 ± 0.1
RPBE PAW	72.2 ± 0.1	55.1 ± 0.3	3.98 ± 0.07
RPBEsol PAW	64.5 ± 0.1	68.9 ± 0.7	4.6 ± 0.1
Theor. benchmark (T=0) [177]	65.01	73.8	3.76
Exp. benchmark (RT) [178]	65.61	74.4	3.69
Exp. benchmark (RT)[263]	65.58	68.5	3.6

Table C.1: Calculated V_0, B_0 and B_0' parameters for bulk LiF for different functionals.

	a (Å)	B_0 (GPa)	B_0'
PBE PAW	5.5 ± 0.4	87.6 ± 0.6	3.71 ± 0.04
Exp. benchmark (RT)			
Exp. benchmark (RT)			

Table C.2: Calculated V_0, B_0 and B_0' parameters for bulk silicon for different functionals.

D

MICROCANONICAL ENSEMBLE FOR DI-ATOMIC MOLECULES

In order to determine the initial internal conditions of a di-atomic molecule, we use a Monte Carlo sampling method [264]. As the complete phase space Ω is huge, we do not sample it directly , but a smaller manageable space on with averaging an observable, $\bar{F}$, is equivalent to averaging over the entire phase space Ω. Here, we present how we derived the form of this smaller space. The way we sampled translational conditions is explained in Sec. 7.1.

CONSIDERATIONS ON THE PHASE SPACE Ω AND NOTATION

In order to simplify our discussions, we will use the following notation

$$\begin{aligned} \left(r, p_r, \theta, p_\theta, \phi, p_\phi\right) &= \omega, \quad \omega \in \Omega && \text{(D.1)} \\ \left(r, p_r\right) &= \omega_r, \quad \omega_r \in \Omega_r && \text{(D.2)} \\ \left(\theta, p_\theta, \phi, p_\phi\right) &= \omega_\alpha, \quad \omega_\alpha \in \Omega_\alpha \ , && \text{(D.3)} \end{aligned}$$

Ω_r and Ω_α being the radial and angular phase spaces. The phase space Ω is constructed as the Cartesian product: $\Omega = \Omega_r \times \Omega_\alpha$, with elements: $\omega = \omega_r \times \omega_\alpha$. Now, we define the Hamiltonian and angular momentum functions of the he system as:

$$H\left(\omega\right) = \frac{p_r^2}{2\mu} + \frac{L^2}{2\mu r^2} + V\left(r\right), \ H : \Omega \to \mathbb{R} \tag{D.4}$$

and

$$L\left(\omega\right) = \left[p_\theta^2 + \left(\frac{p_\phi}{\sin\theta}\right)^2\right]^{\frac{1}{2}}, \ L : \Omega \to \mathbb{R}^+ \ . \tag{D.5}$$

where $\mathbb{R}^+$ is the set of positive (including zero) real numbers, and $V\left(r\right)$ the internal potential of the molecule in vacuum. Note that if we have an element $\omega = \omega_r \times \omega_\alpha$, $L\left(\omega\right) = L\left(\omega_\alpha\right)$, so we can reduce the dominion of L to Ω_α. We have chosen arbitrarily L function to be positive. The Hamiltonian does not depend on this choice. The definition of H and L allow us to partition Ω in the following class sets:

$$\begin{aligned} \left[E\right]_H &= \left\{\omega \in \Omega \ : \ H\left(\omega\right) = E\right\} && \text{(D.6)} \\ \left[L_0\right]_L &= \left\{\omega \in \Omega \ : \ L\left(\omega\right) = L_0\right\} && \text{(D.7)} \\ \left[E, L_0\right]_{H,L} &= \left[E\right]_H \bigcap \left[L_0\right]_L \ . && \text{(D.8)} \end{aligned}$$

The fact that L does not depend on ω_r variables allow us to define a restricted class set $[L_0]_L^{(\alpha)}$ of elements of Ω_α as follows:

$$[L_0]_L^{(\alpha)} = \{\omega_\alpha \in \Omega_\alpha \,:\, L(\omega_\alpha) = L_0\} \,. \tag{D.9}$$

If we now define H_{L_0} as a Hamiltonian with constant angular momentum $L = L_0$, we can construct as well another class of sets in Ω_r:

$$[E]_{H_{L_0}}^{(r)} = \{\omega_r \in \Omega_r \,:\, H_{L_0}(\omega_r) = E\} \,. \tag{D.10}$$

Taking advantage that $[E]_{H_{L_0}}^{(r)}$ and $[L_0]_L^{(\alpha)}$ are classes in Ω_r and Ω_α, we can rewrite Eq. D.8 as:

$$[E, L_0]_{H,L} = [E]_{H_{L_0}}^{(r)} \times [L_0]_L^{(\alpha)} \tag{D.11}$$

All this class sets will be useful to define integration limits in Ω.

In a micro-canonical ensemble, the probability distribution is a function $\rho : [E]_H \to [0,1]$ that satisfies:

$$\left(\forall \omega, \omega' \in [E]_H\right)\ \rho(\omega) = \rho(\omega') \,, \tag{D.12}$$

which means that if two configurations in phase space have the same energy, they have the same probability to be included in the sampling, i.e., that ρ is a uniform probability density in $[E]_H$. As we want to sample states with an specific angular momentum $L = L_0$, we can restrict the domain of ρ to $[E, L_0]_{H,L}$. The density function is then normalized as follows:

$$\int_{[E,L_0]_{H,L}} \rho(\omega)\, d\omega = 1 \,. \tag{D.13}$$

Under such constrains, $\rho(\omega)$ can be written:

$$\rho(\omega) = \rho^{(r)}(\omega_r) \cdot \rho^{(\alpha)}(\omega_\alpha) \,, \tag{D.14}$$

where $\omega = \omega_r \times \omega_\alpha$, being $\rho^{(r)}$ a uniform density probability in $[E]_{H_{L_0}}^{(r)}$ and $\rho^{(\alpha)}$ a uniform density probability in $[L_0]_L^{(\alpha)}$.

SEPARATION OF THE SAMPLING

The average value "$\bar{F}$" of any physical quantity "$F(\omega)$" of a diatomic molecule within a micro-canonical ensemble with fixed energy E and angular momentum L_0 can be written:

$$\bar{F} = \int_{[E,L_0]_{H,L}} F(\omega)\, \rho(\omega)\, d\omega \,. \tag{D.15}$$

Applying Eqs. D.11 and D.14 to the previous equation allow us to separate the integral over $[E, L_0]_{H,L}$ in the following way:

$$\bar{F} = \int_{[E]_{H_{L_0}}^{(r)}} \rho^{(r)}(\omega_r) \cdot \tilde{F}(\omega_r)\, d\omega_r \tag{D.16}$$

with

$$\tilde{F}(\omega_r) = \int_{[L_0]_L^{(\alpha)}} \rho^{(\alpha)}(\omega_\alpha) \cdot F(\omega)\, d\omega_\alpha \,. \tag{D.17}$$

We have two separate uniform samplings: (i) a radial sampling in $[E]_{H_{L_0}}^{(r)}$ (Eq. D.16); (ii) an angular sampling in $[L_0]_L^{(\alpha)}$ (Eq. D.17).

Sampling the radial part

Now that the separation of Eq. D.15 into two different samplings is clear, we can write the radial average (Eq. D.16) in a more convenient way for operational purposes:

$$\bar{F} = N \int_{\Omega_r} \tilde{F}(\omega_r) \cdot \delta\left[H_{L_0}(\omega_r) - E\right] d\omega_r \,, \tag{D.18}$$

where N is a normalization factor, and δ is a Dirac delta function. If we use the Dirac delta properties, the previous equation can be written in a more explicit way:

$$\bar{F} = N \int_{r_{min}}^{r_{max}} \sum_n \tilde{F}\left(r, p_r^{(n)}\right) \cdot \left|\frac{\partial H_{L_0}}{\partial p_r}\right|^{-1}_{p_r = p_r^{(n)}} dr \,, \tag{D.19}$$

where r_{min} and r_{max} are the turning points of the vibrational motion and $p_r^{(n)}$ are the solutions to the equation $H_{L_0}(\omega) = E$ for a given r value.

For the vibrational motion, each r value has two associated p_r values except for the turning points r_{max} and r_{min}. Moreover, taking into account that $dH/dp_r = dr/dt$ we can write:

$$\bar{F} = N \int_0^\tau \tilde{F}(r(t), p_r(t))\, dt \,, \tag{D.20}$$

where τ is the period of the vibrational motion. If we now perform the change of variables $\zeta = t/\tau$, being ζ the phase of the vibrational motion, we can deduce the final expression for the radial sampling:

$$\bar{F} = N \cdot \tau \int_0^1 \tilde{F}(r(\zeta \cdot \tau), p_r(\zeta \cdot \tau))\, d\zeta \,. \tag{D.21}$$

According to this equation, instead of sampling the entire space $[E]_{H_{L_0}}^{(r)}$, we can just uniformly sample ζ variable from 0 to 1. The normalization factor N takes the form: $N = \left(\int_0^1 d\zeta\right)^{-1}$.

Sampling the angular part

Due to the dependence of Eq. D.17 on radial variables ω_r, we can only perform the angular sampling once we have fixed ω_r. To stress this idea, we change $F(\omega)$ to $F_{\omega_r}(\omega_\alpha)$ and $\tilde{F}(\omega_r)$ to $\bar{F}_{\omega_r}$ hereinafter.

Random orientation of angular momentum

Eq. D.17 can be rewritten as follows:

$$\bar{F}_{\omega_r} = N \int_{\Omega_\alpha} F_{\omega_r}(\omega_\alpha) \cdot \delta\left[L(\omega_\alpha) - L_0\right] d\omega_\alpha \,, \tag{D.22}$$

where $\bar{F}_{\omega_r}$ is the angular average of F with fixed ω_r, N a normalization constant, and δ a Dirac delta function. If we perform the variable change $q_\phi = \frac{p_\phi}{\sin\theta}$, then the previous equation reads as:

$$\bar{F}_{\omega_r} = N \int \sin\theta \cdot I_{\omega_r}(\theta, \phi) \cdot d\theta d\phi \,, \tag{D.23}$$

with

$$I_{\omega_r}(\theta, \phi) = \int F_{\omega_r}(\omega_\alpha) \cdot \delta\left[L(\omega_\alpha) - L_0\right] dp_\theta dq_\phi \,. \tag{D.24}$$

Applying the properties of a Dirac delta function, "I" can be written as:

$$I_{\omega_r}(\theta, \phi) = \sum_{n=1}^{2} \int F_{\omega_r}\left(\theta, \phi, p_\theta, q_\phi^{(n)}\right) \cdot \left|\frac{\partial L}{\partial q_\phi}\right|^{-1}_{q_\phi = q_\phi^{(n)}} dp_\theta \,, \tag{D.25}$$

where $q_\phi^{(n)}$ is a solution of $L = L_0$, i.e., $q_\phi^{(1)} = \left(L_0^2 - p_\theta^2\right)^{\frac{1}{2}}$ and $q_\phi^{(2)} = -\left(L_0^2 - p_\theta^2\right)^{\frac{1}{2}}$. If we introduce a new angular variable $\eta \in \left[-\frac{\pi}{2}, \frac{\pi}{2}\right]$ that fulfills the condition:

$$p_\theta = -L_0 \sin\eta, \quad q_\theta^{(n)} = \pm L_0 \cos\eta \,, \tag{D.26}$$

then, after some algebra, Eq. D.25 can be written as:

$$I_{\omega_r}(\theta, \phi) = -L_0 \cdot \int_0^{2\pi} F_{\omega_r}(\theta, \phi, -L_0 \sin\eta, L_0 \sin\theta \cos\eta)\, d\eta \,. \tag{D.27}$$

Now, if we introduce the new form of "I" in Eq. D.23, we end up with the following formula:

$$\bar{F}_{\omega_r} = \frac{1}{8\pi} \cdot \int \sin\theta \cdot \left[\int_0^{2\pi} F_{\omega_r}(\theta, \phi, -L_0 \sin\eta, L_0 \sin\theta \cos\eta)\, d\eta\right] d\theta d\phi \,. \tag{D.28}$$

In order to reduce the space to be sampled by θ, ϕ, and η angular variables, we can write them as a function of a new set of variables whose values are in the range $[0, 1]$:

$$\eta = 2\pi\epsilon_\eta \tag{D.29}$$

$$\phi = 2\pi\epsilon_\phi \tag{D.30}$$

$$\cos\theta = 2\epsilon_\theta - 1 \,, \tag{D.31}$$

where $\epsilon_\eta, \epsilon_\theta, \epsilon_\phi \in [0, 1]$. Therefore, Eq. D.28 is finally written as:

$$\bar{F}_{\omega_r} = \int_0^1 \int_0^1 \int_0^1 F_{\omega_r}\left(\theta(\epsilon_\theta), \phi(\epsilon_\phi), p_\theta(\epsilon_\eta), p_\phi(\epsilon_\theta, \epsilon_\eta)\right) d\epsilon_\theta d\epsilon_\phi d\epsilon_\eta \,, \tag{D.32}$$

which demonstrates that the angular sampling, once ω_r is fixed, can be performed by uniformly sampling ϵ_η, ϵ_θ and ϵ_ϕ variables from 0 to 1.

Fixed orientation of angular momentum

In this case, not all values of θ are allowed since the rotational axis must be in a plane orthogonal to the direction of the angular momentum. To take this into account, we fix partially the orientation of the angular momentum keeping fixed the angle with respect to the z axis through the relation:

$$\cos\theta_p = \frac{p_\phi}{L_0} = \beta \,, \tag{D.33}$$

which applied to Eq. D.22 gives rise to the following expression:

$$\bar{F}_{\omega_r} = N \int F_{\omega_r}\left(\theta, \phi, p_\theta, \beta L_0\right) \cdot \delta\left[L\left(\omega_\alpha\right) - L_0\right] d\theta d\phi dp_\theta \,. \tag{D.34}$$

This is no longer a sample in $[L_0]_L^{(\alpha)}$ but in a restricted subclass $[L_0]_{L_\beta}^{(\alpha)}$, being L_β the function:

$$L_\beta^2 = \frac{p_\theta^2}{1 - \frac{\beta^2}{\sin^2\theta}} \,. \tag{D.35}$$

Clearly, in $[L_0]_{L_\beta}^{(\alpha)}$, θ values are constrained as follows: $\sin\theta > |\beta|$, i.e., $\sin\theta > \left|\cos\theta_p\right|$. If we perform the same change of variables as in the previous section, one can find that:

$$\cos\eta = \frac{\beta}{\sin\theta} \,, \tag{D.36}$$

with $\eta \in [0, \pi]$. Therefore, due to Eq. D.35, $p_\theta = \pm L_0 \sin\eta$. For each value of η, we have two values of p_θ. The angular range in θ is limited by the constraints in $[L_0]_{L_\beta}^{(\alpha)}$. It limits are:

$$\theta_p \leq \frac{\pi}{2} \rightarrow \begin{cases} \theta_{min} & = \frac{\pi}{2} - \theta_p \\ \theta_{max} & = \frac{\pi}{2} + \theta_p \end{cases} \tag{D.37}$$

and

$$\theta_p \geq \frac{\pi}{2} \rightarrow \begin{cases} \theta_{min} & = \theta_p - \frac{\pi}{2} \\ \theta_{max} & = \frac{3\pi}{2} - \theta_p \end{cases} \,. \tag{D.38}$$

Proceeding as in the previous section, and performing some changes to simplify the results, we get:

$$\begin{aligned} \bar{F}_{\omega_r} = N \int_0^{2\pi} d\phi \int_0^1 d\mu \, [& F_{\omega_r}\left(\theta, \phi, L_0 \sin\eta, L_0 \sin\theta\cos\eta\right) \\ & + F_{\omega_r}\left(\theta, \phi, -L_0 \sin\eta, L_0 \sin\theta\cos\eta\right)] \,, \end{aligned} \tag{D.39}$$

where

$$\mu = \frac{1}{\pi}\left[\arcsin\left(\frac{\cos\theta_{min}}{\sin\theta_p}\right) - \arcsin\left(\frac{\cos\theta}{\sin\theta_p}\right)\right] \,, \tag{D.40}$$

and

$$\cos\theta = \sin\theta_p \cos(\pi\mu) \tag{D.41}$$

$$\cos\eta = \frac{\cos\theta_p}{\sin\theta} \,. \tag{D.42}$$

The details of these operations can be found in Refs. [265] and [266]. We can see that in general, the sampling in θ is neither uniform nor a function of $\sin\theta$. In the extreme case of $\theta_p = \frac{\pi}{2}$ (*cartwheel* rotation), then, the distribution is uniform in θ. In the other extreme, if $\theta_p = 0$, (*helicopter* rotation), then, the distribution is uniform in ϕ, but not in θ.

E

LOSS OF ISOTOPIC EFFECTS IN CLASSIC PROBABILITY DISTRIBUTION OF SCATTERED ATOMS ON A SURFACE UNDER FAST GRAZING ANGLE CONDITIONS.

Following the same nomenclature that we have been using up to now in this work, we can distinguish two interesting scattering angles, namely, θ_f and ϕ_f , which are the final deflection angle and the final azimuthal angle (see Fig. 8.2). Any given scattering exit channel is completely characterized by the pair (θ_f, ϕ_f). The dependence of these exit angles with the final momentum of a trajectory is:

$$\phi_f = \arctan\left(\frac{p_f^y}{p_f^x}\right) \tag{E.1}$$

$$\theta_f = \arctan\left(\frac{p_f^z}{p_f^{\parallel}}\right) \tag{E.2}$$

where p_f^x is the final momentum along the incidence direction parallel to the surface, p_f^y is the final momentum along the perpendicular direction to x and parallel to the surface, p_f^z is the final momentum perpendicular to the surface plane and $p_f^{\parallel} = \sqrt{\left(p_f^x\right)^2 + \left(p_f^y\right)^2}$. From expressions E.1 and E.2 it is clear that ϕ_f and θ_f are functions of $\left(p_f^x, p_f^y, p_f^z\right)$ and therefore, if two projectiles with the same initial conditions (same impact parameters, energy and incidence angle) have different masses, differences in the scattering are expected. However, we are going to see that under grazing angle conditions, this isotopic effect is smoothed out.

It is well known that under fast grazing angle conditions the variation of momentum along the incidence direction (x) is negligible compared to the initial momentum [107, 147]. Thus, any momentum exchange (neglecting phonons or non adiabatic effects) should be carried out between y and z directions. This allows us to perform the following approximations:

- $p_f^x \approx p_i$, where $p_i^{\parallel}$ is the initial parallel momentum
- $\Delta p^{\parallel} \approx p_f^y$
- $p_f^z \approx p_i^{\perp} - \Delta p$

From Ref. [265], we can take the explicit form of $\Delta p^{\parallel}$ at first order approximation: $\Delta p^{\parallel} = \frac{-M}{p_i^{\parallel}} \cdot \int_0^d dx \frac{\partial V(x,y)}{\partial y}$, in which M is the mass of the

projectile and d the period of length along x in which the potential of the system $V(x,y)$ repeats itself. Summing up all the approximations and adding them to E.1 and E.2 we find:

$$\phi_f \approx \arctan\left(\frac{-1}{2E_i^{\parallel}} \cdot \int_0^d dx \frac{\partial V(x,y)}{\partial y}\right) \implies \phi_f\left(E_i^{\parallel}, V, d\right) \tag{E.3}$$

$$\theta_f \approx \arctan\left(\sqrt{\frac{E_i^z}{E_i^{\parallel}}} + \frac{1}{2E_i^{\parallel}} \cdot \int_0^d dx \frac{\partial V(x,y)}{\partial y}\right) \implies \theta_f\left(E_i^z, E_i^{\parallel}, V, d\right) \tag{E.4}$$

being $E_i^{\parallel}$ and E_i^z the initial energies. Now, equations E.3 and E.4 do not depend on momenta but on initial energies, the interaction with the surface (V) and the periodicity in x (d). This means that we should expect a similar exit angle distribution in classic dynamics as long as the projectiles have the same energy conditions. A good example of this lack of isotopic effect can be found comparing red dashed lines in Figs. 8.6 and 8.7.

F

BIBLIOGRAPHY

BIBLIOGRAPHY

[1] M. Debiossac, A. Zugarramurdi, H. Khemliche, P. Roncin, A. G. Borisov, A. Momeni, P. Atkinson, M. Eddrief, F. Finocchi, and V. H. Etgens. "Combined experimental and theoretical study of fast atom diffraction on the beta(2)(2x4) reconstructed GaAs(001) surface." In: *PHYSICAL REVIEW B* 90.15 (2014) (cit. on pp. iii, iv, 19, 108).

[2] F. Aigner, N. Simonović, B. Solleder, L. Wirtz, and J. Burgdörfer. "Suppression of Decoherence in Fast-Atom Diffraction at Surfaces." In: *Phys. Rev. Lett.* 101 (25 Dec. 2008), p. 253201 (cit. on pp. iii, 19, 86, 87).

[3] Schüller et al. "Rumpling of LiF(001) surface from fast atom diffraction." In: *Phys. Rev. A* 82 (6 Dec. 2010), p. 062902 (cit. on pp. iii, 19, 87, 89).

[4] J.E. Miraglia M.S. Gravielle. "Influence of the polarization in grazing scattering of fast hellium atoms from LiF(001) surfaces." In: *Phys. Rev. A* 78 (2008), p. 022901 (cit. on pp. iii, 12, 19, 87, 108).

[5] M. S. Gravielle, A. Schueller, H. Winter, and J. E. Miraglia. "Fast atom diffraction for grazing scattering of Ne atoms from a LiF(001) surface." In: *NUCLEAR INSTRUMENTS & METHODS IN PHYSICS RESEARCH SECTION B-BEAM INTERACTIONS WITH MATERIALS AND ATOMS* 269.11, SI (2011). 18th International Workshop on Inelastic Ion-Surface Collisions (IISC-18), Gatlinburg, TN, SEP 26-OCT 01, 2010, 1208–1211 (cit. on pp. iii, 19).

[6] M. S. Gravielle and J. E. Miraglia. "Semiquantum approach for fast atom diffraction: Solving the rainbow divergence." In: *PHYSICAL REVIEW A* 90.5 (2014) (cit. on pp. iii, 19).

[7] Asier Zugarramurdi and Andrei G. Borisov. "Transition from fast to slow atom diffraction." In: *PHYSICAL REVIEW A* 86.6 (2012) (cit. on pp. iii, 19).

[8] Asier Zugarramurdi and Andrei G. Borisov. "When fast atom diffraction turns 3D." In: *NUCLEAR INSTRUMENTS & METHODS IN PHYSICS RESEARCH SECTION B-BEAM INTERACTIONS WITH MATERIALS AND ATOMS* 317.A (2013). 19th International Workshop on Inelastic Ion-Surface Collisions (IISC), GERMANY, SEP 16-21, 2012, 83–89 (cit. on pp. iii, 19).

[9] M. Busch, J. Seifert, E. Meyer, and H. Winter. "Diffraction of fast H atoms during grazing scattering from an Al2O3(11(2)overbaro) surface." In: *NUCLEAR INSTRUMENTS & METHODS IN PHYSICS RESEARCH SECTION B-BEAM INTERACTIONS WITH MATERIALS AND ATOMS* 317.A (2013). 19th International Workshop on Inelastic Ion-Surface Collisions (IISC), GERMANY, SEP 16-21, 2012, 90–95 (cit. on pp. iv, 20).

[10] H. Winter. private communication. 2014 (cit. on pp. iv, 20, 108).

[11] A Salin. "Theoretical study of hydrogen dissociative adsorption on the Cu(110) surface." English. In: *JOURNAL OF CHEMICAL PHYSICS* 124.10 (2006) (cit. on pp. iv, 20, 107).

[12] C. Díaz and F. Martín. "Reactive scattering of H_2 from metal surfaces under fast-grazing-incidence conditions." In: *Phys. Rev. A* 82 (1 July 2010), p. 012901 (cit. on pp. iv, 20, 85).

[13] Irene M. N. Groot, Juan Carlos Juanes-Marcos, Cristina Diaz, Mark F. Somers, Roar A. Olsen, and Geert-Jan Kroes. "Dynamics of dissociative adsorption of hydrogen on a CO-precovered Ru(0001) surface: a comparison of theoretical and experimental results." In: *PHYSICAL CHEMISTRY CHEMICAL PHYSICS* 12.6 (2010), 1331–1340 (cit. on pp. iv, 20, 107).

[14] A. S. Muzas, J. I. Juaristi, M. Alducin, R. Diez Muino, G. J. Kroes, and C. Diaz. "Vibrational deexcitation and rotational excitation of H-2 and D-2 scattered from Cu(111): Adiabatic versus non-adiabatic dynamics." In: *JOURNAL OF CHEMICAL PHYSICS* 137.6 (2012) (cit. on pp. iv, 20).

[15] H.F. Busnengo, A. Salin, and W. Dong. ""Representation of the 6D potential energy surface for a diatomic molecule near a solid surface"." English. In: *Journal Of Chemical Physics* 112.17 (2000), 7641–7651 (cit. on pp. iv, 20, 44, 49, 51, 88, 107, 110).

[16] C Crespos, MA Collins, E Pijper, and GJ Kroes. "Multi-dimensional potential energy surface determination by modified Shepard interpolation for a molecule-surface reaction: H-2+Pt(111)." English. In: *CHEMICAL PHYSICS LETTERS* 376.5-6 (2003), 566–575 (cit. on pp. iv, 20, 107).

[17] Terry J. Frankcombe, Michael A. Collins, and Dong H. Zhang. "Modified Shepard interpolation of gas-surface potential energy surfaces with strict plane group symmetry and translational periodicity." In: *The Journal of Chemical Physics* 137.14 (2012), 144701(10) (cit. on pp. iv, 20, 58, 61, 107, 128).

[18] S Lorenz, A Gross, and M Scheffler. "Representing high-dimensional potential-energy surfaces for reactions at surfaces by neural networks." English. In: *CHEMICAL PHYSICS LETTERS* 395.4-6 (2004), 210–215 (cit. on pp. iv, 20, 107).

[19] Bin Jiang and Hua Guo. “Permutation invariant polynomial neural network approach to fitting potential energy surfaces. III. Molecule-surface interactions.” English. In: *JOURNAL OF CHEMICAL PHYSICS* 141.3 (2014) (cit. on pp. iv, 20, 107).

[20] X. J. Shen, Y. Xiao, W. Dong, X. H. Yan, and H. F. Busnengo. “Molecular dynamics simulations based on reactive force-fields for surface chemical reactions.” English. In: *COMPUTATIONAL AND THEORETICAL CHEMISTRY* 990.SI (2012), 152–158 (cit. on pp. iv, 20, 107).

[21] M.H. Beck, A. Jackle, G.A. Worth, and H.D Meyer. “The multiconfigurational time-dependent Hartree (MCTDH) algorithm: an efficient method for propagating wavepackets of several dimensions.” In: *Physics Reports-Review Section of Physics Letters* 324.1 (2000), pp. 1–105 (cit. on pp. iv, 20, 75, 81, 90, 109, 113, 116, 130).

[22] HD Meyer and GA Worth. “Quantum molecular dynamics: propagating wavepackets and density operators using the multiconfiguration time-dependent Hartree method.” English. In: *THEORETICAL CHEMISTRY ACCOUNTS* 109.5 (2003), 251–267 (cit. on pp. iv, 20, 87, 90, 113, 116).

[23] D. Farías, C. Díaz, P. Rivière, H. F. Busnengo, P. Nieto, M. F. Somers, G. J. Kroes, A. Salin, and F. Martín. “In-Plane and Out-of-Plane Diffraction of H_2 from Metal Surfaces.” In: *Phys. Rev. Lett.* 93 (24 Dec. 2004), p. 246104 (cit. on pp. iv, 9, 19, 20, 71, 85, 87, 90, 107, 117).

[24] C. Díaz, F. Martín, G. J. Kroes, M. Minniti, D. Farías, and R. Miranda. “"H_2 Diffraction from a Strained Pseudomorphic Monolayer of Cu Deposited on Ru(0001)".” In: *J. Phys. Chem. C* 116.25 (2012), 13671–13678 (cit. on pp. iv, 20, 87, 109, 117, 126).

[25] Ya-Huei (Cathy) Chin, Cornelius Buda, Matthew Neurock, and Enrique Iglesia. “"Reactivity of chemisorbed oxygen atoms and their catalytic consequences during CH_4-O-2 catalysis on supported Pt clusters".” English. In: *Journal Of The American Chemical Society* 133.40 (2011), 15958–15978 (cit. on p. 3).

[26] Laura S. Sremaniak and Jerry L. Whitten. “"Theoretical treatment of excited electronic states of adsorbates on metals: Electron attachment to CO2 adsorbed on Pt(111)".” English. In: *Surface Science* 601 (2007), 3755–3759 (cit. on p. 3).

[27] Stefan Vajda et al. “"Subnanometre platinum clusters as highly active and selective catalysts for the oxidative dehydrogenation of propane".” English. In: *Nature Materials* 8.3 (2009), 213–216 (cit. on p. 3).

[28] B. Bogdanovic and M. Schwickardi. “"Ti-doped alkali metal aluminium hydrides as potential novel reversible hydrogen storage materials".” English. In: *Journal Of Alloys And Compounds* 253 (1997), 1–9 (cit. on p. 3).

[29] W. Lohstroh and M. Fichtner. “"Rate limiting steps of the phase transformations in Ti-doped NaAlH4 investigated by isotope exchange".” English. In: *Physical Review B* 75.18 (2007) (cit. on p. 3).

[30] G. Ertl. “"Primary steps in catalytic synthesis of ammonia".” English. In: *Journal Of Vacuum Science & Technology A-vacuum Surfaces And Films* 1.2 (1983), 1247–1253 (cit. on p. 3).

[31] URL: http://www.nobelprize.org/nobel_prizes/chemistry/laureates/2007/ (cit. on p. 3).

[32] A. Gross, S. Wilke, and M. Scheffler. “"6-dimensional quantum dynamics of adsorption and desorption of H_2 at Pd(100) - steering and steric effects".” English. In: *Physical Review Letters* 75.14 (1995), 2718–2721 (cit. on p. 5).

[33] I. Estermann and O. Stern. “Diffraction of molecular beams.” In: *ZEITSCHRIFT FUR PHYSIK* 61.1-2 (1930), 95–125 (cit. on pp. 9, 108).

[34] J.E. Lennard-Jones and A.F. Devonshire. In: *Nature* 137 (1936), p. 1069 (cit. on pp. 9, 108).

[35] A.F. Devonshire. In: *Proc. Roy. Soc. A* 156 (1936), p. 37 (cit. on p. 9).

[36] M-C. Desjonqueres and D. Spanjaard. *Concepts in surface physiscs*. 2nd. Gif sur yvette: Springer, 1996 (cit. on p. 9).

[37] Hans Lüth. *Solid Surfaces, Interfaces and Thin Films*. 6th ed. Graduate Texts in Physics. Springer International Publishing, 2015 (cit. on pp. 9, 11).

[38] D. Farias, H. F. Busnengo, and F. Martin. “Probing reaction dynamics at metal surfaces with H-2 diffraction.” English. In: *JOURNAL OF PHYSICS-CONDENSED MATTER* 19.30 (2007) (cit. on pp. 9, 126).

[39] Daniel Farias and Rodolfo Miranda. “Diffraction of molecular hydrogen from metal surfaces.” English. In: *PROGRESS IN SURFACE SCIENCE* 86.9-10 (2011), 222–254 (cit. on pp. 9, 126).

[40] E. Watts and G.O. Sitz. “"State-to-state scattering in a reactive system: H_2(v=1,J=1) from Cu(100)".” English. In: *Journal Of Chemical Physics* 114.9 (2001), 4171–4179 (cit. on p. 10).

[41] M. Gostein, E. Watts, and G. O. Sitz. “"Vibrational relaxation of H_2 (v=1, J=1) on Pd(111)".” In: *Physical Review Letters* 79 (15 Oct. 1997), pp. 2891–2894 (cit. on p. 10).

[42] CC Huang, DA MacLaren, and W Allison. “Helium atom scattering from an epitaxial nano-structure surface: Ni/Cu(100).” English. In: JOURNAL OF PHYSICS CONFERENCE SERIES 19 (2005). Ed. by Weiner, J and Feenstra, L and Schmiedmayer, J. International Conference on Atoms and Molecules Near Surfaces, Int Wissenschaft Forum Ruprech-Karls Univ, Heidelberg, GERMANY, APR 04-08, 2005, 182–185 (cit. on p. 10).

[43] MF Luo, DA MacLaren, and W Allison. “Migration and abstraction of H-atoms from the Cu(111) surface.” English. In: *SURFACE SCIENCE* 586.1-3 (2005), 109–114 (cit. on p. 10).

[44] DJ Gaspar, AT Hanbicki, and SJ Sibener. “Inelastic multiphonon helium scattering from a stepped Ni(977) surface.” English. In: *JOURNAL OF CHEMICAL PHYSICS* 109.16 (1998), 6947–6955 (cit. on p. 10).

[45] M. Minniti, C. Diaz, J. L. Fernandez Cunado, A. Politano, D. Maccariello, F. Martin, D. Farias, and R. Miranda. “Helium, neon and argon diffraction from Ru(0001).” English. In: *JOURNAL OF PHYSICS-CONDENSED MATTER* 24.35 (2012) (cit. on p. 10).

[46] L MATTERA, R MUSENICH, C SALVO, and S TERRENI. “HYDROGEN DIFFRACTION FROM THE (110) SURFACE OF SILVER.” English. In: *FARADAY DISCUSSIONS* 80 (1985), 115–126 (cit. on p. 10).

[47] G PARSCHAU, E KIRSTEN, A BISCHOF, and KH RIEDER. “DIFFRACTION OF HE AND NE AND SELECTIVE ADSORPTION OF HE ON RH(110).” English. In: *PHYSICAL REVIEW B* 40.9 (1989), 6012–6017 (cit. on p. 10).

[48] DO HAYWARD and AO TAYLOR. “THE DIFFRACTION OF DEUTERIUM AND HELIUM FROM NI(111) SURFACES.” English. In: *JOURNAL OF PHYSICS C-SOLID STATE PHYSICS* 19.15 (1986), L309–L314 (cit. on p. 10).

[49] D Farias, M Patting, and KH Rieder. “A helium atom scattering study of the H/NiAl(110) adsorption system.” English. In: *JOURNAL OF CHEMICAL PHYSICS* 117.4 (2002), 1797–1803 (cit. on p. 10).

[50] M. Gostein, H. Parhikhteh, and G.O. Sitz. “"Survival probability of H_2 (v=1, j=1) scattered from Cu(110)".” English. In: *Physical Review Letters* 75.2 (1995), 342–345 (cit. on p. 10).

[51] A Hodgson, P Samson, A Wight, and C Cottrell. “Rotational excitation and vibrational relaxation of H-2 (upsilon=1,J=0) scattered from Cu(111).” English. In: *PHYSICAL REVIEW LETTERS* 78.5 (1997), 963–966 (cit. on p. 10).

[52] JM HORNE, SC YERKES, and DR MILLER. "AN EXPERIMENTAL INVESTIGATION OF THE ELASTIC-SCATTERING OF HE AND H-2 FROM AG(111)." English. In: *SURFACE SCIENCE* 93.1 (1980), 47–63 (cit. on p. 10).

[53] HJ ROBOTA, W VIELHABER, MC LIN, J SEGNER, and G ERTL. "DYNAMICS OF INTERACTION OF H-2 AND D2 WITH NI(110) AND NI(111) SURFACES." English. In: *SURFACE SCIENCE* 155.1 (1985), 101–120 (cit. on p. 10).

[54] P. Nieto, E. Pijper, D. Barredo, G. Laurent, R.A. Olsen, E.J. Baerends, G.J. Kroes, and D. Farias. ""Reactive and nonreactive scattering of H_2 from a metal surface is electronically adiabatic"." English. In: *Science* 312.5770 (2006), 86–89 (cit. on pp. 10, 107, 126).

[55] C Crespos, HD Meyer, RC Mowrey, and GJ Kroes. "Multiconfiguration time-dependent Hartree method applied to molecular dissociation on surfaces: H-2+Pt(111)." English. In: *JOURNAL OF CHEMICAL PHYSICS* 124.7 (2006) (cit. on pp. 10, 90, 130).

[56] M. F. Bertino, A. P. Graham, L. Y. Rusin, and J. P. Toennies. In: *J. Chem. Phys.* 109 (1998), 8036–8044 (cit. on pp. 10, 126).

[57] A HODGSON, J MORYL, P TRAVERSARO, and H ZHAO. "ENERGY-TRANSFER AND VIBRATIONAL EFFECTS IN THE DISSOCIATION AND SCATTERING OF D(2) FROM CU(111)." English. In: *NATURE* 356.6369 (1992), 501–504 (cit. on p. 10).

[58] D. Farías, R. Miranda, and K. H. Rieder. In: *J. Chem. Phys.* 117 (2002), 2255–2263 (cit. on pp. 10, 125, 126).

[59] M. F. Bertino, F. Hofmann, and J. P. Toennies. In: *J. Chem. Phys.* 106 (1997), 4327–4338 (cit. on pp. 10, 126).

[60] LV Goncharova, J Braun, AV Ermakov, GG Bishop, DM Smilgies, and BJ Hinch. "Cu(001) to HD energy transfer and translational to rotational energy conversion on surface scattering." English. In: *JOURNAL OF CHEMICAL PHYSICS* 115.16 (2001), 7713–7724 (cit. on p. 10).

[61] JP COWIN, CF YU, and L WHARTON. "HD SCATTERING FROM PT(111) - ROTATIONALLY MEDIATED SELECTIVE ADSORPTION." English. In: *SURFACE SCIENCE* 161.1 (1985), 221–233 (cit. on p. 10).

[62] J Baker, JJ Hernandez, J Li, JG Skofronick, SA Safron, and ES Gillman. "High resolution helium atom scattering from an epitaxially grown one monolayer film of KCN on KBr(001)." English. In: *SURFACE SCIENCE* 357.1-3 (1996). 13th International Vacuum Congress/9th International Conference on Solid Surfaces (IVC-13/ICSS-9), YOKOHAMA, JAPAN, SEP 25-29, 1995, 639–644 (cit. on p. 10).

[63] BF MASON and BR WILLIAMS. "ADSORPTION AND DESORPTION OF H-ATOMS ON INSB(001) AS VIEWED BY LEED AND HE ATOM SCATTERING." English. In: *SURFACE SCIENCE* 243.1-3 (1991), L74–L80 (cit. on p. 10).

[64] Junepyo Oh, Takahiro Kondo, Daigo Hatake, Yujiro Honma, Keitaro Arakawa, Takahiro Machida, and Junji Nakamura. "He and Ar beam scatterings from bare and defect induced graphite surfaces." English. In: *JOURNAL OF PHYSICS-CONDENSED MATTER* 22.30 (2010) (cit. on p. 10).

[65] JN SMITH, DR OKEEFE, and RL PALMER. "RARE-GAS SCATTERING FROM LIF . CORRELATION WITH LATTICE PROPERTIES .2." English. In: *JOURNAL OF CHEMICAL PHYSICS* 52.1 (1970), 315–& (cit. on p. 10).

[66] DR OKEEFE, RL PALMER, and JN SMITH. "RARE GAS SCATTERING FROM LIF .3. MULTILOBULAR STRUCTURE FOR NEON." English. In: *JOURNAL OF CHEMICAL PHYSICS* 55.9 (1971), 4572–& (cit. on p. 10).

[67] B WOOD, BF MASON, and BR WILLIAMS. "SCATTERING OF HE AND NE ATOMS FROM A (001) SURFACE OF SODIUM-FLUORIDE." English. In: *JOURNAL OF CHEMICAL PHYSICS* 61.4 (1974), 1435–1454 (cit. on p. 10).

[68] L Guillemot, S Lacombe, M Maazouz, E Sanchez, and VA Esaulov. "Inelastic collisions of Ne atoms and ions with a Si surface and effects of initial stages of oxidation." English. In: *SURFACE SCIENCE* 356.1-3 (1996), 92–100 (cit. on p. 10).

[69] G BOATO, P CANTINI, and L MATTERA. "DIFFRACTION OF NOZZLE MOLECULAR-BEAMS BY CRYSTAL-SURFACES AT LOW-TEMPERATURE." English. In: *JAPANESE JOURNAL OF APPLIED PHYSICS* 2 (1974), 553–556 (cit. on p. 10).

[70] G BOATO, P CANTINI, and L MATTERA. "ELASTIC AND ROTATIONALLY INELASTIC DIFFRACTION OF HYDROGEN MOLECULAR-BEAMS FROM (001) FACE OF LIF AT 80 DEGREESK." English. In: *JOURNAL OF CHEMICAL PHYSICS* 65.2 (1976), 544–549 (cit. on pp. 10, 12, 108).

[71] W. Allison and B. Feuerbacher. ""Rotationally Inelastic Molecule-surface Scattering"." English. In: *Physical Review Letters* 45.25 (1980), 2040–2043 (cit. on pp. 10, 108).

[72] E KOLODNEY and A AMIRAV. "ENERGY-DEPENDENCE OF DIFFRACTIVE AND INELASTIC-SCATTERING OF HE AND H-2 FROM MGO(100)." English. In: *SURFACE SCIENCE* 155.2-3 (1985), 715–731 (cit. on p. 10).

[73] G Benedek, F Traeger, and JP Toennies. “Spectroscopy of shear horizontal surface phonons by rotation-flip scattering of ortho-H-2 molecules.” English. In: *PHYSICAL REVIEW LETTERS* 94.8 (2005) (cit. on p. 10).

[74] G BRUSDEYLINS, G DROLSHAGEN, A KAUFHOLD, J SKOFRONICK, and JP TOENNIES. “DETERMINATION OF THE POTENTIAL FOR SIMULTANEOUS ROTATIONAL-EXCITATION AND DIFFRACTION IN SCATTERING OF D2 FROM LIF(001).” English. In: *SURFACE SCIENCE* 189 (1987), 972–974 (cit. on pp. 10, 12).

[75] Yasin Ekinci. “High Resolution Scattering of He Atoms and D_2 Molecules from the LiF(001) Crystal Surface.” PhD thesis. Georg-August-Universität zu Göttingen, 2003 (cit. on pp. 10, 12).

[76] R Valero, GJ Kroes, Y Ekinci, and JP Toennies. “Rotational transitions and diffraction in D-2 scattering from the LiF(001) surface: Theory and experiment.” English. In: *JOURNAL OF CHEMICAL PHYSICS* 124.23 (2006) (cit. on pp. 10, 12, 108, 109, 126).

[77] C Kittle. *”Introduction to Solid State Physics”*. Ed. by John Wiley and Sons. 1971 (cit. on pp. 10, 29, 30, 35, 40, 163).

[78] Richard M. Martin. *Electronic Structure: Basic Theory and Practical Methods*. Cambridge University Press, 2004 (cit. on pp. 10, 38).

[79] H. Nienhaus, H.S. Bergh, B. Gergen, A. Majumdar, W.H. Weinberg, and E.W. McFarland. “"Electron-hole pair creation at Ag and Cu surfaces by adsorption of atomic hydrogen and deuterium".” English. In: *Physical Review Letters* 82.2 (1999), 446–449 (cit. on p. 11).

[80] Eckart Hasselbrink. “"Non-adiabaticity in surface chemical reactions".” English. In: *Surface Science* 603.10-12 (2009), 1564–1570 (cit. on p. 11).

[81] D. Krix, R. Nuenthel, and H. Nienhaus. “"Generation of hot charge carriers by adsorption of hydrogen and deuterium atoms on a silver surface".” English. In: *Physical Review B* 75.7 (2007) (cit. on p. 11).

[82] B.N.J. Persson and M. Persson. “"Damping of vibrations in molecules adsorbed on a metal-surface".” English. In: *Surface Science* 97.2-3 (1980), 609–624 (cit. on p. 11).

[83] A. Gross and W. Brenig. “"Vibrational-excitation of NO in NO/Ag scattering revisited".” English. In: *Surface Science* 289.3 (1993), 335–339 (cit. on p. 11).

[84] C.T. Rettner. “"Reaction of an H-atom beam with Cl/Au(111) - dynamics of concurrent Eley-Rideal and Langmuir-Hinshelwood mechanisms".” English. In: *Journal Of Chemical Physics* 101.2 (1994), 1529–1546 (cit. on p. 11).

[85] Serge Monturet and Peter Saalfrank. “"Role of electronic friction during the scattering of vibrationally excited nitric oxide molecules from Au(111)".” English. In: *Physical Review B* 82.7 (2010) (cit. on p. 11).

[86] A. Bansal, X. Li, I. Lauermann, N. S. Lewis, S. I. Yi, and W. H. Weinberg. In: *J. Am. Chem. Soc.* 118 (1996), 7225–7226 (cit. on pp. 11, 125).

[87] A. Bansal and N. S. Lewis. In: *J. Phys. Chem. B* 102 (1998), 1067–1070 (cit. on pp. 11, 125).

[88] L. J. Webb and N. S. Lewis. In: *J. Phys. Chem. B* 107 (2003), 5404–5412 (cit. on pp. 11, 125).

[89] S. Maldonado, K. E. Plass, D. Knapp, and N. S. Lewis. In: *J. Phys. Chem. C* 111 (2007), 17690–17699 (cit. on pp. 11, 125).

[90] K. E. Plass, X. Liu, B. S. Brunschwig, and N. S. Lewis. In: *Chem. Mater.* 20 (2008), 2228–2233 (cit. on pp. 11, 125).

[91] S. Maldonado and N. S. Lewis. In: *J. Electrochem. Soc.* 156 (2009), H123–128 (cit. on pp. 11, 125).

[92] MJ CARDILLO, GE BECKER, SJ SIBENER, and DR MILLER. “THE DIFFRACTION OF HE ATOMS AT THE GAAS(110) SURFACE.” English. In: *SURFACE SCIENCE* 107.2-3 (1981), 469–493 (cit. on p. 11).

[93] H Winter. “Scattering of atoms and ions from insulator surfaces.” English. In: *PROGRESS IN SURFACE SCIENCE* 63.7-8 (2000), 177–247 (cit. on p. 12).

[94] J. Lienemann, A. Schüller, D. Blauth, J. Seifert, S. Wethekam, M. Busch, K. Maass, and H. Winter. “"Coherence during scattering of fast H atoms from a LiF(001) surface."” In: *Phys Rev Lett.* 106 (2011), p. 067602 (cit. on pp. 12, 86, 88, 99).

[95] M. Busch, J. Lienemann, J. Seifert, A. Schueller, and H. Winter. “Decoherence in grazing scattering of fast H and He atoms from a LiF(001) surface.” English. In: *VACUUM* 86.10 (2012), 1618–1623 (cit. on p. 12).

[96] MF Bertino, AL Glebov, JP Toennies, F Traeger, E Pijper, GJ Kroes, and RC Mowrey. “Observation of large differences in the diffraction of normal- and para-H-2 from LiF(001).” English. In: *PHYSICAL REVIEW LETTERS* 81.25 (1998), 5608–5611 (cit. on pp. 12, 108, 109).

[97] JC RUIZ SUAREZ, ML KLEIN, MA MOLLER, PA ROWNTREE, G SCOLES, and J XU. "STRUCTURE OF PHYSISORBED OVERLAYERS OF DIPOLAR MOLECULES - A COMBINED STUDY BY ATOMIC-BEAM SCATTERING AND MOLECULAR-DYNAMICS." English. In: *PHYSICAL REVIEW LETTERS* 61.6 (1988), 710–713 (cit. on p. 12).

[98] PA ROWNTREE, G SCOLES, and JC RUIZSUAREZ. "LOW-ENERGY HELIUM SCATTERING FROM ORDERED PHYSISORBED LAYERS OF POLAR-MOLECULES." English. In: *JOURNAL OF PHYSICAL CHEMISTRY* 94.23 (1990), 8511–8522 (cit. on p. 12).

[99] MN Carre, D Lemoine, S Picaud, and C Girardet. "He-diffraction investigation of the (1x1) CO phase on NaCl(100): A fully quantum study." English. In: *SURFACE SCIENCE* 347.1-2 (1996), 128–142 (cit. on p. 12).

[100] A. Schueller, S. Wethekam, and H. Winter. "Diffraction of fast atomic projectiles during grazing scattering from a LiF(001) surface." English. In: *PHYSICAL REVIEW LETTERS* 98.1 (2007) (cit. on p. 12).

[101] P. Rousseau, H. Khemliche, A. G. Borisov, and P. Roncin. "Quantum Scattering of Fast Atoms and Molecules on Surfaces." In: *Phys. Rev. Lett.* 98 (1 Jan. 2007), p. 016104 (cit. on pp. 12, 85, 86, 108).

[102] A. Schüller and H. Winter. ""Supernumerary rainbows in the angular distribution of scattered projectiles for grazing collisions of fast atoms with a LiF(001) surface."" In: *Phys Rev Lett.* 100 (2008), p. 097602 (cit. on pp. 12, 86).

[103] B. Lalmi, H. Khemliche, A. Momeni, P. Soulisse, and P. Roncin. ""High resolution imaging of superficial mosaicity in single crystals using grazing incidence fast atom diffraction"." In: *J Phys Condens Matter.* (2012) (cit. on pp. 12, 86).

[104] U. Specht, M. Busch, J. Seifert, H. Winter, K. Gärtner, R. Włodarczyk, M. Sierka, and J. Sauer. "Classical and quantum mechanical rainbow-scattering of fast He atoms from a KCl(0 0 1) surface." In: *Nuclear Instruments and Methods in Physics Research Section B: Beam Interactions with Materials and Atoms* 269.9 (2011). Atomic Collisions in SolidsProceedings of the 24th International Conference on Atomic Collisions in Solids (ICACS-24), pp. 799–803 (cit. on pp. 12, 86).

[105] Patrick Rousseau, Hocine Khemliche, Nenad Bundaleski, Pierre Soulisse, Anouchah Momeni, and Philippe Roncin. "Surface analysis with grazing incidence fast atom diffraction (GIFAD)." In: *Journal of Physics: Conference Series* 133.1 (2008), p. 012013 (cit. on pp. 12, 93–97, 100, 102, 109, 121, 123, 145).

[106] Y Ekinci and JP Toennies. “Elastic and rotationally inelastic diffraction of D-2 molecules from the LiF(001) surface.” English. In: *PHYSICAL REVIEW B* 72.20 (2005) (cit. on pp. 12, 108, 126, 133, 134).

[107] H. Winter and A. Schueller. “"Fast atom diffraction during grazing scattering from surfaces".” English. In: *Progress In Surface Science* 86.9-10 (2011), 169–221 (cit. on pp. 12–15, 85, 86, 92, 94, 98, 101, 108, 109, 145, 171).

[108] H. Khemliche, P. Rousseau, P. Roncin, V. H. Etgens, and F. Finocchi. “Grazing incidence fast atom diffraction: An innovative approach to surface structure analysis.” In: *Applied Physics Letters* 95.15, 151901 (2009) (cit. on pp. 12, 86).

[109] A. Schueller, M. Busch, S. Wethekam, and H. Winter. “Fast Atom Diffraction from Superstructures on a Fe(110) Surface.” English. In: *PHYSICAL REVIEW LETTERS* 102.1 (2009) (cit. on p. 12).

[110] A. Schüller, M. Busch, J. Seifert, S. Wethekam, H. Winter, and K. Gärtner. “"Superstructures of oxygen and sulphur on a Fe(110) surface via fast atom diffraction".” In: *Physical Review B* 79.23 (2009) (cit. on pp. 12, 86).

[111] J. Seifert, A. Schüller, H. Winter, R. Włodarczyk, J. Sauer, and M. Sierka. “Diffraction of fast atoms during grazing scattering from the surface of an ultrathin silica film on Mo(112).” In: *Phys. Rev. B* 82 (3 July 2010), p. 035436 (cit. on pp. 12, 86, 108).

[112] J. Seifert, M. Busch, A. Schueller, D. Blauth, S. Wethekam, and H. Winter. “Structure of ultrathin silica films on Mo(112) studied via Classical and Quantum Mechanical Rainbow Scattering of Fast Atoms.” English. In: *SURFACE AND INTERFACE ANALYSIS* 42.10-11 (2010). 7th International Symposium on Atomic Level Characterizations for New Materials and Devices, Maui, HI, DEC 06-11, 2009, 1575–1580 (cit. on p. 12).

[113] N. Bundaleski, H. Khemliche, P. Soulisse, and P. Roncin. “"Grazing incidence diffraction of keV helium atoms on a Ag(110) surface."” In: *Phys Rev Lett.* (2008) (cit. on pp. 12, 86).

[114] M. Busch, A. Schüller, S. Wethekam, and H. Winter. “Fast atom diffraction at metal surface.” In: *Surface Science* 603.3 (2009), pp. L23 –L26 (cit. on pp. 12, 86).

[115] RA BARAGIOLA, EV ALONSO, and AO FLORIO. “ELECTRON-EMISSION FROM CLEAN METAL-SURFACES INDUCED BY LOW-ENERGY LIGHT-IONS.” English. In: *PHYSICAL REVIEW B* 19.1 (1979), 121–129 (cit. on p. 13).

[116] H Winter and HP Winter. “Classical model of kinetic electron emission near threshold induced by impact of atomic projectiles on a free-electron gas metal.” English. In: *EUROPHYSICS LETTERS* 62.5 (2003), 739–745 (cit. on p. 13).

[117] H Winter. “Collisions of atoms and ions with surfaces under grazing incidence.” English. In: *PHYSICS REPORTS-REVIEW SECTION OF PHYSICS LETTERS* 367.5 (2002), 387–582 (cit. on p. 13).

[118] DS GEMMELL. “CHANNELING AND RELATED EFFECTS IN MOTION OF CHARGED-PARTICLES THROUGH CRYSTALS.” English. In: *REVIEWS OF MODERN PHYSICS* 46.1 (1974), 129–227 (cit. on p. 15).

[119] H. Winter J. Seifert. “"Structure of monolayer silica on Mo(1 1 2) investigated by rainbow scattering under axial surface channeling".” In: *Surface Science* (2009) (cit. on pp. 15, 86).

[120] G.R. Darling and S. Holloway. “"Angular and vibrational effects in the sticking and scattering of H_2".” English. In: *Journal Of Chemical Physics* 97.7 (1992), 5182–5192 (cit. on p. 17).

[121] G.R. Darling and S. Holloway. “"Dissociation thresholds and the vibrational-excitation process in the scattering of H_2".” English. In: *Surface Science* 307 (1994), 153–158 (cit. on p. 17).

[122] Attila Szabo and Neil S. Ostlund. *Modern Quantum Chemistry, introduction to Advanced Electron Structure Theory*. Ed. by McGraw-Hill publishing. Dover publications, inc., 1989 (cit. on p. 32).

[123] W. Kohn and L.J. Sham. “Self-consistent equations including exchange and correlation effects.” In: *Physical Review* 140.4A (1965), pp. 1133–& (cit. on p. 33).

[124] J.P. Perdew, J.A. Chevary, S.H. Vosko, K.A. Jackson, M.R. Pederson, D.J. Singh, and C. Fiolhais. “"Atoms, molecules, solids, and surfaces - applications of the generalized gradient approximation for exchange and correlation".” English. In: *Physical Review B* 46.11 (1992), 6671–6687 (cit. on pp. 34, 89, 111, 163).

[125] John P. Perdew, Kieron Burke, and Matthias Ernzerhof. “Generalized Gradient Approximation Made Simple.” In: *Phys. Rev. Lett.* 77 (18 1996), pp. 3865–3868 (cit. on pp. 34, 128, 163).

[126] D. Vanderbilt. “"Soft self-consistent pseudopotentials in a generalized eigenvalue formalism".” English. In: *Physical Review B* 41.11 (1990), 7892–7895 (cit. on pp. 38, 163).

[127] P. E. Blöchl. “Projector augmented-wave method.” In: *Phys. Rev. B* 50 (24 Dec. 1994), pp. 17953–17979 (cit. on pp. 38, 39, 89, 112, 128, 163).

[128] G. Kresse. and D. Joubert. “From ultrasoft pseudopotentials to the projector augmented-wave method.” In: *Physical Review B* 59.3 (1999), 1758(18) (cit. on p. 38).

[129] M. Methfessel and A. T. Paxton. “High-precision sampling for Brillouin-zone integration in metals.” In: *Physical Review B* 40.6 (1989), 3616(6) (cit. on p. 41).

[130] G. Kresse and J. Furthmüller. “Efficient iterative schemes for *ab initio* total-energy calculations using a plane-wave basis set.” In: *Phys. Rev. B* 54 (16 Oct. 1996), pp. 11169–11186 (cit. on pp. 41, 89, 111, 127).

[131] G Kresse. “Dissociation and sticking of H-2 On the Ni(111), (100), and (110) substrate.” English. In: *PHYSICAL REVIEW B* 62.12 (2000), 8295–8305 (cit. on p. 44).

[132] R. A. Olsen, H. F. Busnengo, A. Salin, M. F. Somers, G. J. Kroes, and E. J. Baerends. “"Constructing accurate potential energy surfaces for a diatomic molecule interacting with a solid surface: H2+Pt(111) and H2+Cu(100)".” In: *The Journal of Chemical Physics* 116.9 (2002), pp. 3841–3855 (cit. on pp. 44, 49, 107, 110).

[133] M. Alducin, H. F. Busnengo, and R. Díez-Muiño. In: *J. Chem. Phys.* 119 (2008), p. 224702 (cit. on p. 44).

[134] G. Laurent, F. Martin, and H. F. Busnengo. “Theoretical study of hydrogen dissociative adsorption on strained pseudomorphic monolayers of Cu and Pd deposited onto a Ru(0001) substrate.” English. In: *PHYSICAL CHEMISTRY CHEMICAL PHYSICS* 11.33 (2009), 7303–7311 (cit. on pp. 44, 107).

[135] I. Goikoetxea, M. Alducin, R. Diez Muino, and J. I. Juaristi. “Dissociative and non-dissociative adsorption dynamics of N-2 on Fe(110).” English. In: *PHYSICAL CHEMISTRY CHEMICAL PHYSICS* 14.20 (2012), 7471–7480 (cit. on p. 44).

[136] M. Blanco-Rey, E. Díaz, G. A. Bocan, R. Díez-Muiño, M. Alducin, and J. I. Juaristi. In: *Phys. Chem. Chem. Phys.* 14 (2013), p. 7471 (cit. on pp. 44, 107).

[137] Josef Ischtwan and Michael A. Collins. “Molecular potential energy surfaces by interpolation.” In: *Journal of Chemical Physics* 100.11 (1994), pp. 8080–8088 (cit. on pp. 58, 61, 128).

[138] Oded Godsi, Christian R. Evenhuis, and Michael A. Collins. “Interpolation of multidimensional diabatic potential energy matrices.” In: *The Journal of Chemical Physics* 125.10 (2006), 104105(18) (cit. on p. 58).

[139] Hai-Anh Le, Terry J. Frankcombe, and Michael A. Collins. “Reaction dynamics of H-3(+)+CO on an interpolated potential enery surface.” In: *Journal of Physical Chemistry A* 114.40 (2010), pp. 10783–10788 (cit. on p. 58).

[140] .C Crespos, Michael A. Collins, E. Pijper, and Geert-Jan Kroes. "Application of the modified Shepard interpolation method to the determination of the potential energy surface for a molecule-surface reaction H-2+Pt(111)." In: *Journal of Chemical Physics* 120.5 (2004), pp. 2392–2404 (cit. on pp. 58, 107, 128).

[141] C. Díaz, J. K. Vincent, G. P. Krishnamohan, R. A. Olsen, G. J. Kroes, K. Honkala, and J. K. Norskov. ""Reactive and nonreactive scattering of N_2 from Ru(0001): A six-dimensional adiabatic study"." English. In: *Journal Of Chemical Physics* 125.11 (2006) (cit. on pp. 58, 107, 128).

[142] C. Díaz, R. A. Olsen, H. F. Busnengo, and G. J. Kroes. ""Dynamics on Six-Dimensional Potential Energy Surfaces for H_2/Cu(111): Corrugation Reducing Procedure versus Modified Shepard Interpolation Method and PW91 versus RPBE"." English. In: *Journal Of Physical Chemistry C* 114.25 (2010), 11192–11201 (cit. on pp. 58, 107, 128).

[143] K.C. Thompson, M.J.T. Jordan, and Michael A. Collins. "Polyatomic molecular potential energy surfaces by interpolation in local internal coordinates." In: *Journal of Chemical Physics* 108.20 (1998), pp. 8302–8316 (cit. on p. 58).

[144] Ryan P.A. Bettens and Michael A. Collins. "Learning to interpolate molecular potential energy surfaces with confidence: a Bayesian approach." In: *Journal of Chemical Physics* 111.3 (1999), pp. 816–826 (cit. on pp. 61, 128).

[145] J Stoer and R Burlisch. *"Introduction to Numerical Analysis"*. Ed. by New York. Springer, 1993 (cit. on p. 67).

[146] R.A. Leacock and P.W. Oconnor. ""Action-variable theory and classical frequencies"." English. In: *Journal Of Computational Physics* 62.1 (1986), 164–179 (cit. on p. 70).

[147] C. Díaz, P. Rivière, and F. Martín. "Molecular Effects in $\mathbf{H}_2$ Scattering from Metal Surfaces at Grazing Incidence." In: *Phys. Rev. Lett.* 103 (1 June 2009), p. 013201 (cit. on pp. 71, 85, 90, 171).

[148] Haobin Wang and Michael Thoss. "Multilayer formulation of the multiconfigurational time-dependent Hartree theory." In: *Journal of Chemical Physics* 119.3 (2003), pp. 1289–1299 (cit. on p. 74).

[149] M.H. Beck and H.D Meyer. "An efficient and robust integration scheme for the equations of motion of the multiconfiguration time-dependent Hartree (MCTDH) method." In: *ZEITSCHRIFT FUR PHYSIK D-ATOMS MOLECULES AND CLUSTERS* 42.2 (1997), pp. 113–129 (cit. on p. 75).

[150] *On-line documentation of the Heidelberg MCTDH Package*. URL: http://www.pci.uni-heidelberg.de/tc/usr/mctdh/doc.83/ (cit. on pp. 76, 90, 116, 130).

[151] A. Jackle and H.D Meyer. “Product representation of potential energy surfaces.” In: *Journal of Chemical Physics* 104.20 (1996), pp. 7974–7984 (cit. on pp. 76, 92, 116, 131).

[152] A. Jackle and H.D Meyer. “Product representation of potential energy surfaces. II.” In: *Journal of Chemical Physics* 109.10 (1998), pp. 3772–3779 (cit. on pp. 76, 92, 116).

[153] *The Heidelberg MCTDH Package: a set of programs for multi-dimensional quantum dynamics. User guide.* URL: http://www.pci.uni-heidelberg.de/tc/usr/mctdh/doc.83/guide/guide.ps (cit. on pp. 77, 90, 116).

[154] Hans-Dieter Meyer, Fabien Gatti, and Graham A. Worth. “Multidimensional Quantum Dynamics: MCTDH Theory and Applications.” In: First. WILEY-VCH Verlag GmbH & Co. KGaA, 2009. Chap. 20, pp. 249–273 (cit. on pp. 78, 87, 90, 116).

[155] A. Jackle and H.D Meyer. “Time-dependent calculation of reactive flux employing complex absorbing potentials: General aspects abd application within the multiconfigurational time-dependent Hartree wave approach.” In: *Journal of Chemical Physics* 105.16 (1996), pp. 6778–6786 (cit. on p. 80).

[156] A.S. Muzas, F. Martín, and C. Díaz. “"Scattering of H(D) from LiF(1 0 0) under fast grazing incidence conditions: To what extent is classical dynamics a useful tool?"” In: *Nuclear Instruments and Methods in Physics Research Section B: Beam Interactions with Materials and Atoms* 354 (2015). 26th International Conference on Atomic Collisions in Solids, pp. 9–15 (cit. on pp. 85, 93, 101, 108, 111, 117, 122).

[157] E.A. Andreev. “"Quantum and classical characteristics of glancing scattering of fast atoms on the surface of a crystal".” In: *Russian Journal of Physical Chemistry* 76 (2002), p. 164 (cit. on p. 85).

[158] Schüller, A., Wethekam, S., and H. Winter. “Diffraction of Fast Atomic Projectiles during Grazing Scattering from a LiF(001) Surface.” In: *Phys. Rev. Lett.* 98 (1 Jan. 2007), p. 016103 (cit. on pp. 85, 86, 108).

[159] A. Salin. “Classical impact parameter approximation: Application to atomic collisions with n independent electrons and to recoil analysis.” English. In: *The European Physical Journal D* 8.2 (2000), pp. 189–192 (cit. on p. 85).

[160] P. Tiwald, A. Schüller, H. Winter, K. Tökesi, F. Aigner, S. Gräfe, C. Lemell, and J. Burgdörfer. “Interaction potentials for fast atoms in front of Al surfaces probed by rainbow scattering.” In: *Phys. Rev. B* 82 (12 Sept. 2010), p. 125453 (cit. on pp. 86, 108).

[161] C. A. Ríos Rubiano, G. A. Bocan, M. S. Gravielle, N. Bundaleski, H. Khemliche, and P. Roncin. "*Ab initio* potential for the He-Ag(110) interaction investigated using grazing-incidence fast-atom diffraction." In: *Phys. Rev. A* 87 (1 Jan. 2013), p. 012903 (cit. on pp. 86, 87, 108).

[162] H. Winter J. Seifert. ""Young-type interference for scattering of fast helium atoms from an oxygen covered Mo(112) surface."" In: *Phys Rev Lett.* 108 (2012), p. 065503 (cit. on p. 86).

[163] M. Busch, J. Seifert, E. Meyer, and H. Winter. "Evidence for longitudinal coherence in fast atom diffraction." In: *Phys. Rev. B* 86 (24 Dec. 2012), p. 241402 (cit. on p. 86).

[164] A. Schüller, D. Blauth, J. Seifert, M. Busch, H. Winter, K. Gärtner, R. Włodarczyk, J. Sauer, and M. Sierka. "Fast atom diffraction during grazing scattering from a MgO(001) surface." In: *Surface Science* 606.3–4 (2012), pp. 161–173 (cit. on pp. 86, 108).

[165] Schüller, A., Winter, H., Gravielle, M. S., Pruneda, J. M., and J. E. Miraglia. "He-LiF surface interaction potential from fast atom diffraction." In: *Phys. Rev. A* 80 (6 Dec. 2009), p. 062903 (cit. on pp. 86, 87, 108).

[166] H. Winter, J. I. Juaristi, I. Nagy, A. Arnau, and P. M. Echenique. "Energy loss of slow ions in a nonuniform electron gas." In: *Phys. Rev. B* 67 (24 June 2003), p. 245401 (cit. on p. 86).

[167] Antonia Ruiz, José P. Palao, and Eric J. Heller. "Classical and quantum analysis of quasiresonance in grazing atom-surface collisions." In: *Phys. Rev. A* 79 (5 May 2009), p. 052901 (cit. on pp. 86, 108).

[168] Antonia Ruiz and José P. Palao. "Effects of classical nonlinear resonances in grazing diatom-surface collisions." In: *The Journal of Chemical Physics* 137.8, 084302 (2012) (cit. on p. 86).

[169] Ricardo Diez Muino. M. S. Gravielle Gisela Anahí Bocan. ""Diffraction of swift atoms after grazing scattering from metal surfaces: N/Ag(111) system"." In: *Physical Review A* 82 (2010), p. 052904 (cit. on pp. 87, 108).

[170] J. R. Manson, Hocine Khemliche, and Philippe Roncin. "Theory of grazing incidence diffraction of fast atoms and molecules from surfaces." In: *Phys. Rev. B* 78 (15 Oct. 2008), p. 155408 (cit. on p. 87).

[171] C.J. Ray and J.M. Bowman. "Quasiclassical trajectory calculations of He–LiF (001) diffraction scattering." In: *J. Chem. Phys., v. 63, no. 12, pp. 5231-5234* (Dec. 1975) (cit. on pp. 87, 90).

[172] Charles J. Ray and Joel M. Bowman. ""Quasiclassical studies of rigid rotor–solid surface diffraction scattering"." In: *The Journal of Chemical Physics* 66.3 (1977), pp. 1122–1126 (cit. on pp. 87, 90).

[173] J.M. Bowman S.C. Park. “"Another derivation of the cos theta-law for molecules scattered statistically from surfaces".” In: *Chemical Physics Letters* 110 (1984), p. 383 (cit. on p. 87).

[174] Subhash Saini, David A. Dows, and H.S. Taylor. “Quasiclassical trajectory study of H2/LiF(001) corrugated surface scattering: Comparison with other theoretical results.” In: *Chemical Physics* 90.1–2 (1984), pp. 87–98 (cit. on p. 87).

[175] G.J. Kroes. “"Six-dimensional quantum dynamics of dissociative chemisorption of H_2 on metal surfaces".” English. In: *Progress In Surface Science* 60.1-4 (1999), 1–85 (cit. on pp. 87, 107, 109, 113).

[176] G. Kresse and J. Hafner. “*Ab initio* molecular dynamics for liquid metals.” In: *Phys. Rev. B* 47 (1 Jan. 1993), pp. 558–561 (cit. on pp. 89, 111, 127).

[177] N. A. Smirnov. “*Ab initio* calculations of the thermodynamic properties of LiF crystal.” In: *Phys. Rev. B* 83 (1 Jan. 2011), p. 014109 (cit. on pp. 89, 164).

[178] Jun Liu, L. Dubrovinsky, T. Boffa Ballaran, and W. Crichton. “"Equation of state and thermal expansivity of LiF and NaF".” In: *High Pressure Research* 27.4 (2007), pp. 483–489 (cit. on pp. 89, 164).

[179] Neng-Ping Wang, Michael Rohlfing, Peter Krüger, and Johannes Pollmann. “Quasiparticle band structure and optical spectrum of LiF(001).” In: *Phys. Rev. B* 67 (11 Mar. 2003), p. 115111 (cit. on p. 89).

[180] F. W. de Wette, W. Kress, and U. Schröder. “Relaxation of the rocksalt (001) surface: Alkali halides, MgO, and PbS.” In: *Phys. Rev. B* 32 (6 Sept. 1985), pp. 4143–4157 (cit. on p. 89).

[181] C. Díaz, H. F. Busnengo, P. Rivière, D. Farías, P. Nieto, M. F. Somers, G. J. Kroes, A. Salin, and F. Martín. “"A classical dynamics method for H2 diffraction from metal surfaces".” In: *The Journal of Chemical Physics* 122.15, 154706 (2005), pp. – (cit. on p. 90).

[182] R van Harrevelt and U Manthe. “Multiconfigurational time-dependent Hartree calculations for dissociative adsorption of H-2 on Cu(100).” English. In: *JOURNAL OF CHEMICAL PHYSICS* 121.8 (2004), 3829–3835 (cit. on pp. 90, 130).

[183] G. J. Kroes and H.-D. Meyer. “Using n-mode potentials for reactive scattering: Application to the 6D H-2+Pt(111) problem.” English. In: *CHEMICAL PHYSICS LETTERS* 440.4-6 (2007), 334–340 (cit. on p. 90).

[184] G. P. Krishnamohan, R. A. Olsen, G. J. Kroes, F. Gatti, and S. Woittequand. "Quantum dynamics of dissociative chemisorption of CH4 on Ni(111): Influence of the bending vibration." English. In: *JOURNAL OF CHEMICAL PHYSICS* 133.14 (2010) (cit. on pp. 90, 130).

[185] M. del Cueto, A.S. Muzas, G. Füchsel, F. Gati, F. Martín, and C. Díaz. "Role of van der Waals forces in the diffraction of noble gases from metal surfaces." In: *Physical Review B* 93 (2016), 060301(R) (cit. on pp. 90, 130).

[186] Salvador Miret-Artés and Eli Pollak. "Classical theory of atom–surface scattering: The rainbow effect." In: *Surface Science Reports* 67.7–8 (2012), pp. 161–200 (cit. on p. 95).

[187] C. Díaz, E. Pijper, R. A. Olsen, H. F. Busnengo, D. J. Auerbach, and G. J. Kroes. ""Chemically Accurate Simulation of a Prototypical Surface Reaction: H_2 Dissociation on Cu(111)"." English. In: *Science* 326.5954 (2009), 832–834 (cit. on pp. 101, 107).

[188] M. Wijzenbroek and G. J. Kroes. "The effect of the exchange-correlation functional on H-2 dissociation on Ru(0001)." English. In: *JOURNAL OF CHEMICAL PHYSICS* 140.8 (2014) (cit. on pp. 101, 107).

[189] A Gross. ""Reactions at surfaces studied by ab initio dynamics calculations"." English. In: *Surface Science Reports* 32.8 (1998), 291–340 (cit. on p. 107).

[190] GJ Kroes and MF Somers. "Six-dimensional dynamics of dissociative chemisorption of H-2 on metal surfaces." English. In: *JOURNAL OF THEORETICAL & COMPUTATIONAL CHEMISTRY* 4.2 (2005), 493–581 (cit. on pp. 107, 113, 126).

[191] G J. Kroes and C. Díaz. In: *Chem. Soc. Rev* (2016) (cit. on p. 107).

[192] P Riviere, HF Busnengo, and F Martin. "Density functional theory study of H and H-2 interacting with NiAl(110)." English. In: *JOURNAL OF CHEMICAL PHYSICS* 121.2 (2004), 751–760 (cit. on p. 107).

[193] M Luppi, DA McCormack, RA Olsen, and EJ Baerends. "Rotational effects in the dissociative adsorption of H-2 on the Pt(211) stepped surface." English. In: *JOURNAL OF CHEMICAL PHYSICS* 123.16 (2005) (cit. on p. 107).

[194] JK Vincent, RA Olsen, GJ Kroes, M Luppi, and EJ Baerends. "Six-dimensional quantum dynamics of dissociative chemisorption of H-2 on Ru(0001)." English. In: *JOURNAL OF CHEMICAL PHYSICS* 122.4 (2005) (cit. on p. 107).

[195] M. Alducin, R. Diez Muino, H. F. Busnengo, and A. Salin. "Low sticking probability in the nonactivated dissociation of N-2 molecules on W(110)." English. In: *JOURNAL OF CHEMICAL PHYSICS* 125.14 (2006) (cit. on p. 107).

[196] H. Fabio Busnengo and Alejandra E. Martinez. "H-2 chemisorption on W(100) and W(110) surfaces." English. In: *JOURNAL OF PHYSICAL CHEMISTRY C* 112.14 (2008), 5579–5588 (cit. on p. 107).

[197] M. Alducin, H. F. Busnengo, and R. Diez Muino. "Dissociative dynamics of spin-triplet and spin-singlet O-2 on Ag(100)." English. In: *JOURNAL OF CHEMICAL PHYSICS* 129.22 (2008) (cit. on p. 107).

[198] Jian-Cheng Chen, Maxi Ramos, Carina Arasa, Juan Carlos Juanes-Marcos, Mark F. Somers, Alejandra E. Martinez, Cristina Diaz, Roar A. Olsen, and Geert-Jan Kroes. "Dynamics of H-2 dissociation on the 1/2 ML c(2 x 2)-Ti/Al(100) surface." English. In: *PHYSICAL CHEMISTRY CHEMICAL PHYSICS* 14.9 (2012), 3234–3247 (cit. on p. 107).

[199] R van Harrevelt, K Honkala, JK Norskov, and U Manthe. "The reaction rate for dissociative adsorption of N-2 on stepped Ru(0001): Six-dimensional quantum calculations." English. In: *JOURNAL OF CHEMICAL PHYSICS* 122.23 (2005) (cit. on p. 107).

[200] P. N. Abufager, C. Crespos, and H. F. Busnengo. "Modified Shepard interpolation method applied to trapping mediated adsorption dynamics." In: *PHYSICAL CHEMISTRY CHEMICAL PHYSICS* 9.18 (2007), 2258–2265 (cit. on p. 107).

[201] J. Behler, B. Delley, S. Lorenz, K. Reuter, and M. Scheffler. ""Dissociation of O-2 at Al(111): the role of spin selection rules"." English. In: *Physical Review Letters* 94.3 (2005) (cit. on p. 107).

[202] Jorg Behler, Sonke Lorenz, and Karsten Reuter. "Representing molecule-surface interactions with symmetry-adapted neural networks." English. In: *JOURNAL OF CHEMICAL PHYSICS* 127.1 (2007) (cit. on p. 107).

[203] Jeffery Ludwig and Dionisios G. Vlachos. "Ab initio molecular dynamics of hydrogen dissociation on metal surfaces using neural networks and novelty sampling." In: *JOURNAL OF CHEMICAL PHYSICS* 127.15 (2007) (cit. on p. 107).

[204] Joerg Behler. "Neural network potential-energy surfaces in chemistry: a tool for large-scale simulations." In: *PHYSICAL CHEMISTRY CHEMICAL PHYSICS* 13.40 (2011), 17930–17955 (cit. on p. 107).

[205] Bin Jiang and Hua Guo. "Six-dimensional quantum dynamics for dissociative chemisorption of H-2 and D-2 on Ag(111) on a permutation invariant potential energy surface." In: *PHYSICAL CHEMISTRY CHEMICAL PHYSICS* 16.45 (2014), 24704–24715 (cit. on p. 107).

[206] Bin Jiang, Xuefeng Ren, Daiqian Xie, and Hua Guo. "Enhancing dissociative chemisorption of H2O on Cu(111) via vibrational excitation." In: *PROCEEDINGS OF THE NATIONAL ACADEMY OF SCIENCES OF THE UNITED STATES OF AMERICA* 109.26 (2012), 10224–10227 (cit. on p. 107).

[207] P. Morten Hundt, Bin Jiang, Maarten E. van Reijzen, Hua Guo, and Rainer D. Beck. "Vibrationally Promoted Dissociation of Water on Ni(111)." In: *SCIENCE* 344.6183 (2014), 504–507 (cit. on p. 107).

[208] R. Frisch and O. Stern. "Abnormality in the specular reflection and diffraction of molecular beams of crystal cleavage planes. I." In: *ZEITSCHRIFT FUR PHYSIK* 84.7-8 (1933), 430–442 (cit. on p. 108).

[209] R HORNE and LJF HERMANS. "ROTATIONAL POLARIZATION PRODUCED BY MOLECULE-LIF (001) COLLISIONS IN A KNUDSEN PARTICLE FLOW BETWEEN 78-K AND 695-K." In: *JOURNAL OF CHEMICAL PHYSICS* 91.2 (1989), 1261–1267 (cit. on p. 108).

[210] G WOLKEN. "COLLISION OF A DIATOMIC MOLECULE WITH A SOLID SURFACE." In: *JOURNAL OF CHEMICAL PHYSICS* 59.3 (1973), 1159–1165 (cit. on p. 108).

[211] G WOLKEN. "THEORETICAL STUDIES OF ATOM-SOLID ELASTIC-SCATTERING - HE+LIF." In: *JOURNAL OF CHEMICAL PHYSICS* 58.7 (1973), 3047–3064 (cit. on p. 108).

[212] G WOLKEN. "ROTATIONAL TRANSITIONS IN MOLECULE-SOLID SCATTERING." In: *JOURNAL OF CHEMICAL PHYSICS* 62.7 (1975), 2730–2735 (cit. on p. 108).

[213] LM HUBBARD, S SHI, and WH MILLER. "MULTICHANNEL DISTORTED-WAVE BORN APPROXIMATION FOR REACTIVE SCATTERING." In: *JOURNAL OF CHEMICAL PHYSICS* 78.5 (1983), 2381–2387 (cit. on p. 108).

[214] G DROLSHAGEN, A KAUFHOLD, and JP TOENNIES. "QUANTUM CALCULATIONS FOR DIFFRACTIVE AND ROTATIONALLY INELASTIC H2/LIF (001) SCATTERING." In: *JOURNAL OF CHEMICAL PHYSICS* 83.2 (1985), 827–834 (cit. on p. 108).

[215] U GARIBALDI, AC LEVI, R SPADACINI, and GE TOMMEI. "QUANTUM-THEORY OF MOLECULE-SURFACE SCATTERING - ROTATIONAL TRANSITIONS." In: *SURFACE SCIENCE* 55.1 (1976), 40–60 (cit. on p. 108).

[216] TR PROCTOR, DJ KOURI, and RB GERBER. "DELTA-MJ TRANSITIONS IN HOMONUCLEAR MOLECULE-SCATTERING OFF CORRUGATED SURFACES - SQUARE AND RECTANGULAR LATTICE SYMMETRY AND PURELY REPULSIVE INTERACTION." In: *JOURNAL OF CHEMICAL PHYSICS* 80.8 (1984), 3845–3858 (cit. on p. 108).

[217] JV LILL and DJ KOURI. "COMPARISONS OF APPROXIMATE AND EXACT QUANTAL MOLECULE SURFACE SCATTERING CALCULATIONS." In: *CHEMICAL PHYSICS LETTERS* 112.3 (1984), 249–257 (cit. on p. 108).

[218] RC MOWREY and DJ KOURI. "CLOSE-COUPLING WAVE PACKET APPROACH TO NUMERICALLY EXACT MOLECULE SURFACE SCATTERING CALCULATIONS." In: *JOURNAL OF CHEMICAL PHYSICS* 84.11 (1986), 6466–6473 (cit. on p. 108).

[219] AC LEVI and V TARDITI. "ROTATIONAL POLARIZATIONS OF HYDROGEN MOLECULES COLLIDING WITH SURFACES." In: *SURFACE SCIENCE* 219.1-2 (1989), 235–248 (cit. on p. 108).

[220] NR HILL. "QUADRUPOLE INTERACTION IN THE SCATTERING OF H-2 FROM THE SURFACE OF LIF - ROTATIONAL TRANSITIONS." In: *PHYSICAL REVIEW B* 19.8 (1979), 4269–4276 (cit. on p. 108).

[221] GJ KROES and RC MOWREY. "SCATTERING OF H-2 BY LIF(001) STUDIED USING A NEW MODEL POTENTIAL .1. PREDICTION OF LARGE DIFFERENCES IN DIFFRACTION OF COLD BEAMS OF PARA-H-2, AND NORMAL-H-2." In: *JOURNAL OF CHEMICAL PHYSICS* 103.6 (1995), 2186–2201 (cit. on p. 108).

[222] E Pijper and GJ Kroes. "New predictions on magnetic rotational transitions in scattering of H-2 by LiF(001)." English. In: *PHYSICAL REVIEW LETTERS* 80.3 (1998), 488–491 (cit. on pp. 108, 109, 118–121, 146).

[223] H.F. Busnengo, .C Crespos, W. Dong, J.C. Rayez, and A. Salin. ""Classical dynamics of dissociative adsorption for a nonactivated system: The role of zero point energy"." English. In: *Journal Of Chemical Physics* 116.20 (2002), 9005–9013 (cit. on p. 110).

[224] JC LIGHT, IP HAMILTON, and JV LILL. "GENERALIZED DISCRETE VARIABLE APPROXIMATION IN QUANTUM-MECHANICS." In: *JOURNAL OF CHEMICAL PHYSICS* 82.3 (1985), 1400–1409 (cit. on p. 113).

[225] D KOSLOFF and R KOSLOFF. “A FOURIER METHOD SOLUTION FOR THE TIME-DEPENDENT SCHRODINGER-EQUATION AS A TOOL IN MOLECULAR-DYNAMICS.” In: *JOURNAL OF COMPUTATIONAL PHYSICS* 52.1 (1983), 35–53 (cit. on p. 113).

[226] GC COREY and D LEMOINE. “PSEUDOSPECTRAL METHOD FOR SOLVING THE TIME-DEPENDENT SCHRODINGER-EQUATION IN SPHERICAL COORDINATES.” In: *JOURNAL OF CHEMICAL PHYSICS* 97.6 (1992), 4115–4126 (cit. on p. 113).

[227] M.D. Feit, J.A. Fleck, and A. Steiger. “"Solution of the Schrodinger-equation by a spectral method".” English. In: *Journal Of Computational Physics* 47.3 (1982), 412–433 (cit. on p. 115).

[228] GG BALINTKURTI, RN DIXON, and CC MARSTON. “TIME-DEPENDENT QUANTUM DYNAMICS OF MOLECULAR PHOTOFRAGMENTATION PROCESSES.” In: *JOURNAL OF THE CHEMICAL SOCIETY-FARADAY TRANSACTIONS* 86.10 (1990), 1741–1749 (cit. on p. 115).

[229] G.G. Balintkurti, R.N. Dixon, and C.C. Marston. “"Grid methods for solving the schrodinger-equation and time-dependent quantum dynamics of molecular photofragmentation and reactive scattering processes".” English. In: *International Reviews In Physical Chemistry* 11.2 (1992), 317–344 (cit. on p. 115).

[230] E Pijper, GJ Kroes, RA Olsen, and EJ Baerends. “Reactive and diffractive scattering of H-2 from Pt(111) studied using a six-dimensional wave packet method.” In: *JOURNAL OF CHEMICAL PHYSICS* 117.12 (2002), 5885–5898 (cit. on p. 115).

[231] Kevin J. Nihill, Zachary M. Hund, A.S. Muzas, C. Díaz, M. del Cueto, T. Frankcombe, D. Campi, F. Martín, N.S. Lewis, and S.J. Sibener. To be published. 2016 (cit. on pp. 125, 126, 133).

[232] J. S. Becker, R. D. Brown, E. Johansson, N. S. Lewis, and S. J. Sibener. In: *J. Chem. Phys.* 133 (2010), p. 104705 (cit. on p. 125).

[233] R. D. Brown, Z. M. Hund, D. Campi, L. E. O’Leary, N. S. Lewis, M. Bernasconi, G. Benedek, and S. J. Sibener. In: *Phys. Rev. Lett.* 110 (2013), p. 156102 (cit. on p. 125).

[234] R. D. Brown, Z. M. Hund, D. Campi, L. E. O’Leary, N. S. Lewis, M. Bernasconi, G. Benedek, and S. J. Sibener. In: *J. Chem. Phys.* 141 (2014), p. 024702 (cit. on p. 125).

[235] H. Yu, L. J. Webb, R. S. Ries, S. D. Solares, W. A. Goddard, J. R. Heath, and N. S. Lewis. In: *J. Phys. Chem. B* 109 (2005), 671–4 (cit. on p. 125).

[236] H. Yu, L. J. Webb, J. R. Heath, and N. S. Lewis. In: *Appl. Phys. Lett.* 88 (2006), p. 252111 (cit. on p. 125).

[237] R. Hunger, R. Fritsche, B. Jaeckel, W. Jaegermann, L. Webb, and N. S. Lewis. In: *Phys. Rev. B* 72 (2005), p. 045317 (cit. on p. 125).

[238] A. Bansal, X. Li, S. I. Yi, W. H. Weinberg, and N. S. Lewis. In: *J. Phys. Chem. B* 105 (2001), 10266–10277 (cit. on p. 125).

[239] L. J. Webb, S. Rivillon, D. J. Michalak, Y. J. Chabal, and N. S. Lewis. In: *J. Phys. Chem. B* 110 (2006), 7349–56 (cit. on p. 125).

[240] L. E. O'Leary, E. Johansson, B. S. Brunschwig, and N. S. Lewis. In: *J. Phys. Chem. B* 114 (2010), 14298–302 (cit. on p. 125).

[241] K. T. Wong and N. S. Lewis. In: *Acc. Chem. Res.* 47 (2014), 3037–3044 (cit. on p. 125).

[242] D. A. King and M. G. Wells. In: *Surf. Sci.* 29 (1972), 454–482 (cit. on p. 125).

[243] D. Barredo, G. Laurent, P. Nieto, D. Farías, and R. Miranda. In: *J. Chem. Phys.* 133 (2010), p. 124702 (cit. on p. 126).

[244] D. Farías, R. Miranda, K. H. Rieder, W. A. Diño, K. Fukutani, T. Okano, H. Kasai, and A. Okiji. In: *Chem. Phys. Lett.* 359 (2002), 127–134 (cit. on p. 126).

[245] G. Laurent, D. Barredo, D. Farías, R. Miranda, C. Díaz, P. Rivière, M. F. Somers, and F. Martín. In: *Phys. Chem. Chem. Phys.* 12 (2010), 14501–14507 (cit. on pp. 126, 135).

[246] Chien-fan Yu, K.B. Whaley, C.S. Hogg, and S.J. Sibener. "'"Investigation of the spatially isotropic component of the laterally averaged molecular hydrogen/Ag(111) physisorption potential"." English. In: *Journal of Chemical Physics* 83 (8 1985), 4217–34 (cit. on p. 126).

[247] D. Cvetko, A. Morgante, A. Santaniello, and F. Tommasini. In: *J. Chem. Phys.* 104 (1996), 7778 –7783 (cit. on p. 126).

[248] K. B. Whaley, C. Yu, C. S. Hogg, J. C. Light, and S. J. Sibener. In: *J. Chem. Phys.* 83 (1985), 4235–4255 (cit. on pp. 126, 127).

[249] P. Nieto, D. Farías, R. Miranda, M. Luppi, E. J. Baerends, M. F. Somers, M. J. T. C. van der Niet, R. A. Olsen, and G. J. Kroes. In: *Phys. Chem. Chem. Phys.* 13 (2011), 8583–8597 (cit. on p. 126).

[250] G.-J. Kroes and C. Díaz. In: *Chem. Soc. Rev.* (2015) (cit. on p. 126).

[251] H.J. Monkhorst and J.D. Pack. In: *Phys. Rev. B* 13 (1976), 5188–5192 (cit. on p. 128).

[252] T. Hom, W. Kiszenik, and B. Post. In: *J. Appl. Cryst.* 8 (1975), 457–458 (cit. on p. 128).

[253] C. Díaz, J. K. Vincent, G. P. Krishnamohan, R. A. Olsen, G. J. Kroes, K. Honkala, and J.K. Nørskov. In: *Phys. Rev. Lett.* 96 (2006), 1–4 (cit. on p. 128).

[254] Michael A. Collins. “Molecular potential-energy surfaces for chemical reaction dynamics.” In: *Theoretial Chemistry Accounts* 108 (2002), pp. 313–324 (cit. on p. 129).

[255] W. C. Swope, H. C. Andersen, P. H. Berens, and K. R. Wilson. In: *J. Chem. Phys.* 76 (1982), 637–649 (cit. on p. 130).

[256] H. F. Busnengo, W. Dong, P. Sautet, and A. Salin. In: *Phys. Rev. Lett.* 87 (2001), 127601–1 (cit. on p. 130).

[257] C. Díaz, H. F. Busnengo, F. Martin, and A. Salin. In: *J. Chem. Phys.* 118 (2003), 2886–2892 (cit. on p. 130).

[258] M Ehara, HD Meyer, and LS Cederbaum. “Multiconfiguration time-dependent Hartree (MCTDH) study on rotational and diffractive inelastic molecule-surface scattering.” English. In: *JOURNAL OF CHEMICAL PHYSICS* 105.19 (1996), 8865–8877 (cit. on p. 130).

[259] A Capellini and APJ Jansen. “Convergence study of multi-configuration time-dependent Hartree simulations: H-2 scattering from LiF(001).” English. In: *JOURNAL OF CHEMICAL PHYSICS* 104.9 (1996), 3366–3372 (cit. on p. 130).

[260] D. Neuhauser. In: *Chem. Phys. Lett.* 173 (1992) (cit. on p. 131).

[261] YK Zhang and WT Yang. “Comment on “Generalized gradient approximation made simple”.” English. In: *PHYSICAL REVIEW LETTERS* 80.4 (1998), 890 (cit. on p. 163).

[262] J.P. Perdew, A. Ruzsinszky, G.I. Csonka, O.A. Vydrov, G.E. Scuseria, L.A. Constantin, X. Zhou, and K. Burke. In: *Phys. Rev. Lett.* 100 (2008), p. 136406 (cit. on p. 163).

[263] T. Yagi. In: *Phys. Chem. Solids* 39 (1978), p. 563 (cit. on p. 164).

[264] C Crespos, HF Busnengo, W Dong, and A Salin. “"Analysis of H_2 dissociation dynamics on the Pd(111) surface".” English. In: *Journal Of Chemical Physics* 114.24 (2001), 10954–10962 (cit. on p. 165).

[265] Cristina Díaz. “"Difusión molecular por superficies metálicas: H_2/Pd(111 y H_2/Pd(110)".” PhD thesis. Universidad Autónoma de Madrid, 2004 (cit. on pp. 170, 171).

[266] Paula Rivière Herrera. “Dissociative adsorption and scattering of H_2 molecules from the NiAl(110) surface.” PhD thesis. Universidad Autónoma de Madrid, 2005 (cit. on p. 170).